

Laser Characterization and Stabilization for Precision Interferometry

Von der Fakultät für Mathematik und Physik
der Gottfried Wilhelm Leibniz Universität Hannover
zur Erlangung des Grades

Doktor der Naturwissenschaften
– **Dr. rer. nat.** –

genehmigte Dissertation
von

Dipl.-Phys. Patrick Kwee

geboren am 10. Juni 1979 in Hannover

2010

Referent: Prof. Dr. Karsten Danzmann
Korreferent: Priv. Doz. Dr. Benno Willke
Tag der Promotion: 8. Januar 2010

Preface

The last four years, during my doctoral studies at the Albert-Einstein-Institute in Hannover, have been a great and fascinating time, which I enjoyed a lot, but which at the same time also went by much too fast. The institute, the people, and the field of research contributed each in their own way to this period of my life. During my studies it was especially a pleasure to design, plan and perform experiments and to carry out my own ideas. Interferometric gravitational wave detectors are an exciting and in particular a wide-ranging field of research. Thus I learned many different aspects from the experts at the institute, ranging from optics over electronics to data analysis. Of course many persons contributed to this enjoyable time and I would like to express my gratitude at this point.

I would like to thank Karsten Danzmann for the exceptional infrastructure of the Albert-Einstein-Institute, which allowed me to concentrate on the really important aspects of research. I want to thank Benno Willke for the very personal and dedicated mentoring, for his guidance, and for the countless scientific discussions. For the friendly working atmosphere, the interesting group meetings and the joint laboratory work I am grateful to my colleagues of the *laser group*, Tobias Meier, Henning Ryll, Jessica Dück, Marc Tesch, Anatoli Fedynitch, Hyunjoo Kim, Christina Krämer, Marina Dehne, and Robin Bähre. In particular I would like to thank Frank Seifert for the many years of close collaboration, Michaela Pickenpack for taking over the fabrication of the diagnostic breadboards, and Jan Pöld for the dedicated support in working with the Advanced LIGO laser – not to forget all the other colleagues of the institute, with whom it was a pleasure to share ideas and experiences, and the electrical and mechanical workshop, which built so many components for my experiments. I would like to thank the colleagues of the Laser Zentrum Hannover, Lutz Winkelmann, Oliver Puncken, Christian Veltkamp, Bastian Schulz, Sascha Wagner, Matthias Hildebrandt, Maik Frede, and Peter Weßels, for such a good collaboration concerning various laser systems. I thank Albrecht Rüdiger for many helpful comments and proofreading of not only this thesis but also of several articles in the last few years.

Finally a special thanks goes to my family, in particular to my wife, for their support of my doctoral studies and everything beyond.

Patrick Kwee, November 2009

Abstract

Lasers for high-precision optical measurements, in particular for ground-based interferometric gravitational wave detectors, were characterized and stabilized. A compact, automated laser beam diagnostic instrument, based on an optical ring resonator, was developed and used to characterize the output beam of different continuous-wave, single-frequency lasers at wavelengths of 1064 nm and 1550 nm. The laser beam fluctuations in power, frequency and pointing as well as the spatial beam quality were investigated. The results were used, amongst others, for laser stabilization design.

Different laser stabilization methods are reviewed and the laser stabilization concept for the second-generation gravitational wave detector *Advanced LIGO* is described. Important components of this stabilization were developed, such as the so-called *pre-mode-cleaner* resonator for filtering various laser beam parameters.

Furthermore, several laser power stabilization experiments were performed. A high-sensitivity, quantum-noise-limited detector for power fluctuations consisting of an array of photodiodes was developed and was used to stabilize the output power of a laser in the audio frequency band, achieving an independently measured relative power noise of $2.4 \times 10^{-9} \text{ Hz}^{-1/2}$ at 10 Hz. In addition, a novel power-fluctuation detection technique, called *optical ac coupling*, which is based on photo-detection in reflection of an optical resonator, was investigated theoretically and experimentally. This technique allows new power stabilization schemes, especially important for next generation gravitational wave detectors, and it can beat the theoretical quantum limit of traditional schemes by up to 6 dB, among other benefits. A sensitivity of $7 \times 10^{-10} \text{ Hz}^{-1/2}$ for relative power fluctuations was experimentally demonstrated at radio frequencies using an optical ac coupled photodetector.

Keywords: laser characterization, laser power stabilization, gravitational wave detector.

Kurzfassung

Laser für optische Präzisionsmessungen, insbesondere für interferometrische Gravitationswellendetektoren, wurden charakterisiert und stabilisiert. Ein kompaktes, automatisiertes Diagnoseinstrument für Laserstrahlen, basierend auf einem optischen Ringresonator, wurde entwickelt und verwendet, um die Strahlen verschiedener einfrequenter Dauerstrichlaser bei Wellenlängen von 1064 nm und 1550 nm zu charakterisieren. Dabei wurde das Rauschen der Ausgangsleistung, der Frequenz und der Strahllage als auch die Strahlqualität untersucht. Die Ergebnisse wurden unter anderem für das Design von Laserstabilisierungen verwendet.

Verschiedene Laserstabilisierungsverfahren und das Stabilisierungskonzept für den Gravitationswellendetektor zweiter Generation *Advanced LIGO* sind beschrieben. Bedeutende Komponenten dieser Stabilisierung wurden entwickelt, wie z.B. der so genannte *pre-mode-cleaner* Resonator, der mehrere Laserstrahlparameter filtert.

Darüber hinaus wurden mehrere Experimente zur Leistungsstabilisierung von Lasern durchgeführt. Ein hochempfindlicher, quantenrauschbegrenzter Detektor für Leistungsfluktuationen, der aus mehreren Photodioden bestand, wurde entwickelt und benutzt, um die Ausgangsleistung eines Lasers im Audiofrequenzbereich zu stabilisieren. Dabei wurde ein unabhängig gemessenes relatives Leistungsrauschen von $2.4 \times 10^{-9} \text{ Hz}^{-1/2}$ bei 10 Hz erreicht. Weiterhin wurde eine neuartige Detektionstechnik für Leistungsfluktuationen, das so genannte *optical ac coupling*, basierend auf der Leistungsdetektion in Reflexion eines optischen Resonators, theoretisch und experimentell untersucht. Diese Technik ermöglicht neue Leistungsstabilisierungsschemata, die insbesondere für die nächste Generation von Gravitationswellendetektoren bedeutend sein werden und die neben anderen Vorteilen die theoretische Quantengrenze traditioneller Schemata um bis zu 6 dB unterbieten können. Eine Empfindlichkeit von $7 \times 10^{-10} \text{ Hz}^{-1/2}$ für relatives Leistungsrauschen bei Radiofrequenzen konnte mithilfe eines *optical ac coupled* Photodetektors experimentell demonstriert werden.

Schlagworte: Lasercharakterisierung, Laserleistungsstabilisierung, Gravitationswellendetektor.

Contents

1	Introduction	1
2	Laser Characterization	3
2.1	Laser Beam Parameters	4
2.2	Diagnostic Breadboard	7
2.2.1	Experiment and Methods	7
2.2.2	Experimental Challenges	16
2.2.3	Control and Automation	21
2.3	Characterizations	25
2.3.1	Nonplanar Ring Oscillator	26
2.3.2	Advanced LIGO Laser	31
2.3.3	Photonic Crystal Fiber Laser	34
2.3.4	Fiber Laser at 1550 nm	36
2.4	Summary	37
3	Laser Stabilization	39
3.1	Review of Stabilization Methods	40
3.1.1	Passive Filtering vs. Active Feedback	40
3.1.2	Power Stabilization	42
3.1.3	Frequency Stabilization	45
3.1.4	Pointing Stabilization	47
3.1.5	Beam Quality	49
3.2	Stabilization Concept of Advanced LIGO	50
3.2.1	Advanced LIGO	51
3.2.2	Power Stabilization Concept	54
3.2.3	Frequency Stabilization Concept	57
3.2.4	Pointing Stabilization Concept	58
3.2.5	Beam Quality	60
3.2.6	Pre-mode-cleaner	60
3.3	Summary	62

4	Traditional Power Stabilization	63
4.1	Quantum Limit	64
4.2	High Power Photodiode Array	70
4.2.1	Optical and Mechanical Design	70
4.2.2	Electronics	73
4.3	Power Stabilization Experiment	75
4.3.1	Experimental Setup	75
4.3.2	Results	77
4.4	Summary	80
5	Optical AC Coupling	83
5.1	Optical AC Coupling Technique	84
5.2	Quantum Limit of Power Stabilization Schemes	87
5.2.1	Limit of Different Stabilizations	88
5.2.2	Case Study	95
5.3	Experiments	97
5.3.1	Setup	98
5.3.2	Experimental Challenges	102
5.4	Noise Couplings	106
5.4.1	Residual Frequency Noise	107
5.4.2	Mode Fluctuations	108
5.4.3	Resonator-internal Scattering	110
5.5	Results	121
5.6	Summary	126
6	Conclusion	129

Abbreviations

ACC	ac coupling cavity
A/D	analog to digital
AOM	acousto-optical modulator
CDS	control and data systems
D/A	digital to analog
DAQ	data acquisition
DBB	diagnostic breadboard
DWS	differential wave front sensing
EOAM	electro-optic amplitude modulator
EOM	electro-optic modulator
FSR	free spectral range
GWD	gravitational wave detector
HEPA	High Efficiency Particulate Air
IMC	input mode-cleaner
InGaAs	indium gallium arsenide
IO	input optics
LIGO	Laser Interferometer Gravitational-Wave Observatory
Nd:YAG	neodymium-doped yttrium aluminum garnet
NPRO	nonplanar ring oscillator
PDH	Pound-Drever-Hall
PMC	pre-mode-cleaner
PRC	power recycling cavity
PRM	power recycling mirror
PSL	pre-stabilized laser
PZT	piezoelectric transducer
RF	radio frequency
RPN	relative power noise
TEM	transversal electromagnetic wave
ULE	ultra low expansion glass

Symbols

α	carrier amplitude, see Eq. 4.6
$\alpha^2, \alpha_{\text{las}}^2$	average laser beam photon flow
$\epsilon, \epsilon_x, \epsilon_y$	beam pointing, see Eq. 2.6
ζ	Gouy phase
θ_D	Gaussian beam half divergence angle
λ	wavelength
ν	optical frequency

Symbols

ϕ_0, ϕ_1	phase shift for one resonator round-trip, see Eq. 5.47
Ω	optical angular frequency
ω	angular frequency
A, A^\dagger	lowering and raising operator, see Eq. 4.5
a	impedance matching, see Eq. 5.2
C	scattering coupling factor, see Eq. 5.47
c	vacuum speed of light, $c = 299\,792\,458$ m/s
c_{lm}	modal weights, see Eq. 2.1
e	elementary charge, $e = 1.602 \times 10^{-19}$ C
\mathcal{F}	optical resonator finesse
f	frequency
f_0	resonator bandwidth
g	maximum gain of $G(f)$, see Eq. 5.4
$G(f)$	transfer function of the optical ac coupling, see Eq. 5.4
h	Planck constant, $h = 6.626 \times 10^{-34}$ J s
$H(f)$	feedback control loop gain
$h(f)$	approximated transfer function of a resonator, see Eq. 5.3
I	photocurrent
N	photon number operator, see Eq. 4.2
$ n\rangle$	Fock state, see Eq. 4.2
\bar{n}	expectation value of N , see Eq. 4.8
p	relative power in parasitic modes, see Eq. 5.6
$P_{\text{fund}}/P_{\text{tot}}$	fundamental power, see Eq. 2.5
P	laser beam power
R	mirror curvature radius
r	beam splitter power reflectivity
r_0, r_1	amplitude reflectivity for one resonator round-trip, see Eq. 5.47
S	double-sided power spectrum, see Eq. 4.10
s	single-sided linear spectral density, see Eq. 4.11
s_q	quantum noise single-sided linear spectral density
t	time
U	complex field amplitude
$U_{\text{circ}}, \vec{U}_{\text{circ}}$	resonator-internal circulating complex field amplitude
$U_{\text{in}}, \vec{U}_{\text{in}}$	input complex field amplitude
$U_{\text{refl}}, \vec{U}_{\text{refl}}$	reflected complex field amplitude
$U_{\text{trans}}, \vec{U}_{\text{trans}}$	transmitted complex field amplitude
$\text{Var}(N)$	variance of N , see Eq. 4.9
w_0	Gaussian beam waist radius
X_1	amplitude quadrature operator, see Eq. 4.7

Introduction

The invention of the laser in the 1960's revolutionized metrology. Light produced by a laser allowed measurements of unprecedented precision due to its collimated, monochromatic, temporally and spatially coherent beam. Furthermore, due to the rapid development in the field of lasers and other technologies over the last few decades, the first direct detection of a gravitational wave is close at hand.

These waves of spacetime-curvature, predicted by Albert Einstein in 1916 using his general theory of relativity, are radiated by accelerated massive objects and in general cause a distance change between free test objects (see e.g. [Mis73]). However, these length changes are so tiny that even astrophysical events – such as supernova explosions, inspiraling neutron stars or black holes, where gigantic massive objects are extremely accelerated – cause unimaginably small relative length changes in the order of 10^{-24} to 10^{-22} on Earth (see e.g. [Cut02]). Nevertheless in the last few years several laser Michelson interferometers [Abr92, Wil02, Ace02, And01] achieved such a sensitivity that they can measure differential length changes of less than 10^{-19} m (1/10 000 of the proton diameter) of their interferometer arms, which have a length of up to a few kilometers. At the moment this first generation of ground-based, interferometric gravitational wave detectors (GWDs) observe the sky and wait for a strong astrophysical event in order to directly detect a gravitational wave for the first time.

Meanwhile second generation detectors [Fri03, Fla05] are almost ready and will be installed in the next few years. These detectors have an anticipated, tenfold better sensitivity than the first generation and will presumably detect gravitational waves on a day-to-day basis. They will open the door for gravitational wave astronomy (see e.g. [Sch99]) and allow a new view of the universe, maybe helping to solve the cosmological mysteries of our time.

However, to achieve the ambitious sensitivity of these gravitational wave observatories, much technology had to be and still has to be developed. One key technology is the laser system, as already mentioned. On the one hand these lasers need a high output power to reach a high signal-to-noise ratio in the gravitational wave channel. On the other hand they have to be very stable concerning almost all beam parame-

ters at the same time, since otherwise laser noise coupling to the gravitational wave channel could mask the faint signals. This thesis is about *laser characterization*, which is essential for the development of such lasers and their stabilizations, and about *laser stabilization*, which reduces technical laser noise and is indispensable for GWDs to make such high-precision measurements possible.

Outline of the Thesis

Many aspects of this thesis were motivated by the second generation GWD *Advanced LIGO* (Laser Interferometer Gravitational-Wave Observatory) and the laser system specifically developed for it.

Chapter 2 describes a laser beam characterization instrument, the so-called *diagnostic breadboard*, which was developed as part of this thesis. This instrument allows one to quickly and accurately characterize a laser, which is essential for the development of new laser systems and their stabilizations. This versatile instrument was used to characterize several lasers, and it will be an important part of the Advanced LIGO laser diagnostics.

Chapter 3 presents the Advanced LIGO laser stabilization concept, where the characterization results of the previous chapter played a decisive role. In this context many different laser stabilization methods are reviewed and the Advanced LIGO detector and the coupling mechanisms of laser noise are described in more detail. An important element of the stabilization, the *pre-mode-cleaner*, was developed in this thesis. The most demanding and critical aspect of the Advanced LIGO laser stabilization is the laser power stabilization. Several experiments performed are described in the subsequent chapters.

Laser power stabilization is crucial not only for Advanced LIGO, but also leads the way in the development of high-sensitivity photodetectors, which are essential for nearly all optics experiments. In order to improve their quantum-noise-limited sensitivity, the detected laser power has to be increased. However, the maximum power handling capability of photodetectors commonly used is already reached. Two different, complementing approaches were taken in this thesis to increase the effective detected laser power and with it the sensitivity of the power detector:

Chapter 4 describes an array of multiple photodiodes, which increases the total power detected by scaling the number of photodiodes. In a power stabilization experiment the so far best sensitivity for power fluctuations in the audio frequency bands has been demonstrated.

Chapter 5 presents a novel detection technique, the so-called *optical ac coupling*, which increases the sensitivity of a photodetector without increasing the average power detected. This technique opens a new range of achievable power stabilities and photodetector sensitivities. A sensitivity for relative power noise in the upper $10^{-10} \text{ Hz}^{-1/2}$ range in the radio frequency band has been demonstrated for the first time.

Finally in Chapter 6, the main conclusions and implications of the thesis are summarized.

Laser Characterization

Laser characterization is essential for development, selection, stabilization, and monitoring of lasers. Depending on the application field or experiment the characterization criteria differ. In this thesis lasers developed for ground-based interferometric GWDs are characterized. In general these continuous-wave, single-frequency, and linearly polarized lasers stand out due to high intrinsic stability and high output power. In this field a highly sensitive characterization of the power, frequency, and pointing noise in the acoustic frequency band (≈ 10 Hz to 10 kHz) as well as the spatial beam quality, and output power is especially important since the sensitivity of the GWDs (see Chapter 3) depends on these parameters.

In the field of laser development characterizations are necessary, e.g., to analyze the laser performance or to verify design requirements. For the stabilization of lasers, which is indispensable for GWDs, the characterization results are used to select between active and passive stabilization methods and to determine the required noise suppression. Finally lasers are essential but often complex components in experiments. Thus a continuous monitoring and characterization of important laser beam parameters is worthwhile in order to quickly detect malfunctions and determine long-term trends for projections.

Several laser characterizations in combination with laser stabilization can be found in the literature [Day91, Bon96, Ueh97, Wil98, Sei06]. However, these characterizations mainly considered only one or a few laser beam parameters important for GWDs. Furthermore the measurement equipment was often tightly integrated in the experiment so that no other laser system could be characterized with the same instruments. To my knowledge no compact transportable instrument was available so far which was able to characterize all important beam parameters for GWDs. Only subsets of these beam parameters could be characterized with similar instruments [Her02, Kwe05].

Therefore a laser beam diagnostic tool, called diagnostic breadboard (DBB), was developed to allow fast, complete and automated laser characterizations. The DBB was used to perform comparable characterizations of different laser systems with important results for the development and stabilization of lasers.

In the following sections the characterization methods are described, starting with a brief definition of the most important laser beam parameters (Sec. 2.1) and followed by a description of the DBB (Sec. 2.2) including the measurement methods. In the subsequent Section 2.3 a selection of characterization results of several laser systems is presented and discussed. These results were important aspects in the design of the laser stabilization described in Chapter 3.

The main results of this chapter have already been published in [Hil06, Kwe07, Fre07b, Kwe08a].

2.1 Laser Beam Parameters

In the following a model for laser beams is introduced, which is used to define the laser beam parameters characterized in this thesis.

With this model continuous-wave, single-frequency, linear-polarized laser beams can be described. The complex field amplitude $U(\vec{r}, t)$ of the laser beam is expressed in the paraxial approximation as

$$U(\vec{r}, t) = U_0(t) \times \exp(2\pi i \nu(t) t) \times \sum_{l,m \geq 0} c_{lm}(t) \Phi_{lm}(\vec{r}), \quad (2.1)$$

where U_0 is the time dependent amplitude, ν is the laser frequency, Φ_{lm} are the complex amplitudes of the Hermite-Gaussian modes TEM_{lm} [Sie86, Chap. 16.4], and c_{lm} the complex expansion coefficients or modal weights. The functions Φ_{lm} form an orthogonal, complete set of functions that depends on the beam axis, waist size, and waist position. The coefficients c_{lm} and the functions Φ_{lm} are normalized according to

$$\int dx dy |\Phi_{lm}(\vec{r})|^2 = 1 \quad \text{and} \quad \sum_{l,m \geq 0} |c_{lm}(t)|^2 = 1. \quad (2.2)$$

The properties of a laser beam can be divided into categories according to the three terms in Eq. (2.1): The power of the laser beam is determined by $U_0(t)$, the frequency by $\nu(t)$ and the beam geometry, including the spatial beam quality¹, beam pointing, mode matching, astigmatism, and ellipticity, by the modal weights $c_{lm}(t)$.

Power

The absolute power $P(t)$ of the laser beam is deduced from the amplitude $U_0(t)$

$$P(t) \propto |U_0(t)|^2, \quad [P(t)] = \text{W}. \quad (2.3)$$

¹An exact definition of *spatial beam quality* is given in this section later on.

Power fluctuations are often normalized with the average absolute power. Thus the relative power $P(t)/P_0$ is given by

$$P(t)/P_0 = |U_0(t)|^2 / \overline{|U_0(t)|^2} \quad \text{with} \quad \overline{|U_0(t)|^2} = \frac{1}{T} \int_T dt \cdot |U_0(t)|^2, \quad (2.4)$$

where T is the measurement duration. The fluctuations of $P(t)/P_0$ are called *relative power fluctuations* or *relative power noise* (RPN, often also called RIN for *relative intensity noise*) and are often characterized by their single-sided linear spectral density, the root-mean-square (rms) or peak-to-peak value.

Frequency

The average frequency ν of the laser beam is often given by the vacuum wavelength $\lambda=c/\nu$. Fluctuations of ν , called frequency fluctuations or frequency noise, are as well characterized by their single-sided linear spectral density, the rms or peak-to-peak value.

Beam Quality

Most laser beam parameters, such as the power, frequency, or pointing, are used unambiguously in the literature; however, the spatial beam quality is an exception. Often the deviation of the laser beam from an ideal Gaussian fundamental mode (TEM_{00}) is used to characterize the beam quality. Different definitions have been established for the various fields of application in order to quantify the beam quality. If for example the beam propagation is important for the application, then the M^2 factor [Sie90] is often used. This factor primarily compares the divergence of the test beam with the divergence of an ideal TEM_{00} beam.

In fields of applications where optical resonators are involved, the power in the fundamental mode TEM_{00} compared with the overall power is a better criterion for the beam quality since the resonators are often stabilized to a resonance of the TEM_{00} mode. In this thesis this ratio, $P_{\text{fund}}/P_{\text{tot}}$, is called *fundamental power* and directly specifies the power fraction that can be coupled into an ideal optical resonator that is resonant to the TEM_{00} mode. A high beam quality corresponds to a fundamental power near 100%.

$$P_{\text{fund}}/P_{\text{tot}} = |c_{00}|^2 / \sum_{l,m} |c_{lm}|^2 = |c_{00}|^2, \quad [P_{\text{fund}}/P_{\text{tot}}] = 1. \quad (2.5)$$

Many optical resonators are used in GWDs and therefore the fundamental power is the appropriate value to quantify the beam quality. Since the fundamental power cannot be determined from the M^2 factor as shown in [Kwe07] this factor is not suitable for beam quality characterizations in this field.

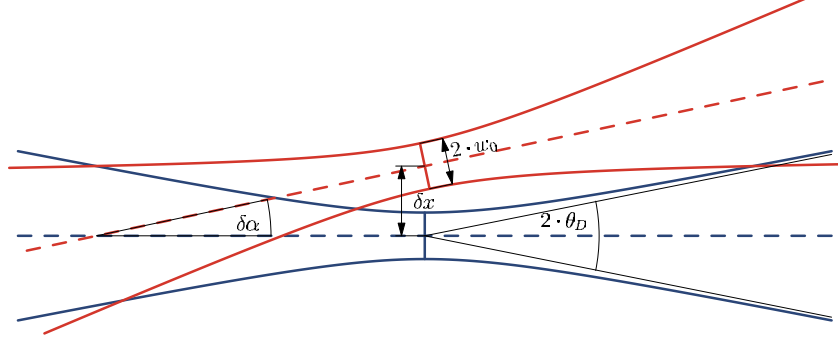


Figure 2.1: Two Gaussian beams and their relative beam pointing.

Beam Pointing

Beam pointing and its fluctuation relative to a given reference axis can be described by the complex quantity $\epsilon(t)$,

$$\epsilon(t) = \frac{\delta x}{w_0} + i \frac{\delta \alpha}{\theta_D}, \quad [\epsilon] = 1, \quad (2.6)$$

where δx is the transversal shift at the position of the waist and $\delta \alpha$ the tilt of the beam (Fig. 2.1). These parameters are normalized with the beam waist radius w_0 and the half divergence angle θ_D of the Gaussian beam. The complex amplitude of such a shifted and tilted beam can be expanded in Hermite-Gauss modes of the reference beam in the $\epsilon \ll 1$ limit [And84, Avi06]:

$$U(\epsilon_x, \epsilon_y) \approx \Phi_{00} + \epsilon_x \Phi_{10} + \epsilon_y \Phi_{01}. \quad (2.7)$$

Therefore $\epsilon_x(t)$ and $\epsilon_y(t)$ can be determined by measuring the relative field amplitudes of the TEM_{10} and TEM_{01} modes:

$$\epsilon_x(t) \approx c_{10}/c_{00}, \quad \epsilon_y(t) \approx c_{01}/c_{00}. \quad (2.8)$$

In a similar way the quality of the mode matching², the ellipticity, and the astigmatism of the beam can be determined in first order from the TEM_{20} and TEM_{02} modes, i.e. from c_{20} and c_{02} [And84, Avi06, Kwe07].

An instrument for measuring these laser beam parameters is described in the next section. Low fluctuations of these parameters are crucial for GWDs, especially in the gravitational wave detection band from about 10 Hz to 10 kHz, since they can limit the sensitivity of the GWD. The actual coupling of laser beam fluctuations to the gravitational wave channel is described within the scope of the laser stabilization (see Chapter 3).

²In this context *mode matching* accounts only for the matching of beam waist size and position.

2.2 Diagnostic Breadboard

The diagnostic breadboard (DBB) is a general purpose instrument for laser beam diagnostics, which was developed in this thesis and was used for many laser characterizations. It allows one to measure the laser beam parameters defined in the previous section: power noise, frequency noise and beam pointing fluctuations in a Fourier frequency band from 1 Hz to 100 kHz as well as power noise at radio frequencies (RF) up to 100 MHz and the spatial beam quality. The functioning and the sensitivity of the DBB are described in this section.

The DBB was developed since to my knowledge no instrument existed so far that was able to characterize all important beam parameters in one compact automated device. In several previous experiments lasers and laser beams were characterized, especially in combination with a stabilization of the output power [Sei06, Wil98], the frequency [Day91, Bon96], or the beam quality [Ueh97, Wil98]. However, these characterizations were optimized for the individual experiments and only a few of the beam parameters accessible with the DBB were analyzed. The DBB is an extended and improved version of the instruments described in [Kwe07, Kwe05, Her02].

The DBB can be used in several important application fields: In the field of laser development the laser performance can be quickly measured and dependencies on laser design parameters can be analyzed. Furthermore, the long-term performance of laser systems can be monitored due to the automation, and the DBB can be helpful in localizing laser faults. Thus the DBB will be integrated into the Advanced LIGO laser system [Kin08] and the fabrication of six DBBs has already started. Finally a complete and accurate characterization is necessary for the stabilization of laser systems (see Chapter 3) in order to choose appropriate stabilization methods, sensors, and actuators.

The following subsections describe the experimental setup, the measurement methods used, the sensitivity, the main experimental challenges, and the control and automation with computer systems. Examples of laser characterizations performed with the DBB are presented in the next Section 2.3.

2.2.1 Experiment and Methods

The DBB is optimized for lasers developed for GWDs, concerning the accessible laser beam parameters (Sec. 2.1), the measurement methods, and the sensitivity. In general these lasers have a very low free-running noise in power and frequency, and a very high beam quality (see e.g. Sec. 2.3.1).

The optical design of the DBB is independent of the laser wavelength; however, appropriate coatings of the optical components and photodiode materials have to be used. Several DBBs were built for the wavelength 1064 nm, at which most lasers for current GWDs and other high precision experiments operate, and one was built for 1550 nm. Lasers at 1550 nm are interesting for future GWDs, since silicon, which is one candidate as test mass material, has very low absorption at this wavelength.

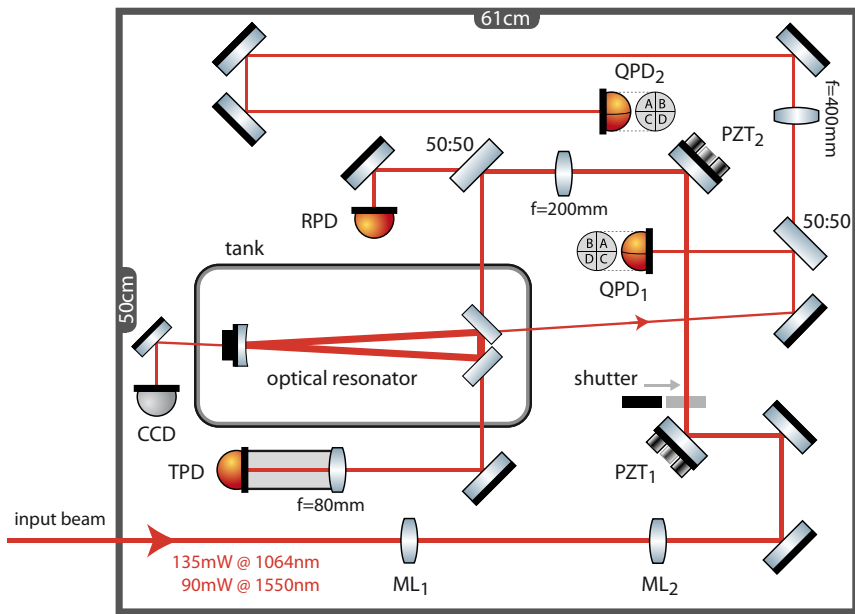
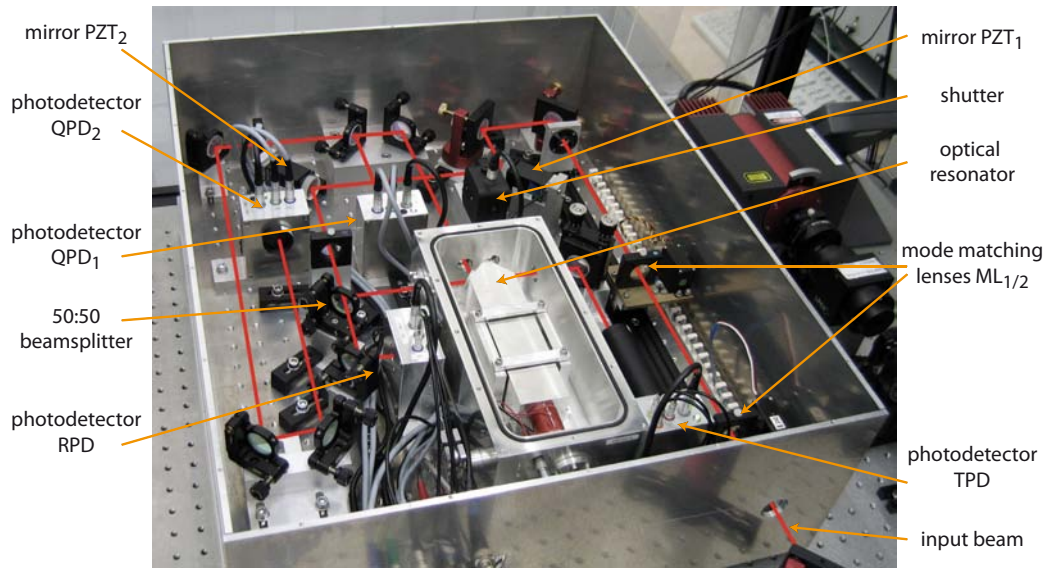


Figure 2.2: Photograph with illustrated beam path and schematic of the diagnostic breadboard optical setup. The tank surrounding the optical resonator is sealed pressure-tight in normal operation and was opened only for the photograph.

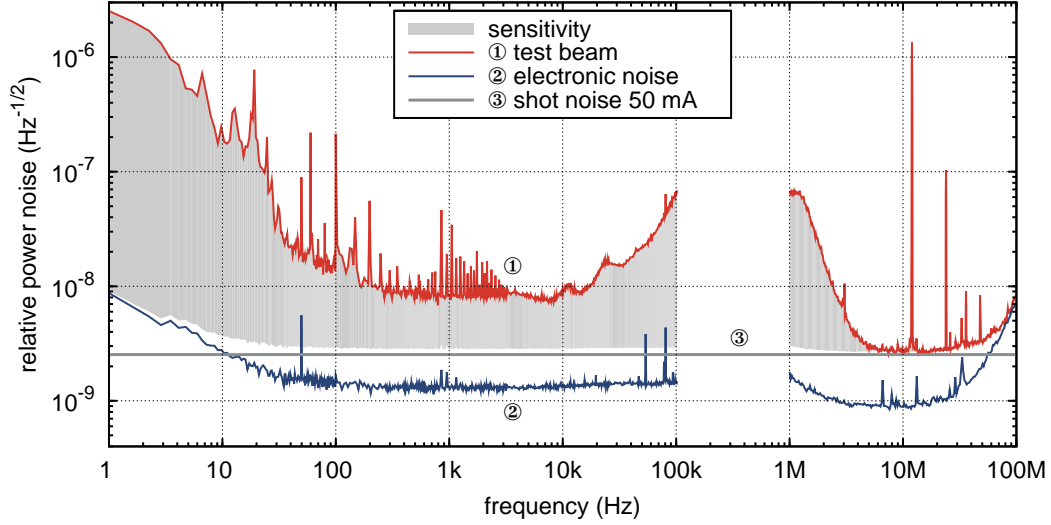


Figure 2.3: Sensitivity for relative power fluctuations. The sum of electronic noise and shot noise is the lower limit for the sensitivity. An upper limit was measured with a power-stabilized test beam. The actual sensitivity is somewhere in the shaded area.

All optical components of the DBB are mounted on a transportable, compact breadboard (61 cm \times 50 cm) (Fig. 2.2). The key component is an optical ring resonator that is used for frequency, pointing and beam quality measurements. Four photodetectors are used to measure the various properties of the input beam. The DBB is optimized and calibrated for an operating point with an input power of 135 ± 15 mW at 1064 nm or 90 ± 10 mW at 1550 nm of p-polarized (horizontal) light. A crate (19 in, six height units) contains all necessary electronics except for power supplies.

The measurement methods, the calibration procedures and the sensitivity are briefly described in the following. Some of the more challenging experimental problems encountered during the development are described in the next Subsection 2.2.2.

Power Noise Measurement

The power of the input beam and the power fluctuations are measured with the photodetector RPD (Fig. 2.2).

This photodetector consists of a 2 mm InGaAs photodiode (Perkin Elmer, C306-42G), a low-noise high-current transimpedance amplifier and signal-conditioning electronics. In the operating point a photocurrent of 50 mA is detected with a -3 dB bandwidth of ≈ 45 MHz. The integrated signal-conditioning electronics optimizes the signal for measurements in the two frequency bands 1 Hz to 100 kHz and 1 MHz to 100 MHz.

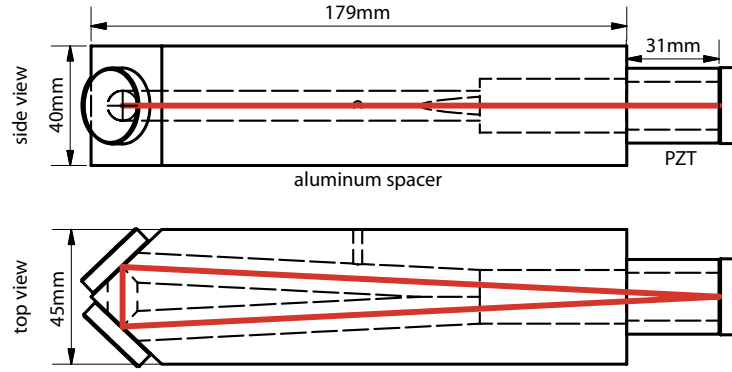


Figure 2.4: Sketch of the optical resonator with illustrated beam path.

A lower limit for the relative power noise sensitivity of the photodetector is given by the electronic noise (measured with no light on the photodetector) and the shot noise level³ calculated from the average photocurrent (Fig. 2.3). An upper limit for the sensitivity can be derived from a measurement of a power-stabilized test beam: For the radio frequency band from 1 MHz to 100 MHz this test beam was prepared by sending a laser beam (NPRO, see Sec. 2.3.1) through an optical resonator with a bandwidth of 1 MHz, which attenuates the technical power noise to a level below the shot noise of about 70 mW for frequencies ≥ 5 MHz. A shot noise limited sensitivity (RPN of $2.5 \times 10^{-9} \text{ Hz}^{-1/2}$ at 50 mA) of the photodetector for frequencies of 5 MHz to 60 MHz was verified with this test beam (Fig. 2.3). In a different experiment the power of the test beam was stabilized for frequencies below 100 kHz using an acousto-optic modulator and a photodetector in front of the DBB. The residual power noise was then measured independently with the DBB. These values can serve as an upper limit for the relative power noise sensitivity of the DBB (Fig. 2.3).

The signal of the RPD photodetector is also used to trigger an interlock in case of excessive input power. In such an event a mechanical shutter on the DBB is closed in order to protect the photodetectors.

Frequency Noise Measurement

Frequency fluctuations of the input beam are measured with the optical ring resonator as frequency reference (Fig. 2.2, 2.4).

The resonator is similar to the design described in [Wil98, Ueh97]. It consists of two plane 45° mirrors – 1 inch diameter, with a power transmission of 0.88% for the 1064 nm DBB and of 1.1% for the 1550 nm DBB (all quantities are given for p-polarized light) – and one curved high-reflectivity mirror with a curvature of -1 m.

³In principle, shot noise is not a limit, e.g., for amplitude-squeezed beams. However, since the DBB was developed for classical laser beams, non-classical light sources are not considered and thus shot noise is a lower limit for the power noise measurements.

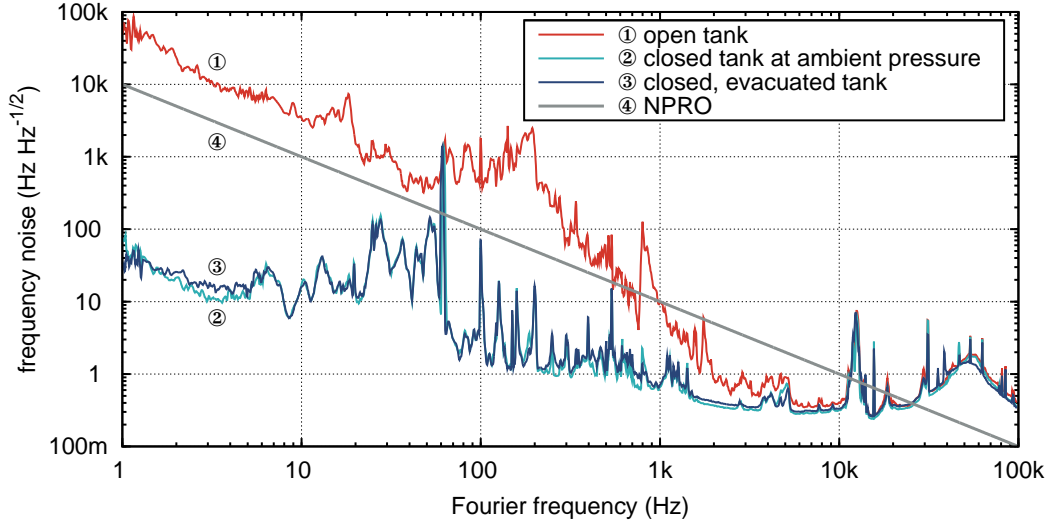


Figure 2.5: Upper limit for the sensitivity for frequency noise in different tank configurations. The typical free-running frequency noise of an NPRO laser is given as reference.

The round-trip length of 420 mm is electronically adjustable by about $5 \mu\text{m}$ with a piezoelectric element (PZT) at the curved mirror. A finesse of $\mathcal{F} \approx 356$ at 1064 nm and $\mathcal{F} \approx 208$ at 1550 nm was measured and a free spectral range (FSR) of 715 MHz was calculated. The waist radius and the half divergence angle of the fundamental mode are $w_0 = 372 \mu\text{m}$ and $\theta_D = 910 \mu\text{rad}$ at 1064 nm and $w_0 = 459 \mu\text{m}$ and $\theta_D = 1075 \mu\text{rad}$ at 1550 nm, and the beam waist is located between the two flat mirrors. The resonator is placed inside an aluminum tank for acoustic shielding and in order to avoid contamination of the resonator mirrors.

The resonator is stabilized to the frequency of the input beam using a dither-lock: The round-trip length of the resonator is modulated at 1 MHz with the PZT in order to create phase modulation sidebands inside the resonator (for more details see Sec. 2.2.2). The input beam and the phase modulated beam leaking out of the resonator are superposed at the input coupling mirror and are detected with photodetector QPD₁. The demodulated sum signal of this quadrant photodetector is used as error signal for the control of the resonator round-trip length. The dither-lock, which has already been described as transmission lock in [Whi65], can be understood as a variant of the well known Pound-Drever-Hall locking method [Bla01, Dre83] but with the phase modulation sidebands being generated in the resonator by length modulation. The resonator is stabilized to a resonance of the fundamental mode with a bandwidth of a few kilohertz using a feedback control loop and the PZT as actuator.

Frequency fluctuations of the input beam are calculated from the control and error signal in a Fourier frequency band from 1 Hz to 100 kHz. The dither-lock

frequency of 1 MHz limits the bandwidth of the frequency noise measurement to about 100 kHz.

In this frequency measurement setup the resonance frequency of one fundamental mode of the resonator is used as frequency reference. The stability of this reference depends on the round-trip length stability of the resonator. The spacer of the resonator was manufactured of aluminum, and its stability as frequency reference is limited for Fourier frequencies below 1 Hz by environment temperature fluctuations.

The frequency noise measurements are calibrated with the macroscopic round-trip length of the resonator: The FSR of the resonator is calculated from the round-trip length and thus the control signal at the PZT is calibrated by determining the signal needed to scan exactly one FSR. At frequencies above the control loop bandwidth a transfer function from the control signal to the error signal is measured to calibrate the error signal as well.

With a frequency-stabilized test beam an upper limit of the sensitivity for frequency fluctuations was measured (Fig. 2.5). The test beam was stabilized to a high-finesse in-vacuum reference resonator made of ultra low expansion glass (ULE). Additional investigations showed that the tank on the DBB significantly improves the stability of the resonator as frequency reference. Compared with a closed tank, the measured frequency fluctuations increase with an open one in some frequency bands by two to three orders of magnitude. In a further experiment the tank was evacuated, but the sensitivity of the measurement system was unaffected. Thus a closed tank at atmospheric pressure is used for all further experiments.

Beam Pointing Measurement

The pointing fluctuations of the input beam are measured by using the differential wave front sensing technique (DWS) and the ring resonator as pointing reference.

This measurement method uses a laser beam as reference and measures the shift and tilt between the input beam and the reference beam by analyzing the interference of the input and the reference beam. The reference beam is the fundamental mode of the ring resonator, which is excited by the test beam itself. To measure the relative shift and tilt, the DWS method [Mor94a] is used, which as an interferometric measurement method allows a very accurate measurement of relative shift and tilt of the beams. Although the input beam itself excites the fundamental eigenmode of the resonator, the fraction of this mode leaking out of the resonator is a good beam pointing reference due to the mode-cleaning effect of the resonator, as described in more detail in [Kwe07]. Two quadrant photodetectors, QPD₁ and QPD₂, and subsequent demodulation electronics are used to detect the DWS signals. The four degrees of freedom, translation and tilt in horizontal and vertical direction (called 1X, 1Y, 2X, 2Y), are measured in order to calculate the quantities ϵ_x and ϵ_y . Dependent on the considered position along the beam axis, the 1X/1Y degree of freedom can correspond to a translation, tilt or a mixture of both. Due to the optical design of the DBB the 1X/1Y degree of freedom corresponds to a pure tilt of the beam wavefronts at the position of mirror PZT₁ and photodiode QPD₁ (for more details see Sec. 2.2.2). Accordingly the 2X/2Y degree of freedom

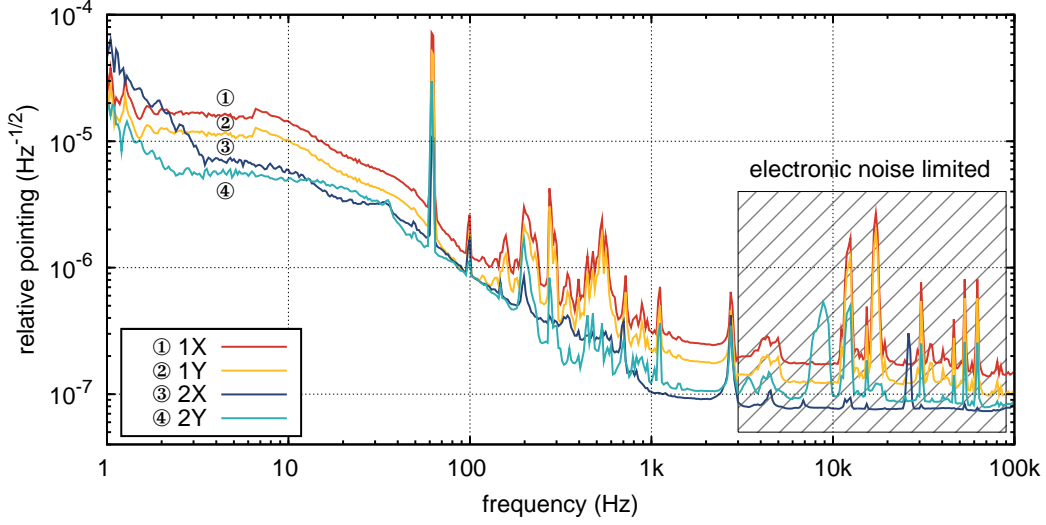


Figure 2.6: Upper limit for the sensitivity for pointing fluctuations. At higher frequencies the sensitivity is limited by electronic noise.

corresponds to a pure tilt at mirror PZT₂ and photodiode QPD₂. All four degrees of freedom are orthogonal.

The detectors QPD₁ and QPD₂ each consist of a silicon quadrant photodiode for the 1064 nm DBB (and of a germanium quadrant photodiode for 1550 nm) and four transimpedance amplifiers. The modulation signal at 1 MHz is amplified in the detectors and demodulated in the electronic crate. The demodulated DWS signals have a bandwidth of about 100 kHz.

In order to stay in the linear range of the DWS sensors, the pointing of the input beam is adjusted in servo loops using two mirrors (PZT₁, PZT₂) that can be tilted with PZTs. The four servo loops have a bandwidth of a few 100 Hz and the tilt range of PZT₁ and PZT₂ is about 4 mrad, which corresponds to $|\epsilon| \approx 6$ and $|\epsilon| \approx 5$ at 1064 nm and 1550 nm, respectively (see Sec. 2.1). Since the four degrees of freedom are already orthogonal, the design of these servo loops is simplified as no orthogonalization step is required (see Sec. 2.2.2). A welcome side effect is that the servo loops automatically compensate misalignments introduced by moving lenses during the process of manually mode-matching the input beam to the resonator fundamental mode.

The pointing measurement and control signals at the PZTs are calibrated using the resonator: The power of the first order TEM modes that are excited in the resonator by a misaligned TEM₀₀ input beam depends on the input beam pointing ϵ with

$$\frac{|c_{10}|^2}{|c_{00}|^2} = |\epsilon_x|^2, \quad \frac{|c_{01}|^2}{|c_{00}|^2} = |\epsilon_y|^2. \quad (2.9)$$

For calibration, this power ratio is measured using the modescan technique (explained in the following) while varying the alignment control signals.

An upper limit of the sensitivity for beam pointing fluctuations was measured with a pointing-stabilized test beam. The pointing of the test beam was stabilized by using a single-mode fiber-coupled beam that was further filtered by a resonator with a finesse of about 350 in front of the DBB. The residual beam pointing fluctuations of the test beam were then measured with the DBB (Fig. 2.6). Unfortunately this measurement was possibly spoiled by a high air particle count, which was realized after the experimental setup was disassembled. Therefore this measurement really serves as an upper limit only.

Beam Quality Measurement

The beam quality of the input beam is measured by performing a high-resolution modal analysis of the input beam.

The measurement method, called *modescan*, decomposes the input beam with the aid of the optical ring resonator into an expansion of Hermite-Gaussian modes (with the exception of certain degeneracies) in order to determine the power in higher order TEM modes. The eigenmodes of the resonator are in very good approximation the Hermite-Gaussian TEM modes, since the smallest aperture inside the resonator is about ten times larger than the beam width at this point. Nevertheless the eigenmodes are slightly elliptical and have a small astigmatism outside the resonator as explained in [Kwe07].

For the measurement of the beam quality, the input beam is aligned and mode matched to the resonator using the mirrors PZT₁ and PZT₂ and the lenses ML₁ and ML₂. A good alignment and mode matching is crucial for this measurement method, since higher TEM_{lm} modes are excited by a misalignment or mis-modematching and will therefore reduce the fundamental power determined. The quality of the alignment and mode matching can, however, be determined from the measurement data. In the next step the resonator round-trip length is changed by several micrometers within a second using a ramp signal at the PZT that caused a shift of the resonance frequencies by several FSR. The transmitted power is simultaneously measured with photodetector TPD. This detector is optimized for linearity, dynamic range and is shielded from stray light in the optical setup (for more details see Sec. 2.2.2). Since the resonance frequencies of the TEM resonator eigenmodes are generally different, the power in the individual modes can be measured.

The measurements are automatically analyzed by a computer program that identifies the modes using their resonance frequencies. Since the expansion of the PZT at the resonator depends nonlinearly on the applied voltage and shows a hysteresis, a calibration of the PZT is necessary before the identification. A detailed description of the data analysis and the program is given in [Kwe05].

Besides the fundamental power the quality of the input beam alignment can be derived from the power in the TEM₁₀ and TEM₀₁ modes as well as a combined value for the mode matching, ellipticity, and astigmatism can be derived from the power of the TEM₂₀ and TEM₀₂ mode (see Sec. 2.1).

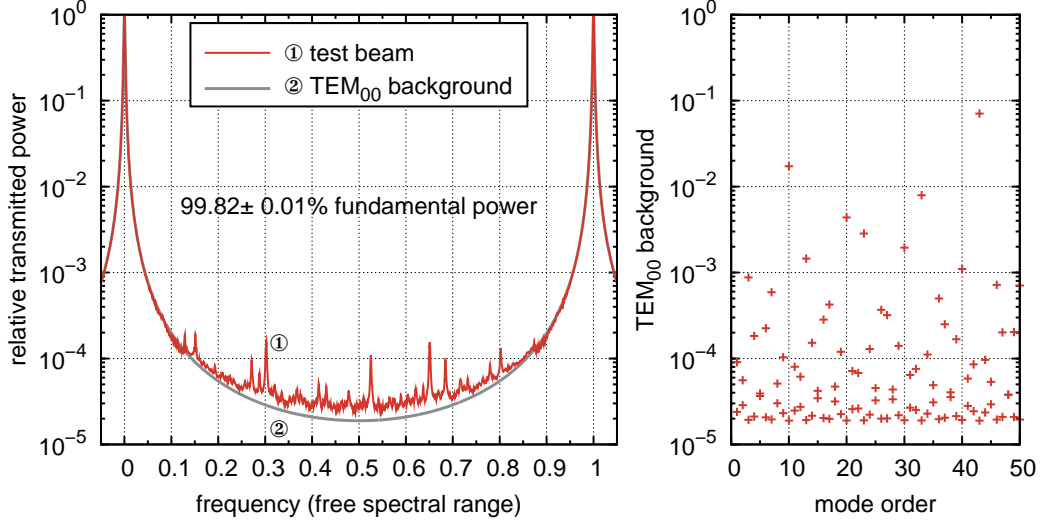


Figure 2.7: Sensitivity of the beam quality measurement. A lower limit is given by the background of TEM₀₀ mode and an upper limit by the measurement of the test beam (left). The TEM₀₀ background power at the resonance frequencies of the higher-order modes was calculated as function of their mode order (right).

On the one hand the sensitivity of the measurement method is limited by the background of modes with high power, mainly the TEM₀₀ mode, and on the other hand by the beam distortion of deflection mirrors, lenses, and resonator mirrors of the DBB. The sensitivity limit due to the background B of the TEM₀₀ mode depends on the resonance frequency of the higher-order mode TEM _{lm} (Fig. 2.7) and is given by

$$B(\phi) = \frac{1}{1 + (2\mathcal{F}/\pi)^2 \sin^2(\phi/2)}, \quad (2.10)$$

where ϕ is the resonance phase which depends on the mode order l, m and the round-trip Gouy phase. An upper limit for the sensitivity was determined with a test beam of very high beam quality. This test beam was prepared by sending a 35 W beam from an amplifier laser system [Fre07b] through an optical resonator (finesse about 380) that was used as mode-cleaner. The power determined in higher-order modes was $0.18 \pm 0.01\%$ in this experiment (Fig. 2.7), and modes with relative powers of down to 10^{-5} were detected. A calculation of the TEM₀₀ background power showed that this background is below 10^{-1} of the TEM₀₀ power for modes of orders up to 50, and generally below 10^{-3} for most modes (Fig. 2.7).

The beam quality cannot be measured simultaneously with the frequency or pointing noise since the resonator cannot be stabilized to a fundamental mode and at the same time being scanned by several FSRs. Still the fundamental power of the input beam can be measured directly with a stabilized resonator by measuring

simultaneously the beam power on detector TPD and detector RPD. However, by using this measurement method no information about the mode composition and deduced parameters, such as the ellipticity or astigmatism, is gathered⁴.

2.2.2 Experimental Challenges

During the development of the DBB many experimental and technical problems had to be solved. In the following a selection of the problems that occurred and their solutions are described.

Dither-lock at 1 MHz

The dither-lock technique is used to stabilize a TEM_{00} mode resonance of the DBB resonator to the input beam (see Sec. 2.2.1). This technique involves the modulation of the resonator round-trip length with a PZT at a frequency of 1 MHz. The technical challenge was to modulate the PZT despite of its low impedance at these frequencies, which was finally achieved with an electrical resonance circuit. In the following the dither-lock technique is briefly motivated, the modulation problem is explained, and the implemented solution is described.

From many different resonator stabilization methods [Bar73, Han80, Sha99] the dither-lock technique, that is a variant of the Pound-Drever-Hall (PDH) method [Bla01, Dre83], was chosen since a phase modulation of the laser beam is necessary for the DWS technique used for pointing measurements. Usually the phase of the input beam is modulated with an electro-optic modulator (EOM) for the PDH technique. In contrast, for the dither-lock technique, the phase modulation is generated inside the resonator by modulating the round-trip length with a PZT. This has the advantage that possible beam distortions by an EOM are avoided, which in turn improves the sensitivity of beam quality measurements, and furthermore, since the PZT is needed anyway for resonator length stabilization and modescans, the number of components is reduced.

The modulation frequency of 1 MHz is a tradeoff between error signal bandwidth and modulation depth: The dither-lock error signal and the DWS signals are obtained by demodulation of various photodetector signals at 1 MHz. The bandwidth of these signals is limited to about a factor of 5 to 10 below the modulation frequency due to lowpass filters in the demodulation electronics. Frequency and pointing fluctuations should be measured up to 100 kHz with the DBB, which yields a lower bound for the modulation frequency of ≈ 1 MHz. On the other hand the modulation frequency cannot be significantly increased since the bandwidth of the optical resonator is about 1 MHz and hence phase modulations above this frequency would be reduced by the filter effect of the resonator.

⁴So far no detailed, experimental comparison of this direct measurement method and the mode-scan method was performed. Thus the accuracy of this direct method is unknown.

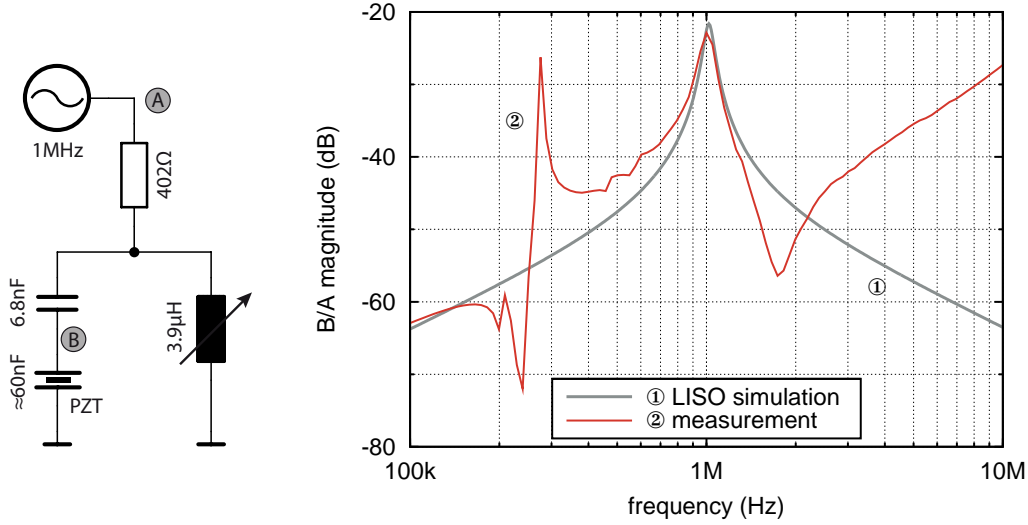


Figure 2.8: Schematic and transfer function of the electronic resonance circuit. The transfer function was measured from A to B.

The problem for the modulation of the PZT was the low electrical impedance: A 5 mm thick ring PZT (PAHH-005, Physik Instrumente) is used which has an electrical capacitance of about 60 nF up to several MHz. At the modulation frequency of 1 MHz this corresponds to an impedance of 2.6Ω .

In order to obtain a good signal-to-noise ratio for the demodulated signals the light power at the photodetectors should be dominated by the phase modulation sidebands and not by, e.g., non-resonant higher-order TEM modes. A sideband power of about 2% was chosen which corresponds to a modulation amplitude of about 50 mV at the PZT. The driver electronics is located in the electronics crate of the DBB and is connected to the PZT with cables of varying length dependent on the actual setup (up to about 10 m). Since the impedance of the cable was significantly larger than the PZT impedance at 1 MHz due to inductance and since the cable length varied from setup to setup, the PZT could not be directly modulated in this way.

The modulation problem was solved by integrating the PZT in a parallel electrical resonance circuit (Fig. 2.8) with components placed near the PZT on the breadboard. The impedance of this resonance circuit is 400Ω at 1 MHz, which is easy to drive even with long cables. An adjustable coil is used to tune the resonance frequency exactly to 1 MHz. In order to avoid the transfer of a small modulation signal of only 50 mV along long cables, an additional capacitor is connected in series with the PZT acting like a 1:10 voltage divider. The transfer function of the circuit was simulated with the program LISO [Hei00] and was later on measured for comparison (Fig. 2.8). The measurement and the simulation agree well near the resonance frequency. The resonance circuit has the additional advantage that noise

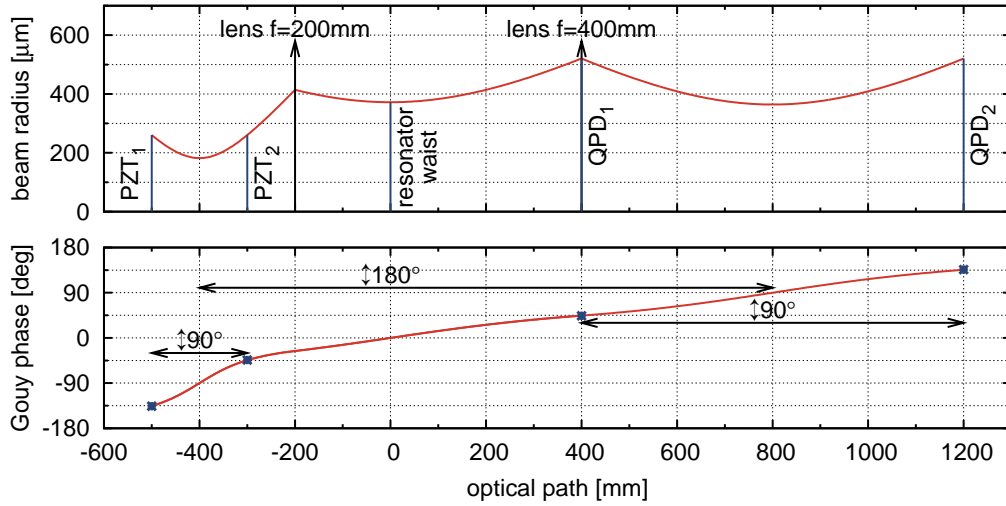


Figure 2.9: Optical design of the diagnostic breadboard. The size and Gouy phase of the fundamental mode and the position of important components are shown. The beam size is calculated for the DBB at 1064 nm, the Gouy phase and the component positions are wavelength independent.

of the driver electronics is suppressed in the actual measurement band from 1 Hz to 100 kHz and therefore cannot influence the length stability of the resonator.

Optical Orthogonalization of Alignment Control Loops

Feedback control loops are used to optimize the alignment of the input beam to the resonator of the DBB (see Sec. 2.2.1). In general these four control loops can be strongly coupled, which causes stability problems of the control loops and complicates the data analysis for pointing fluctuation measurements. Due to the optical design of the DBB, i.e. by placing the sensors and actuators at specific Gouy phases of the laser beam, the control loops are orthogonal.

The pointing of a laser beam has four degrees of freedom: translation and tilt of the beam axis in horizontal and vertical direction, described by two complex parameters ϵ_x, ϵ_y (see Sec. 2.1). Accordingly four sensors and four actuators are necessary to measure and control all degrees of freedom. Mirrors that can be tilted with PZTs are used as actuators. These actuators tilt the beam axis at the position of the actuator. Quadrant photodetectors are used as sensors that measure the tilt of the wavefronts at the sensor with the DWS technique. The control loop decoupling in horizontal and vertical direction is easily realized since the actuators tilt the beam only in horizontal or vertical direction and the quadrant photodetectors are read out so that the wavefront tilt is measured only in horizontal and vertical direction. In contrast the coupling between translation and tilt depends on the Gouy phase of the Gaussian beam and therefore on the actual position of

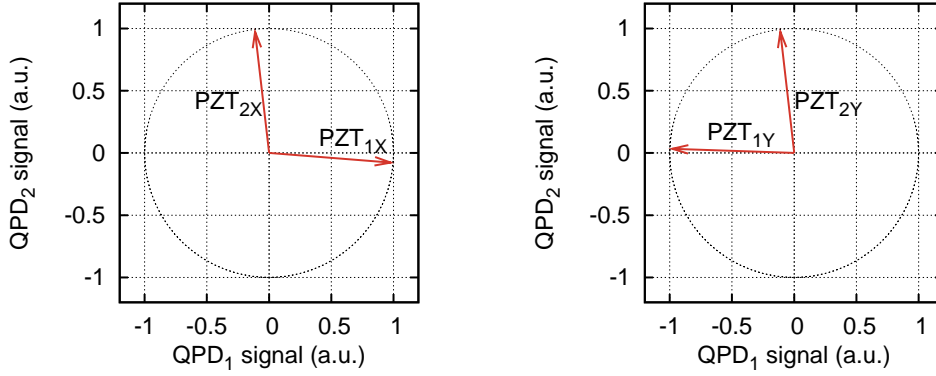


Figure 2.10: Measured optical orthogonalization in horizontal and vertical direction.

the sensors and actuators along the beam axis. On the one hand a coupling of these degrees of freedom causes problems with the control loop stability, the four control loops influence each other and the whole system has to fulfill a stability criterion, and on the other hand the data analysis is complicated since the error and control signals cannot be associated with single orthogonal alignment signals.

Often the decoupling of the control loops is achieved by using an orthogonalization electronics (see e.g. [Gro04]). This electronics combines the four sensor or actuator signals to generate four orthogonal signals.

A different, purely optical approach was used for the DBB: Depending on the exact position of the actuator the tilt causes a mixture of tilt and translation at the resonator waist which is the reference position for ϵ . The actuator causes a pointing ϵ [Kwe05]

$$\epsilon \propto i \exp(i\eta_p), \quad (2.11)$$

where η_p is the Gouy phase difference between the actuator position and the resonator waist. The DWS sensor measures only the wavefront tilt at the sensor position which corresponds to a projection S_{DWS} of ϵ

$$S_{DWS} \propto \Im(\epsilon \exp(-i\eta_d)), \quad (2.12)$$

where η_d is the Gouy phase difference between the sensor position and the resonator waist.

The control loops are decoupled if the Gouy phase difference between each actuator and the sensor of the other control loop is just $\pi/2 + n \cdot \pi$ ($n = 0, 1, 2, \dots$) which is equivalent to $\Im[\exp(i\eta_p - i\eta_d)] = 0$. In that case the actuator causes a pure translation of the wavefronts at the sensor of the other control loop, which this sensor cannot measure. The other way round the Gouy phase difference between sensor and actuator of the same control loop should be $n \cdot \pi$ in order to maximize the signal transmission from actuator to sensor.

The optical design of the DBB (Fig. 2.9) fulfills the mentioned criteria. The actuators and sensors are placed symmetrically around two waists. The distance

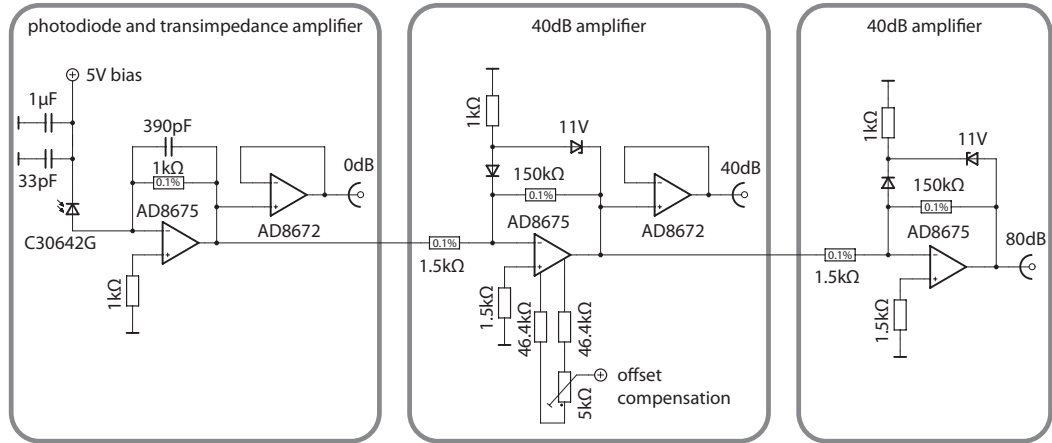


Figure 2.11: Schematic of the electronic circuit of the high dynamic range photodetector.

to the waist is the Rayleigh length of the beam in each case. Thus the Gouy phase difference between both actuators and both sensors is 90° . Furthermore, with two lenses a Gouy phase difference between the two waists of 180° is obtained.

This optical design is independent of the laser wavelength since the propagation of the Gouy phase and the lens transformations depend only on the Rayleigh length. The Rayleigh length in turn is given only by the geometry of the resonator. However, the beam size changes with the wavelength.

The residual coupling of the control loops was measured in an experiment and was between -29 dB and -18 dB (Fig. 2.10). This is small enough, such that the control loops can be treated individually and an easy data analysis within the general calibration accuracy is possible.

High Dynamic Range Photodetector

For the modescan technique a photodetector in transmission of the DBB resonator is needed (see Sec. 2.2.1, TPD in Fig. 2.2). A regular photodetector in combination with a single data acquisition (DAQ) channel does not have the required dynamic range to measure weak higher-order modes with relative powers down to 2×10^{-5} . This problem was solved by using a photodetector with integrated signal conditioning and several DAQ channels.

The standard DAQ channels that are available for the DBB (see Sec. 2.2.3) have an effective resolution of about 14 bit. Thus under ideal circumstances a dynamic range of 10^4 can be achieved. However, the weakest higher-order modes that can be detected with the modescan technique due to the background of the TEM_{00} mode have relative powers of $1/(1 + (2\mathcal{F}/\pi)^2) \approx 2 \times 10^{-5}$. Besides the dynamic range problem, regular photodetectors often have an electronic offset which is easily as

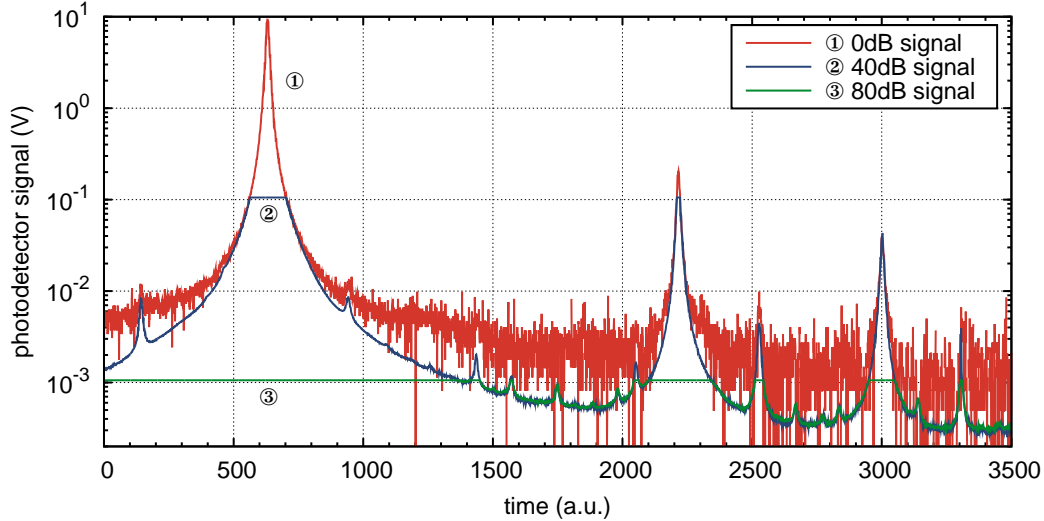


Figure 2.12: Modescan measurement with the high dynamic range photodetector showing all three output signals of the detector.

large as a weak higher-order mode and therefore complicates the modescan data analysis.

A special photodetector was developed for the DBB to solve the problems mentioned. This detector consists of an InGaAs photodiode, a transimpedance amplifier, and two saturable dc-coupled 40 dB amplifiers (Fig. 2.11). A low-noise, low-offset ($\approx 10 \mu\text{V}$) operational amplifier (AD8675) with sufficient bandwidth is used for the amplifiers. The offset of the circuit can be further reduced at the first amplifier stage with a potentiometer. Precision resistors with a small temperature coefficient are used where appropriate in order to reduce nonlinearities caused by self heating. A controlled saturation of the amplifiers is achieved with a Zener diode in the feedback path of the operational amplifiers. An additional diode in series with the Zener diode is used to reduce the leakage current of the Zener diode. The detector has a bandwidth of about 100 kHz. Three DAQ channels are used to measure the photodiode signal in three different amplifications (0 dB, 40 dB, and 80 dB). Afterwards the digitalized signals are combined to one signal with higher dynamic range.

The example measurement (Fig. 2.12) clearly shows the high dynamic range by using three signals. This detector in combination with three DAQ channels has a dynamic range four orders of magnitude higher compared to a regular photodetector.

2.2.3 Control and Automation

The DBB is designed to be completely controllable by a computer system in order to perform beam characterizations remotely. Thus laser beam measurements can be automated by computer programs and the instrument can be used, e.g., to

measure the long-term performance of a laser by periodical characterizations or to continuously monitor a laser system. Furthermore, due to the automation careless mistakes are minimized and the results can be compared more easily since each measurement is performed in the same way.

In general more complex electronics is necessary to allow a remote control. The electronic modules of the DBB are designed in such a way that all settings that could be made with the front panel controls can be overridden by analog and digital signals on the crate bus. Further all measurement signals are available on this bus. The opto-mechanical components are computer controllable as well: The lenses used for mode-matching (ML_1 , ML_2 in Fig. 2.2) can be moved along the beam axis by about 2 cm and the alignment of the input beam can be controlled with two mirrors attached to PZT elements (PZT_1 , PZT_2 in Fig. 2.2).

Two different computer interfaces were developed: The first interface connects to a laboratory computer with a Windows operating system. This computer system was used for most characterizations presented in the next Section 2.3, among others for the long-term characterization of the NPRO.

The second interface connects to the *control and data system* (CDS) of Advanced LIGO. This system is based on a network of several computers with realtime Linux operating systems controlled by EPICS (Experimental Physics and Industrial Control System) process variables. An interface to this system was developed in order to monitor the Advanced LIGO laser system with the DBB. In the following both interfaces are briefly described and compared.

Laboratory Computer

A laboratory computer, consisting of a usual PC with an A/D and a D/A converter card for data acquisition and signal generation, respectively, is used to automate the DBB. Windows is used as operating system, and analog signals are measured and generated with the help of the A/D and D/A card driver programming interfaces.

The hardware interface between the crate bus and the laboratory computer is realized with a dedicated interface module in the electronic crate (Fig. 2.13). Several digital input/output channels and D/A converters in this electronic module are connected via an I²C bus and an RS-232 link with the computer in order to read and write digital signals and to set the slow analog signals on the bus. Compared to the Advanced LIGO CDS the laboratory computer controls only the parameters of the analog feedback control loops. Feedback control loops can be turned on and off, offsets can be adjusted, and gains can be changed among other things with bus signals.

The actual analog measurement signals on the crate bus are distributed with a multiplexer to four channels. Each channel consists of a signal conditioning unit and an anti-aliasing filter. These conditioned signals are simultaneously digitalized with an A/D converter card in the computer (PCI-6122, National Instruments) at a sampling rate of 250 kHz and a resolution of 16 bit (effective \approx 14 bit). A fast

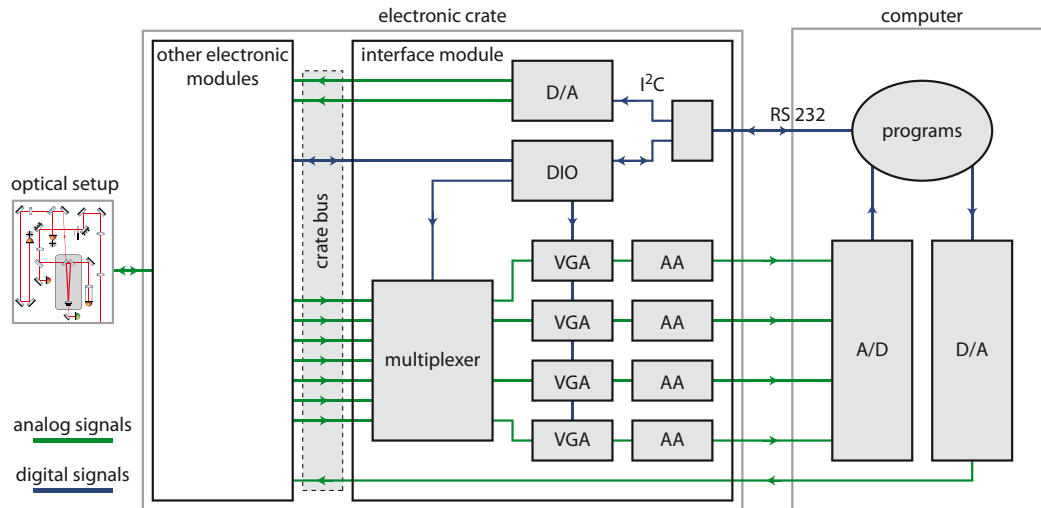


Figure 2.13: Block diagram of the laboratory computer interface. D/A: digital to analog converter, A/D: analog to digital converter, DIO: digital input output, VGA: variable gain amplifier, AA: anti-aliasing filter.

analog signal injection for measuring transfer functions is realized with a D/A card (PCI-6251, National Instruments).

Almost all measurements with the DBB are automated with programs and scripts (except for RPN measurements at radio frequencies since the bandwidth of the anti-aliasing filters and the A/D converter card is limited to about 100 kHz). Thus the system is able to automatically measure and calibrate the beam quality as well as the power noise, the frequency noise, and the pointing noise up to 100 kHz. Even the lock acquisition for stabilizing the resonator to a fundamental mode resonance is automated. Since the computer system has only four DAQ channels the different measurements can only be performed one after the other. Programs are also used to automatically analyze the signals acquired: Thus among other things the linear spectral density of the time signals is calculated and calibrated with corresponding transfer functions and modescans are analyzed.

With this computer system it is possible to perform fully automated laser beam characterizations including the data analysis.

Advanced LIGO Control and Data Systems

The Advanced LIGO CDS is a complex computer system specifically developed for the control and data acquisition in Advanced LIGO. In the following the CDS and the DBB interface is briefly described.

The CDS consists of a network of several computers (Fig. 2.14). The control and data acquisition is performed by a computer, called *frontend*, running a realtime Linux operating system. This computer is connected to A/D and D/A converter

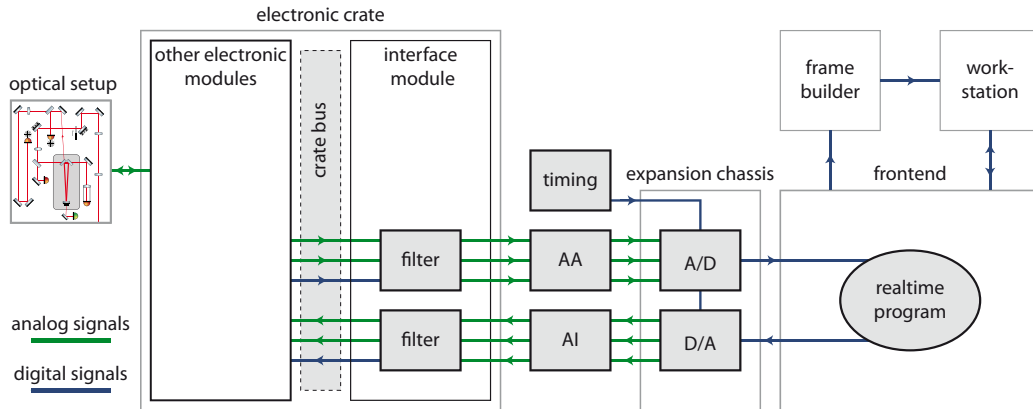


Figure 2.14: Block diagram of the CDS interface. D/A: digital to analog converter, A/D: analog to digital converter, AA: anti-aliasing filter, AI: anti-imaging filter.

cards in an expansion chassis. Analog signals are digitalized with the A/D card, processed with a realtime program, and are put out with a D/A card. Selected signals are forwarded by the realtime program to a different computer (*frame builder*) responsible for data archiving. The realtime program is controlled by EPICS [EPI] messages generated by any computer on the network, e.g. by a user on a workstation. In general for every application of the CDS the realtime program needs to be adjusted since only a few parameters, such as the transfer function of filter blocks, can be changed during runtime. More information about the CDS can be found in [Bor08a, Bor08b].

A dedicated electronic module is used as interface between the DBB crate bus and the CDS (Fig. 2.14). This module contains a fixed signal conditioning filter for each signal. In total 24 A/D and 16 D/A channels are used for the data acquisition and for the control of the DBB. The analog signals are simultaneously sampled with a frequency of 65 kHz and the digital signals are converted with 131 kHz to analog ones, in each case with 16 bit. The timing signal for the A/D and D/A cards is synchronized with a GPS (Global Positioning System) clock.

The digitalized signals are processed with a realtime program, which also replaces the analog feedback control loops of the DBB with digital ones. All five control loops (1× resonator length control, 4× input beam alignment control) are digitally implemented. The bandwidth of the digital control loops is limited to a few kilohertz due to a time delay of about 65 μs in the CDS. Nevertheless similar bandwidths are achieved compared to the analog control loops. The digital signal processing allows the implementation of a faster and more robust lock acquisition for stabilizing the resonator, an automatic calibration of error signals, and a software interlock that protects the PZTs from oscillations.

The data analysis is not completely automatized with this computer system. As far as possible the realtime program calibrates the time signals that are archived

afterwards. With different programs and tools the linear spectral density, minimum and maximum values, or trends can be calculated using the archived time signals.

With this computer system it is possible to perform most of the DBB measurements and to analyze the archived calibrated time signals in many different ways later on.

Comparison

With both computer interfaces the DBB can be controlled and characterization measurements can be performed. Despite the same main functionality there are significant differences between the two systems that are discussed in the following.

The laboratory computer interface has the advantage that all measurements and especially the data analysis are automatized. At the moment the CDS system delivers only calibrated time signals, which of course can later be processed in a more flexible way.

All important measurement data can be acquired simultaneously with the CDS system. Thus a laser beam can be characterized faster and continuously, whereas the different measurements with the laboratory computer need to be performed one after the other since only four DAQ are available.

On the other hand the sampling rate of the laboratory system is with 250 kHz much higher than the 65 kHz sampling rate of the CDS system. Therefore fluctuations can be measured up to 100 kHz using the laboratory system and only up to ≈ 30 kHz with the CDS.

Since the feedback control loops are digitally implemented in the CDS, less analog electronics is necessary and the transfer functions of the control loops can be adjusted fast and easily. Furthermore filters, e.g. for compensating mechanical resonances, can be realized digitally much more precisely. Such filters are complicated to build with analog electronics due to tolerances of the electrical components.

Finally the laboratory computer system is simple whereas the CDS interface is much more complex but provides a seamless integration with Advanced LIGO.

The conclusion is that the CDS interface is suited for continuously monitoring a laser system whereas the laboratory computer interface is more suited for single beam characterizations, e.g. in the field of laser development.

2.3 Characterizations

Several different laser systems were characterized with the diagnostic breadboard. The most important laser beam parameters (Sec. 2.1) and laser internal actuators were characterized. The results presented in this section were used to check the suitability of laser systems for specific applications and were as well used as basis for stabilization concepts.

The characterized systems are continuous-wave, single-frequency, linear polarized lasers at wavelengths of 1064 nm and 1550 nm. Since these lasers were developed among other things for GWDs, they are optimized for low levels of frequency and

power noise, a high beam quality, a reliable operation, and a high output power. The following lasers were characterized:

- The nonplanar ring oscillator (NPRO) is a very proven, commercially available monolithic Nd:YAG solid-state laser at 1064 nm wavelength, which is used in many precision experiments. This laser type is available with output power levels up to 2 W, which is too low for GWD applications, but the laser has a very good free-running frequency stability. See Sec. 2.3.1.
- The Enhanced LIGO laser is a Nd:YAG master-oscillator Nd:YVO₄ power-amplifier system operating at a wavelength of 1064 nm that was developed specifically for Enhanced LIGO. This laser is an integral part of the Advanced LIGO laser and has an output power of about 35 W. The characterization results are not presented in this section but are partly published in [Fre07b].
- The Advanced LIGO laser is a three stage solid-state laser system (Nd:YAG master laser, Nd:YVO₄ amplifier, Nd:YAG oscillator) at 1064 nm that is at the moment developed specifically for Advanced LIGO. The laser stages are coupled via injection locking and deliver an output power of about 200 W in total. See Sec. 2.3.2.
- The photonic crystal fiber laser is a master-oscillator fiber-amplifier system at 1064 nm that uses an ytterbium-doped photonic-crystal fiber as amplifier. This laser achieved with quite low effort a high output power of about 150 W. See Sec. 2.3.3.
- The fiber laser at 1550 nm is a commercially available, two stage laser system consisting of an erbium fiber laser and an amplifier with a total output power of about 2 W. See Sec. 2.3.4.

In the following the characterized laser systems are described in more detail and a selection of measurements is presented and discussed.

2.3.1 Nonplanar Ring Oscillator

The NPRO [Kan85] is a commercially available single-frequency solid-state laser. In this thesis NPROs (Mephisto 2000 NE LIGO, Innolight) with an output power of 2 W at a wavelength of 1064 nm are characterized. The resonator and the active medium of the laser is a monolithic neodymium-doped yttrium aluminum garnet (Nd:YAG) crystal. The active medium is pumped by two laser diodes at a wavelength of 808 nm. The lasers come with a built-in power stabilization called *Noise Eater* for suppressing the relaxation oscillation at about 1 MHz. This laser is described in more detail in [Fre95].

This kind of laser is frequently used in precision experiments since it has a high intrinsic frequency stability due to the monolithic laser resonator/crystal and has proven to be very reliable. Thus a detailed characterization is important not only

Power	Initial	Long-term
	Output power slope	•
Output power	•	
Relative output power trend		•
Output power fluctuations, rms 0.6 mHz ... 1 Hz	•	•
RPN, 1 Hz ... 100 kHz, with Noise Eater	•	•
RPN, 1 Hz ... 100 kHz, w/o Noise Eater	•	
RPN trend at selected frequencies		•
RF RPN, 1 MHz ... 100 MHz, with and w/o Noise Eater	•	
Relaxation oscillation frequency	•	

Frequency	Initial	Long-term
	Frequency noise, 1 Hz ... 100 kHz	•
Frequency noise trend at selected frequencies		•
PZT frequency actuator	•	
Temperature frequency actuator	•	

Spatial Mode	Initial	Long-term
	Pointing fluctuations, rms 0.6 mHz ... 1 Hz	•
Pointing, 1X, 1Y, 2X, 2Y, 1 Hz ... 100 kHz	•	•
Pointing trend at selected frequencies		•
Beam quality	•	
Beam quality trend		•
Relative ellipticity/astigmatism	•	
Mode matching trend		•

Table 2.1: Measurements performed for the initial characterization of all eight lasers and for the long-term characterization of one laser. The shaded measurements are presented in this section.

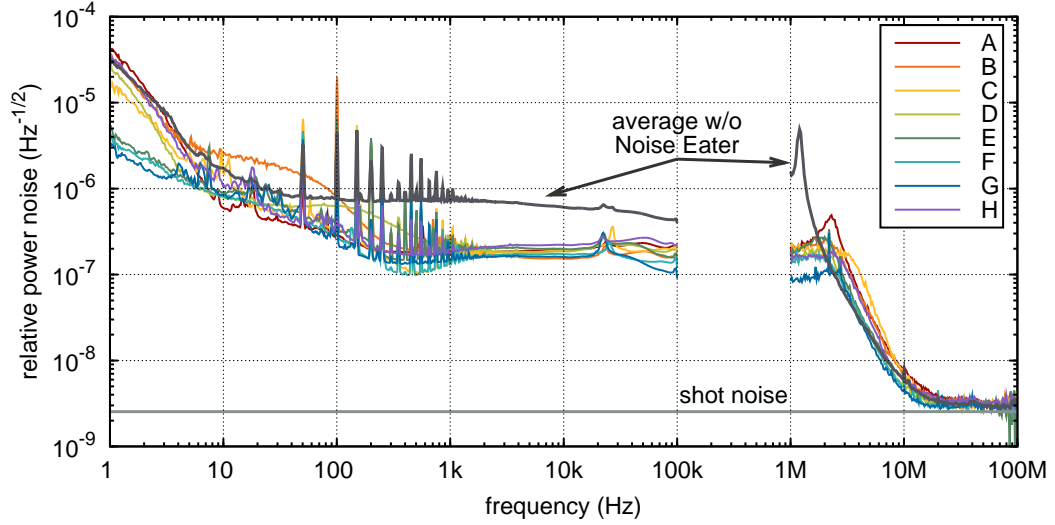


Figure 2.15: Relative power noise during the initial characterization of all eight NPRO lasers (A to H) with activated Noise Eater. The average power noise level without Noise Eater is shown for comparison.

for GWDs but also for many other optic experiments. The NPROs characterized in this thesis are used as master lasers in the Advanced LIGO laser systems (Sec. 2.3.2).

Eight lasers of the same model were extensively characterized with the DBB directly after delivery, and further on one laser was operated continuously and periodically characterized in a long-term measurement. For the long-term characterization the laser was automatically characterized every 24 h for more than 2600 h (≈ 3.5 months) using the DBB laboratory computer interface (Sec. 2.2.3). This showed that the diagnostic breadboard is reliable and can be operated fully automated for several months. Thus a permanent integration into a laser system is possible in order to automatically monitor the performance and to quickly identify problems.

An overview of all performed measurements, which are divided into measurements during the initial characterization of all eight lasers and the long-term measurement of one laser, is given in Table 2.1. In the following only the power and pointing noise of the lasers are presented in more detail.

Power Noise Investigations

The power noise of the lasers was measured in the frequency band from 1 Hz to 100 kHz and from 1 MHz to 100 MHz (Fig. 2.15). The linear spectral density of the RPN was almost flat at a level of $7 \times 10^{-7} \text{ Hz}^{-1/2}$ from 10 Hz to 100 kHz with Noise Eater disabled. The differences between the eight lasers were small. Below 10 Hz the RPN was increasing very fast towards lower frequencies with more than one order of magnitude per decade. A comparison with measurements with activated Noise Eater showed that this power stabilization reduced the noise level starting

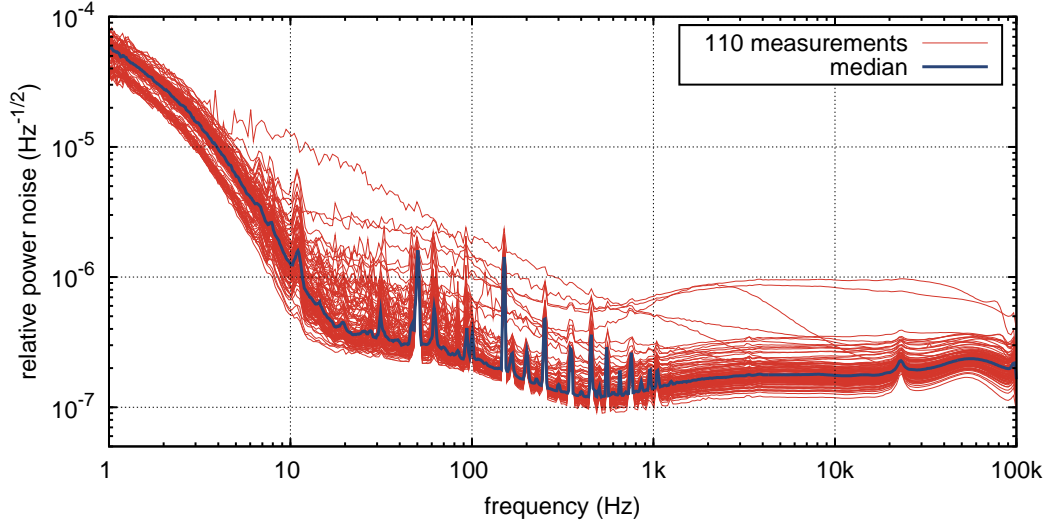


Figure 2.16: Relative power noise during the long-term characterization. The median power noise of the 110 measurements is shown for reference.

from about 100 Hz. Above around 300 Hz the RPN with Noise Eater was almost flat at a level of $\approx 2 \times 10^{-7} \text{ Hz}^{-1/2}$. There was no significant difference of the RPN below 10 Hz with or without Noise Eater. Variations between the samples were rather small for measurements with Noise Eater.

As can be seen from the long-term measurements, there were a couple of outliers that were almost an order of magnitude above the median RPN level at some frequencies (Fig. 2.16). Especially for frequencies around and above 100 Hz some measurements strongly differed from the median. Over some period the air particle count was monitored during the long-term measurements. The average particle count of 0.7 ft^{-3} with a size of larger than $0.3 \mu\text{m}$ was very low and no significant correlation between the particle count and the RPN could be observed. According to this, air particles did not seem to cause the outliers.

In general the RPN with activated Noise Eater at frequencies above 10 Hz was between $1 \times 10^{-7} \text{ Hz}^{-1/2}$ and $1 \times 10^{-6} \text{ Hz}^{-1/2}$ except for some outliers.

The relaxation oscillation of the lasers was at an average frequency of 1.1 MHz with values ranging from 900 kHz to 1.23 MHz. With activated Noise Eater this oscillation was suppressed by a factor of about 50 and the RPN level was at about $2 \times 10^{-7} \text{ Hz}^{-1/2}$ (Fig. 2.15). Between 2 MHz and 10 MHz the Noise Eater slightly increased the RPN which was, however, still decreasing very rapidly with increasing frequency. For frequencies above 20 MHz the RPN was at or below the shot noise of about 50 mA photocurrent.

All in all the power noise of the NPROs is rather low. Experiments that use an NPRO directly as light source profit from this low power noise. However, if an NPRO is used as master oscillator in a multistage laser system the power noise at low frequencies ($< 100 \text{ kHz}$) is often irrelevant since in many cases the power

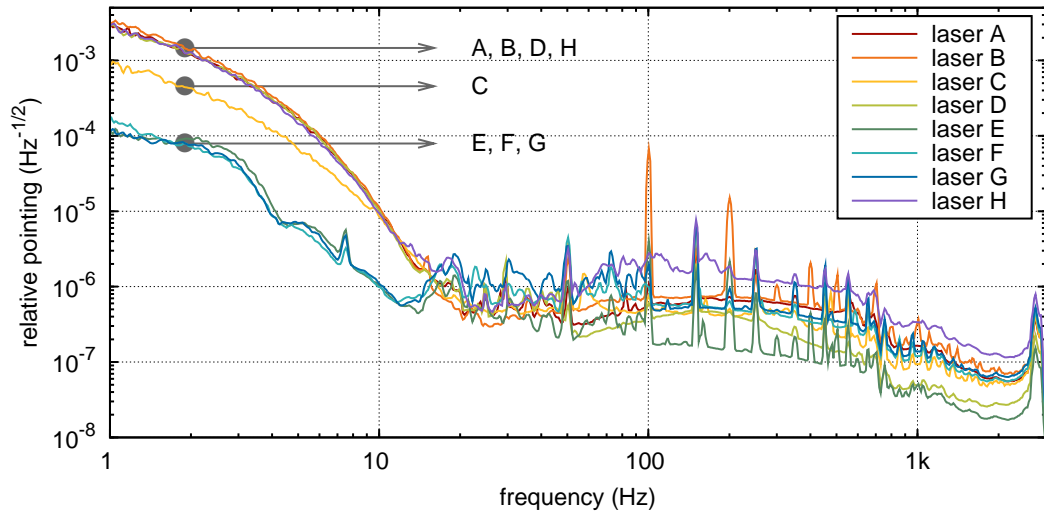


Figure 2.17: Relative pointing fluctuations in 2Y direction (see Sec. 2.2.1) during the initial characterizations. The lasers were characterized at three different locations in the following groups: lasers A, B, D, H; laser C; and lasers E, F, G.

noise of a multistage system is dominated by the last stage. The power noise at radio frequencies of the complete laser system is, however, usually determined by the NPRO. At these frequencies the power noise decreases with about $1/f^2$ for frequencies above the relaxation oscillation at ≈ 1 MHz. This oscillation in turn is very well suppressed by the internal Noise Eater.

Pointing Noise Investigations

The pointing fluctuations of the lasers were measured between 1 Hz and 3 kHz (Fig. 2.17) (for frequencies above ≈ 3 kHz the measurements were limited by electronic noise). Furthermore, the noise below 20 Hz seemed to be dominated by the environment: During the course of characterizing all eight lasers, the experimental setup had to move twice to different laboratories situated in the same building. Especially in the 2Y direction there were three groups of noise levels corresponding to the three different locations. No differences between these locations causing the different noise levels were obvious. Above 20 Hz the variation between the lasers was relatively large, up to about one order of magnitude. The relative pointing noise level was about $1 \times 10^{-6} \text{ Hz}^{-1/2}$.

The interpretation of the pointing measurement results is rather difficult since the environment parameters, such as air currents, that influenced the measurements are not known. To further investigate the influence of environment parameters the pointing was measured at different flowbox speeds. In general this flowbox was used to provide an environment with clean air in order to reduce the influence of

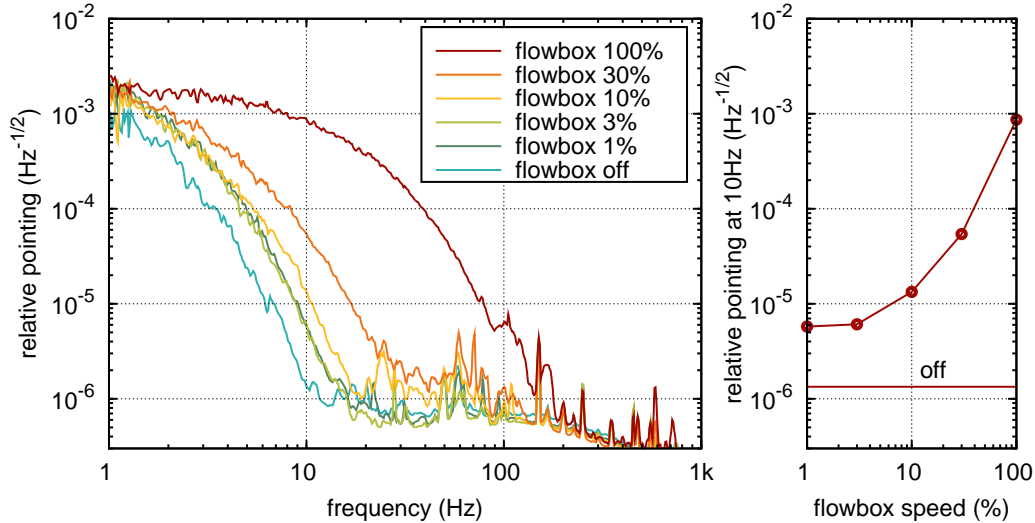


Figure 2.18: Relative pointing fluctuations at different flow speeds of the flowbox. This measurement was performed with laser C. A setting of 100% corresponds to a flow speed of 0.32 m/s.

dust particles. The noise increased at low frequencies with the flow speed of the flowbox (Fig. 2.18). At low flow speeds (see 1% and 3% curve in Fig 2.18) the influence of the air speed on the pointing noise seemed to be gone; however, as soon as the flowbox was turned off completely the pointing noise was again significantly reduced. All measurements in Fig. 2.17 were performed with a slow running flowbox. Furthermore broadband acoustic coupling could be ruled out as the dominant noise source in further experiments with a loudspeaker.

The characterization measurements listed in Table 2.1 but not presented here are partly published in [Kwe08a]. Together with these measurement results the characterization verified that NPROs are highly stable laser sources and that the variation between different samples is rather small. They are ideal for operation in GWDs and are especially suited as master oscillators for amplifiers or injection lock configurations.

2.3.2 Advanced LIGO Laser

The Advanced LIGO laser is a three-staged solid-state laser with an output power of about 200 W at 1064 nm. The first two stages together are called *frontend*, which are also the laser system for Enhanced LIGO. The first stage is an NPRO used as master oscillator (see Sec. 2.3.1). Since the subsequent stages are coupled to the master oscillator the complete laser system has the high frequency stability of the NPRO. The second stage amplifies the NPRO beam with four Nd:YVO₄ crystals to about 35 W. These crystals are pumped with fiber coupled laser diodes

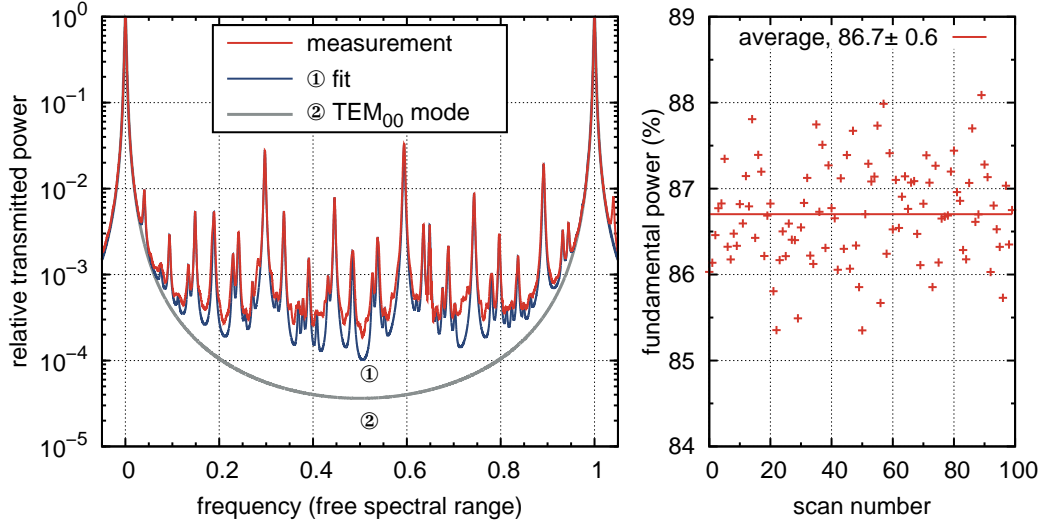


Figure 2.19: Beam quality measurement of the Advanced LIGO functional prototype laser. One hundred modescans were measured and analyzed to determine the statistical distribution.

at 808 nm. The last stage, the high power oscillator, is a ring laser with four laser heads. Each laser head consists of a water cooled Nd:YAG crystal as active medium, which is pumped by seven fiber-coupled laser diodes at 808 nm combined to a fiber bundle. The output of this bundle is passed through a fused silica rod to achieve a homogenous spatial profile of the combined pump power. The high power oscillator is coupled by injection locking [Sie86, Chap. 29][Zaw03, Chap. 3] using the PDH method to the second stage. The laser system is described in more detail, e.g., in [Fre07a, Fre04, Fre05].

This laser system was developed by the Laser Zentrum Hannover (LZH) and a prototype, the so-called *functional prototype*, was characterized. A characterization of this system was important for the development of the next prototypes and for the stabilization design described in Chapter 3.

A full characterization of the functional prototype was performed with the DBB: The measured frequency noise verified that the complete laser system has the frequency stability of the master oscillator. Furthermore pointing fluctuations were measured, though the measurements were limited by vibrations and air turbulences caused by several fan-cooled power meters on the optical table. In the following the beam quality and the power noise measurements are described in more detail.

Beam Quality Investigations

The beam quality was measured with the modescan technique and yielded a fundamental power of 0.867 ± 0.006 (Fig. 2.19). Thus with an total output power of about 181 W the system had ≈ 157 W in the TEM₀₀ mode. For Advanced LIGO the laser

system has to deliver at least 165 W in the TEM₀₀ mode in order to achieve the desired power inside the interferometer and with it the design sensitivity [Wil09]. Thus the combination of output power and beam quality of this functional prototype does not yet fulfill the Advanced LIGO requirements. The two strongest higher-order modes had an order of two (combination of TEM₀₂ and TEM₂₀ at 0.3 FSR) and four (combination of TEM₀₄, TEM₂₂, and TEM₄₀ at 0.6 FSR). The second order mode could have been caused by an ellipticity and astigmatism of the laser beam and a not completely optimized mode matching between laser output and DBB (see Sec. 2.1).

The quite low fundamental power compared to other lasers developed for GWDs is caused by aberrations in the four laser heads of the high power oscillator. On the one hand these thermally caused aberrations decrease the beam quality, but on the other hand these aberrations are also needed for a single transverse mode operation of the laser [Win09].

During the characterization of other prototypes of this laser system a corona in the beam profile was observed using a CCD (charge-coupled device) camera. Since the corona is significantly larger than the beam size a beam quality measurement using the modescan technique and the DBB yields only a rough estimate of the fundamental power. The precision of the modescan is limited in such a case since on the one hand the corona is prone to be clipped at apertures inside the DBB and on the other hand the power of the corona is distributed to many high order modes in the modescan.

Power Noise Investigations

The power noise of the laser was measured at two locations: once on a beam sample directly at the laser output and once downstream of an optical resonator (Fig. 2.20). The relative power noise was between $10^{-7} \text{ Hz}^{-1/2}$ and $10^{-2} \text{ Hz}^{-1/2}$ for frequencies from 1 Hz to 100 kHz. The largest power noise, up to $5 \times 10^{-3} \text{ Hz}^{-1/2}$, was observed at low frequencies. The power stability of this prototype is significantly worse compared to an NPRO.

For frequencies below 1 kHz the power noise is larger downstream of the optical resonator. This can be explained by spatial mode fluctuations, e.g. caused by beam pointing fluctuations, since the optical resonator acts as a mode-cleaner and turns mode fluctuations into power fluctuations (see Sec. 3.1.4). The power noise downstream of the optical resonator is important for the stabilization of this laser system since the power stabilization sensor in Advanced LIGO will be placed downstream of a suspended optical resonator to eventually achieve a very low power noise in front of the interferometer, according to the level shown in Fig. 2.20. For this prototype a power stabilization would have to suppress power noise by up to six orders of magnitude.

In a further measurement the peak-to-peak power fluctuation was measured in a 5 min interval at 250 kHz sampling rate. A peak-to-peak fluctuation of 28% (−22% to 6%) upstream and of 33% (−21% to 12%) downstream of the resonator were

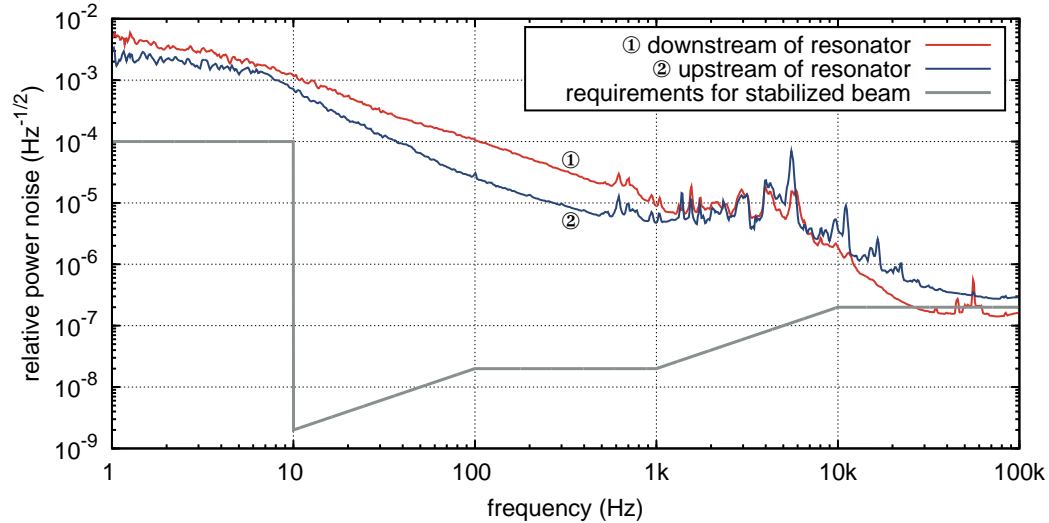


Figure 2.20: Relative power noise of the Advanced LIGO functional prototype laser upstream and downstream of an optical resonator.

measured. This high level of power fluctuations causes problems for the power stabilization since so far no power actuator with sufficient dynamic range is available or has been tested.

To summarize, the laser system has a quite high power noise which in principle can be suppressed by a power stabilization. However, so far no power actuator for the stabilization is available that has enough dynamic range to compensate the peak-to-peak power fluctuation. Promising results were achieved with an acousto-optical modulator (AOM) placed into the high power beam, but so far the Advanced LIGO power stability requirements have not been achieved with the current prototype. The peak-to-peak power fluctuations need to be reduced in future prototypes and new high dynamic range power actuators are required.

2.3.3 Photonic Crystal Fiber Laser

The photonic crystal fiber laser is a master-oscillator fiber-amplifier system with an output power of about 150 W at 1064 nm. The first stage is an NPRO master laser (see Sec. 2.3.1) which is amplified in the second stage by a 4 m long ytterbium doped double-clad photonic crystal fiber. The amplified beam has the same frequency stability as the NPRO. Due to the special photonic structure and the coiling of the fiber, increasing propagation losses for higher-order modes, the fiber is still single-mode although the fiber core is several times larger compared to traditional single-mode fibers. Non-linear effects such as stimulated Brillouin scattering, which often limits the output power of fiber amplifiers, are reduced due to this larger fiber core. The ytterbium doped core is pumped via the pump cladding at 976 nm with

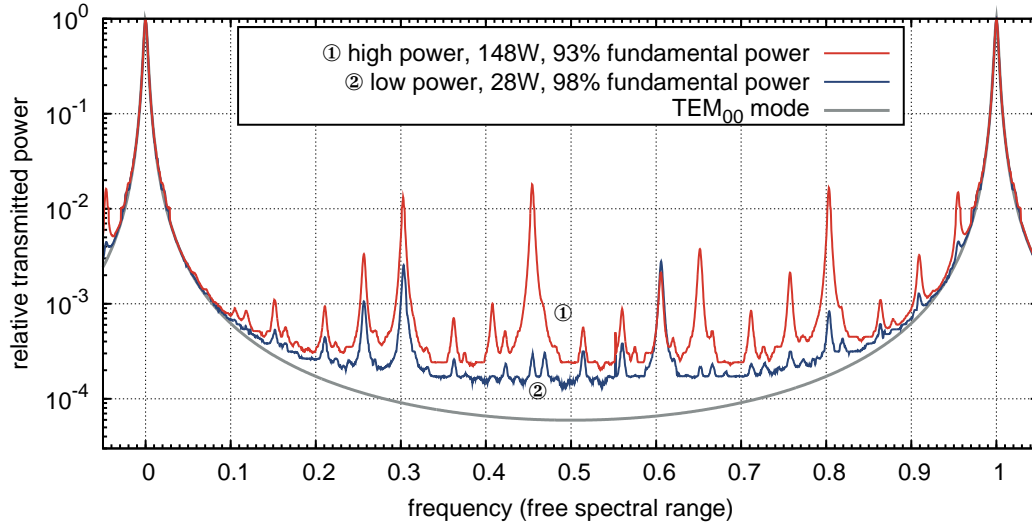


Figure 2.21: Beam quality measurement of the photonic crystal fiber laser at two different output powers.

a fiber-coupled laser diode module. This fiber laser is described in more detail in [Hil06, Hil09c].

This laser system was an early prototype and was characterized to determine if such a system can be used in GWDs. Especially the beam quality was of interest due to the photonic structure of the fiber amplifier.

Beam Quality Investigations

The beam quality was measured with the modescan technique at low (28 W) and high (148 W) output power (Fig. 2.21). Despite of the photonic structure a fundamental power of 98% was measured at low output power. This is a high beam quality which is comparable to the beam quality of an NPRO.

At high amplification leading to an output power of 148 W the beam quality degraded to a fundamental power of 93% (138 W in TEM₀₀ mode). Thermal effects inside the fiber seem to degrade the beam quality; however, the fiber coiling diameter and thus the propagation losses of higher-order modes were not optimized at these power levels. Anyhow the achieved beam quality and output power is comparable with the Advanced LIGO functional prototype laser. At high output power particularly a few higher-order modes (second order at 0.3 FSR and 0.8 FSR, third order at 0.45 FSR) degrade the fundamental power compared to the low power operation mode.

A fiber laser based on a stable NPRO master laser and a high power photonic crystal fiber amplifier is very promising as light source for GWDs. With quite low effort compared to, e.g., the Advanced LIGO laser a high output power with a good beam quality is achieved. However, the reliability and long-term performance of

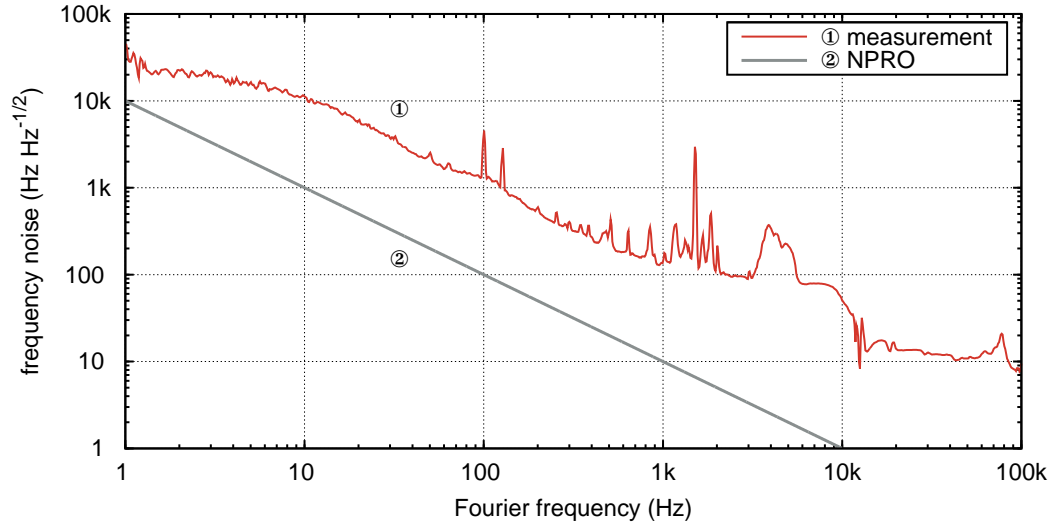


Figure 2.22: Frequency noise of the fiber laser at 1550 nm. The typical free-running frequency noise of an NPRO laser at 1064 nm is shown for comparison.

such a laser concept has to be investigated since due to the high power densities in the fiber and at the fiber ends the fiber can easily fail. Such a long-term monitoring could, e.g., be performed with periodic, automated DBB measurement sequences.

2.3.4 Fiber Laser at 1550 nm

This laser is a commercial single-frequency fiber laser (Koheras BoostiK, NKT Photonics) operating at 1550 nm with an output power of about 2 W. An erbium DFB (distributed feedback) fiber laser is used as low power master oscillator in order to achieve a high free-running frequency stability. The higher output power of the system is achieved with a subsequent two-staged amplifier. More information about this laser can be obtained from the manufacturer [NKT09].

All current GWDs operate at a wavelength of 1064 nm and lots of development work was spent in the field of lasers and optical coatings specifically for this wavelength. Despite these technological advancements at 1064 nm the wavelength 1550 nm is important for future GWDs since silicon has a very low absorption coefficient at this wavelength and is a good candidate as test mass material for cryogenic GWDs.

A characterization of this laser is especially important for future GWDs since this laser is one of the few commercially available lasers at this wavelengths that fulfill the rough requirements of GWDs.

Frequency Noise Investigations

The frequency noise of the laser was characterized with the 1550 nm DBB. The other beam parameters accessible to the DBB were not characterized since for a

power fluctuations measurement the laboratory environment was not clean enough, a very good beam quality due to the fiber coupled output can be assumed, and beam pointing fluctuations mainly depend on the stability of the fiber output coupler and not the laser itself.

The frequency noise of the laser was between $10 \text{ Hz Hz}^{-1/2}$ and $100 \text{ kHz Hz}^{-1/2}$ in a frequency band from 1 Hz to 100 kHz (Fig. 2.22). The noise decreased towards higher frequency with about $1/f$ similar to an NPRO. Compared to an NPRO the frequency fluctuations were about one, at some frequencies up to two orders of magnitude larger, although a direct comparison is problematic since the NPRO emits at a different wavelength.

For future GWDs operating at 1550 nm the frequency noise of this laser is probably acceptable assuming that these GWDs require similar frequency stabilities as current detectors. NPROs are used in current GWDs as master lasers and the free-running frequency noise of these lasers has to be reduced by about ten orders of magnitude (see Sec. 3.2). Accordingly a frequency stabilization at 1550 nm will be definitely necessary, and similar stabilized frequency stability levels should be achievable assuming appropriate frequency actuators are available. The output power of about 2 W is yet much too low to be directly used in GWDs, but in principle the output power could be increased with subsequent amplifier stages.

2.4 Summary

A fast and reliable characterization of laser beams is crucial for the development of new lasers, for designing laser stabilizations, and for monitoring the performance of laser systems in operation.

So far no sensitive instrument for characterizing all important beam parameters (Sec. 2.1) such as power, frequency, and pointing noise or the beam quality was available. Thus the diagnostic breadboard (Sec. 2.2) was developed which is a compact, transportable, automatized laser beam diagnostic tool specifically optimized for GWD lasers. Several experimental problems (Sec. 2.2.2) were solved, the sensitivity of the measurement methods used (Sec. 2.2.1) was determined, and two different computer interfaces (Sec. 2.2.3) were implemented.

Afterwards different laser systems at 1064 nm and 1550 nm were characterized with the aid of the DBB. Among these lasers were a well established, proven system (NPRO, Sec. 2.3.1), a current high power system for the next generation of GWDs (Advanced LIGO laser, Sec. 2.3.2) and new fiber lasers (Sec. 2.3.3, Sec. 2.3.4) that might be used in future precision experiments.

The DBB proved its usability for fast characterizations in the field of laser development as well as for automatized long-term monitoring of laser systems in operation. Therefore the DBB is suited for the diagnostics and monitoring of the Advanced LIGO laser system. The automation of the DBB simplifies the execution and analysis of beam characterizations and can minimize careless mistakes. Though it cannot replace an accurate knowledge of the measurement and analysis methods used since just due to the automation a careful evaluation of the characterization results is

necessary. Only with such knowledge, limitations and measurement errors, such as the corona in the Advanced LIGO laser (Sec. 2.3.2) or the strong environmental dependence of pointing measurements (Sec. 2.3.1), can be revealed. In principle the DBB could easily be adapted to other laser wavelengths due to the wavelength independent optical design.

The characterization results of the NPROs verified that they are highly stable laser sources that are ideal for precision experiments and as master oscillators in amplifier or injection-lock configurations. For the functional prototype of the Advanced LIGO laser the characterization revealed that this prototype does not fulfill the requirements for the combination of output power and beam quality and that the necessary power stabilization of this system cannot be realized yet due to high peak-to-peak power fluctuations. The results of the two fiber lasers showed that these lasers are in general compatible with the requirements of precision experiments such as GWDs.

All in all sensitive and extensive laser beam characterizations were performed with the DBB yielding important results for the development of new laser prototypes and used for stabilization concepts described in the next Chapter 3.

Laser Stabilization

Laser stabilization is an important and often inevitable part of high precision measurements, quantum optic experiments and gravitational wave detectors. In many cases laser fluctuations couple to the actual measurement signal, masking signals or limiting the sensitivity. Therefore it is essential to stabilize the laser beam in order to achieve the performance desired. In such a stabilization effort one has to take the design goal as well as the free-running laser noise and coupling mechanism between several observables into account.

Usually a laser beam parameter should be stabilized only after the origin of the free-running noise is investigated. It is always preferable to avoid fluctuations in the first place instead of reducing them afterwards with complicated stabilizations. Dust particles, e.g., can cause power fluctuations when passing the laser beam, which can be simply avoided using filtered air. Another example are vibrations of mirror mounts producing beam pointing fluctuations, which can be reduced with better damping of the mounts or seismically isolated optical tables. For the investigation of these fluctuations and their causes the diagnostic breadboard described in Chapter 2 can be of good use.

In a second step, prior to the implementation of a stabilization, the coupling mechanism between the laser beam parameter noise and the actual measurement signal of the main experiment should be investigated. By reducing the coupling the requirements for the tolerable laser fluctuations can be relaxed. As an example, in some experiments it is possible to reduce the coupling by carefully choosing an appropriate operating point or to minimize the coupling at low frequencies by shifting the measurement signal to higher Fourier frequencies using modulation techniques.

As final step passive and active stabilizations of laser beam parameters should be considered as well, which is described in detail in this chapter. In many experiments a subtle combination of avoiding free-running fluctuations, reducing the coupling factor, and suppressing fluctuations with stabilizations has to be chosen.

In the following sections an overview of stabilization methods frequently used is given (Sec. 3.1) and the interaction of different methods is explained in the scope of the Advanced LIGO stabilization concept (Sec. 3.2). Furthermore two concrete laser stabilization experiments are described in the subsequent Chapters 4 and 5.

3.1 Review of Stabilization Methods

Many different methods can be used to stabilize lasers. In this section various active and passive stabilization methods, which are especially, but not exclusively, used in the field of GWDs, are briefly described and reviewed.

3.1.1 Passive Filtering vs. Active Feedback

For selecting the appropriate stabilization methods the free-running noise is crucial. In Chapter 2 methods for characterizing all important laser beam parameters are described. The required suppression dependent on the Fourier frequency can be deduced from the characterized free-running fluctuations and the level of fluctuations tolerable in the experiment. The stabilization methods can be divided into passive and active methods.

Passive Filtering

In a passive stabilization the filter property of an optical component is exploited to reduce the fluctuations of a laser beam parameter. For example, the transmission of a laser beam through an optical resonator can reduce power fluctuations for frequencies above the resonator bandwidth, or the transmission through a birefringent crystal (polarizer) can suppress polarization fluctuations.

Most components reduce the laser beam noise by a constant, possibly frequency dependent, factor that depends only on the properties of the optical component. Additional noise can of course couple into the beam at this component, which might reduce the effective filtering. As an example scattered light in the mentioned optical resonator or mechanical instabilities of the mentioned birefringent crystal can limit the filter efficiency.

Dependent on the characterized free-running noise, one can determine if the passive filtering factor is sufficient to reduce the noise to a level below the requirements.

Active Feedback

In active stabilization schemes sensors and actuators together with a feedback control loop are used to reduce laser fluctuations. An optical resonator, e.g., can be used to measure frequency fluctuations of the laser beam. Then the measured fluctuations can be suppressed with an electronic feedback controller and an AOM actuator shifting the laser frequency. Further examples of sensors and actuators of different beam parameters have been already described in Sec. 2.2.

The achievable noise reduction depends on the one hand on the loop gain of the feedback control loop and on the other hand on the sensor sensitivity: In general the free-running noise is suppressed by the control loop gain. The loop gain often depends on the bandwidth of the control loop, which in turn is frequently limited by the bandwidth of the sensor or the actuator. Usually the higher the bandwidth of the control loop, the higher the loop gain is at a specific frequency. The lower limit for the residual noise with operating stabilization is the intrinsic sensor noise. Thus at Fourier frequencies with high loop gain the performance of the stabilization is limited by the sensor noise and therefore it is important for active stabilizations to use low-noise sensors.

Another important property besides the bandwidth is the dynamic range of the actuator since only fluctuations that can be compensated with the actuator can be suppressed. Thus the selection of the actuator strongly depends on the free-running peak-to-peak fluctuations. Frequently an actuator either has a large dynamic range or a high bandwidth but not both of them. In such a case several actuators can be combined: On the one hand an actuator with high bandwidth and small dynamic range can be used to increase the bandwidth of the control loop. On the other hand a slow high dynamic range actuator is the right choice to compensate large fluctuations that are often present mainly at low frequencies.

The intrinsic sensor noise limits the achievable stability and, depending on the characterized free-running noise, the required dynamic range of the actuator and the bandwidth of control loop can be determined.

Comparison

Passive stabilization methods have the advantage that a constant noise reduction is achieved independent of the original laser beam noise (assuming no new noise sources are limiting the reduction). Thus passive methods are suitable to be cascaded. However, due to the constant filter factor the residual noise depends directly on the free-running noise.

With an active stabilization a significantly higher noise suppression can be reached in general, depending only on the loop gain and the sensor noise. Furthermore the loop gain and with it the noise suppression can be influenced more easily than the filter factor in passive schemes. However, the intrinsic sensor noise is an absolute stabilization limit.

A passive filtering is superior to an active stabilization as soon as the filtered free-running noise is smaller than the sensor noise in an equivalent active scheme. Otherwise a higher noise suppression can be achieved with an active stabilization.

The selection of the stabilization scheme also depends strongly on the Fourier frequencies and the availability of appropriate passive filters, sensors, and actuators at these frequencies. In the field of power stabilization, e.g., passive and active methods can be combined very well: For radio frequencies above about 10 MHz only few power actuators are available whereas the passive filtering with a rather small optical resonator can already achieve a high noise suppression. However at low

frequencies of a few hertz an extremely large optical resonator would be necessary to provide a passive filtering whereas many power actuators are available at these frequencies. Thus in such a case the combination of an active stabilization at low frequencies and a passive filtering at radio frequencies provides high power-stability in both frequency bands.

Active and passive schemes can not only be combined for different Fourier frequencies but can also be cascaded. Thus the free-running noise can first be reduced with an active stabilization to the sensor noise, and afterwards the residual noise can be further filtered with a passive scheme. This can be illustrated, e.g., in the case of a pointing stabilization: The pointing noise of a laser beam compared to a rigid optical resonator can be suppressed with mirrors attached to PZTs upstream of the resonator and the DWS technique in an active stabilization. Due to the mode-cleaning effect of the resonator, pointing fluctuations are further reduced in the transmitted beam.

The *optical ac coupling* technique described in Chapter 5 uses yet another combination of passive and active schemes and provides even more advantages. There the passive filter effect of an optical resonator is used to reduce the sensor noise of an active stabilization scheme. Thus the filter effect of a passive method that is not influenced by any sensor noise is combined with the high noise suppression of an active stabilization.

3.1.2 Power Stabilization

The power noise of a laser beam can be divided into two types: On the one hand the so-called *technical power noise* caused, e.g., by laser pump power fluctuations or particles passing the beam, and on the other hand the *quantum noise* caused by the quantization of the beam energy into photons. For large numbers of photons the quantum noise level depends only on the power P and the photon energy hc/λ and is in particular frequency independent. The single-sided linear spectral density s_q of the relative quantum power noise is (see Sec. 4.1)

$$s_q = \sqrt{\frac{2 \cdot hc}{P\lambda}} = 2 \times 10^{-8} \text{ Hz}^{-1/2} \cdot \sqrt{\frac{1 \text{ mW}}{P}} \cdot \sqrt{\frac{1064 \text{ nm}}{\lambda}} \quad (3.1)$$

where h is the Planck constant, c is the speed of light in vacuum, and λ is the vacuum wavelength. The quantum power noise is often called shot noise – both terms are used in this thesis.

Passive and active stabilization methods¹ can only reduce the technical part of the power noise. Thus the lowest possible power noise consists solely of quantum noise.

¹Stabilization methods that use non-classical states of light, such as squeezed light, are not considered here.

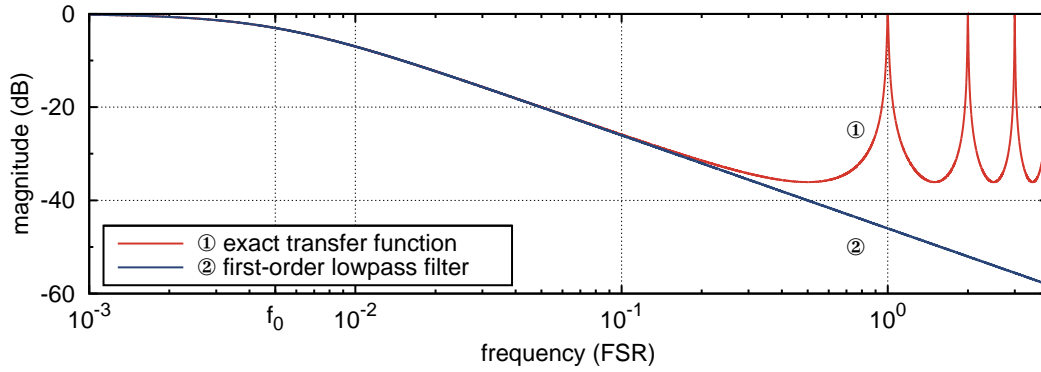


Figure 3.1: Transfer function of an optical resonator ($\mathcal{F} = 100$, bandwidth $f_0 = 5 \times 10^{-3}$ FSR) for power fluctuations and lowpass approximation.

Passive Filtering

Power fluctuations have been successfully reduced with different passive methods. The filter effect of an optical resonator was used to reduce power noise in a broad frequency band at radio frequencies [Wil98, Gra07]. Technical power fluctuations above the bandwidth of the resonator are suppressed in the transmitted beam. The exact transfer function of the resonator for power noise [Sie86, Chap. 11] can be approximated by a first-order lowpass filter for frequencies in the range of the resonator bandwidth (Fig. 3.1). The highest noise suppression occurs at half the FSR and depends on the resonator finesse. The suppression decreases for higher frequencies again.

In another experiment an asymmetric Mach-Zehnder interferometer was used to reduce power noise by up to 30 dB in a narrow frequency band at the relaxation oscillation frequency [Csö05]. One arm of the interferometer was about 100 m longer causing a phase shift of 180° at the relaxation oscillation frequency due to the additional time delay in this arm. The contrast of the interferometer limited the noise suppression achieved.

In principle saturated amplifiers can be used to reduce power noise for frequencies below a characteristic frequency that depends on the amplifier gain dynamics. The relative power noise of the amplified beam is smaller than the noise of the seed beam [Fre93, Nov02, Sar05, Fre07b]. Often, however, other noise sources such as pump power noise couple to the amplified beam, easily masking the described noise reduction effect.

Active Feedback

Power noise has been reduced with active power stabilizations using various actuators and control loop designs in different frequency bands: A strong source of power noise in many lasers is the relaxation oscillation. This oscillation is caused by a

resonant coupling between the laser medium inversion and the resonator field. The frequency of the oscillation depends on many laser parameters and is usually between a few tens kilohertz and a few megahertz. Many active power stabilizations using a photodetector as sensor and the pump power of the laser as actuator are described in the literature [Kan90, Har94, Row94, Tac96, Buc98, Csö03, Zha03].

In the gravitational wave frequency band (about 10 Hz to 10 kHz) various power stabilization experiments can be found in the literature as well. All stabilizations use photodetectors, feedback control loops, and different actuators to reduce technical noise in this frequency band.

Many experiments use the laser pump power to control the output power of the system [Tsu92, Har94, Row94, Ott00, Abb01, Mus01, Zaw02, Noc04, Rol04, Bar05, Mio07]. Since pump power fluctuations often cause the laser output power fluctuations in this frequency band it is in such a case reasonable to use the pump power as actuator. Furthermore in many cases the output power of the laser can be decreased and, even more important, increased with the pump power. This is a clear advantage over external power actuators since these can only decrease the output power in general. On the other hand laser internal actuators can more easily cause cross couplings to other beam parameters [Que03] such as the laser frequency [Wil00] since they are influencing the laser dynamics and its spatial and thermal environment. This kind of couplings occur less often with external power actuators.

Acousto-optical modulators (AOMs) can be used as external power actuator by varying the electrical RF drive power. The diffraction efficiency of an AOM depends linearly on the drive power. Thus the beam power remaining in the zeroth diffraction order can be controlled electronically. This actuator was used, e.g., in [Lay79, Sei06, Kim07, Tak08]. Electro-optical modulators (EOMs), which are also called electro-optical amplitude modulators (EOAMs) in this context, and the Faraday effect can be used to rotate the polarization of a laser beam with an electrical signal. With a subsequent polarizing beam splitter the polarization rotation can be turned into a power modulation. Several experiments used an EOAM [Rob86, Nag98, Iva07, Kwe09b] and the Faraday effect [Yos82].

However in most experiments the performance achieved was not limited by the actuators but by noise sources coupling into the power sensor of the control loop. Thus in many experiments significant, unexplained differences were in the noise level measured by the photodetector used for the stabilization (in-loop) and the photodetector used for an independent measurement (out-of-loop). In the ideal case the in-loop and out-of-loop detector are solely limited by quantum noise (see Sec. 4.1, [Tau95]). However the power noise measured out-of-loop is often higher than the expected quantum noise level, especially at low frequencies of a few tens of hertz. Many different noise sources were identified that in principle can cause this discrepancy, such as photodiode internal low-frequency noise, resistor current noise, beam pointing in combination with spatial inhomogeneous photodiodes, dust particles passing the beam, temperature fluctuations, photodiode bias voltage fluctua-

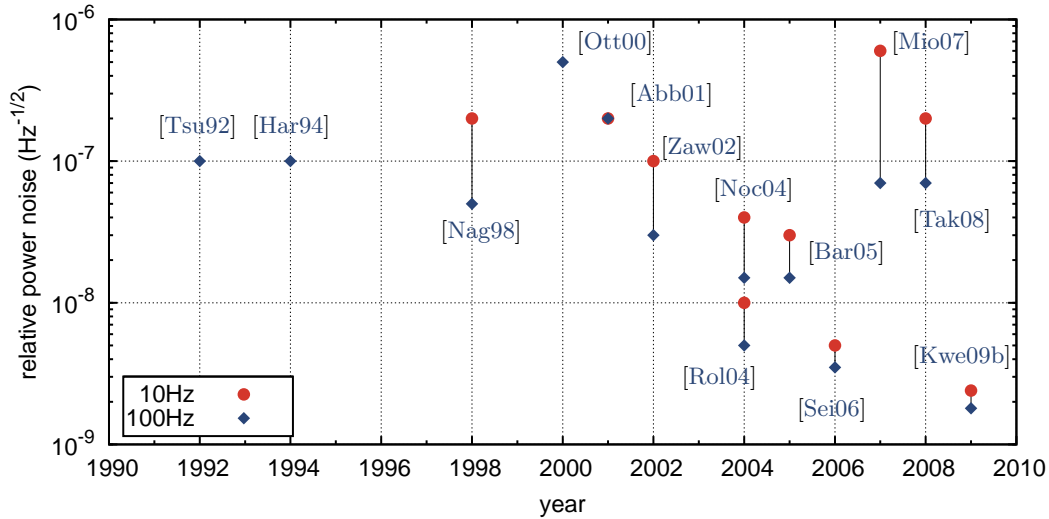


Figure 3.2: Out-of-loop measured residual power noise at 10 Hz and 100 Hz of several power stabilization experiments from 1992 to 2009.

tions, scattered light, electronic grounding noise, or polarization fluctuations [Rol04, Bar05, Sei06, Kwe09b, Sei09]. In order to suppress some of these noise sources mode-cleaning resonators or optical fibers and vacuum or pressure-tight tanks were used in a few experiments [Noc04, Rol04, Bar05, Sei06, Mio07, Tak08, Kwe09b].

The out-of-loop residual power noise achieved in different selected experiments is shown in Fig. 3.2. The highest power stability so far in the gravitational wave frequency band was achieved with a high-sensitivity photodiode array [Kwe09b]. This experiment is described in more detail in Chapter 4.

3.1.3 Frequency Stabilization

The frequency noise of a laser beam can be divided into technical and quantum noise contributions. Technical frequency noise can be caused, e.g., by laser resonator length fluctuations or the Doppler effect at shaking mirrors. Again, the quantum noise is the fundamental limit for every frequency stabilization. Stabilizations can reduce only the technical noise contribution. The shot noise of the photons causes a Fourier frequency independent, white phase noise, which corresponds to a Fourier frequency dependent frequency noise. The single-sided linear spectral density $s_{q,\nu}$ of the frequency noise is [Hun07]

$$s_{q,\nu}(f) = \pi f \cdot \sqrt{\frac{2 \cdot hc}{P\lambda}} = 61 \text{ nHz Hz}^{-1/2} \cdot \left(\frac{f}{1 \text{ Hz}}\right) \cdot \sqrt{\frac{1 \text{ mW}}{P}} \cdot \sqrt{\frac{1064 \text{ nm}}{\lambda}} \quad (3.2)$$

where hc/λ is the photon energy, P is the beam power, and λ is the vacuum wavelength.

Only a few experiments were performed in order to suppress frequency noise with passive methods. These experiments used optical resonators to reduce frequency fluctuations at Fourier frequencies above the resonator bandwidth in the transmitted beam [Dub04, Hal05, Lab07]. This filter effect, working in the same way for power fluctuations, was already explained in Sec. 3.1.2 (see Fig. 3.1).

Many different active frequency stabilizations are described in the literature. Necessary for a stabilization are a sensor measuring frequency fluctuations, an actuator controlling the frequency of the laser beam, and a feedback control loop. The sensor consists of a frequency discriminator that converts frequency fluctuations to amplitude fluctuations, which in turn can be measured with photodetectors. The frequency discriminator serves as frequency reference in these active stabilizations.

Different frequency discriminators have been already used, such as hyperfine transitions in iodine [Ari92, Ari93], asymmetric Mach-Zehnder [Gre98, Cra02] and Michelson [Kéf09] interferometers, wavelength meters based on Fizeau interferometers [Kob07], or other laser beams [Che90]. However most experiments use optical resonators as frequency discriminators. Among them are many using high-finesse rigid-spacer resonators [Fri89, Sho89, Day92, Sam93, Ueh93, Nak94, Bon96, Ruo97, Con03, Web04] and a few using optical resonators with individually suspended mirrors [Ara97, Mus97, Clu00, Nag03, Kaw97]. Resonators with rigid spacers are especially suited to stabilize the frequency at low Fourier frequencies. In these experiments spacer materials with a low thermal expansion coefficient such as ULE or Zerodur are selected, and furthermore special mounting techniques [Naz06, Lud07, Liu09] or cryogenic cooling [Sch95, See97, Sto98] are used to improve the resonator resonance-frequency stability. On the other hand resonators with suspended mirrors are only good frequency references for Fourier frequencies above the mechanical resonance of the suspension. Since these resonators frequently have a much larger round-trip length than rigid-spacer resonators they have a superior frequency stability at high Fourier frequencies, but are also much more complex since the mirror alignment has to be actively stabilized.

For optical resonators different methods were developed to convert frequency fluctuations to an amplitude signal. Among them are well-known methods, such as the *fringe locking* [Bar73], which stabilizes the frequency slightly next to the exact resonance frequency using a photodetector in transmission, or the *dither lock* [Whi65], which modulates the laser frequency or the resonator resonance frequency and demodulates the photodetector signal in transmission or reflection at the same frequency. A method frequently used is the so-called *Pound-Drever-Hall* method, which is a radio-frequency phase-modulation scheme with a photodetector in reflection of the resonator [Dre83, Bla01]. Furthermore the *Hänsch-Couillaud* method [Han80] uses a polarization dependence of the resonator, and the *tilt locking* [Sha99, Sla02] uses non-resonant higher-order TEM modes.

In order to verify the achieved frequency stability many experiments used several laser beams each stabilized to an independent resonator and measured the beat frequency between the beams [Sam93, Nak94, Bon96, See97, Web04, Liu09]. Using such a setup an upper bound for the achieved residual frequency noise can be de-

terminated since frequency discriminator noise and readout method noise is included. These experiments showed that several technical noise sources such as seismic and acoustic noise, thermal fluctuations, scattered light, mechanical spacer resonances or beam pointing fluctuations [Sal88, Fri93, Cal97] can limit the achieved frequency stability. Thus the best frequency stabilities were achieved with resonators carefully isolated from many noise sources using, e.g., seismic isolations, thermal stabilizations, and vacuum tanks.

One fundamental noise source is the thermal noise of the spacer, the mirrors and the coatings [Num04]. The thermal noise can be slightly influenced by the geometry and the material of the spacer and mirrors, as well as by the coating type. Besides thermal noise, shot noise is another fundamental noise source. However this can be reduced more easily by increasing the detected laser power [Ueh94].

In a few experiments [Kaw97, Nag03] complicated multi-stage feedback control loops were used. This has the advantage that different frequency references can be used for different Fourier frequency bands, such as rigid spacer resonators at low frequencies and suspended mirror resonators at higher ones, and that the total loop gain can be distributed to several stages. Especially in the field of GWDs such multi-stage stabilization concepts are necessary.

In general different actuators are used to control the frequency of the laser beam. In most cases laser internal actuators are used controlling the laser resonator length, e.g., with PZTs or temperature changes. In addition external high-bandwidth actuators are used. AOMs shifting the laser frequency of the first diffraction order by the RF control frequency [Sho89, Nak94, Clu00, Web04, K ef09] or EOMs controlling the laser phase and with it the laser frequency at high Fourier frequencies [Bon96, Kaw97, Clu00] were used.

Many different experiments are described in the literature and various methods were developed to stabilize the laser beam frequency. These experiments were motivated by countless application fields for frequency stabilized lasers, such as optical frequency standards, high-resolution spectroscopy, coherent optical communications systems and of course GWDs.

3.1.4 Pointing Stabilization

The quantum noise caused by the shot noise of the photons limits every measurement of the relative pointing ϵ (see Sec. 2.1), i.e. the measurement of the position and tilt of the laser beam. With passive and active stabilizations only the technical noise caused, e.g., by shaking mirrors or air refractive index fluctuations can be suppressed. The single-sided linear spectral density $s_{q,\epsilon}$ of an arbitrary projection of ϵ (see Sec. 2.2.2, Eq. 2.12) of a quantum noise limited beam is [Hsu04, Del06]

$$s_{q,\epsilon} = \frac{1}{2} \cdot \sqrt{\frac{2 \cdot hc}{P\lambda}} = 1 \times 10^{-8} \text{ Hz}^{-1/2} \cdot \sqrt{\frac{1 \text{ mW}}{P}} \cdot \sqrt{\frac{1064 \text{ nm}}{\lambda}} \quad (3.3)$$

where hc/λ is the photon energy, P is the beam power, and λ is the vacuum wavelength. This yields for a pure translation $s_{q,\delta x}$ or a pure tilt $s_{q,\delta\alpha}$

$$s_{q,\delta x} = 1 \text{ pm Hz}^{-1/2} \cdot \left(\frac{w_0}{100 \text{ }\mu\text{m}} \right) \cdot \sqrt{\frac{1 \text{ mW}}{P}} \cdot \sqrt{\frac{1064 \text{ nm}}{\lambda}} \quad (3.4)$$

$$s_{q,\delta\alpha} = 33 \text{ prad Hz}^{-1/2} \cdot \left(\frac{\theta_D}{3.4 \text{ mrad}} \right) \cdot \sqrt{\frac{1 \text{ mW}}{P}} \cdot \sqrt{\frac{1064 \text{ nm}}{\lambda}} \quad (3.5)$$

where w_0 is the beam radius and θ_D is the half divergence angle of the Gaussian beam.

In several experiments beam pointing fluctuations were passively reduced by transmission through an optical resonator [Rüd81, Ara97]. In these experiments beam pointing was stabilized in a broad frequency band with respect to the fundamental mode of the resonator. As already mentioned, beam pointing fluctuations can be described by power fluctuations of higher-order TEM modes (see Sec. 2.1). Since the resonance frequency of these higher-order modes is in general different from the fundamental mode, higher-order modes are reflected by the resonator whereas the fundamental mode is transmitted. Thus pointing fluctuations are converted to power fluctuations of the transmitted beam, which usually are rather small and can be suppressed with an additional power stabilization or might be tolerable.

In a similar way pointing fluctuations can be passively suppressed with single-mode fibers since they only guide the fundamental mode and no higher-order modes [Sho88, Hei99, Mei06]. In such a case the beam pointing is stabilized with respect to the fiber output coupler.

Several different active stabilizations are described in the literature. These experiments differ in the pointing references used, the sensing schemes, and the actuators. In some experiments photodetectors, optical components with angle dependent transmission, or Shack-Hartmann sensors, all mounted to the optical table, were used as pointing reference [Gra88, Lev96, Mae96, Gra01]. Other experiments used another laser beam as reference, which in turn can be represented by the fundamental mode of an optical resonator or an interferometer [Sam90, Mor94a, Mor94b, Fri98, Rom05].

Different methods were developed to measure the relative pointing of a beam with respect to the fundamental mode of an optical resonator: The pointing degrees of freedom can be modulated directly, as described e.g. in [Daw08], or radio-frequency phase modulations at the resonance frequencies of the higher-order modes corresponding to the beam misalignments were used [And84, Sam90]. Another method frequently used is the differential wavefront sensing (DWS), where radio frequency modulations are measured in reflection of the resonator [Mor94a, Mor94b]. This method can also be used to measure the beam pointing in interferometers [Fri98] or with respect to other laser beams [Mül05].

Different actuators were used to control the beam pointing. In many cases two mirrors were used as actuator that can be electronically tilted with PZT elements [Gra88, Sam90, Mü105], by the suspension [Mor94b, Ara97, Hei99, Gro02], or as part of galvanometer scanners [Gro02, Sla05, Rom05]. With deformable mirrors it is not only possible to tilt the beam but also to correct geometrical beam distortions [Avi06]. Finally prisms out of electro-optical material can be used to tilt the beam with very high bandwidth as proposed in [Ami02].

The conclusion is that beam pointing fluctuations can be reduced very well with passive and active methods.

3.1.5 Beam Quality

In general the beam quality is improved by suppressing higher-order spatial modes and hence maximizing the fundamental power². As starting point for improving the beam quality, beam distortions should be avoided in the first place, via, e.g., reducing aberrations in the laser resonator or using high quality optical components with small wavefront distortions. Nonetheless it is necessary for some experiments to further reduce higher-order spatial modes and their fluctuations with different passive and active methods.

The transmission through an optical resonator [Rüd81] is a frequently used passive method. In this context the resonator is often called *mode-cleaner*. Since the resonance frequencies of higher-order spatial modes differ in general from the resonance frequency of the fundamental mode the higher-order modes are mainly reflected at the resonator whereas the fundamental mode is transmitted. Thus the transmitted beam has significantly reduced higher-order modes and has a higher beam quality. This requires of course that the optical resonator is frequency stabilized to the fundamental mode with one of the many methods described in Sec. 3.1.3. The suppressed spatial mode fluctuations are converted to power fluctuations of the transmitted beam by the resonator. Rigid-spacer resonators [Wil98] as well as resonators with suspended mirrors [Ara97, Nag02, Goß03] have been used as mode-cleaner.

The reduction of higher-order spatial modes is limited by two effects: The suppression factor of the mode-cleaner for individual higher-order modes, depending on the finesse and the round-trip Gouy phase of the resonator, is limited. Furthermore, it is not possible to achieve a high suppression for all higher-order modes simultaneously. Modes of very high order can have resonance frequencies close to the fundamental mode and are therefore well transmitted through the mode-cleaner. This problem was, e.g., solved in [Goß03] by cascading two mode-cleaners of slightly different designs. The second effect limiting the performance of a mode-cleaner is

²Beam pointing fluctuations can be described by spatial mode fluctuations of the TEM₁₀ and TEM₀₁ modes. Pointing stabilization methods have already been reviewed in Sec. 3.1.4 (see Eq. 2.5). Thus in the following only methods are described that reduce higher-order modes besides the TEM₁₀ and TEM₀₁ modes.

the quality of the resonator fundamental mode itself. Especially at high circulating laser power in the mode-cleaner, the beam quality of the resonator eigenmode can easily degrade due to thermal effects [Ueh97, Bul08]. Furthermore, the eigenmode can have an astigmatism outside of the resonator when leaving the resonator through a mirror not at normal incidence [Bar06].

Besides optical resonators, single-mode fibers were used as well to suppress higher-order spatial modes [Sho88, Mei06]. Compared to resonators no locking scheme is necessary. However, fibers cannot be used for a simultaneous temporal filtering, such as filtering of power or frequency noise (see Sec. 3.1.2, Sec. 3.1.3).

A few experiments were performed to improve the beam quality with active methods. In these experiments Shack-Hartmann sensors [Bak02, Cal03], interferometric phase-front detections [Avi04, Avi06], or heterodyne detections [Mue00] were used to measure spatial mode fluctuations. These fluctuations were compensated with deformable mirrors, however due to the low resolution of the sensors and actuators only low order spatial distortions could be reduced. For compensating low order spatial mode fluctuations on minute time scales, e.g., thermal lenses controlled by an auxiliary laser were used [Que06, Ara07b].

All in all higher-order spatial modes and their fluctuations can be suppressed very well with optical resonators and fibers improving the beam quality of the transmitted beam, whereas the performance of the few active stabilization methods is quite limited up to now.

3.2 Stabilization Concept of Advanced LIGO

Comprehensive laser stabilization is necessary for the GWD Advanced LIGO in order to achieve the design sensitivity. In this section the coupling of laser noise, the tolerable residual laser noise, and the stabilization concept are described.

GWDs require extremely stable lasers as light source for the interferometer in order to reach a sensitivity capable of detecting gravitational waves [Som06, Wil08]. Cosmic events, such as supernova explosions, inspiraling neutron stars or black holes, cause relative length changes at the order of 10^{-23} [Sch99]. Such tiny length changes can be measured with laser Michelson interferometers with arm lengths of several kilometers and suspended test masses. Several long baseline GWDs are operated in a worldwide network, LIGO [Abr92], GEO600 [Wil02], VIRGO [Ace02] and TAMA300 [And01], and the next generation of detectors, Advanced LIGO [Fri03, Adv07], Advanced VIRGO [Fla05, VIR07] and LCGT (Large Scale Cryogenic Gravitational Wave Telescope) [Kur03, Oha08], is developed at the moment. In order to avoid that laser noise is masking gravitational wave signals, very stable laser systems with small free-running noise are used, fluctuations of all important beam parameters are reduced with passive and active methods, and the coupling of laser noise to the gravitational wave channel is kept small by optical design and by choosing an appropriate operating point of the interferometer.

In Section 3.1 the stabilization methods for the different beam parameters were separately reviewed. In this section the stabilization concept of Advanced LIGO is described, where all the important beam parameters need to be stabilized simultaneously. First of all Advanced LIGO and in particular the laser system is described in more detail.

3.2.1 Advanced LIGO

The LIGO detectors operating at the moment will be replaced by the second generation Advanced LIGO detectors. The components and subsystems are currently fabricated and are expected to be installed in 2011 at two sites in the USA.

The Advanced LIGO detector consists of a Michelson interferometer with 4 km arms (Fig. 3.3). With optical resonators the circulating laser power in the arms is increased in order to reduce the shot-noise contribution in the gravitational wave channel. An additional mirror (power recycling mirror, PRM) at the input of the interferometer is used to further increase the power inside the interferometer. This technique is called *power recycling* [Bil81] [Sau94, Chap. 12.7]. Gravitational waves cause differential arm length changes in the interferometer. In order to better extract these signals, a mirror (signal recycling mirror, SRM) at the output of interferometer is used (resonant sideband extraction [Mee88] [Sau94, Chap. 12.7]). The actual gravitational wave signal is measured at the output of the interferometer with the dc-readout technique [Hil09b], which requires an additional resonator (output mode-cleaner, OMC). The laser light source of the interferometer is first of all pre-stabilized and then filtered by an optical resonator (input mode-cleaner, IMC) before it is injected into the interferometer.

The GWD is divided into several subsystems [Fri08], among others the pre-stabilized laser (PSL) and input optics (IO) subsystems, which are described in more detail in the following.

The PSL consists of the Advanced LIGO laser, a diagnostic breadboard for monitoring, and a pre-stabilization to reduce power, frequency, and pointing fluctuations as well as higher-order spatial modes [Kin08, Wil09]. The primary task of the PSL is to deliver a 165 W pre-stabilized laser beam.

The Advanced LIGO laser itself consists of an NPRO master oscillator, a 35 W medium power stage, and a 200 W high power stage (see Sec. 2.3.2). The frequency of the high power stage is coupled to the master laser using the injection lock and the PDH technique. The required phase modulation sidebands are generated with an EOM between NPRO and medium power stage. The output beam of the medium and high power stage can be characterized and monitored with the diagnostic breadboard (see Sec. 2.2). An optical resonator in bow-tie configuration, called *pre-mode-cleaner* (PMC), is used to passively stabilize several beam parameters and acts as optical interface to the IO subsystem. This resonator is stabilized to a TEM₀₀ mode with the PDH technique reusing the phase modulation sidebands of the injection locking. The primary tasks and the current design of the PMC are described in more detail in Sec. 3.2.6. An additional high-finesse rigid-spacer linear

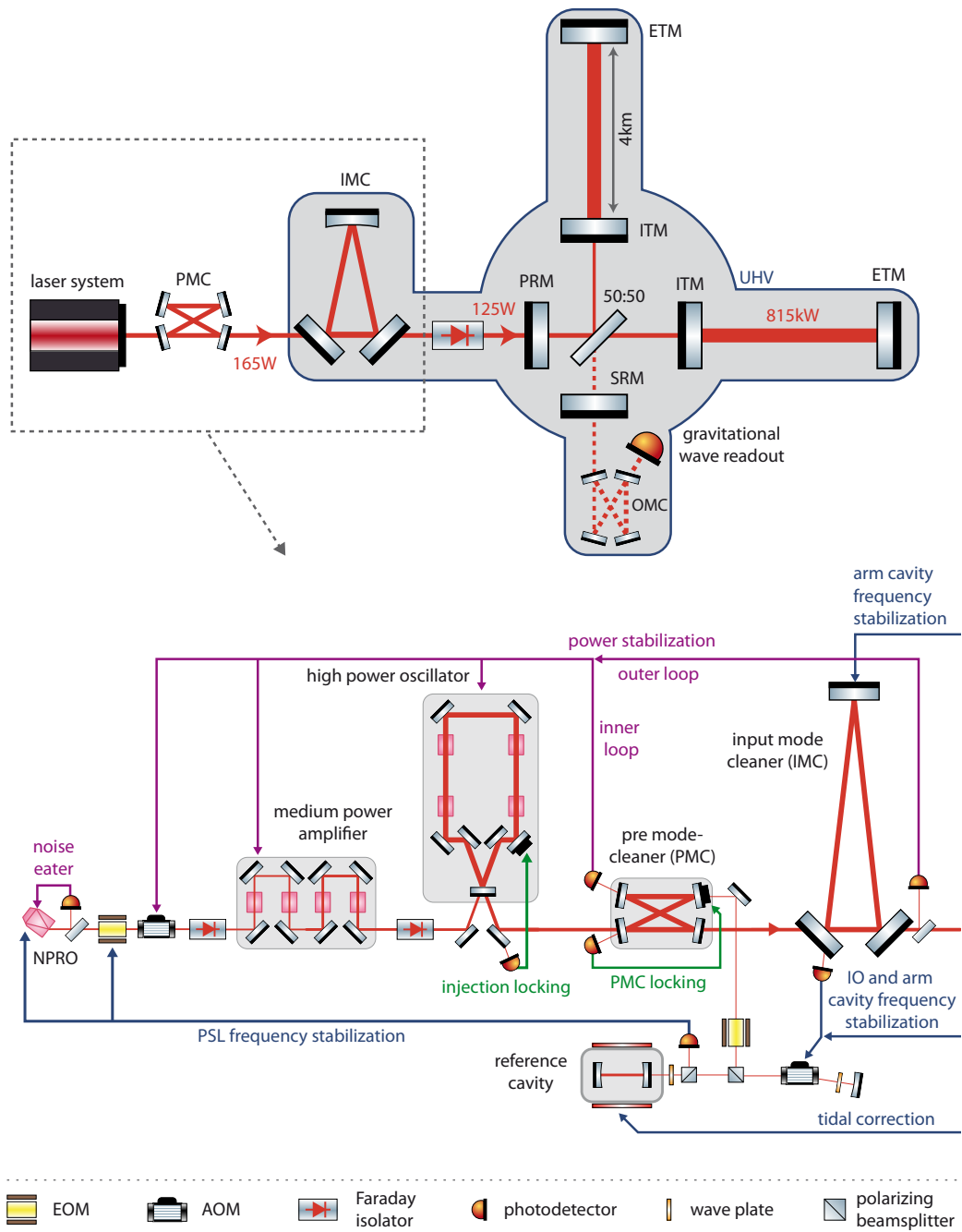


Figure 3.3: Schematic of the Advanced LIGO optical layout and detailed layout of the pre-stabilized laser subsystem (PSL) including stabilization feedback control loops [Fri08, Kin08]. (PMC, pre-mode-cleaner; IMC, input mode-cleaner; PRM, power recycling mirror; ITM, input test mass; ETM, end test mass; SRM, signal recycling mirror; OMC, output mode-cleaner; UHV, ultra-high vacuum.)

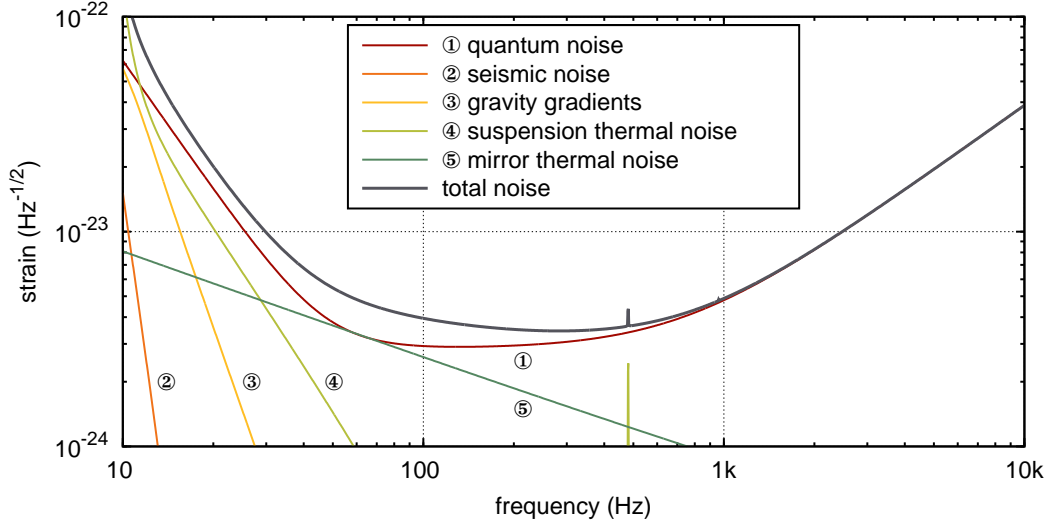


Figure 3.4: Anticipated sensitivity of Advanced LIGO due to fundamental noise sources for an interferometer input power of 125 W and zero-detuning of the signal recycling mirror [LIG09b, LIG09a].

resonator, called *reference cavity*, is used for the frequency pre-stabilization. The other components of the PSL are described as part of the stabilization concept later on.

The IO subsystem consists of the suspended input mode-cleaner, telescopes to inject the laser beam into the interferometer, and phase modulators generating control sidebands [Ami02, Ara07a]. The main task of the IO is to further reduce laser beam noise and to inject the beam into the interferometer.

At the moment the PSL and IO subsystem are in the final design phase. This means that parts of the subsystems can still change – including the stabilization concept described in this section.

Sensitivity

The design sensitivity of Advanced LIGO is limited by fundamental noise sources, such as quantum noise or thermal noise of the mirror coatings or the suspensions [Abb08a] (Fig. 3.4). Compared to the first generation of GWs a tenfold better sensitivity is anticipated. In order to reach this sensitivity goal all technical noise sources in the gravitational wave channel have to be much smaller than the fundamental ones. Thus each technical noise source should be a factor ten below the design sensitivity such that only the uncorrelated sum of at least 100 technical noise sources would generate a noise level equivalent to the design sensitivity.

Several of these technical noise sources are caused by laser noise. By estimating the coupling between laser noise and the gravitational wave channel, requirements can be deduced for the maximal tolerable laser noise. With this the required noise

suppression of the laser stabilization can be determined using the free-running fluctuations.

In the following the coupling to the gravitational wave channel, the deduced requirements, and the stabilization concept for the different beam parameters are described.

3.2.2 Power Stabilization Concept

The coupling mechanism and the stabilization concept for power fluctuations can be divided into two frequency bands, the gravitational wave band from 10 Hz to 10 kHz and the radio frequency band from 9 MHz to 200 MHz.

In the gravitational wave band, power noise causes radiation pressure fluctuations at the test masses and in addition directly couples to the output of the interferometer and the signal readout [Fri01, Wil09]. It is assumed that the circulating power of about ≈ 815 kW in the two arm resonators will differ by about 1% due to small finesse variations³. Thus power fluctuations cause slightly different radiation pressure fluctuations in the arms that cannot be distinguished from gravitational wave signals. Furthermore, power fluctuations directly couple to the actual signal since the dc-readout method is used to measure the gravitational wave signal.

The current baseline for the power stabilization in the gravitational wave band is a cascaded active and passive stabilization. At first an active stabilization with sensors directly in front of the interferometer is used and subsequently power noise is passively filtered by the power recycling cavity (PRC).

The PRC is an optical resonator consisting of the PRM and the interferometer. It has a bandwidth of about 1 Hz and a FSR of 37.5 kHz.

The tolerable power fluctuations in the arm resonators can be calculated using the assumed circulating power imbalance and the tolerable technical noise contribution in the gravitational wave channel. Taking the passive filter effect of the PRC into account the tolerable power noise in front of the PRM can be deduced (Fig. 3.5). Hence this power stability has to be achieved with the active stabilization.

The active stabilization in turn is a two-level hierarchical stabilization with an inner loop and an outer loop (Fig. 3.3) [Kin08]. The inner loop is responsible for a pre-stabilization of the laser to a level of about $10^{-8} \text{ Hz}^{-1/2}$ and the outer loop has to achieve the requirements (Fig. 3.5) directly at the interferometer input [Wil09]. The outer loop is necessary since residual pointing and frequency fluctuations in front of the suspended mode-cleaner cause power fluctuations between $10^{-7} \text{ Hz}^{-1/2}$ and $10^{-8} \text{ Hz}^{-1/2}$ in the transmitted beam [Mül08].

For the inner loop a photodetector in transmission of the PMC is used as sensor and the output power of the laser system is controlled with an AOM between the

³As already mentioned in order to reduce the technical noise in the gravitational wave channel, a reduction of the coupling factor should be considered besides a laser power stabilization. A method to balance the finesse and with it the power in the arms using etalons was proposed, which would relax the power and frequency noise requirements [Hil09a].

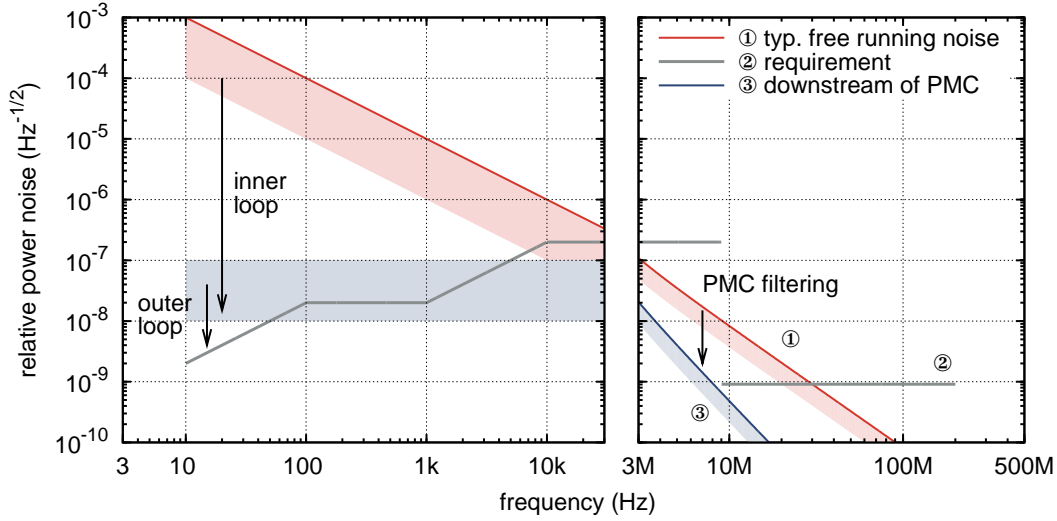


Figure 3.5: Upper bound of typical free-running power noise at the laser output, Advanced LIGO requirements in front of the power recycling mirror, and expected power noise downstream of the pre-mode-cleaner [Wil09].

NPRO and the medium power stage [Sei09, Chap. 5]. This actuator has a bandwidth of about 450 kHz and can compensate power fluctuations of up to $\approx 2\%$. The functional prototype of the laser has very high peak-to-peak fluctuations of about 30%, which of course cannot be compensated by this AOM alone (see Sec. 2.3.2). Even with another external, high dynamic range actuator this would mean that the average power of the laser system has to be reduced by about 15% in order to compensate all power fluctuations. Thus the free-running power fluctuations have to be reduced in the final laser system and new high-power actuators with high dynamic range have to be investigated.

For the outer loop a high-sensitivity photodetector will be placed in the vacuum system detecting a sample of the beam between suspended mode-cleaner and PRM [Sei09, Chap. 5]. The signal of this photodetector is conditioned by a control loop filter and injected into the error point of the inner power stabilization loop in order to adjust the output power of the laser. The main challenge of the outer loop is a vacuum compatible, high-power photodetector with a sensitivity of $2 \times 10^{-9} \text{ Hz}^{-1/2}$ at 10 Hz. A precursor of such a photodetector is described in Chapter 4.

Furthermore, amplitude fluctuations of the phase modulation sidebands can spoil the power stabilization: As already mentioned, power fluctuations couple to the gravitational wave channel by radiation pressure in the arm resonators. Thus the power inside the arm resonator has to be stabilized. Since the sensor for the outer loop is placed in front of the interferometer, the total power at this point will be stabilized, but this beam consists of several phase modulation sidebands besides the arm resonator mode. As these sidebands do not enter the arm cavities the

amplitude of the sidebands has to be very stable in order not to spoil the power stabilization for the arm resonator mode⁴.

At radio frequencies between 9 MHz and 200 MHz a high power-stability is required since at these frequencies control sidebands for the interferometer are generated and detected. Thus radio frequency power fluctuations can couple indirectly to the gravitational wave channel via an interferometer control loop.

The requirements on the relative power noise at these frequencies are deduced from the power handling ability of the photodetectors used to measure the control sidebands. Photodetectors able to detect a photocurrent of up to 100 mA are available, which in principle could detect signals down to $1.8 \times 10^{-9} \text{ Hz}^{-1/2}$, the quantum noise of 100 mA photocurrent. The uncorrelated sum of technical power noise and quantum noise of 100 mA should not exceed the quantum noise by more than 1 dB [Abb08b]. Hence a technical noise level of up to $9 \times 10^{-10} \text{ Hz}^{-1/2}$ is tolerable.

Almost no power actuator is available for radio frequencies and therefore only passive stabilization methods can be used. The PMC is used in the stabilization concept to filter RF power fluctuations. The passive filtering of the suspended mode-cleaner cannot be used since the FSR of 9 MHz is too small to suppress the fluctuations in the whole frequency band from 9 MHz to 200 MHz and furthermore, the EOMs generating the control sidebands are placed upstream of the mode-cleaner. Therefore the mode-cleaner is not allowed to filter RF power fluctuations near the sideband frequencies, since otherwise they would not be transmitted to the interferometer.

The RF power noise of the laser system is dominated by the NPRO, which has been characterized in Sec. 2.3.1 (see Fig. 2.15). The required suppression for power noise was deduced from the free-running noise and the requirements, and a PMC with about 600 kHz bandwidth was designed. The typical free-running noise and the expected noise downstream of the PMC is shown in Fig. 3.5.

To summarize, the power stabilization concept in the gravitational wave band consists of a subtle combinations of active and passive methods. The sensor for the active stabilization is placed as far downstream as possible, so that power fluctuations caused by upstream components are suppressed by the control loop, but in front of the PRM, so that the passive filter effect of the PRC can be exploited.

The stabilization at radio frequencies is performed with passive methods since no actuator with sufficient bandwidth is available at these frequencies. Here it makes sense to filter the power noise as soon as possible, actually directly downstream of the NPRO, since subsequent components cause almost no fluctuations at these frequencies.

⁴In principle the outer loop sensor could be placed inside the arm resonator to avoid this problem. However in this scenario the passive filter effect of the PRC cannot be used and therefore a much higher power stability has to be achieved with the active stabilization, which in turn is not possible since no power sensor with sufficient sensitivity exists.

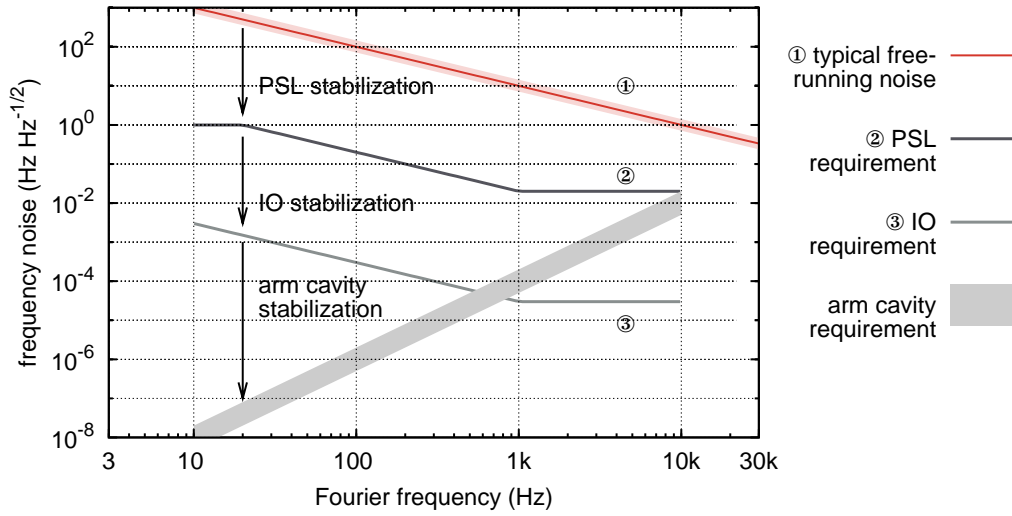


Figure 3.6: Typical free-running frequency noise, Advanced LIGO pre-stabilization requirements for the PSL and IO subsystem, and ultimate frequency noise requirements with arm cavity stabilization [Wil09, Mül02].

3.2.3 Frequency Stabilization Concept

In the gravitational wave band laser frequency fluctuations couple to the gravitational wave channel by slightly different storage times of the interferometer arm resonators [Fri01]. This storage time difference is caused by differences in the mirror transmissions and the arm resonator losses.

For estimating the coupling and deducing the requirements, a fractional transmission difference of 1% and a loss difference of 20 ppm is assumed. The required frequency stability in the interferometer is shown in Fig. 3.6.

The current stabilization baseline is a three-stage hierarchical active frequency stabilization. In the first stage the laser frequency is stabilized to the reference cavity on the optical table of the laser system (Fig. 3.3) [Kin08]. The reference cavity is a seismically isolated linear resonator with a fused silica spacer in a temperature stabilized vacuum tank. In this way the resonator is isolated from external noise sources in order to achieve a high length stability and with it a high frequency stability. The PDH technique is used to generate error signals for the feedback control loop. Three different frequency actuators are used to achieve a high unity-gain frequency of about 500 kHz on the one hand and a high dynamic range of several gigahertz on long time scales on the other hand. The temperature of the NPRO crystal is used as slow, high dynamic range actuator. The frequency can be adjusted by several gigahertz with a bandwidth of about 160 mHz [Kwe08a]. A PZT attached to the NPRO crystal is used for intermediate frequencies controlling the laser frequency by about 200 MHz to 400 MHz with a bandwidth of a few 100 kHz. Finally a broadband EOM between NPRO and the medium power stage is used to

control the phase and with it the frequency at high Fourier frequencies up to about 100 MHz. This first frequency stabilization stage is part of the PSL subsystem and has to achieve the stability shown in Fig. 3.6.

The second stabilization stage uses the suspended input mode-cleaner as frequency reference. For frequencies above the mechanical resonance of the suspension, this resonator is a more stable frequency reference than the reference cavity. An AOM is used in a double-pass configuration in front of the reference cavity to shift the frequency by twice the RF driver frequency of the beam that is stabilized to the reference cavity. By controlling the RF driver frequency, the laser frequency can be controlled in order to stabilize it to the suspended mode-cleaner. This second frequency stabilization stage is part of the IO subsystem and has to achieve the requirements shown in Fig. 3.6.

The third and final stabilization stage uses the common-mode length of the 4 km arm resonators of the interferometer to stabilize the laser frequency. This stage has to achieve the final frequency stability for the interferometer (Fig. 3.6).

On time scales of several hours the laser frequency can be controlled by adjusting the temperature of the reference cavity with heaters attached to the vacuum tank. The small temperature expansion coefficient of the fused silica spacer is exploited. This frequency actuator is used to compensate slow resonance frequency drifts of the arm resonators due to tidal forces on the test masses.

In the end, the arm resonators of the interferometers are the best frequency reference in the gravitational wave band due to the extremely long arm length and the elaborate suspensions. Thus it makes sense to use this frequency reference in the final stabilization stage. The previous stages are necessary for lock acquisition of the suspended resonators and for distributing the total loop gain of about ten orders of magnitude to several control loops.

3.2.4 Pointing Stabilization Concept

Beam pointing fluctuations couple to the gravitational wave channel by small differential misalignments of the suspended interferometer optics since the length of the arm resonators depends in such a case on the actual beam position on the optics [Fri01].

Assuming an estimated, residual, differential misalignment of the interferometer mirrors of about 10^{-9} rad, the requirements for the tolerable pointing can be calculated for the input of the interferometer [Mue09] (Fig. 3.7).

The stabilization concept is a cascaded passive and active stabilization. In the first stage pointing fluctuations of the laser system are filtered by the PMC in the PSL subsystem. The free-running pointing fluctuations of the functional prototype (see Sec. 2.3.2) were measured and an upper bound was deduced, which was used to determine the required suppression factor of the PMC. The PSL requirements (Fig. 3.7) have to be fulfilled at its IO interface so that the subsequent stabilization stages are able to achieve the final pointing stability for the interferometer.

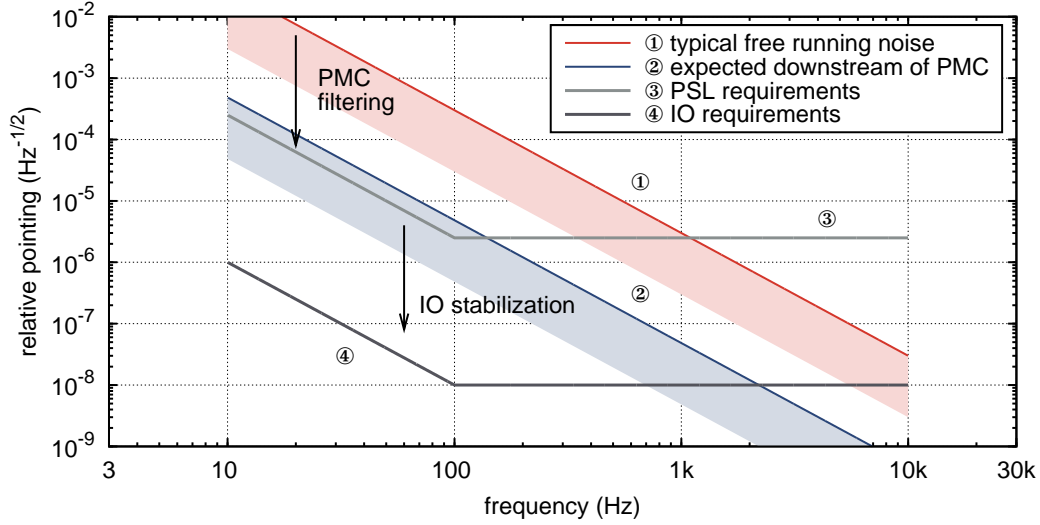


Figure 3.7: Upper bound of typical free-running pointing noise and Advanced LIGO requirements at the PSL IO optical interface and at the interferometer input [Wil09, Ara07a, Mue09].

The PMC has to reduce pointing fluctuations at least by a factor of 120. The actual suppression factor depends on the finesse and the round-trip Gouy phase of the resonator. Since the pointing requirements were tightened after the PMC design has been finished, a pointing suppression by only a factor of 62 is achieved with the current PMC. Nevertheless preliminary pointing measurements at the next Advanced LIGO laser prototype indicate that this prototype has lower beam pointing fluctuations, and therefore the suppression factor of the current PMC might be sufficient [Pöl09, Chap. 5].

The two subsequent stabilization stages are a cascaded active and passive stabilization. First of all the beam is actively stabilized to the fundamental mode of the suspended input mode-cleaner using DWS sensors and a feedback control loop with a bandwidth of a few kilohertz⁵ [Ami02]. Afterwards the pointing fluctuations are filtered by the suspended input mode-cleaner itself [Ara07a]. In the current design a passive suppression of at least 250 is anticipated. These two stabilization stages have to fulfill the pointing requirements directly in front of the interferometer (Fig. 3.7).

In general the stabilization stages reduce pointing fluctuations with respect to different reference systems, whose pointing relative to each other can also fluctuate. In the first stage the pointing of the laser is stabilized with respect to the PMC, which is mounted to the optical table, whereas in the second and third stabilization stage the suspended input mode-cleaner is used as reference system. Hence care

⁵As already mentioned the design of the IO subsystem is not finalized yet. At the moment it seems that this active stabilization stage can be skipped, and still the IO pointing requirements at the interferometer input can be met.

has to be taken that the fluctuations of these reference systems with respect to each other is smaller than the acceptable pointing noise at their interface, which seems to be the case [Mue09].

3.2.5 Beam Quality

The beam quality or spatial mode fluctuations do not directly couple to the gravitational wave channel. Nonetheless since all resonators of the GWD, such as the PMC, the IMC (input mode-cleaner), or the arm resonators of the interferometer, are stabilized to the TEM₀₀ mode, laser power in higher-order TEM modes does not contribute to the circulating power inside the interferometer. Furthermore, the higher-order modes are reflected at the resonators and cause additional shot noise at the RF photodetectors used to detect control sidebands. In principle this shot noise can couple to the gravitational wave channel via the affected control loop.

A maximum power of 5 W in higher-order modes in conjunction with a power of at least 165 W in the TEM₀₀ mode was specified as requirement for the PSL subsystem. This corresponds to a fundamental power of at least 97%.

The current concept consists of a multi-stage filtering to achieve the required beam quality at the interferometer input. In the PSL subsystem the laser beam is filtered by the PMC. The measured beam quality of the functional prototype (see Sec. 2.3.2) was used to determine the required filter effect of the PMC. With the current PMC the fundamental power of 87% is increased to 99% assuming the measured mode distribution⁶.

In a second stage the beam is filtered by the suspended input mode-cleaner before it is injected into the interferometer [Ara07a].

3.2.6 Pre-mode-cleaner

The PMC is an important component of the PSL subsystem and is used for the stabilization of several laser beam parameters, as already mentioned. Therefore the main tasks of the PMC are once again summarized and the current design is described in more detail. The PMC was developed in collaboration with J.H. Pöld, and experiments performed with a first prototype are described in [Pöl09].

The primary task of the PMC is to filter RF power, beam pointing, and spatial mode fluctuations. The filter effect of the PMC depends on several resonator parameters, mainly the round-trip length, the mirror reflectivity, and the mirror curvature.

A computer program was developed and used to calculate the filter effect as function of the resonator parameters. The required filter effect of the PMC design was verified and the influence of manufacturing tolerances was estimated with a Monte Carlo simulation. Technical limitations, such as the optical damage threshold of

⁶Potential distortions of the fundamental mode of the PMC, e.g. due to thermal effects, are not taken into account.

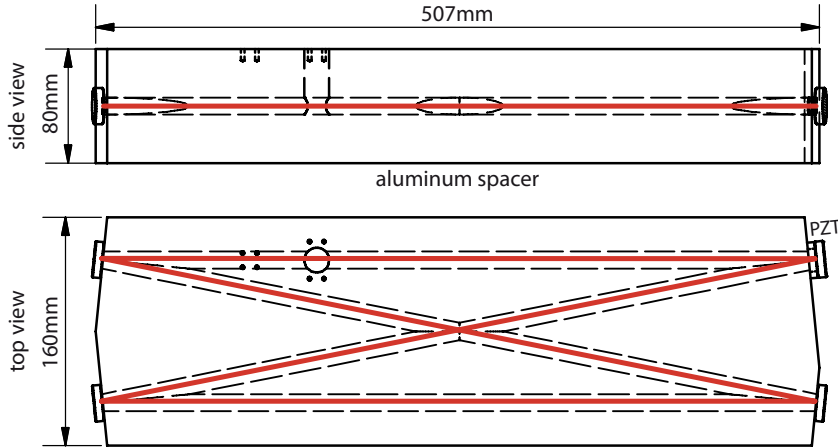


Figure 3.8: Sketch of the pre-mode-cleaner with illustrated beam path.

the mirror coatings, or the maximum size of the resonator spacer, were taken into account during the design process. This led to the following PMC design.

The PMC is a resonator in bow-tie configuration with an optical round-trip length of 2 m and a finesse of $\mathcal{F}=129$ (Fig. 3.8). Thus it has a FSR of 149 MHz and a bandwidth of 576 kHz. At an input power of 200 W a circulating power of 8 kW is expected. The flat input and output coupling mirrors have a transmission of 2.4% and the curved high reflectivity mirrors have a curvature of -3 m. The input/output beam has a waist radius of about $547 \mu\text{m}$ and the round-trip Gouy phase is 1.75 rad. The power of TEM_{10} and TEM_{01} modes is suppressed by a factor of 3960 in the transmitted beam whereby pointing fluctuations are suppressed by a factor of 63. In general higher-order spatial modes are suppressed in the transmitted beam of the PMC, and assuming a mode distribution measured at the functional prototype (see Sec. 2.3.2, Fig. 2.19), the total higher-order mode power is reduced by a factor of 63. Thus the beam quality and the relative power in the TEM_{00} mode, the fundamental power, is increased. Due to the bow-tie configuration the incidence angle at the mirrors is quite small and an even number of reflections occur for one round-trip. Therefore the resonance frequency for p- (horizontal) and s-polarized (vertical) beam is almost identical and no polarization filter effect can be expected from the PMC.

A PZT at one of the curved high reflectivity mirrors is used to stabilize the round-trip length to the laser frequency using the PDH technique. This actuator has a dynamic range of about 2.5 FSR with a bandwidth of several 10 kHz. To compensate larger drifts of the resonator length or the laser frequency, the spacer made of aluminum is temperature controlled with attached heaters. This slow actuator with a time constant of about 3 h has a dynamic range of about 44 FSR/K with a maximum temperature increase of ≈ 5 K limited by the heater electronics.

The PMC is placed inside a pressure-tight tank at atmospheric pressure for acoustic shielding and to avoid contamination of the resonator mirrors.

A first prototype of the PMC was fabricated and is tested at the moment. Preliminary measurements verify the expected filter effect at a circulating power of about 6.6 kW.

3.3 Summary

Laser stabilization is – besides of improving the free-running laser noise and reducing the coupling factor – one of the most important tools to increase the sensitivity of precision experiments.

Passive and active stabilization methods used to suppress fluctuations in power, frequency, pointing, and spatial mode were reviewed and compared. Furthermore the fundamental limit of every stabilization, the quantum limit, was described (Sec. 3.1). The subtle combination and the concrete application of these methods together with the coupling mechanisms and the deduced stability requirements were described in the scope of the stabilization concept for the GWD Advanced LIGO, which requires one of the most demanding laser stabilizations as of today (Sec. 3.2). Only due to the complex stabilization concept will it be possible to achieve the anticipated sensitivity of Advanced LIGO and other second generation GWDs.

A key component in the pre-stabilization of the Advanced LIGO laser is the PMC, which was designed using the characterization results from Chapter 2. A first prototype of the optical resonator verified the most important filter properties and was tested at almost full laser power. Thus the PSL requirements for the RF power noise, the pointing fluctuations, and the beam quality will most likely be fulfilled by the passive filtering of this PMC.

The complete stabilization concept of the PSL subsystem will be tested with the next prototype of the Advanced LIGO laser anytime soon. Especially cross couplings between different stabilizations have to be investigated and the integration of all components, such as the computer control, has to be studied.

Among the different stabilizations of the Advanced LIGO laser system the power stabilization in the gravitational wave band turned out to be the most demanding one. In the subsequent chapters two different power noise sensors accompanied by stabilization experiments are described, which on the one hand demonstrated for the first time the Advanced LIGO power stability requirement (Chapter 4) and on the other hand used new advanced techniques able to increase the sensitivity of power sensors by about one order of magnitude (Chapter 5).

Traditional Power Stabilization

Active power stabilization of laser systems is necessary for many high precision experiments since power fluctuations often couple to the actual measurement signal (see Chapter 3). Today, probably the most demanding power stability requirements are defined by GWDs, for the laser beam injected into the interferometer. The coupling of power fluctuations via radiation pressure at the test masses and via the readout scheme, and also the stringent requirements derived for Advanced LIGO have been already described in Sec. 3.2.2.

Several power stabilization experiments were performed especially in the field of GWDs (see Sec. 3.1.2 and Fig. 3.2). Active feedback control loops, photodiodes as sensors, and various power actuators were used. In order to distinguish this commonly used active power stabilization scheme from new schemes (see Chapter 5) it is called *traditional power stabilization* in this thesis.

Two experiments [Rol04, Sei06] were performed specifically for Advanced LIGO, and although the published results were the best ones worldwide at the time of publication, the stability required by Advanced LIGO has not been demonstrated so far. Both experiments showed especially at low frequencies (≈ 10 Hz) that many technical noise sources at the detector for power fluctuations were preventing a quantum noise limited performance. A high-sensitivity photodetector turned out to be the crucial component in power stabilization experiments.

Thus a new low-noise detector consisting of an array of photodiodes was developed in this thesis. The output power of a Nd:YAG laser was stabilized with this detector, and for the first time a power stability fulfilling the Advanced LIGO requirements was achieved. The high sensitivity of this new detector was in this way demonstrated and all limiting noise sources were identified.

In the following sections the quantum limit of traditional power stabilizations (Sec. 4.1) and the new high-sensitivity power detector (Sec. 4.2) are described first. Subsequently the traditional power stabilization experiment is described and the results are presented and discussed (Sec. 4.3).

The main results of this chapter have already been published in [Kwe09b].

4.1 Quantum Limit

Power stabilizations can be limited by technical and quantum noise. Technical noise sources can be significantly reduced in many cases whereas quantum noise is a fundamental limit. In the following the quantum noise limit of traditional power stabilizations is described.

A fundamental limit of the relative power noise of a laser beam is given by the quantum noise s_q , which depends only on the beam power P and the photon energy hc/λ (see Sec. 3.1.2, Eq. 3.1):

$$s_q = \sqrt{\frac{2 \cdot hc}{P\lambda}}. \quad (4.1)$$

This quantum noise, the power noise of a so-called *coherent beam*, can be reduced only with non-classical states of light, such as squeezed states, which are not considered here since the generation of these states is complicated and, to my knowledge, they were not used in any power stabilization experiment so far. Most laser output beams are not quantum noise limited in the frequency band of interest. However by filtering a beam, e.g., with an optical resonator, a quantum noise limited power stability can be achieved (see Sec. 3.1.2).

It is not possible to reach this limit with traditional power stabilization, though. This is due to two reasons: On the one hand beam power needs to be detected with a photodetector (in-loop detector) for compensating power fluctuations with the control loop. This reduces the beam power for the actual experiment (out-of-loop beam) and increases the relative quantum noise since that depends on the beam power P . On the other hand the quantum noise measured by the in-loop detector is imprinted on the beam by the control loop, which in turn increases the power noise of the out-of-loop beam. Thus the out-of-loop relative power noise in a traditional power stabilization is above the quantum noise of the original beam even neglecting any technical noise sources. In the following the quantum limit¹ is deduced after briefly introducing the quantum mechanical formalism used, which is described in more detail, e.g., in [Bac04]. This formalism will be used as well to calculate the quantum limit of advanced power stabilization schemes in Sec. 5.2.

Quantum Mechanics

The power of a laser beam, being in state $|\phi\rangle$, is measured with the photon number operator N . This operator measures the number of photons in the light field. The expectation value of this operator for state $|\phi\rangle$ is the average photon number and

¹The quantum limits of a laser beam and of a power stabilization have to be distinguished. The quantum noise of a laser beam is given by the beam power and the photon energy. The quantum noise of a power stabilization is the out-of-loop power noise neglecting any technical noise sources. The power noise of the out-of-loop beam is in general above the quantum noise of the beam itself.

the variance of this operator is used to calculate the power noise. The eigenstates of the number operator are called *Fock states* $|n\rangle$. The light field described by such a state contains an exactly defined number of photons:

$$N |n\rangle = n |n\rangle. \quad (4.2)$$

Especially the vacuum state $|0\rangle$ is a Fock state. Different light fields, such as coherent states, can be expanded in the Fock state basis. The number operator can be expressed by using the so-called *raising operator* A^\dagger and the *lowering operator* A

$$N = A^\dagger \cdot A, \quad (4.3)$$

which obey the commutation rule

$$[A, A^\dagger] = AA^\dagger - A^\dagger A = 1 \quad (4.4)$$

and transform Fock states in the following way:

$$A |n\rangle = \sqrt{n} |n-1\rangle \quad \text{and} \quad A^\dagger |n\rangle = \sqrt{n+1} |n+1\rangle. \quad (4.5)$$

When measuring light fields with large amplitude and small fluctuations the operators A^\dagger and A can be linearized. This approximation is valid for many bright laser beams, among others for beams considered in power stabilizations. The operators A^\dagger and A are linearized in the following way:

$$A^\dagger(t) = \alpha + \delta A^\dagger(t) \quad \text{and} \quad A(t) = \alpha + \delta A(t), \quad (4.6)$$

where α describes the time independent carrier amplitude, and δA^\dagger and δA describe the small fluctuations, so that the expectation values of δA^\dagger and δA are zero. The classical amplitude of a light field corresponds to α . The number operator N can be approximated with the linearized operators

$$N = A^\dagger A \approx \alpha^2 + \alpha \delta X1, \quad (4.7)$$

where $\delta X1 := \delta A^\dagger + \delta A$ is called *amplitude quadrature operator*.

Using this linearized model, the expectation value \bar{n} and the variance $\text{Var}(N)$ of N can be calculated

$$\bar{n} := \langle \phi | N | \phi \rangle = \langle N \rangle \approx \alpha^2 + \alpha \langle \phi | \delta X1 | \phi \rangle = \alpha^2, \quad (4.8)$$

$$\text{Var}(N) := \langle \phi | N^2 | \phi \rangle - \langle \phi | N | \phi \rangle^2 \approx \alpha^2 \text{Var}(\delta X1). \quad (4.9)$$

Thus the expectation value and the variance of N depend only on the classical amplitude α and the variance of $\delta X1$. The double-sided power spectrum S of the power noise can be calculated with the spectral variance $\text{Var}(N(\omega))$ where all

operators are transferred to Fourier space. To calculate the relative noise, the spectrum is normalized with \bar{n}^2 :

$$S = \frac{\text{Var}(N(\omega))}{\bar{n}^2} = \frac{\text{Var}(\delta X1(\omega))}{\alpha^2}. \quad (4.10)$$

The single-sided linear spectral density s , used more frequently in experiments, is given by

$$s = \sqrt{2S}. \quad (4.11)$$

Thus with these equations the relative power noise of a laser beam can be calculated using the operator N and the state $|\phi\rangle$ of the beam.

For example the above-mentioned power noise of a quantum limited beam can be deduced: A coherent beam has an amplitude α and the fluctuations of the amplitude quadrature $\delta X1$ are identical to the fluctuations of the vacuum state $|0\rangle$. Therefore the relative power noise of such a beam is

$$S_q = \frac{\text{Var}(\delta X1)}{\alpha^2} = \frac{1}{\alpha^2} \quad (4.12)$$

$$\text{with } \text{Var}(\delta X1) = \langle 0 | \delta X1^2 | 0 \rangle - \langle 0 | \delta X1 | 0 \rangle^2 = 1. \quad (4.13)$$

For a coherent beam with power P and photon energy hc/λ the average photon flow is $\bar{n} = \alpha^2 = P\lambda/hc$ and thereby, the spectrum mentioned in Eq. 4.1 is obtained:

$$S_q = \frac{hc}{P\lambda}, \quad [S_q] = \text{Hz}^{-1} \quad \text{and} \quad s_q = \sqrt{\frac{2 \cdot hc}{P\lambda}}, \quad [s_q] = \text{Hz}^{-1/2}. \quad (4.14)$$

To calculate the power noise of a beam in a more complex system, as in a traditional power stabilization, the number operator N of the out-of-loop beam has to be determined. This operator can be determined by using the classical equations for the field amplitudes and the canonical quantization, where the field amplitudes in the classical equations are substituted by the operator A . Using the equations for A , the number operator N or the amplitude quadrature $\delta X1$ can be deduced in order to determine the power noise. If the system has multiple input fields, the state of the system is represented by a product state and operators of different fields commute.

Limit of Traditional Power Stabilizations

The model shown in Fig. 4.1 is used to calculate the quantum limit of traditional power stabilizations. In this model the laser beam is split by a beam splitter with power reflectivity r . The power fluctuations of the reflected beam A_{i1} are measured with the in-loop photodetector. The measured fluctuations are suppressed using an actuator and a feedback control loop. The complex, frequency dependent loop gain of the control loop is given by $H(f)$. The transmitted beam A_{o1} is used for the

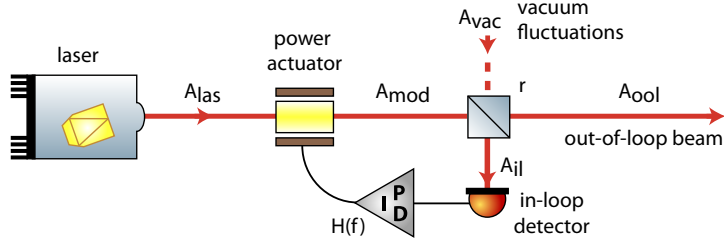


Figure 4.1: Model of an active laser power stabilization used to calculate power noise of the out-of-loop beam A_{ool} due to quantum noise.

actual downstream experiment. The quantum limit of the stabilization is the power noise of the out-of-loop beam A_{ool} caused by quantum noise at different positions in the model. Vacuum fluctuations A_{vac} couple into the system via the open port of the beam splitter. For clarity and in order to deduce the theoretical limit of the stabilization, loss-less beam splitters and photodetectors (quantum efficiency of 1) are assumed. Furthermore the loop gain of the control loop should be very high for all frequencies of interest ($H(f) \rightarrow \infty$), which is the case in most power stabilizations anyway.

For calculating the out-of-loop power noise, the operator δA_{ool} is needed. This operator is obtained by the canonical quantization of the classical field equations. The following equations are derived for the model:

$$\delta A_{mod} = \delta A_{las} + H(f)\delta A_{il}, \quad (4.15)$$

$$\delta A_{il} = \sqrt{r} \delta A_{mod} + \sqrt{1-r} \delta A_{vac}, \quad (4.16)$$

$$\delta A_{ool} = \sqrt{1-r} \delta A_{mod} - \sqrt{r} \delta A_{vac}. \quad (4.17)$$

With the control loop closed, Eq. 4.15 and 4.16 can be combined to the steady state solution

$$\delta A_{mod} = \frac{\delta A_{las} + \sqrt{1-r} H(f) \delta A_{vac}}{1 - \sqrt{r} H(f)}, \quad (4.18)$$

which yields for δA_{ool} in the limit $H(f) \rightarrow \infty$:

$$\delta A_{ool} = \frac{\sqrt{1-r} \delta A_{las} + (H(f) - \sqrt{r})\delta A_{vac}}{1 - \sqrt{r} H(f)} \stackrel{H \rightarrow \infty}{=} \frac{\delta A_{vac}}{\sqrt{r}}. \quad (4.19)$$

At high loop gain the out-of-loop field depends only on the vacuum fluctuations A_{vac} , and the laser noise A_{las} is completely suppressed. The spectrum of the out-of-loop power noise is given by Eq. 4.10,

$$S_{ool} = \frac{\text{Var}(\delta X 1_{ool})}{\langle N_{ool} \rangle} = \frac{\text{Var}(\delta X 1_{vac})}{r \langle N_{ool} \rangle} = \frac{1}{r \langle N_{ool} \rangle}. \quad (4.20)$$

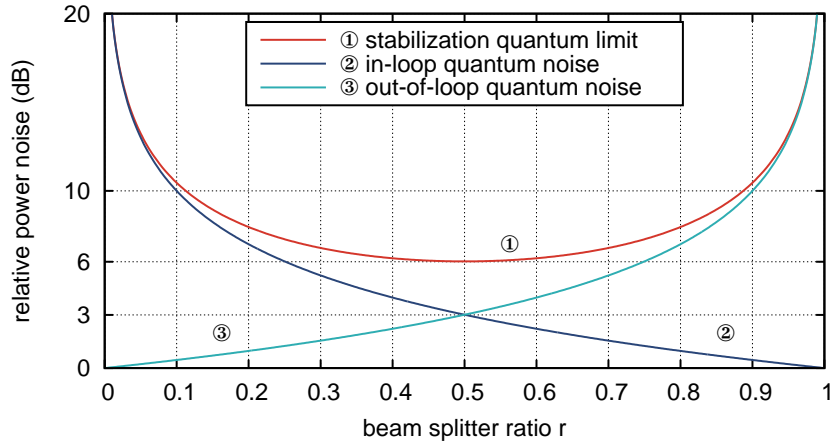


Figure 4.2: Quantum limit of a traditional power stabilization as function of the beam splitter ratio. The in-loop and out-of-loop quantum noise contribution and the total power noise relative to the quantum noise of the original beam (= 0 dB) is shown.

The average photon flow $\langle N_{\text{ool}} \rangle$ can be calculated classically, where α_{las}^2 is the average photon flow of the laser beam A_{las} :

$$S_{\text{ool}} = \frac{1}{r} \cdot \frac{1}{(1-r)\alpha_{\text{las}}^2}. \quad (4.21)$$

Compared with the relative quantum noise of the original beam², $S_{\text{q,las}}=1/\alpha_{\text{las}}^2$ (see Eq. 4.12), the relative power noise of the out-of-loop beam, depending on the beam splitting ratio r , is at least 6 dB larger³ (Fig. 4.2):

$$S_{\text{ool}}/S_{\text{q,las}} = \frac{1}{r(1-r)}. \quad (4.22)$$

The lowest power noise is achieved with a 50:50 beam splitter $r=0.5$. In this case the quantum noise measured with the in-loop detector and imprinted on the laser beam by the control loop, and the quantum noise of the out-of-loop beam (the vacuum fluctuations reflected at the beam splitter) contribute equally to the total noise. With lower reflectivity of the beam splitter ($r<0.5$) the in-loop quantum

²The relative power noise of the out-of-loop beam is compared to the quantum noise of the original beam. In contrast it is often compared to its own quantum noise in the literature. Due to this different power noise reference, the quantum limit of traditional power stabilizations is sometimes cited as 6 dB and sometimes as 3 dB.

³A ratio of power spectral densities expressed in decibels is defined as $10 \log_{10}(S_{\text{ool}}/S_{\text{q,las}})$, which is consistent with the definition $20 \log_{10}(s_{\text{ool}}/s_{\text{q,las}})$ in case of linear spectral densities. Thus 6 dB corresponds to a ratio of about 4 in the power spectral density and to a ratio of about 2 in the linear spectral density.

noise and with higher reflectivity ($r > 0.5$) the out-of-loop beam quantum noise is dominating the total out-of-loop power noise. For high reflectivity ($r \rightarrow 1$), a quantum noise limited beam can be produced. However, this beam has a significantly lower power than the original beam and therefore a much higher relative power noise compared to the case $r = 0.5$.

Finally the single-sided linear spectral density of the quantum limit s_q of a traditional power stabilization is given by

$$\begin{aligned} s_q &= \sqrt{\frac{1}{r(1-r)}} \sqrt{\frac{2 \cdot hc}{P\lambda}} \\ &= 4 \times 10^{-8} \text{ Hz}^{-1/2} \cdot \sqrt{\frac{0.5^2}{r(1-r)}} \cdot \sqrt{\frac{1 \text{ mW}}{P}} \cdot \sqrt{\frac{1064 \text{ nm}}{\lambda}}, \end{aligned} \quad (4.23)$$

where P is the total power of the original beam. The achieved power stability depends on the beam splitting ratio r and the photon flow $P\lambda/hc$. To achieve a good power stability, a large photon flow and therefore a high power P has to be detected and a splitting ratio of $r = 0.5$ has to be chosen.

In actual experiments losses of optical components and the quantum efficiency of the photodiode have to be taken into account. Thus it is often easier to use the electrical photocurrents I_{il} and I_{ool} of the in-loop and out-of-loop detector, respectively, to calculate the quantum limit. The average photon flow α_{las}^2 in Eq. 4.21 is replaced by the average electron flow $(I_{il} + I_{ool})/e$,

$$s_q = \sqrt{\frac{2e}{I_{il}} + \frac{2e}{I_{ool}}} = 1.8 \times 10^{-8} \text{ Hz}^{-1/2} \cdot \sqrt{\frac{1 \text{ mA}}{I_{il}} + \frac{1 \text{ mA}}{I_{ool}}}, \quad (4.24)$$

where e is the elementary charge.

Although the best relative power stability is achieved for $r = 0.5$, many experiments operate at $r \ll 0.5$. In many cases the laser power can be more useful in the actual experiment instead of being sacrificed for the power stabilization. Furthermore, photodetectors available are far from being able to handle 50% of the output power of lasers typically used.

The quantum limit described in this section is the fundamental limit of every traditional power stabilization. However, in many experiments this limit is not achieved due to technical noise sources. Thus it does not make sense to increase the power detected in order to lower the quantum limit in such experiments. This is another reason for experiments to operate at $r \ll 0.5$.

To summarize, the theoretically best power stability in a traditional stabilization is achieved with 50% of the available power detected by the control loop sensor. The relative power noise of the beam for the actual downstream experiment is at least 6 dB above the relative quantum noise of the original laser beam. However, with passive stabilization methods and advanced techniques such as the optical ac coupling, better power stabilities can be achieved (see Chapter 5).

4.2 High Power Photodiode Array

A new high-sensitivity detector for power fluctuations was developed since so far no detector existed (see Sec. 3.1.2), to my knowledge, that had a sensitivity required for the Advanced LIGO power stabilization (see Sec. 3.2.2). In this section the optical, mechanical, and electrical design of this low-noise high-power vacuum-compatible photodiode array is described. The sensitivity was examined in a power stabilization experiment as will be described in Section 4.3.

The photodiode array was developed for an Advanced LIGO power stabilization precursor experiment. Hence several requirements for the power detector had to be fulfilled, such as high sensitivity for power fluctuations, vacuum compatibility, and low optical back reflections.

Every traditional power stabilization in the 10^{-9} stability range needs to detect a rather large photocurrent in order to lower the quantum noise to an acceptable level and in that way to achieve the desired sensitivity. A photocurrent of at least 80 mA has to be detected to reach the sensitivity $2 \times 10^{-9} \text{ Hz}^{-1/2}$ required by Advanced LIGO⁴. In order to allow for some small, remaining noise contributions from technical noise sources, the power detector was designed for a total photocurrent of about 200 mA. Such a high photocurrent would cause thermal effects, would require a complicated cooling scheme and an extremely low-noise readout electronics if only one photodiode is used for detection. These problems were avoided by distributing the power to four photodiodes each read out by its own electronics. Thus a simple passive cooling scheme for the photodiodes was sufficient and the requirements for the readout electronics were relaxed.

To fulfill the vacuum compatibility more easily, the complete readout electronics was moved out of the vacuum tank and the photodiodes were connected with long cables to this electronics. This avoided a complicated sealing, simplified the cooling, and allowed an easy modification of the electronics.

Back reflections of the detector were minimized by hitting the photodiodes at an incidence angle of 45° and by absorbing residual reflections with glass filters. All optical components were hit at large incidence angles. Therefore back scattering that is usually lower at large angles, is reduced as well.

4.2.1 Optical and Mechanical Design

The laser beam was split with a single 50:50 beam splitter into four partial beams using multiple reflections. The optical layout was designed with the optics simulation program OptoCAD [Sch05] in order to achieve nearly equal and small distances between the partial beams at the photodiodes (Fig. 4.3). Thus it was possible to compactly mount the photodiodes in a row on a base plate.

⁴The photocurrent was calculated using Eq. 4.24. In Advanced LIGO a 125 W laser beam has to be stabilized to $2 \times 10^{-9} \text{ Hz}^{-1/2}$. Thus a traditional power stabilization with $r \rightarrow 0$ can be used, which is equivalent to $I_{\text{ool}} \rightarrow \infty$ in Eq. 4.24.

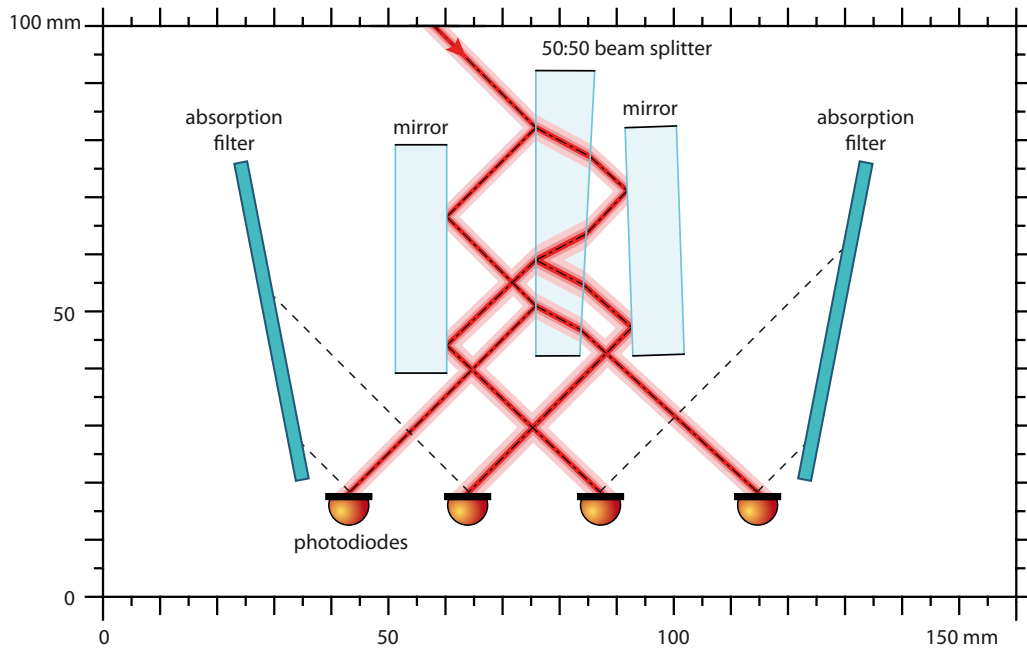


Figure 4.3: Optical layout and beam paths of the photodiode array calculated with the program OptoCAD [Sch05].

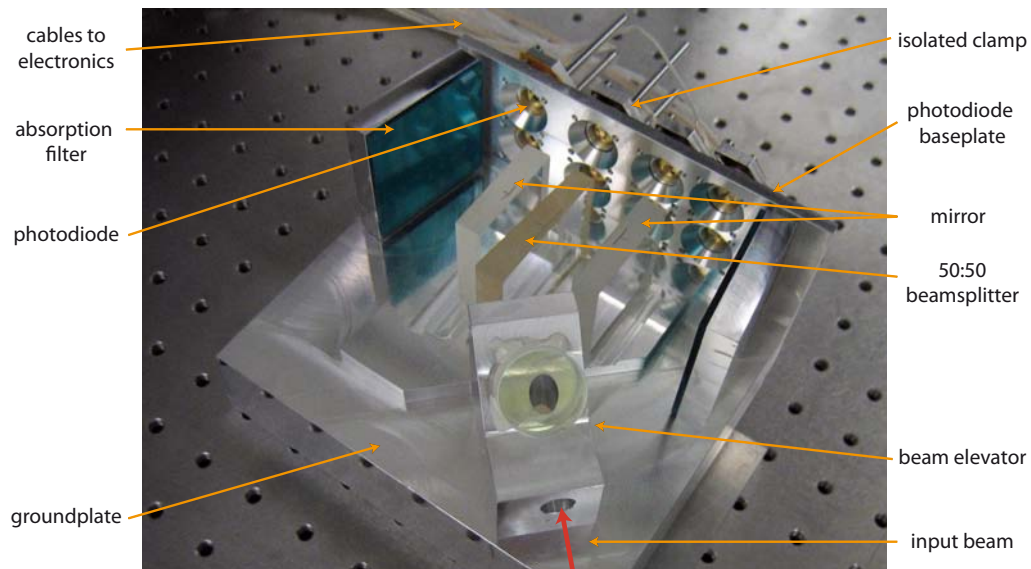


Figure 4.4: Photograph of the photodiode array.

The photodiode array consisted of Perkin Elmer C30642 InGaAs photodiodes with an active diameter of 2 mm. The beam radius on the photodiodes was about $545 \pm 14 \mu\text{m}$ and $386 \pm 10 \mu\text{m}$ in horizontal and vertical direction, respectively. The uncoated glass windows of the photodiode packages were removed in order to avoid spurious reflections. Since the beams, horizontally polarized, hit the photodiodes at an incidence angle of 45° , it was easy to absorb residual reflections at the photodiode surface with glass filters (Schott BG39) at the Brewster angle. Therefore significantly less back reflection⁵ and scattering were expected of this detector than to detectors with photodiodes usually hit at normal incidence.

The optical components were not aligned using a laser beam, but rather a mechanical template was used to glue the components to a ground plate ($150 \times 122 \text{ mm}^2$), to which the photodiode base plate was mounted as well (Fig. 4.4). In order to compensate tolerances of the optical components and the template, a laser beam was used after glueing of the components to measure the exact laser beam position on the photodiode base plate with thermo-sensitive paper. Afterwards the final mechanical machining of the base plate was performed, so that the photodiodes could be mounted at the laser beam positions measured. Furthermore each photodiode could be moved transversely by $\pm 1 \text{ mm}$ to its incident beam in order to precisely align the photodiode. They were aligned to the position of the smallest coupling of lateral beam jitter to the photodiode signal, which was determined by modulating the input beam pointing.

Each photodiode was glued into a small aluminum case mounted electrically insulated with Kapton foils to the aluminum base plate to avoid electrical ground loops.

The base plate was in addition used as heat sink to passively cool the photodiodes. At the maximum photocurrent of 50 mA an electrical power of about 250 mW (5 V bias voltage) was dissipated in each photodiode. This caused a $\approx 6 \text{ K}$ temperature increase of the small photodiode aluminum cases. The complete detector was insulated electrically and isolated thermally with Macor components from the environment.

All materials used for the detector, such as aluminum, Macor, coated fused silica and glass components, glues, Kapton foils, and Teflon isolated cables, were vacuum compatible and were selected for a low outgassing rate.

Two detectors (in-loop and out-of-loop) are necessary for the power stabilization experiment described in Sec. 4.3. Rather than duplicating the detector described so far, an additional 50:50 beam splitter and a beam elevator at the input of the detector was used to produce four additional partial beams in a vertically shifted plane using the same optics. So only four additional photodiodes in this plane were required for the second detector.

⁵In principle the photodiodes could be hit at the Brewster angle ($\approx 74^\circ$ for InGaAs) to avoid back reflections in the first place. However an incidence angle of 45° was chosen to allow a compact mechanical design.

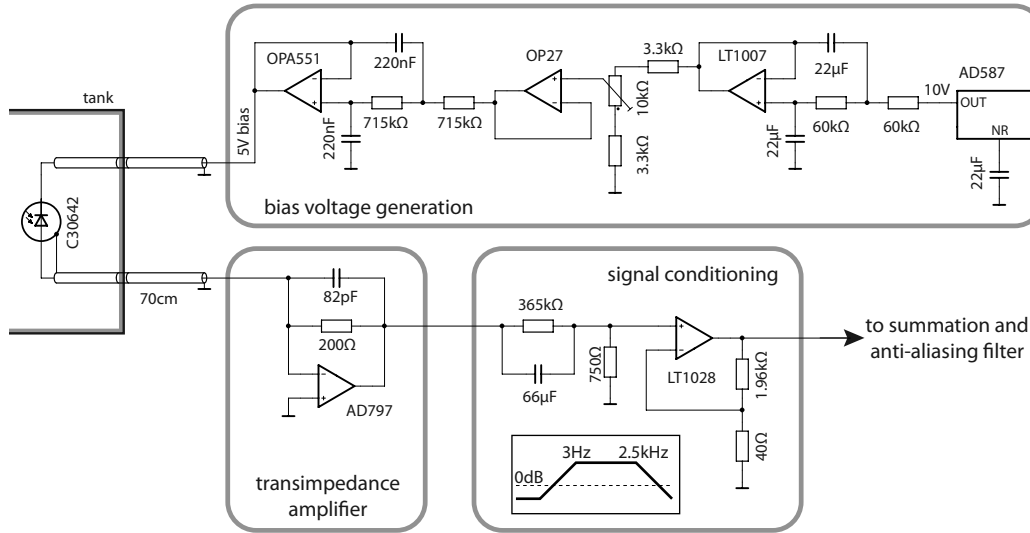


Figure 4.5: Schematic of the bias voltage generation, the readout electronics, and the cabling for one photodiode.

4.2.2 Electronics

The electronics for the photodiodes were placed outside of the vacuum tank. Each photodiode was connected with a pair of shielded cables (≈ 70 cm) to the electronics. The tank feedthroughs were pluggable and individually insulated from the tank. It turned out that the cable shield was crucial to avoid couplings at the power line frequency of 50 Hz and its harmonics. No performance difference was observed when using longer cables of up to 5 m length.

Each pair of cables connected one photodiode with a filtered 5 V bias voltage and a low-noise transimpedance amplifier with a low current-noise⁶ 200 Ω resistor (Fig. 4.5). At the operating point each photodiode detected a photocurrent of about 50 nA.

In the subsequent stage the signal of the transimpedance amplifier was amplified between 3 Hz and 2.5 kHz with a low-noise amplifier. At the same time, the much stronger signal at very low frequencies was attenuated by a factor of 10, so that the signals of the different photodiodes could be added more easily. The transfer functions of the transimpedance amplifier and the subsequent signal conditioning filter were measured and used for calibration.

The electronic noise of the circuit was simulated with the program LISO [Hei00] and was measured with no light on the photodiodes (Fig. 4.6). This electronic noise severely limits the sensitivity of the detector. Furthermore the noise at the actual operating point was measured with a low-noise battery (NiMH, nickel-metal hydride) current source. For this the photodiode was replaced with the current

⁶See [Sei09, Chap. 4.2] for a selection of characterized low current-noise resistors.

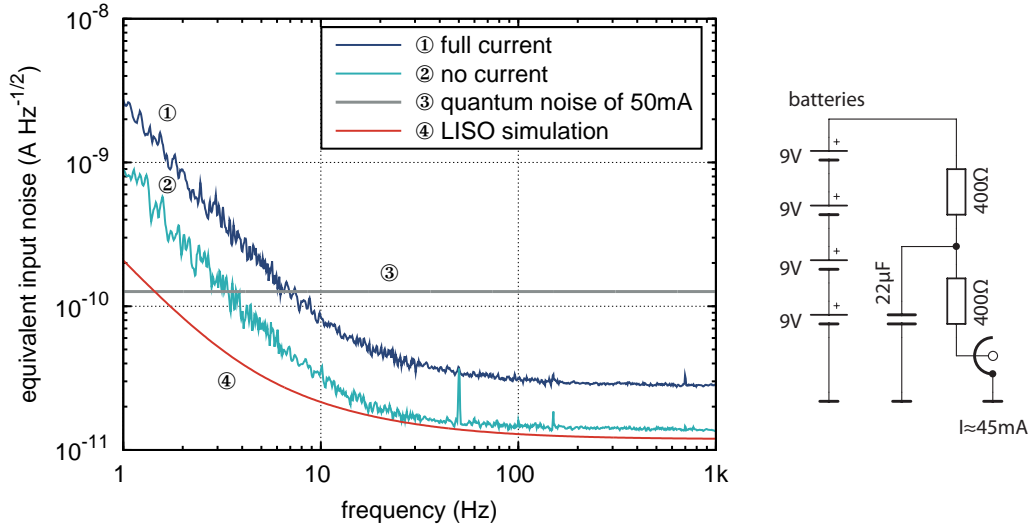


Figure 4.6: Electronic noise of the transimpedance amplifier and the signal conditioning filter at different operating points and schematic of the current source.

source (800Ω output impedance, schematic in Fig. 4.6) and the noise was measured at this operating point (Fig. 4.6). The noise with full current is larger than in the situation with no light on the photodiodes. The electronic noise is equal to the expected quantum noise of 50 mA photocurrent at about 7 Hz. Thus in principle a quantum noise limited power detection should be possible for frequencies greater than 7 Hz.

The signals of the four photodiodes were summed after passing the signal conditioning filters. On the one hand this sum signal can be subtracted from an onboard voltage reference in order to be used as in-loop signal for the power stabilization or on the other hand this signal can be passed through an onboard anti-aliasing filter and transmitted to an A/D converter card in a computer to be used as out-of-loop signal. More details concerning the power stabilization are described in Sec. 4.3.

The average responsivity of the photodiodes were measured with a power meter and yielded $0.79 \pm 0.08 \text{ A/W}$, which corresponds to a quantum efficiency of 0.92.

All in all the high-power photodiode array described is a compact detector for power fluctuations that was developed for a power stabilization in the field to GWDs at frequencies between 10 Hz and 10 kHz. The detector is designed for a total photocurrent of 200 mA and 400 mA for four and eight photodiodes, respectively. All optical and mechanical components are vacuum compatible, the electronics can be operated outside of the vacuum tank, and the optical design minimizes back reflection and scatter.

The electronic noise was measured in the operating point with full current and is an lower limit for the sensitivity. Since no quantum-noise-limited light source of

several 100 mW power at the frequencies of interest was available, the sensitivity of the detector with light on the photodiodes could not be measured directly. Among other things this is the reason for performing the power stabilization described in Sec. 4.3.

4.3 Power Stabilization Experiment

The high-power photodiode array was used to stabilize the output power of a Nd:YAG laser at 1064 nm for frequencies between 1 Hz and 1 kHz. This experiment demonstrated simultaneously the high sensitivity of this detector and for the first time the power stability required by Advanced LIGO. The experiment, the results and their implications are described in this section.

Several experiments (see Sec. 3.1.2, specifically [Rol04, Sei06]) already tried to achieve the power stability for Advanced LIGO. In these experiments the power noise measured out-of-loop was significantly above the in-loop and quantum noise, and could not be explained completely. This is an indication that the photodetector sensitivity is not sufficient and that other noise sources couple to the sensor. Thus the key challenge in a power stabilization is to realize a high-sensitivity detector for power fluctuations (see Sec. 4.2) and to minimize the coupling from external noise sources. This means as well that it is in principle not important to stabilize a 200 W beam from the Advanced LIGO laser to demonstrate the power stabilization for this laser system. As no Advanced LIGO laser was available for the experiment a 2 W NPRO was used instead.

4.3.1 Experimental Setup

In the experimental setup (Fig. 4.7) an NPRO (see Sec. 2.3.1) with an output power of 2 W at 1064 nm was used as laser. An EOAM along with a subsequent polarizing beam splitter was used to control the beam power. With $\lambda/4$ and $\lambda/2$ wave plates upstream of the EOAM, the average power and the dynamic range of the EOAM were adjusted. The EOAM has a high bandwidth of about 100 MHz, which, however, was not needed for this experiment.

An optical ring resonator and the photodiode array were placed in a pressure-tight tank for acoustic shielding. The tank was pumped down and vented with HEPA (High Efficiency Particulate Air) filtered air to reduce the number of particles potentially passing the laser beam. All components inside the tank were mounted on a breadboard which was placed on Viton pads for isolating and damping mechanical vibrations.

The ring resonator with a design similar to the one used in the DBB (see Sec. 2.2.1) served as mode-cleaner, reducing beam pointing fluctuations. The finesse was about 370 with a bandwidth of about 980 kHz. The Pound-Drever-Hall method (see Sec. 3.1.3, [Dre83, Bla01]) with phase modulation sidebands at 29 MHz was used to stabilize the laser frequency to one fundamental mode resonance of the resonator. An additional resonant EOM generated the phase modulation. The

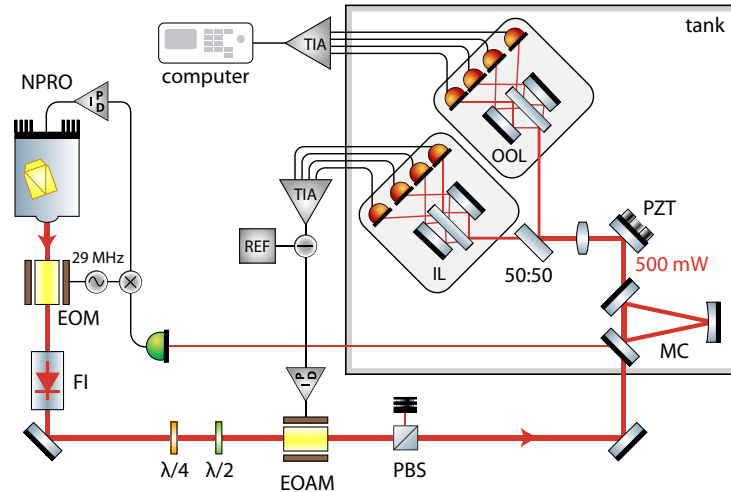


Figure 4.7: Experimental setup of the power stabilization. EOM, electro-optic phase modulator; FI, Faraday isolator; EOAM, electro-optic amplitude modulator; PBS, polarizing beam splitter; MC, mode-cleaner; IL, in-loop detector; OOL, out-of-loop detector; PZT, mirror attached to piezoelectric elements; TIA, transimpedance amplifier; REF, voltage reference; $\lambda/2$, $\lambda/4$, wave plates.

laser frequency was controlled by the temperature of the laser resonator and a PZT element attached to the laser crystal.

The laser power in front of the photodiode array was about 500 mW. The beam size on the eight photodiodes was adjusted with a lens, and a mirror glued to a three-axis PZT was used to create pointing modulations downstream of the mode-cleaner. The laser beam was distributed to the eight photodiodes of the array and each photodiode was connected to its own readout electronics outside the tank.

The signals of four photodiodes were added and used to stabilize the laser power (in-loop) and the remaining four signals were added and used to verify the power stability (out-of-loop). For the stabilization, the in-loop signal was subtracted from a lowpass filtered voltage reference, amplified in analog servo electronics, and fed back to the EOAM. This dc-coupled feedback control loop had a bandwidth of about 80 kHz with a loop gain of more than 68 dB for frequencies below 1 kHz.

The noise of the different photodiode signals was measured with a computer. For this the signals were passed through anti-aliasing filters and were differentially transmitted to an A/D converter card (PCI-6122, National Instruments) in the computer. The time series of the signals was recorded at a sampling rate of 10 kHz and used to calculate the linear spectral density of the relative power noise between 1 Hz and 1 kHz.

Since grounding noise turned out to be a critical noise source in previous power stabilization experiments, the whole experiment was carefully wired (Fig. 4.8). The

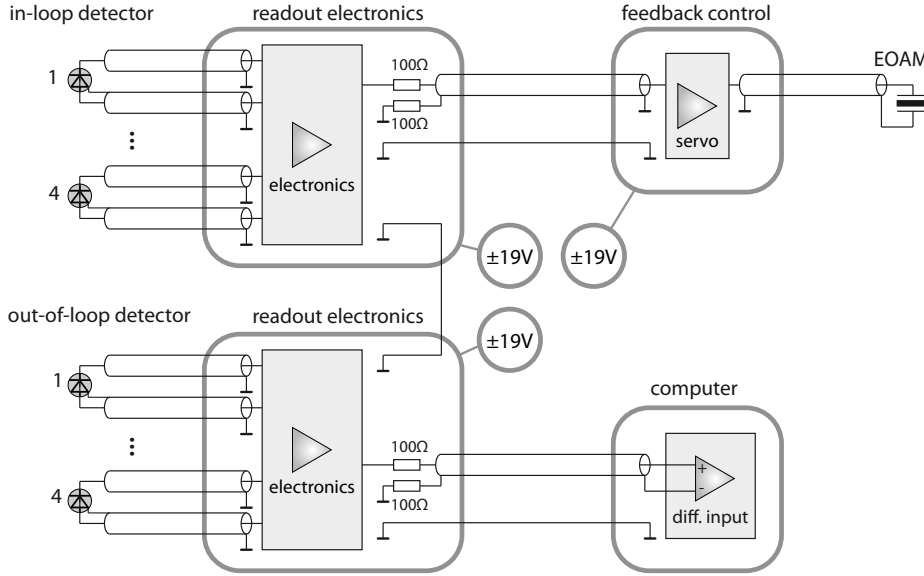


Figure 4.8: Cabling of the different power stabilization electronic modules. Each block has a separate floating power supply.

servo and the two readout electronics were each connected to an independent power supply. No performance difference with battery packs as power supplies was observed.

In general the experimental setup is based on the envisaged power stabilization setup of Advanced LIGO (see Sec. 3.2.2). In Advanced LIGO two detectors will measure the power fluctuations downstream of the suspended input mode-cleaner, which is simulated in this experiment by the ring resonator. The suspended input mode-cleaner and the power detectors will be in UHV (ultra high vacuum), which is imitated by the vacuum tank. However in this precursor experiment the significantly lower lowpass corner frequency (about 8.8 kHz [Ara07a]) of the suspended mode-cleaner, potential low frequency pointing fluctuations between mode-cleaner and power detectors, and the much more complex power actuator of the laser system are not simulated.

4.3.2 Results

The free-running relative power noise downstream of the mode-cleaner was $1 \times 10^{-7} \text{ Hz}^{-1/2}$ to $1 \times 10^{-6} \text{ Hz}^{-1/2}$ in the frequency band from 1 Hz to 1 kHz. With closed feedback loop the out-of-loop measured power noise (Fig. 4.9) was at the expected level, defined by the uncorrelated sum of the quantum noise and electronic noise of both, the in- and out-of-loop detectors in the whole frequency band. For frequencies up to 7 Hz, the measured noise was dominated by the electronic noise of the in-loop and out-of-loop detector and for higher frequencies by quantum noise

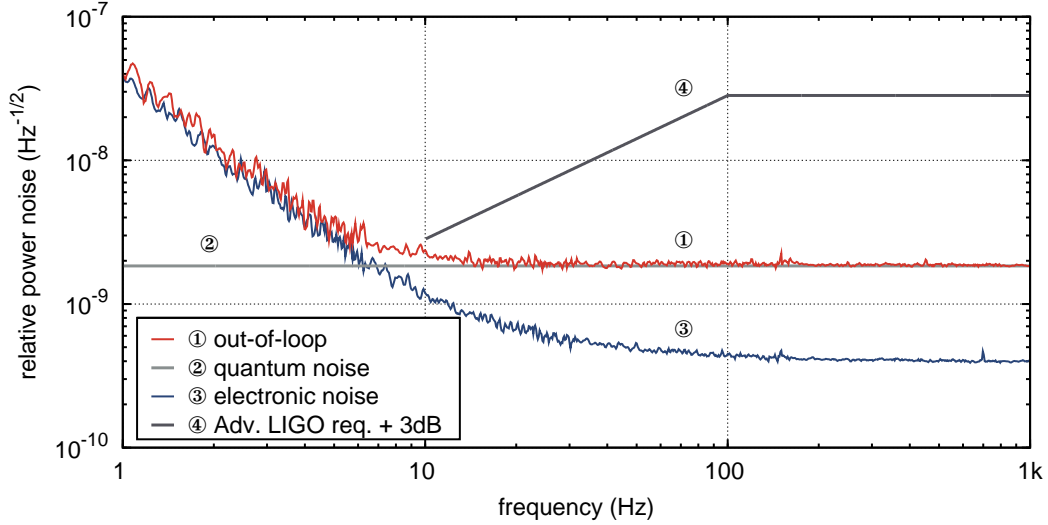


Figure 4.9: Out-of-loop measured power noise and limiting noise sources. The Advanced LIGO power noise requirement is shifted by 3 dB in the plot to account for the noise of the out-of-loop detector.

at a level of $1.8 \times 10^{-9} \text{ Hz}^{-1/2}$. The relative quantum noise level of this experiment was calculated using the total in-loop ($I_{\text{il}}=200 \text{ mA}$) and out-of-loop photocurrent ($I_{\text{ool}}=189 \text{ mA}$) (see Sec. 4.1). The measured power noise was closer than 1 dB (the estimated calibration accuracy was 1 dB) to the quantum noise level for frequencies from 15 Hz on upwards. At 10 Hz a relative power noise of $2.4 \times 10^{-9} \text{ Hz}^{-1/2}$ on the out-of-loop detector was measured.

Since the in-loop and out-of-loop detectors were built identically, the noise of in-loop and out-of-loop detectors should contribute equally to the measurement noise. With this assumption and by subtracting the noise contribution of the out-of-loop detector, a 3 dB lower relative power noise of the laser beam of $1.7 \times 10^{-9} \text{ Hz}^{-1/2}$ at 10 Hz and $1.3 \times 10^{-9} \text{ Hz}^{-1/2}$ at higher frequencies is deduced and in this way the Advanced LIGO power noise requirements (Fig. 4.9) are demonstrated.

The experiment showed the described performance for a period of six hours, only interrupted by relocks of the mode-cleaner due to thermal drifts (Fig. 4.10). By careful cabling, using independent power supplies, and differential signal transmission all peaks at the power line frequency of 50 Hz and harmonics were eliminated in the measurement.

In first experiments each photodiode was aligned to the responsivity maximum and the coupling of lateral beam jitter to the out-of-loop relative power noise, C_j , was measured.

$$C_j = \frac{1}{P(0)} \cdot \left. \frac{dP(x)}{dx} \right|_{x=0}, \quad [C_j] = \text{m}^{-1}, \quad (4.25)$$

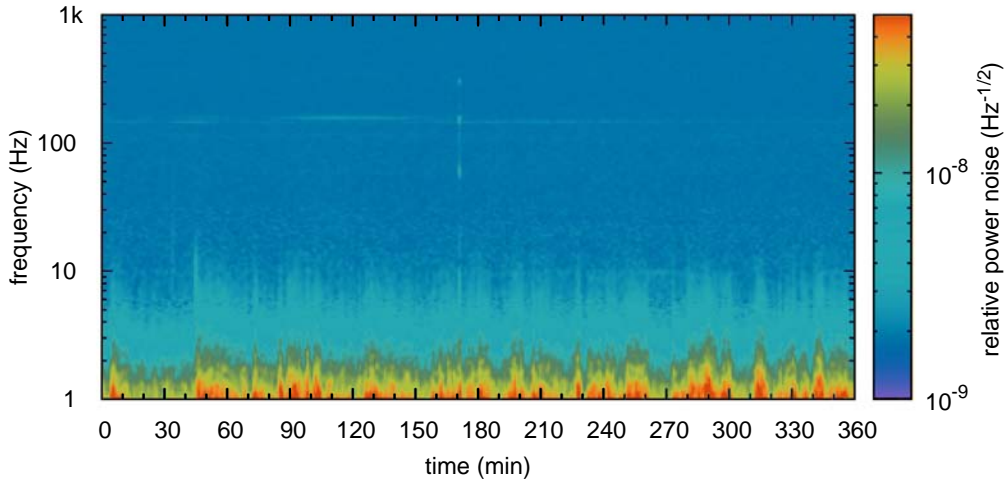


Figure 4.10: Long-term residual power noise of the stabilization experiment.

where $P(x)$ is the out-of-loop beam power as function of the beam position x . A coupling of $C_j \approx 50 \text{ m}^{-1}$ was measured and many peaks at mechanical resonance frequencies were visible in the power noise (Fig. 4.11). In the final experiment the photodiodes were aligned by minimizing the jitter coupling. Then the coupling factors of $2.8 \pm 0.3 \text{ m}^{-1}$ and $1.0 \pm 0.1 \text{ m}^{-1}$ in horizontal and vertical direction, respectively, were measured using the mirror attached to the PZT.

The stabilization was performed in a closed tank at atmospheric pressure as well as in an evacuated tank. No performance difference of the power stabilization between the situation when the tank was filled with HEPA filtered air or when it was evacuated ($\approx 100 \text{ Pa}$) was observed. With unfiltered laboratory air (particle count of about $8500 \text{ m}^{-3} \approx 250 \text{ ft}^{-3}$, particle size $\geq 0.3 \mu\text{m}$) it was impossible to take a stationary measurement due to signal glitches caused by particles.

Since the photodiodes were connected with pluggable tank feedthroughs to the electronics, the assignment of the photodiodes to in- and out-of-loop detector was easily changeable. No performance difference depending on which photodiodes were used for the in-loop and out-of-loop signals was found. In particular no difference was observed when using mainly transmitted beams for the in-loop and mainly reflected beams for the out-of-loop detector. This indicated that potential splitting ratio fluctuations of the beam splitters were not limiting the measurement.

Finally in a separate experiment the power stability dependence on the beam size at the photodiodes was measured. The same readout electronics but only two photodiodes to speed up the alignment process were used. No performance difference for beam radii from $60 \mu\text{m}$ to $720 \mu\text{m}$ was observed.

To summarize, the required but hitherto unattained power stability for Advanced LIGO of $2 \times 10^{-9} \text{ Hz}^{-1/2}$ at 10 Hz has been achieved by scaling the number of photodiodes, reducing the beam jitter coupling and by the use of low-noise electronics.

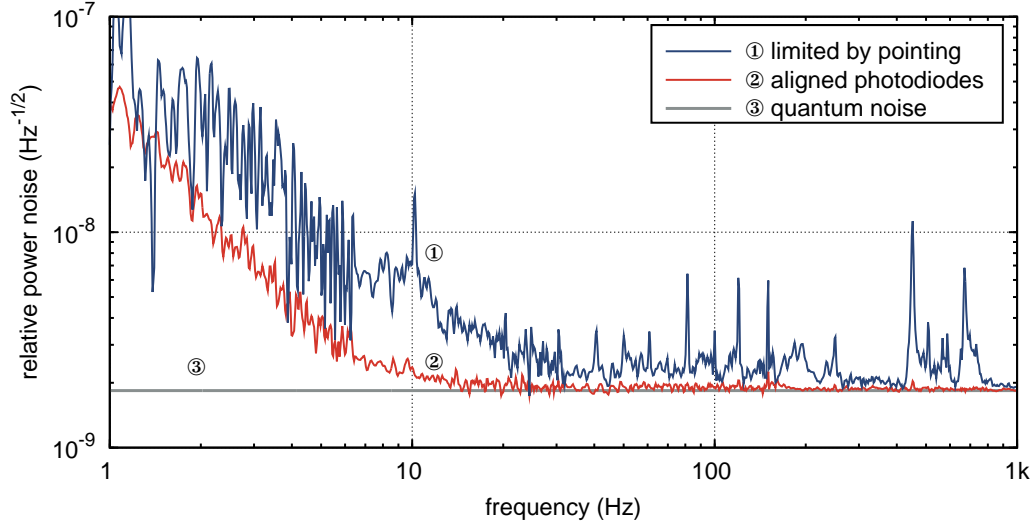


Figure 4.11: Out-of-loop measured power noise limited by pointing fluctuations (photodiodes aligned to the responsivity maximum) and power noise with photodiodes aligned to minimum jitter coupling.

An out-of-loop relative power noise of $2.4 \times 10^{-9} \text{ Hz}^{-1/2}$ ($1.7 \times 10^{-9} \text{ Hz}^{-1/2}$ with subtracted out-of-loop detector noise) at 10 Hz was demonstrated, with no line harmonics present in the measurement. The power stability was prone to be limited by beam jitter especially at mechanical resonance frequencies but the coupling coefficient has been kept small by appropriate alignment.

The high sensitivity of the photodiode array detector was demonstrated and it is ideal to be used in the upcoming generation of GWDs due to the demonstrated performance, the low back reflection/scatter design, and the vacuum compatibility.

Since the limiting noise sources were identified, the power stability can probably be further improved in the future. At low frequencies the electronic noise needs to be lowered and at high frequencies the total detected photocurrent has to be increased to reduce the relative quantum noise.

4.4 Summary

Laser power stabilization is essential for many high precision experiments in order to achieve the desired sensitivity, especially for GWDs.

The fundamental limit of traditional power stabilizations caused by quantum noise was deduced in Section 4.1. This limit is at least 6 dB above the quantum noise of the original laser beam. Almost no experiment reached this limit at low frequencies ($\approx 10 \text{ Hz}$) and in particular the power stability of $2 \times 10^{-9} \text{ Hz}^{-1/2}$ at 10 Hz required by Advanced LIGO could not be achieved in previous experiments.

Therefore a new high-sensitivity power detector was developed, and its optical, mechanical, and electrical design was described in Section 4.2. The detector consisted of eight InGaAs photodiodes each detecting a photocurrent of about 50 mA. Technical problems that often occurred in similar experiments were avoided: complicated cooling and electronics was avoided by distributing the beam power to several photodiodes, back reflections and scatter were avoided by large incidence angle optical design, in-vacuum electronics was avoided by using remote electronics, and out-gassing was avoided by using only vacuum-compatible materials.

The output power of an NPRO was stabilized between 1 Hz and 1 kHz in order to demonstrate the sensitivity of the detector (Sec. 4.3). As precursor experiment for the Advanced LIGO power stabilization, the experimental setup was based on the stabilization concept for Advanced LIGO.

The best power stability so far ($2.4 \times 10^{-9} \text{ Hz}^{-1/2}$ at 10 Hz and $1.8 \times 10^{-9} \text{ Hz}^{-1/2}$ from 15 Hz upwards) was achieved with this experiment. To my knowledge this is the first experiment in this power stability range for which the limiting noise sources were identified, which was closer than 1 dB to the quantum noise limit for frequencies above 15 Hz, and which fulfilled the Advanced LIGO requirements. Since the limiting noise sources were identified, the detector can be systematically improved in the future: At low frequencies the electronic noise needs to be lowered and at high frequencies the total detected photocurrent has to be increased to reduce the relative quantum noise. Since the manufacturer's maximum power handling capability of the photodetectors has been already reached and no low-frequency experiment has demonstrated so far a comparable power stability using photodiodes operating at higher photocurrents, the only feasible way to increase the total detected photocurrent seems to further scale the number of photodiodes.

Furthermore, beam pointing noise turned out to be a serious noise source, which, however, can be suppressed by carefully aligning the photodiodes to their incident beams. No performance difference of the power stabilization was observed between the situation when the tank was filled with HEPA filtered air or when it was evacuated, between different beam sizes at the photodiodes, and between using batteries as power supplies or ordinary laboratory power supplies.

All in all this experiment demonstrated that traditional power stabilizations in the range of a few $10^{-9} \text{ Hz}^{-1/2}$ can be realized with this photodiode array detector, which is even compatible with technical constraints set by future GWDs. Furthermore this detector can be combined with advanced power stabilization techniques to be described in Chapter 5. These advanced techniques can pave the way to significantly better power stabilities in the future.

Optical AC Coupling

High-sensitivity detectors for power fluctuations are required in many precision experiments. In particular they are the key components in power stabilization experiments. As described in Chapter 3, a very high power stability, which in the case of Advanced LIGO has been demonstrated using a multi-photodiode detector (Chapter 4), is necessary for future GWDs.

However, the power stabilization experiment using the multi-photodiode detector showed that the sensitivity of this traditional detection technique seems to be improvable only by further scaling the number of photodiodes in the future. The technical effort is roughly proportional to the number of photodiodes or the beam power detected, whereas the sensitivity increases only with the square root of the power detected (see Sec. 4.1). Thus today a sensitivity for relative power noise at, e.g., the $10^{-10} \text{ Hz}^{-1/2}$ level seems to be out of reach or only achievable with extreme effort when using traditional detection techniques.

The high beam power that needs to be detected causes the most technical problems. In the traditional detection technique the light field carrier that contains almost the complete beam power has to be detected, although only the sidebands contain the actual information about the power fluctuations to be measured. In contrast, the advanced technique, called *optical ac coupling*, which is described in this chapter, uses an optical resonator to suppress the carrier in reflection of the resonator, whereas the fluctuation sidebands are almost completely preserved for frequencies above the resonator bandwidth. Therefore the average power on the photodetector in reflection of the resonator can be reduced while keeping the same sensitivity for power fluctuations. If one, however, decides to maintain the average power on the photodetector, the sensitivity can be increased by about one order of magnitude.

In the following sections the optical ac coupling technique is studied theoretically and experimentally. At first the technique is described (Sec. 5.1) and the quantum noise limit of a power stabilization with optical ac coupling is derived and compared with other stabilization schemes (Sec. 5.2). Afterwards, experiments (Sec. 5.3), the

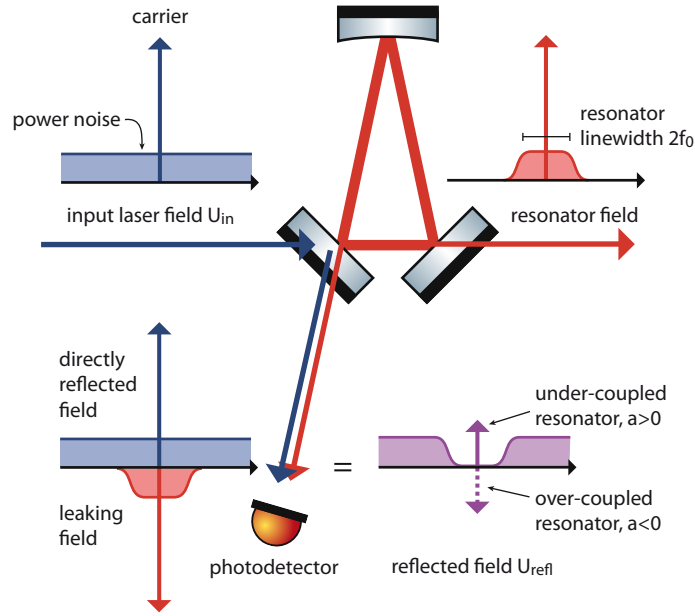


Figure 5.1: Illustration of the optical fields in the sideband picture at a resonant optical resonator. The field in reflection U_{refl} , given by the interference of the beam directly reflected and the beam leaking from the resonator, is detected in the optical ac coupling technique.

associated investigations for noise couplings and sources (Sec. 5.4), and the results and their implications (Sec. 5.5) are described.

The main results of this chapter have already been published in [Kwe08b, Kwe09a].

5.1 Optical AC Coupling Technique

The optical ac coupling technique is a high-sensitivity detection method for power fluctuations based on photo-detection in reflection of an optical resonator with a specific impedance matching. In this section this novel technique is described, including the prerequisites, the transfer function for power fluctuations, and the detection quantum noise limit.

Conventionally, electrical ac coupling is used to measure small fluctuations on top of large dc signals or of slowly varying ones in order to increase the detection sensitivity for these fluctuations. The reflection at an optical resonator is used to create a similar effect, where the signal is attenuated at low Fourier frequencies, for measuring laser power fluctuations. The optical ac coupling can be interpreted as signal conditioning in the optical domain.

The transmission of an optical resonator for power fluctuations decreases for frequencies above the resonator bandwidth (in Sec. 3.1.2, see Fig. 3.1). Accordingly power fluctuation sidebands are mainly reflected at the resonator for high frequen-

cies, whereas the carrier is almost completely transmitted for a nearly impedance matched resonator (Fig. 5.1). Thus the average power in reflection is reduced while the fluctuation sidebands are fully preserved. However, a special impedance-matching of the resonator and a very good mode-matching is required to fully exploit this effect. The same method was already used to, e.g., detect squeezed light [Mil87].

The compound detector, consisting of the resonator and the photodetector in reflection, is also called *optical ac coupled detector* in this thesis. This compound detector is significantly more sensitive to power fluctuations than the photodetector without resonator, assuming the same photocurrent is detected. This effect can be described very well by the transfer function for relative power fluctuations from the beam upstream of the resonator to the beam in reflection:

Consider the field amplitude U_{in} of a laser beam with the average amplitude U_0 that is amplitude modulated at a frequency $f = \omega/2\pi$ with a modulation index $m \ll 1$ in the plane-wave model:

$$U_{\text{in}} = U_0 (1 + me^{i\omega t}) . \quad (5.1)$$

This input beam is coupled into a resonant optical resonator (Fig. 5.1). Then the field amplitude U_{refl} of the reflected beam is given by the sum of the directly reflected field and the field leaking out of the resonator:

$$\begin{aligned} U_{\text{refl}} &= \underbrace{U_0 (1 + me^{i\omega t})}_{\text{directly reflected}} - \underbrace{(1 - a)U_0 [1 + me^{i\omega t}h(f)]}_{\text{leaking}} \\ &= U_0 (a + me^{i\omega t} [1 - (1 - a)h(f)]) \end{aligned} \quad (5.2)$$

$$\text{with } h(f) = \frac{1}{1 + if/f_0} , \quad (5.3)$$

where $h(f)$ describes the approximated power fluctuation filter effect of the resonator with bandwidth f_0 (see Sec. 3.1.2). The amplitude reflectivity of the input coupling mirror is approximated by unity assuming a high-finesse resonator. The parameter a describes the impedance matching of the resonator. The resonator is under-coupled for $a \in (0, 1]$, impedance matched for $a = 0$ and over-coupled for $a \in [-1, 0)$ [Sie86, Chap. 11.3]. In the under-coupled case the carrier directly reflected is larger than the carrier leaking out of the resonator. For the over-coupled resonator the situation is reversed.

The average power in reflection of the resonator is reduced by $\overline{|U_{\text{refl}}|^2} / \overline{|U_{\text{in}}|^2} = a^2$, the so-called *carrier reduction*. The transfer function $G(f)$ of relative power fluctuation from $|U_{\text{in}}|^2$ to $|U_{\text{refl}}|^2$ at the frequency f is given by

$$G(f) = g - (g - 1) \cdot h(f), \quad |G(f)| = \sqrt{\frac{1 + g^2 \cdot f^2/f_0^2}{1 + f^2/f_0^2}} , \quad (5.4)$$

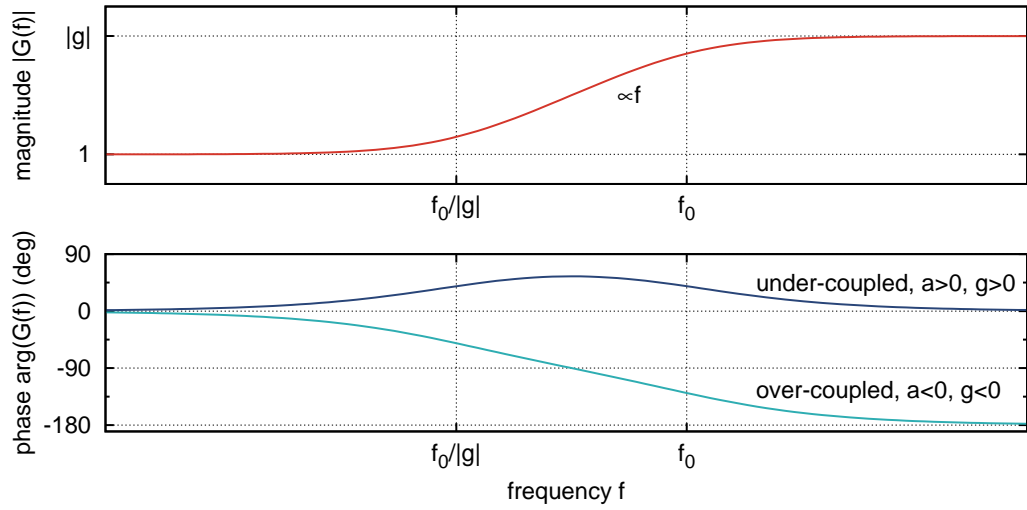


Figure 5.2: Transfer function $G(f)$ of the optical ac coupling from relative power fluctuations upstream to relative power fluctuations in reflection of the resonator. The phase of the transfer function is shown once for under-coupled and once for over-coupled resonator. The factor $|g|$ is the maximal magnitude reached for high frequencies.

with $g(a) = 1/a$ (see Fig. 5.2). At low frequencies the transfer function or gain is $G(f \rightarrow 0) = 1$. Already starting at frequencies (f_0/g) below the resonator bandwidth, the magnitude $|G|$ increases and thus a higher sensitivity is achievable with an optical ac coupled detector. For frequencies higher than the resonator bandwidth, the gain is $G(f \rightarrow \infty) = g$ and at the corner frequency of the resonator only 3 dB less $|G(f=f_0)| = |g|/\sqrt{2}$. At high frequencies the phase of the transfer function depends on the sign of g and thus on the impedance matching. In order to achieve a high gain in sensitivity with the optical ac coupling technique a nearly impedance matched resonator is required ($|a| \ll 1$, but $a \neq 0$).

Until now it was assumed that the laser beam U_0 completely consists of resonant modes and power was reflected at the resonator only due to the impedance mismatching ($a \neq 0$). In real experiments, non-resonant higher-order spatial modes or radio frequency modulation sidebands above the resonator bandwidth are reflected as well at the resonator, both called *parasitic modes* in the following. The influence of these modes can be calculated with the following modified ansatz:

$$U_{\text{in}} = (U_0 + U_1) (1 + m e^{i\omega t}) , \quad (5.5)$$

where U_0 describes the resonant modes and U_1 the non-resonant parasitic ones. In the same way as before the same transfer function $G(f)$ can be derived, where now g depends not only on the impedance matching a but also on the power in parasitic modes:

$$g(a, p) = \frac{p + a(1 - p)}{p + a^2(1 - p)} \quad \text{with} \quad p = \frac{|U_1|^2}{|U_0|^2 + |U_1|^2}, \quad (5.6)$$

where p is the relative power in parasitic modes. For $p=0$ the same result as before is obtained ($g(a, p=0) = 1/a$). The maximum value $G(f \rightarrow \infty) = g(a, p)$ depends on the impedance matching and is reduced by non-resonant, parasitic modes in the input beam and is thus in principle limited only by the controllability of a and p .

The fundamental limit¹ of the sensitivity of a photodetector for power noise is given by the quantum noise. The detection limit for relative power noise is $s_q = (2e/I)^{1/2}$, where I is the photocurrent and e the elementary charge (see Sec. 4.1). An optical ac coupled detector has a better quantum-limited sensitivity for power fluctuations upstream of the resonator:

$$s_q(f) = \frac{1}{G(f)} \cdot \sqrt{\frac{2e}{I}}. \quad (5.7)$$

In the optimal case ($p=0$) for high frequencies ($f \gg f_0$) this corresponds to the sensitivity of a photodetector placed in front of the resonator detecting the full beam power. However, the advantage of the optical ac coupling technique compared to this direct detection is that in many cases the high power upstream of the resonator cannot be handled by the photodetector. Furthermore, with the optical ac coupling technique almost the complete power is preserved in the beam transmitted by the resonator for potential downstream experiments.

To summarize, the sensitivity of a photodetector for power fluctuations can be increased for frequencies above the resonator bandwidth with the optical ac coupling technique. The effect can be described very well with the transfer function $G(f)$. More power is available for potential downstream experiments and technical limitations, such as the maximal power handling capability of photodetectors, can be circumvented. The higher sensitivity of an optical ac coupled detector in a power stabilization yields a better quantum limited power stability than traditional stabilization schemes, as will be described in Section 5.2.

5.2 Quantum Limit of Power Stabilization Schemes

In contrast to technical noise, quantum noise is a very fundamental limit in power stabilizations. This quantum limit was already derived for a traditional power stabilization in Sec. 4.1. In this section the quantum limit of different, extended power stabilization schemes, including schemes utilizing the optical ac coupling technique, are described, compared and evaluated theoretically as well as in realistic examples.

¹Non-classical states of light are not considered in this thesis.

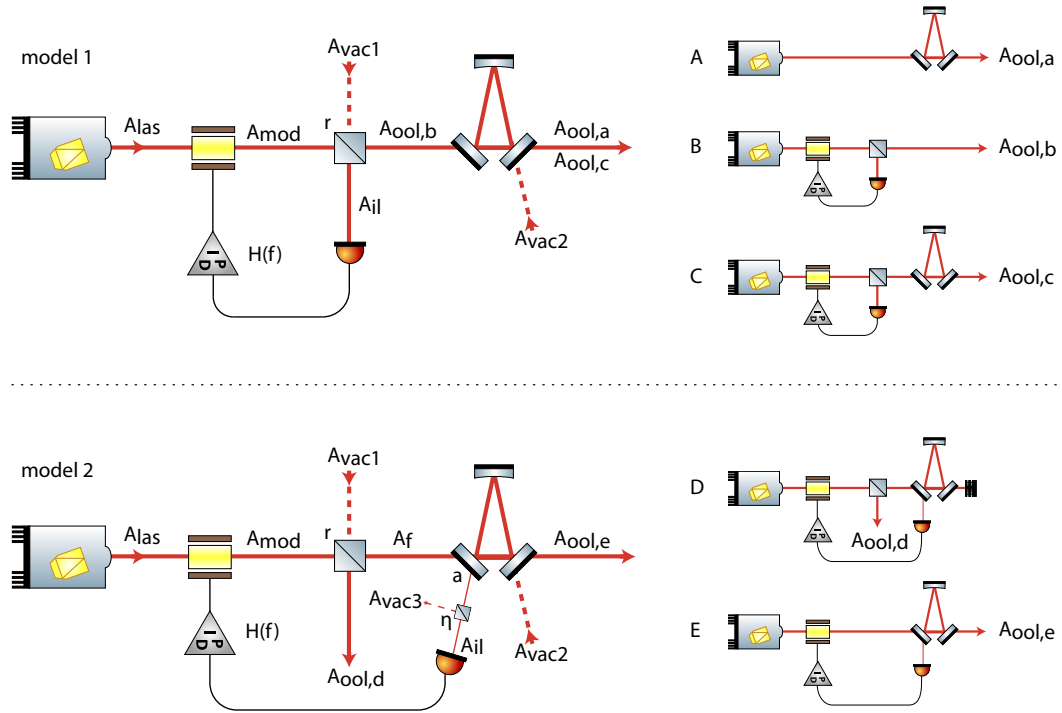


Figure 5.3: Models used to calculate the quantum noise limit of five different power stabilization schemes. Model 1 (top) showing the schemes A, B and C with out-of-loop fields $A_{ool,a}$ to $A_{ool,c}$, model 2 (bottom) showing schemes D and E with out-of-loop fields $A_{ool,d}$ and $A_{ool,e}$.

The fundamental limit² of any passive and active power stabilization is the quantum noise of the original beam (see Sec. 4.1, Eq. 4.1), which cannot be reached with a traditional power stabilization, as already mentioned. In the optimal case the out-of-loop relative power noise is 6 dB above the quantum noise of the original beam in the traditional scheme. In contrast, stabilization schemes extended in different ways with optical resonators can get closer than 6 dB to the absolute limit. In the following the methods introduced in Sec. 4.1 are used to calculate the quantum limit of these extended power stabilization schemes.

5.2.1 Limit of Different Stabilizations

Two models are used to calculate the quantum limit of five power stabilization schemes (Fig. 5.3). The fields $A_{ool,a}$ to $A_{ool,e}$ are the out-of-loop³ fields of the five

²Only classical beams are considered.

³In the following the term *out-of-loop beam* refers to the power stabilized beam that is in principle available for downstream experiments, even though in scheme A no control loop is involved at all.

schemes A to E and are relevant for potential downstream experiments. In all active schemes (B to E) the field A_{in} , called in-loop field, is used for the control loop sensor in order to compensate power fluctuations of the laser field A_{las} with an actuator. The required feedback loop is characterized by the frequency dependent loop gain $H(f)$. Vacuum fluctuations A_{vac1} to A_{vac3} couple into the system at open ports of the beam splitters and the resonator.

Model 1 is an extended version of the model used in Sec. 4.1 (see Fig. 4.1), where an additional optical resonator is placed in the out-of-loop beam $A_{ool,b}$. Depending on the parameters r and $H(f)$ and the out-of-loop beam considered, three resulting schemes can be analyzed: a purely passive stabilization (scheme A, for $r=0, H=0$), a traditional active power stabilization (scheme B, for $r>0, H\rightarrow\infty$), and a traditional one, but with subsequent resonator in the out-of-loop beam (scheme C, for $r>0, H\rightarrow\infty$).

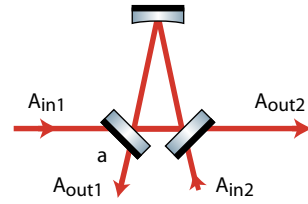
In model 2 a beam splitter with power reflectivity r is used to allow for a potential out-of-loop measurement ($A_{ool,d}$) in front of the resonator. The transmitted beam is coupled into a resonant optical resonator, which has a small impedance mismatching, such that a field fraction a is reflected at the resonator and detected by the in-loop detector. An additional beam splitter with power transmission η directly in front of the in-loop detector can be used to attenuate the beam power. With this model the quantum limit of power stabilizations with optical ac coupled in-loop detector and out-of-loop beam upstream (scheme D, for $r>0, H\rightarrow\infty$) or downstream (scheme E, for $r=0, H\rightarrow\infty$) of the resonator can be calculated.

The spectral variance of the number operator N of the individual out-of-loop fields $A_{ool,a}$ to $A_{ool,e}$ has to be calculated to determine the power noise of the different schemes (see Sec. 4.1). For linearized operators this variance depends on the operators $\delta A_{ool,a}$ to $\delta A_{ool,e}$, which can be deduced using the classical field equations and the canonical quantization.

In both models the optical resonator is a crucial element. Thus the classical field equations at a resonator are considered first. The output fields A_{out1} and A_{out2} are given as function of the input fields A_{in1} and A_{in2} assuming a high-finesse resonator by [Bac04, Chap. 5.3]

$$A_{out1} = \frac{(a + if)A_{in1} + \sqrt{1 - a^2}A_{in2}}{1 - if}, \quad (5.8)$$

$$A_{out2} = \frac{(-a + if)A_{in2} + \sqrt{1 - a^2}A_{in1}}{1 - if}, \quad (5.9)$$



where f is the Fourier frequency in units of the resonator bandwidth and a is the impedance matching factor. A resonator can be seen as frequency dependent beam splitter with high transmission for power fluctuation sidebands at frequencies below the resonator bandwidth and low transmission for higher frequencies.

Model 1

The following operator equations are obtained for model 1 using the classical equations and the above-mentioned resonator equations (see Fig. 5.3):

$$\delta A_{\text{mod}} = \delta A_{\text{las}} + H(f)\delta A_{\text{il}} \quad (5.10)$$

$$\delta A_{\text{il}} = \sqrt{r}\delta A_{\text{mod}} + \sqrt{1-r}\delta A_{\text{vac1}} \quad (5.11)$$

$$\delta A_{\text{ool,b}} = \sqrt{1-r}\delta A_{\text{mod}} - \sqrt{r}\delta A_{\text{vac1}} \quad (5.12)$$

$$\delta A_{\text{ool,c}} = \delta A_{\text{ool,a}} = \frac{if\delta A_{\text{vac2}} + \delta A_{\text{ool,b}}}{1-if} \quad (5.13)$$

where an impedance matched resonator ($a=0$) was assumed. These equations can be solved for $A_{\text{ool,b}}$ and $A_{\text{ool,c}}$ yielding⁴

$$\delta A_{\text{ool,b}} = \frac{\sqrt{1-r}\delta A_{\text{las}} + (H(f) - \sqrt{r})\delta A_{\text{vac1}}}{1 - \sqrt{r}H(f)} \quad (5.14)$$

$$\delta A_{\text{ool,c}} = \frac{\sqrt{1-r}\delta A_{\text{las}} + if[1 - \sqrt{r}H(f)]\delta A_{\text{vac2}} + (H(f) - \sqrt{r})\delta A_{\text{vac1}}}{1 - if - \sqrt{r}(1 - if)H(f)} \quad (5.15)$$

Using the operators $\delta A_{\text{ool,b}}$ and $\delta A_{\text{ool,c}}$ the variance of the number operators can be calculated in order to determine the power spectrum of the relative power noise:

$$\begin{aligned} S_{\text{ool,b}} &= \frac{\text{Var}(\delta X 1_{\text{ool,b}})}{\langle N_{\text{ool,b}} \rangle} \\ &= \frac{(1-r)\text{Var}(\delta X 1_{\text{las}}) + |H(f) - \sqrt{r}|^2}{|1 - \sqrt{r}H(f)|^2} \cdot \frac{1}{(1-r)\alpha_{\text{las}}^2} \end{aligned} \quad (5.16)$$

$$\begin{aligned} S_{\text{ool,c}} &= \frac{\text{Var}(\delta X 1_{\text{ool,c}})}{\langle N_{\text{ool,c}} \rangle} \\ &= \frac{(1-r)\text{Var}(\delta X 1_{\text{las}}) + |H(f) - \sqrt{r}|^2 + f^2|1 - \sqrt{r}H(f)|^2}{|1 - if - \sqrt{r}(1 - if)H(f)|^2 \cdot (1-r)\alpha_{\text{las}}^2} \end{aligned} \quad (5.17)$$

Both equations will be simplified when considering the additional assumptions for r and H in schemes A to C.

Scheme A This scheme is a passive stabilization of the laser power noise in the beam transmitted by the optical resonator, which yields for $r=0, H=0$:

$$S_{\text{ool,a}} = \frac{\text{Var}(\delta X 1_{\text{las}}) + f^2}{1 + f^2} \frac{1}{\alpha_{\text{las}}^2} \quad (5.18)$$

⁴ Since $\delta A_{\text{ool,a}} = \delta A_{\text{ool,c}}$ only the equations for $\delta A_{\text{ool,c}}$ are considered in the following.

The power spectrum depends on the laser noise, to which it is equal at low frequencies $S_{\text{ool,a}}(f \ll 1) \approx \text{Var}(\delta X_{1\text{las}})/\alpha_{\text{las}}^2$ since the resonator has a high transmission for noise sidebands at low frequencies. For higher frequencies $f > 1$ the resonator transmission decreases such that the contribution of the laser noise $\text{Var}(\delta X_{1\text{las}})$ in the out-of-loop noise is reduced. At the same time the reflection of the vacuum fluctuations A_{vac2} increases, dominating the out-of-loop power noise at high frequencies. This corresponds to a lowpass filter effect for technical power noise of transmitted fields. The laser noise is reduced with $1/f^2$ (corresponds to $1/f$ in the linear spectral density), limited by the level of the quantum noise $1/\alpha_{\text{las}}^2$ for $f \rightarrow \infty$.

The power noise of this scheme is shown in Fig. 5.4, ① assuming a frequency independent, arbitrarily chosen laser noise of 30 dB above the quantum noise of the laser beam.

Scheme B This scheme is a traditional active power stabilization, usually operated at a high control loop gain ($H \rightarrow \infty$). This scheme was already described in detail in Sec. 4.1 and the resulting quantum limit is repeated for the sake of completeness:

$$S_{\text{ool,b}} = \frac{1}{r(1-r)\alpha_{\text{las}}^2}. \quad (5.19)$$

The relative power noise (Fig. 5.4, ②) does not depend on the laser noise δA_{las} due to the high-gain feedback loop and is frequency independent. The noise is minimal $S_{\text{min,b}} = 4/\alpha_{\text{las}}^2$ for $r=0.5$ (Fig. 5.5, ①) and thus is 6 dB above the quantum noise of the original beam ($1/\alpha_{\text{las}}^2$) or 3 dB above its own quantum noise ($2/\alpha_{\text{las}}^2$).

Scheme C This scheme is a combination of a traditional active power stabilization (scheme B) and a passive resonator filtering (scheme A):

$$S_{\text{ool,c}} = \frac{rf^2 + 1}{r(1-r)(1+f^2)\alpha_{\text{las}}^2}. \quad (5.20)$$

The resonator has a high transmission at low frequencies and thus its filtering effect is insignificant. The power noise is equal to the noise of a traditional stabilization $S_{\text{ool,c}}(f \ll 1) \rightarrow S_{\text{ool,b}}$. At high frequencies the reflectivity of the resonator and hence its filtering effect for noise at point $A_{\text{ool,b}}$ increases. However, the reflectivity for the field A_{vac2} increases as well such that the power noise is at these frequencies equal to the quantum noise of the out-of-loop beam $1/[(1-r)\alpha_{\text{las}}^2]$, which in general is above the quantum noise of the original beam. The quantum limit is shown in Fig. 5.4, ③ for $r=0.5$.

The optimal reflectivity of the beam splitter r_{opt} and the minimal power noise $S_{\text{min,c}}$ now depends on the frequency and are given by (see Fig. 5.5, ②)

$$r_{\text{opt}}(f) = \frac{\sqrt{f^2 + 1} - 1}{f^2}, \quad S_{\text{min,c}}(f) = \frac{f^4}{(f^2 + 1) \left(\sqrt{f^2 + 1} - 1 \right)^2 \alpha_{\text{las}}^2}. \quad (5.21)$$

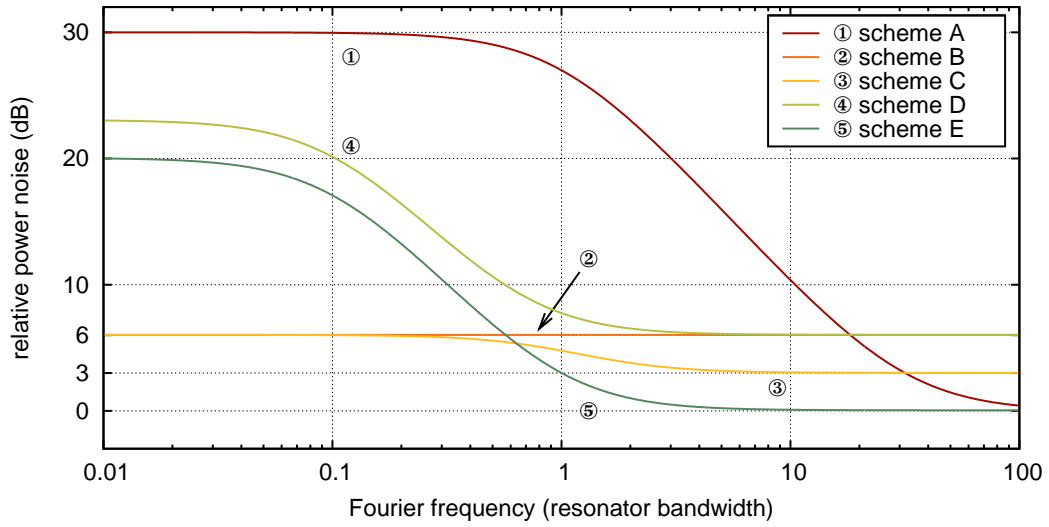


Figure 5.4: Quantum noise limits for the different power stabilization schemes. The limits are given in relation to the relative quantum noise of the original beam. The following representative parameters were chosen: 30 dB free-running noise (relevant only in scheme A); scheme B and C, $r=0.5$; scheme D, $r=0.5, a=0.1$; scheme E, $a=0.1$.

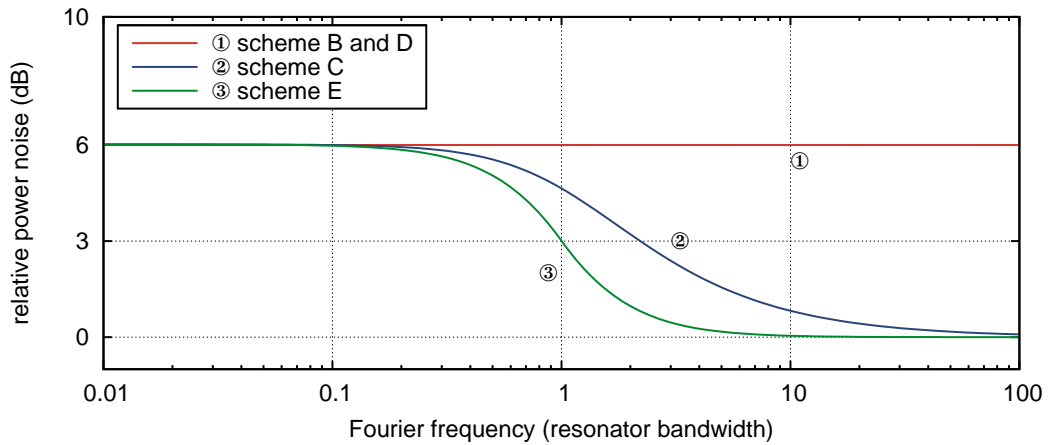


Figure 5.5: Minimal quantum limit for the four active stabilization schemes B to E, where the beam splitter reflectivity and the impedance matching were optimized for each Fourier frequency.

It should be noted that this minimal power noise cannot be achieved in the whole frequency band simultaneously since a very special frequency dependent beam splitter would be necessary. At low frequencies $r_{\text{opt}}(f \ll 1) \rightarrow 0.5$ and at high frequencies $r_{\text{opt}}(f \gg 1) \rightarrow 0$ yield the best stability.

Model 2

The power noise of the out-of-loop beams in model 2 is calculated in the same way as in model 1. The initial equations are given by (see Fig. 5.3):

$$\delta A_{\text{mod}} = \delta A_{\text{las}} + H(f)\delta A_{\text{il}} \quad (5.22)$$

$$\delta A_{\text{ool,d}} = \sqrt{r}\delta A_{\text{mod}} + \sqrt{1-r}\delta A_{\text{vac1}} \quad (5.23)$$

$$\delta A_{\text{f}} = \sqrt{1-r}\delta A_{\text{mod}} - \sqrt{r}\delta A_{\text{vac1}} \quad (5.24)$$

$$\delta A_{\text{il}} = \frac{(a + if)\delta A_{\text{f}} + \sqrt{1-a^2}\delta A_{\text{vac2}}}{1 - if} \cdot \sqrt{\eta} + \sqrt{1-\eta}\delta A_{\text{vac3}} \quad (5.25)$$

$$\delta A_{\text{ool,e}} = \frac{(-a + if)\delta A_{\text{vac2}} + \sqrt{1-a^2}\delta A_{\text{f}}}{1 - if} \quad (5.26)$$

These equations yield the spectrum of the relative power noise in scheme D and E after a short calculation.

Scheme D In this scheme an optical ac coupled in-loop detector is used and a beam splitter in front of the resonator extracts the out-of-loop beam. The scheme is equivalent to a traditional power stabilization, but with optical ac coupled in-loop detector (the compound detector consisting of the resonator and the photodetector).

$$S_{\text{ool,d}} = \frac{a^2 + f^2 + r(1 - a^2) + r(1 - \eta)(1 + f^2)/\eta}{(a^2 + f^2)(1 - r)} \frac{1}{r\alpha_{\text{las}}^2}. \quad (5.27)$$

The attenuation controlled by η in front of the in-loop detector is integrated in the model only to be able to take technical limitations into account later on. Thus for the rest of this subsection $\eta=1$ is assumed.

For high frequencies the resonator has a high reflectivity and acts like a normal mirror. The same power noise as in a traditional stabilization is achieved at these frequencies $S_{\text{ool,d}}(f \gg 1) \rightarrow S_{\text{ool,b}}$. At low frequencies the resonator reflectivity is reduced to a^2 causing a higher relative quantum noise at the in-loop detector, which is imprinted to the out-of-loop beam by the control loop. The quantum limit is shown in Fig. 5.4, ④ for $r=0.5$ and $a=0.1$.

In principle the power noise is minimal for $r=0.5$, $a=1$ and yields $S_{\text{min,d}} = 4/\alpha_{\text{las}}^2$ (Fig. 5.5, ①). By choosing $a=1$, the resonator acts like a normal mirror and scheme D is transformed into scheme B. Thus scheme D, involving the optical

ac coupling, has no advantage over the traditional scheme B when considering only the theoretical quantum limit.

Scheme E Finally in this scheme the laser beam is first actively stabilized using an optical ac coupled in-loop detector and is then passively filtered by the resonator.

$$S_{\text{ool,e}} = \frac{1 + f^2 + (1 - a^2)(1 - \eta)/\eta}{a^2 + f^2} \frac{1}{(1 - a^2)\alpha_{\text{las}}^2}. \quad (5.28)$$

As in scheme D, $\eta=1$ is assumed for the rest of this subsection. For low frequencies the resonator has a high transmission and the imprinted noise of A_{il} is dominant at the out-of-loop field $A_{\text{ool,e}}$. For these frequencies the stabilization is comparable to a traditional power stabilization with a beam splitter reflection of $r=a^2$ ($S_{\text{ool,e}}(f \rightarrow 0, a^2=r) = S_{\text{ool,b}}$). For small impedance mismatches, the out-of-loop noise $S_{\text{ool,e}}(a \ll 1) \approx 1/(a^2\alpha_{\text{las}}^2)$ is about a factor of $1/a^2$ above the quantum noise of the original beam A_{las} .

The reflection of the resonator increases for higher frequencies causing two effects: On the one hand the noise imprinted by the control loop onto A_{mod} is reduced (similar to a traditional power stabilization with large beam splitter reflection, $S_{\text{ool,b}}$ for $r \rightarrow 1$). On the other hand the vacuum fluctuations A_{vac2} are mainly reflected by the resonator and dominate the power noise of $A_{\text{ool,e}}$ (similar to the traditional power stabilization with a resonator in the out-of-loop beam, $S_{\text{ool,c}}$ for $r=a^2$ and $f \rightarrow \infty$). In the end, the relative power noise of $A_{\text{ool,e}}$ is only a factor $1/(1 - a^2)$ above the quantum noise of the original beam $S_{\text{ool,e}}(f \rightarrow \infty) = 1/(1 - a^2)\alpha_{\text{las}}^2$. The power noise $S_{\text{s,ool,e}}$ is shown in Fig. 5.4, ⑤ for $a=0.1$.

The quantum limit could in principle be optimized for a specific frequency by altering the impedance matching a . The minimal noise $S_{\text{min,e}}$ (Fig. 5.5, ③) is reached for

$$a_{\text{opt}}(f) = \begin{cases} \sqrt{\frac{1 - f^2}{2}} & \text{for } f < 1 \\ \rightarrow 0 & \text{for } f \geq 1 \end{cases}, \quad S_{\text{min,e}}(f) = \begin{cases} \frac{4}{1 + f^2} \frac{1}{\alpha_{\text{las}}^2} & \text{for } f < 1 \\ \frac{1 + f^2}{f^2} \frac{1}{\alpha_{\text{las}}^2} & \text{for } f \geq 1 \end{cases}. \quad (5.29)$$

At low frequencies an impedance matching of $a^2=0.5$ is ideal. In this case and at these frequencies the resonator acts like a 50:50 beam splitter, which is as well optimal in the traditional stabilization scheme. In contrast a nearly perfectly impedance matched resonator yields the best stability at high frequencies and the minimal noise approaches the quantum noise of the original beam $S_{\text{min,e}}(f \rightarrow \infty) = 1/\alpha_{\text{las}}^2$.

Comparison

The quantum limit of the different stabilization schemes is shown in Fig. 5.4 for a small, representative selection of the model parameters r , a , and η . Scheme E

involving the optical ac coupling is superior compared to the other schemes at frequencies $f > 1$. Scheme A only achieves at much higher frequencies, depending on the laser noise, a similar performance. However, at low frequencies the traditional power stabilization scheme B and its modification, scheme C, achieve the lowest power noise.

A comparison of the minimal power noise of the active schemes (Fig. 5.5) shows that for a fixed Fourier frequency, the quantum limit of scheme E is at or below the quantum limit of the other schemes. As already mentioned, this minimal power noise cannot be reached simultaneously in the whole frequency band for scheme C and E, since a beam splitter and resonator with a special frequency dependent reflectivity and impedance matching, respectively, would be necessary.

5.2.2 Case Study

So far the performance of the different power stabilization schemes were compared and evaluated using only the theoretical quantum limit. However, in real experiments several technical limitations have to be considered as well. The maximum photocurrent that can be detected with quantum-noise-limited noise performance at frequencies of interest for GWDs is about 100 mA. This corresponds to a beam power of 117 mW at 1064 nm wavelength ($hc/\lambda = 1.87 \times 10^{-19}$ J) and a photodiode quantum efficiency of 1. For frequencies above 10 Hz this is a typical limit in experiments (see Sec. 3.1.2, [Rol04, Sei06, Kwe09b]). Furthermore, in current experiments the impedance matching has to be $a \geq 0.1$ so that additional technical noise sources, e.g. caused by non-resonant modes, do not limit the achievable stability with optical ac coupling (see Sec. 5.1 and 5.4). This corresponds to a maximal carrier reduction down to $a^2=1\%$.

In the following two realistic cases are described, where laser beams with powers of 10 mW ($\alpha_{\text{las}}^2 = 5.4 \times 10^{16}$ Hz) and 100 W ($\alpha_{\text{las}}^2 = 5.4 \times 10^{20}$ Hz) are stabilized. The free-running power noise of typical lasers with these power levels is several orders of magnitude above the quantum noise for frequencies below the relaxation oscillation (see e.g. Sec. 2.3). Hence the case study is limited to the active schemes B to E, since in general they have a higher noise suppression at low frequencies than the passive scheme A.

10 mW Laser

The relative quantum noise of the laser beam with 10 mW power is 6.1×10^{-9} Hz $^{-1/2}$. The quantum limits of the four schemes are shown in Fig. 5.6, left. For scheme B $r=0.5$ is chosen and scheme C is optimized once for $f=1$ and once for $f=10$. Scheme D achieves the same performance as scheme B with $r=0.5, a=1$. The lowest quantum limit in scheme E is achieved for $a \rightarrow 0$ for frequencies $f \geq 1$. However, due to the technical limit ($a \geq 0.1$) an impedance matching of $a=0.1$ has to be chosen, but the power noise still gets as close as 0.04 dB to the fundamental quantum limit.

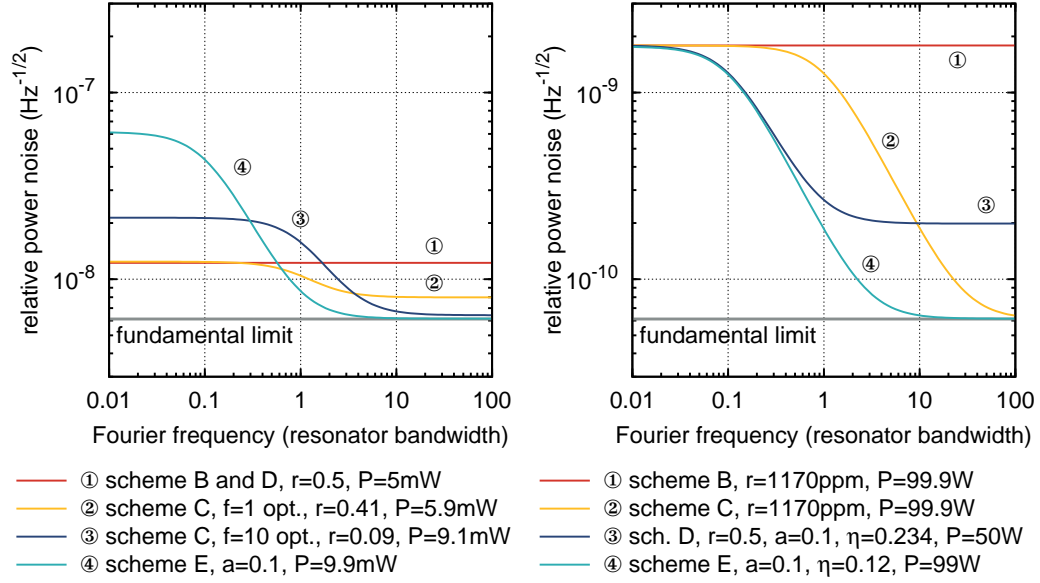


Figure 5.6: Out-of-loop achievable power noise for the different power stabilization schemes for laser beams of 10 mW (left) and 100 W (right). The model parameters chosen and the OOL available power are given in the legend.

At low frequencies $f < 1$ the traditional power stabilization scheme B and the more complicated schemes C (optimized for $f=1$) and D achieve the best stability, whereas at high frequencies $f > 1$ the optical ac coupling scheme E achieves a better one. Scheme C (optimized for $f=10$) gives comparable results to scheme E at very high frequencies $f > 10$.

The out-of-loop power noise of the schemes differs only by at most 6 dB at high frequencies and thus the achieved stabilities are close to each other. However the 5 mW beam power, available for experiments downstream of the power stabilization, is in scheme B and D significantly lower compared to 9.9 mW in scheme E. If a power noise difference of 6 dB and a beam power difference of a factor of up to 2 is acceptable for the downstream experiment, a traditional power stabilization should be used since it is less complex and no optical resonator is needed.

100 W Laser

The relative quantum noise of a 100 W beam is $6.1 \times 10^{-11} \text{ Hz}^{-1/2}$ (Fig. 5.6, right). Due to the technical limit of the in-loop photodetector in scheme B and C a reflectivity of $r=1.17 \times 10^{-3}$ has to be chosen. Scheme D and E are limited by the photodetector as well as by the impedance matching. Since even with $a=0.1$ the power on the in-loop detector is too high, the power needs to be attenuated with η (see Fig. 5.3, model 2). For Scheme D the lowest power noise is reached for $r=0.5$, $\eta=0.234$ and for scheme E the attenuation $\eta=0.12$ is required. The quantum limits

of the four schemes are shown in Fig. 5.6, right, and in all cases most of the laser power is available in the out-of-loop beam (99 W to 99.9 W), except for scheme D, where 50% of the power is used for the stabilization⁵.

The differences between the schemes are more significant at the high laser power of 100 W. The best stability is achieved with scheme E. Up to frequencies of the resonator bandwidth scheme D achieves a comparable performance. Scheme C is at most frequencies a factor of 10 worse, but reaches the same power noise as scheme E at very low and very high frequencies. In the whole frequency band the traditional power stabilization achieves the worst performance. For reaching a power stability close to the quantum limit of the original beam, only scheme C or E can be used. At this laser power level the higher experimental complexity of a power stabilization with optical ac coupling compared to a traditional stabilization might well be justified by the requirement of the downstream experiment.

The conclusion is that the power stabilization scheme with optical ac coupling can achieve a better quantum limited performance than the other schemes – especially the traditional scheme – at frequencies above the resonator bandwidth. This is the case when considering the theoretical quantum limit and as well when taking additional technical limitations into account. Among other things, the better power stability was demonstrated experimentally, as described in the following sections.

5.3 Experiments

Several experiments with an optical ac coupled photodetector were performed to demonstrate the feasibility of this detection scheme and the high sensitivity for power fluctuations. In this section the experimental setup (Sec. 5.3.1) and a selection of experimental challenges (Sec. 5.3.2) are described.

Two main experiments with slightly different setups were performed. In both cases the power noise of an NPRO at 1064 nm was measured (see Sec. 2.3.1).

In one experiment, the *power sensing experiment*, the high sensitivity of an optical ac coupled photodetector was demonstrated at high frequencies of several megahertz. The NPRO power noise rolls off steeply at these frequencies towards higher frequencies and thus the detector noise could be measured directly and was compared with the expected quantum limit.

At lower frequencies between 1 kHz and 1 MHz, the technical power noise of the laser was much higher than the expected noise of the optical ac coupled detector. Therefore the sensitivity of the detector could not be measured directly at these frequencies. Instead the optical ac coupled detector was used in a slightly modified setup as part of an active power stabilization (scheme D in Sec. 5.2), the *power stabilization experiment*. Thus the feasibility of a power stabilization with optical ac coupled detector and the high sensitivity of the detector at low frequencies were

⁵In principle most of this power would be available in the transmitted beam of the resonator for a potential second downstream experiment.

demonstrated simultaneously. Compared to the experiment described in Chapter 4, the laser power was stabilized at rather high frequencies since the full sensitivity gain of the optical ac coupling is only present for frequencies at or above the resonator bandwidth, which is in this case about 35 kHz. The resonator bandwidth in turn was limited to this high frequency by the size of the resonator (all experiments performed were table-top experiments) and by the achievable finesse.

Furthermore the coupling of technical noise sources was investigated using these experiments, as described in more detail in Sec. 5.4.

5.3.1 Setup

The experimental setups of the two main experiments are similar and are described together in the following (Fig. 5.7). The differences between the power sensing and the power stabilization experiment are summarized at the end.

An NPRO with an output power of 2 W at a wavelength of 1064 nm was used. The laser had an integrated power stabilization (called *Noise Eater*) to suppress the relaxation oscillation at about 1 MHz. This power stabilization was activated in the power stabilization experiment and deactivated in the power sensing experiment. A resonant EOM was used to create phase modulation sidebands at 29 MHz for a PDH stabilization (see Sec. 3.1.3, [Dre83, Bla01]) of the mode-cleaner described later on.

The subsequent broadband EOM was one of three different actuators used to control the laser frequency: At low Fourier frequencies (<1 Hz), the temperature of the laser crystal was used as an actuator; for Fourier frequencies up to about 20 kHz, the PZT of the laser crystal was the actuator; and, for Fourier frequencies up to about 1 MHz, the broadband EOM was used as the actuator. The laser beam power was controlled with an EOAM for the downstream experiment. The EOAM was used to electronically control the polarization, and in this way the laser power after a subsequent polarizing beam splitter could be changed. With a $\lambda/4$ and a $\lambda/2$ wave plate in front of the EOAM, the modulation coefficient and the total power downstream of the polarizing beam splitter were adjusted. A $\lambda/2$ wave plate and a polarizing beam splitter were used to additionally control the beam power.

An optical three-mirror ring resonator similar to the one used in the DBB (see Sec. 2.2.1) served as a mode-cleaner in order to suppress higher-order transverse modes of the beam and to stabilize the beam pointing (see Sec. 3.1.4 and 3.1.5). A mode matching of better than 99% to the subsequent *ac coupling cavity* (ACC) was only possible thanks to this mode-cleaner. Mode-cleaners with different bandwidths were used in the two main experiments. One mode-cleaner had a low bandwidth of about 980 kHz and a measured finesse of about 366 and was used in the power sensing experiment. The other high-bandwidth mode-cleaner had a finesse of only 46 and a bandwidth of 7.8 MHz and was used in the power stabilization experiment. The round trip length, and thus the resonance frequencies of the resonators, was electronically controlled with a PZT adjusting the position of the curved mirror. The PDH method was used to stabilize a fundamental mode of the resonator to the laser frequency using the 29 MHz sidebands. The polarization of the transmit-

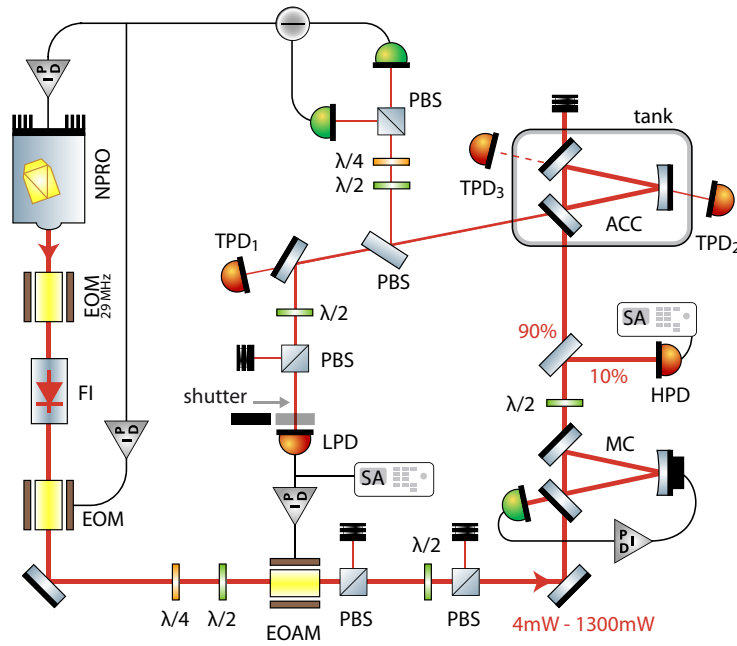


Figure 5.7: Experimental setup of the power sensing and stabilization experiment. EOM, electro-optic phase modulator; FI, Faraday isolator; EOAM, electro-optic amplitude modulator; PBS, polarizing beam splitter; MC, mode-cleaner; ACC, ac-coupling cavity; LPD, HPD, TPD, photodetectors; $\lambda/2$, $\lambda/4$, wave plates; SA, spectrum analyzer.

ted beam was rotated with a $\lambda/2$ wave plate such that 98.6% of the beam was s-polarized (vertically).

About 10% of the beam was sampled and detected with photodetector HPD. This detector consisted of a 2 mm InGaAs photodiode and a low-noise transimpedance amplifier. A bandwidth of about 20 MHz and a quantum noise limited performance up to about 60 MHz was achieved at photocurrents of 50 mA to 60 mA. This high-power, high-sensitivity detector was used to measure the laser power noise independently.

The remaining beam power of up to 900 mW was directed to the ACC that was used for the optical ac coupling. This resonator, which was placed in a pressure-tight aluminum vessel at atmospheric pressure in order to reduce acoustic effects, had the same geometry as the mode-cleaner but mirrors with different reflectivities. Two very similar resonators were used for the experiments. The main difference was that the curved high-reflective mirror of one resonator was mounted in a mirror mount that was glued to the spacer to be able to tilt the curved mirror. However, this mirror mount had a strong mechanical resonance at a few kilohertz limiting the power noise measurement in this frequency range. Hence another, quasi-monolithic

resonator was used as well, where all mirrors were glued to the spacer. The technical details of these two resonators are given in the following.

The quasi-monolithic resonator used in the power stabilization experiment had a measured finesse of about 10 000, a bandwidth of 35.7 kHz, and a beam waist of $w_0=372\ \mu\text{m}$. The resonator was slightly under-coupled, such that 0.8% of the incident beam power was reflected due to the impedance mismatch. All three resonator mirrors and a resonator-internal baffle with an aperture of only 3 mm diameter ($\approx 4\times 2w_0$) were glued to an aluminum spacer in order to avoid mechanical resonances of ordinary mirror mounts. The additional fractional losses for the fundamental mode of 10^{-14} due to the aperture were negligible compared with the total transmission of the mirrors of about 600 ppm. The larger losses for higher-order spatial modes introduced by this aperture were, however, crucial for the power stabilization experiment (see Sec. 5.5). Without this additional aperture, the smallest aperture with a diameter of 14 mm ($\approx 19\times 2w_0$) was given by the spacer itself.

The other, adjustable resonator had a slightly higher finesse of 10 400, a bandwidth of 34 kHz and was used in the power sensing experiment. By tilting the curved mirror of the resonator, the reflection angles of the resonator modes were changed in order to accurately adjust the impedance matching (see Sec. 5.3.2). For the main measurement the ACC was adjusted to be slightly under-coupled and, along with parasitic modes, about 0.4% of the impinging power was reflected. This resonator contained no additional aperture.

The laser frequency was stabilized with the Hänsch-Couillaud method to a fundamental mode resonance of the ACC (see Sec. 3.1.3, [Han80]). The p- (horizontal) and s-polarized eigenmodes of the resonator have different resonance frequencies due to non-normal incidence of their reflections in the resonator. Therefore no additional polarizing element inside the resonator was necessary in order to use the Hänsch-Couillaud method (see Sec. 5.3.2). The frequency feedback control loop had a bandwidth of about 1 MHz and used the three frequency actuators already mentioned.

To summarize, the mode-cleaner was stabilized to the laser frequency, which was stabilized to the resonance frequency of the ACC.

The power of the remaining beam reflected off the ACC was adjusted with a $\lambda/2$ wave plate and a polarizing beam splitter and was then detected with the photodetector LPD, which was protected by a shutter from excessively high laser power, arising in case the ACC got non-resonant.

Two different LPD detectors were used for the two experiments: For the power stabilization experiment this detector consisted of a 0.5 mm InGaAs photodiode with a transimpedance amplifier. A laser power of about 0.4 mW (0.3 mA photocurrent) was detected with a bandwidth of 80 MHz. The electronic noise was a factor of 3 below the shot noise of the detected photocurrent. This detector was used as in-loop detector in the power stabilization experiments. The reference current of 0.3 mA was directly subtracted from the photocurrent.

The other detector used in the power sensing experiment consisted of a 1 mm InGaAs photodiode and a transimpedance amplifier with a bandwidth of ≈ 55 MHz. A photocurrent of 3 mA was detected.

Furthermore several auxiliary photodetectors TPD₁, TPD₂, and TPD₃ were used to measure different signals in the setup, explained in more detail later on.

Power Sensing Experiment

In the power sensing experiment the internal power stabilization of the NPRO, the Noise Eater, was deactivated. In this way the laser power noise could be predicted at frequencies of several megahertz by using a laser model fitted to the measured power noise at the relaxation oscillation [Sie86, Chap. 25.1]. This prediction was compared with the power noise measured with the optical ac coupled detector. The mode-cleaner with high finesse ($\mathcal{F}=366$) was used to further reduce technical laser noise in the measurement frequency band. The ACC with adjustable curved-mirror tilt was used since the mechanical resonance of its mirror mount was far below the measurement band and it was thus possible to easily optimize the impedance matching of the ACC during the experiment. The photodetector with 3 mA photocurrent was used as optical ac coupled detector LPD.

The following main measurements were performed: The transfer function $G(f)$, from relative power fluctuations in front of the ACC to the fluctuations in the reflected beam, was measured with a network analyzer and the detectors HPD and LPD. For this the laser power was modulated with the EOAM. The carrier reduction between the resonant and non-resonant ACC was measured with the detector TPD₁.

Then the optical ac coupled power noise was measured with detector LPD. The RPN in front of the ACC was calculated using the measured transfer function $G(f)$. To verify the measurement, the RPN was measured in a traditional setup with detector HPD. A power modulation was applied with the EOAM at 20 MHz during all measurements to additionally verify the calibration. The results of these measurements are presented in Sec. 5.5.

Power Stabilization Experiment

At lower frequencies many technical noise sources are significantly larger than at frequencies of several megahertz. Hence in the power stabilization experiment it was much more complicated to isolate the experiment from these noise sources.

The Noise Eater of the NPRO was activated to pre-stabilize the power in the frequency band of interest. The mode-cleaner transfer function was part of the power stabilization control loop, which had an extremely high unity-gain frequency of about 10 MHz. Therefore the finesse of the mode-cleaner was reduced compared to the power sensing experiment, and the low-finesse ($\mathcal{F}\approx 46$), high-bandwidth mode-cleaner was used. The ACC with adjustable impedance matching could not be used

due to the mechanical resonance of the mirror mount. Thus the quasi-monolithic ACC was used in this experiment. Furthermore, this ACC had a resonator-internal aperture used to suppress resonant scattering to higher-order spatial modes (see Sec. 5.4.3). For the LPD detector, the low-power high-bandwidth photodetector with 0.3 mA photocurrent was used.

For the power stabilization, a bandwidth-optimized low-noise feedback controller and the EOAM were used. The bandwidth of the feedback control loop was about 10 MHz with a loop gain of >20 dB for Fourier frequencies below 1 MHz (see Sec. 5.3.2). For the design of the controller, the optical ac coupling transfer function $G(f)$ and the mode-cleaner lowpass were taken into account.

The laser power was stabilized with the optical ac-coupled detector LPD (in-loop detector) and was independently measured with the detector HPD (out-of-loop detector). This corresponds to the power stabilization scheme D in Sec. 5.2. Although this scheme was inferior to scheme E in all aspects considered in Sec. 5.2, it was chosen for this power stabilization experiment. The reason for this selection is that the residual power noise introduced by the control loop (beam A_{mod} in Fig. 5.3) should be independently measured in this experiment in order to demonstrate the sensitivity of the optical ac coupled in-loop detector. In contrast the out-of-loop detector in scheme E measures mainly the vacuum fluctuations $A_{\text{vac}2}$ reflected at the ACC for frequencies above the resonator bandwidth. The technical residual power noise of A_{mod} , which should be measured, is filtered by the transmission through the ACC in scheme E.

5.3.2 Experimental Challenges

Many experimental and technical problems had to be solved for realizing the power sensing and stabilization experiment. In the following a selection of the problems that occurred and their solutions are described.

Impedance Matching

The impedance matching of the ACC resonator is one of the most important parameters of the optical ac coupling technique (see Sec. 5.1). However, usually this resonator parameter cannot be controlled easily since it depends very sensitively on transmission differences of the resonator mirrors. This problem was solved using a ring resonator, where the reflection angle of the resonator mode on the resonator mirrors was adjusted by tilting one resonator mirror. Since the transmissivity of the resonator mirrors depended on the incidence angle, the impedance matching could be precisely controlled.

The impedance matching a depends on the transmissivity of the input coupling mirror and on additional losses inside the resonator, such as the transmission losses of the output coupling mirror or absorption and scattering losses at the mirrors in general:

$$a(r_{\text{in}}, r_{\text{out}}, r_{\text{loss}}) = \frac{r_{\text{in}} - r_{\text{out}}r_{\text{loss}}}{1 - r_{\text{in}}r_{\text{out}}r_{\text{loss}}}, \quad (5.30)$$

where r_{in}^2 and r_{out}^2 are the power reflectivities of the input and output coupling mirrors, respectively, and $1-r_{\text{loss}}^2$ is the power loss due to absorption and scattering at the mirrors and due to transmission of potential further resonator mirrors. For high-finesse resonators, $r_{\text{in}}r_{\text{out}}r_{\text{loss}}\rightarrow 1$, the impedance matching depends very sensitively on the difference $r_{\text{in}}-r_{\text{out}}r_{\text{loss}}$. Impedance matched resonators ($a=0$) can be realized by reducing resonator internal losses ($r_{\text{loss}}\rightarrow 1$) and using input and output coupling mirrors with identical coatings ($r_{\text{in}}=r_{\text{out}}$).

However, for the optical ac coupling technique it is important to have a resonator with a slight impedance mismatch. In the experiments an ACC of high finesse $\mathcal{F}\approx 10\,000$ and with an impedance matching of $|a|\approx 0.1$ was used. For this an input coupling mirror with reflectivity of 99.965% and an output coupling mirror with 99.972% would be necessary neglecting any losses ($r_{\text{loss}}=1$). The typical manufacturer tolerances ($\pm 10\%$ for the power transmission) are too big to produce mirrors with such defined reflectivity difference.

This problem was solved by exploiting the incidence angle dependence of the mirror transmission. According to the manufacturer information, the transmission of the input and output coupler mirror had a first-order angle dependence of about $-15\text{ ppm}/^\circ$ with about 300 ppm at 45° incidence angle. The resonator geometry was similar to the resonator of the DBB (in Sec. 2.2.1, see Fig. 2.4). Using an ordinary mirror mount glued to the resonator spacer, the curved high-reflectivity resonator mirror was tilted. Thus the beam path of the fundamental mode in the resonator and with it the incidence angles for the input and output coupler mirrors were changed. In this way the impedance matching was accurately adjusted.

A ray tracing simulation was performed to calculate the incidence angle as function of the mirror tilt. The curved mirror can be tilted up to $\pm 1.9^\circ$ with less than 10^{-8} power loss per round-trip before the beam is obstructed by the baffles at the mirrors⁶. With this boundary condition the impedance matching can be theoretically changed in the range $a \in [-0.2, 0.2]$.

The power reflected off the ACC was measured in the experiment as function of the mirror tilt (Fig. 5.8). Due to higher-order spatial modes in the input beam, the reflected power did not vanish completely at perfect impedance matching.

For the power stabilization experiment, a quasi-monolithic resonator was used. This resonator was built by first adjusting the impedance matching as described and then glueing the curved mirror to the spacer without changing the alignment.

Hänsch-Couillaud Locking

The laser beam has to be stabilized to a fundamental mode resonance of the ACC for the optical ac coupling technique. Most stabilization methods (see Sec. 3.1.3) use non-resonant modes as phase reference. However, these are parasitic modes for the optical ac coupling reducing the maximum gain of the transfer function $G(f)$

⁶An effective mirror diameter of 20 mm was assumed and the drills along the beam path in the spacer had a larger diameter than in the resonator spacer for the DBB.

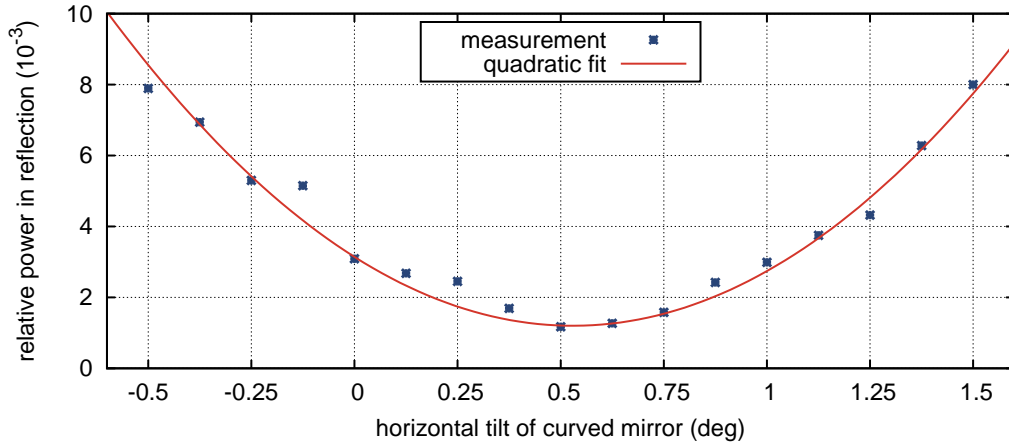


Figure 5.8: Measurement of the reflected power at the ACC as function of the resonator mirror tilt angle. The power varies, quadratically in first order, due to a change of the impedance matching of the resonator.

(see Sec. 5.1). An adapted Hänsch-Couillaud locking scheme was used to solve this problem.

Different non-resonant modes were used as phase references, such as non-resonant phase modulation sidebands in the Pound-Drever-Hall method [Dre83, Bla01], non-resonant higher-order spatial modes in the tilt-locking method [Sha99], or a non-resonant orthogonal polarized mode in the Hänsch-Couillaud method [Han80]. Furthermore the PDH method is not really suited for stabilizing the ACC since an EOM in front of the ACC would be necessary to generate phase modulation sidebands. This EOM would cause small beam distortions, which would complicate the demanding mode matching required.

In principle, tilt-locking could be used in the double-pass configuration since then no additional non-resonant higher-order spatial modes would be reflected to the optical ac coupled detector. However, the bandwidth of the error signals would be significantly smaller in this configuration, which in turn would complicate the high unity-gain frequency control loop necessary (see Sec. 5.4.1).

An additional mode-cleaner directly in front of the optical ac coupled photodetector could be used in principle to suppress non-resonant parasitic modes, but this resonator would cause additional experimental effort.

However, the Hänsch-Couillaud method can be used very well to solve the problem described. Since another polarization is used as phase reference, a polarizing beam splitter directly in front of the optical ac coupled detector can be used to reduce the parasitic power caused by the locking method.

Due to the geometry of the resonator, the resonance frequencies of the fundamental mode depends on the polarization. Therefore no additional polarizing ele-

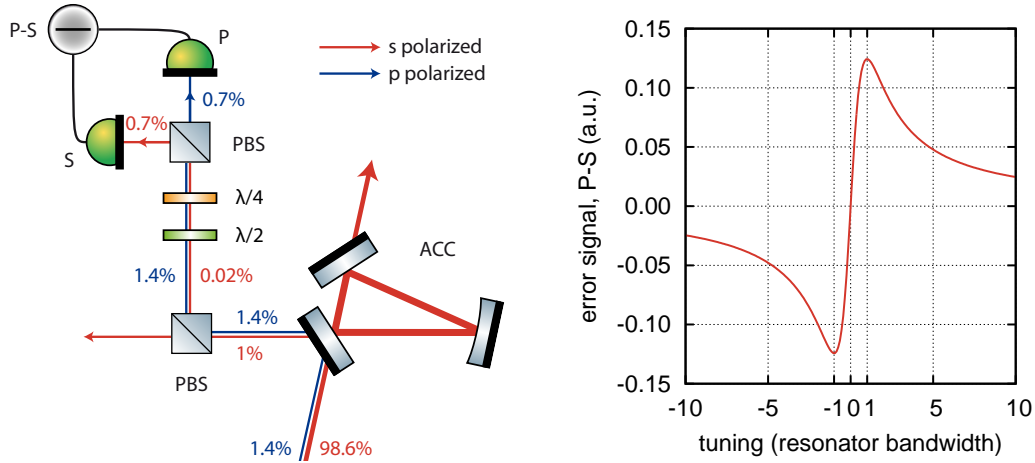


Figure 5.9: Schematic of the experimental setup (left) for generating the Hänsch-Couillaud error signals and simulation of the error signals (right). The different power levels of the two orthogonal polarizations are given for resonant s-polarized fundamental mode. Due to the impedance mismatch, s-polarized light is partly reflected at resonance.

ment inside the resonator is necessary⁷. At each of the three non-normal-incident reflections inside the resonator, the phase of p-polarized light is shifted by 180° compared to the phase of s-polarized light. Thus the resonance frequencies of p- and s-polarized modes are shifted to each other by half an FSR.

A polarizing beam splitter was used in the beam reflected off the ACC to separate the Hänsch-Couillaud error signals from the power fluctuation signals for the optical ac coupling (Fig. 5.9). The extinction ratio of this beam splitter was different for the reflected ($R_p=99.9\%$, $R_s=2\%$) and transmitted beam ($T_p=0.1\%$, $T_s=98\%$). The very pure polarization state in transmission was used for the optical ac coupled detector. Due to the high residual reflection of $R_s=2\%$, the beam reflected consisted of a mixture of p- and s-polarized light, which was used for the error signal generation. Two InGaAs photodiodes and a second polarizing beam splitter were used to generate Hänsch-Couillaud error signals. With two wave plates in front of this polarizing beam splitter, the symmetry and the offset of the error signal was adjusted. A simulated error signal is shown in Fig. 5.9.

10 MHz Bandwidth Power Stabilization

The sensitivity enhancement of the optical ac coupling technique is maximal only for frequencies above the ACC bandwidth (see Sec. 5.1). Since the experiments performed were table-top experiments, only optical resonators with quite high band-

⁷Originally the Hänsch-Couillaud method was applied to linear resonators which need an additional polarizing element inside the resonator.

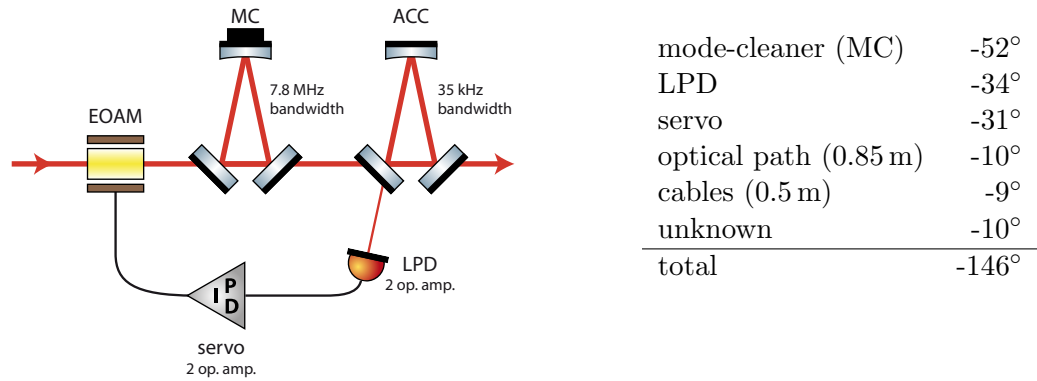


Figure 5.10: Schematic of the power stabilization control loop and phase budget at 10 MHz.

width of about 35 kHz, limited by the resonator size and the finesse, could be used. To reach a high power noise suppression for frequencies above 35 kHz, a control loop with significantly higher bandwidth is necessary.

A unity-gain frequency of about 10 MHz was targeted for the power stabilization experiment. At 10 MHz several effects cause significant phase losses: The signal transmission through a coaxial cable, e.g., cause a phase loss of about $18^\circ/\text{m}$ or an optical signal transmission of $12^\circ/\text{m}$. Furthermore each operational amplifier causes a phase loss. Even though high-bandwidth operational amplifiers were used, a phase loss of about 7° at 10 MHz per operational amplifier was measured.

The total phase loss at 10 MHz was kept below 180° by minimizing the signal transmission lengths and the number of operational amplifiers. The components of the control loop and their contributions to the total phase shift (phase loss) are shown in Fig. 5.10. Besides the phase loss due to time delays, the phase loss caused by poles of the transfer functions of the electronics and the mode-cleaner have to be considered as well. Taking these effects into account, the measured total phase loss was explained except for about 10° . During the experiment the loop gain was optimized by adjusting the actuator coefficient of the EOAM with the wave plates in front. A stable control loop and a unity-gain frequency of about 10 MHz was achieved with a loop gain of more than 20 dB for frequencies below 1 MHz.

5.4 Noise Couplings

Because of the resonator required for the optical ac coupling, additional couplings for technical noise sources arise, not present in traditional power noise detections. The increased quantum-limited sensitivity of an optical ac coupled detector is prone to be degraded by these noise sources. In this section several different coupling mechanisms and noise sources, among others a new resonator-internal scattering noise source, are described.

Mainly the performance of the power stabilization experiment was initially limited since the noise sources were especially large at low frequencies. In contrast, the power sensing experiment at higher frequencies of several megahertz was nearly unaffected by these noise sources. Models for the couplings were developed and were verified in the experiment. In the end, the performance of the power stabilization experiment was significantly improved by systematically minimizing the coupling factors and the noise sources, and the models can be used to better estimate the noise of future experiments.

5.4.1 Residual Frequency Noise

In most experiments, where a laser is coupled into an optical resonator, the laser frequency and the resonance frequency of the resonator are not stable enough, and therefore an active stabilization of at least one frequency is necessary. Fluctuations of the remaining difference between laser frequency and resonance frequency of the ACC couple into power fluctuations. For example, due to offset fluctuations of the electronic parts used for the frequency stabilization, it is almost inevitable that a small frequency offset Δf remains between the two frequencies. The coupling of residual frequency noise to power noise in reflection of the ACC depends on this offset and can be described with the following model.

Consider the complex field amplitude U_{in} of a laser beam that is coupled to the ACC. Residual frequency noise can be represented as a phase modulation at a Fourier frequency $f = \omega/2\pi$ with a modulation index $m \ll 1$:

$$U_{\text{in}} = U_0 \cdot \exp(i\Omega t + im \cos(\omega t)) \approx U_0 \cdot \left(1 + i\frac{m}{2}e^{i\omega t} + i\frac{m}{2}e^{-i\omega t}\right) \cdot e^{i\Omega t}, \quad (5.31)$$

where Ω is the optical angular frequency. This beam has a frequency modulation of $imfe^{i\omega t}$ in first order. The field inside the resonator U_{circ} is given by

$$U_{\text{circ}} \propto U_0 \left(h(\Delta f) + i\frac{m}{2}e^{i\omega t}h(f + \Delta f) + i\frac{m}{2}e^{-i\omega t}h(-f + \Delta f) \right). \quad (5.32)$$

Assuming a small offset $\Delta f \ll f_0$ and using the approximations

$$h(\Delta f) = \frac{1}{1 + i\Delta f/f_0} \approx 1 - \frac{i\Delta f}{f_0} \quad \text{and} \quad (5.33)$$

$$h(f + \Delta f) \approx h(f) - h^2(f) \cdot \frac{i\Delta f}{f_0}, \quad (5.34)$$

the field in reflection of the high-finesse resonator is given by:

$$\begin{aligned} U_{\text{refl}} = & U_0 \left[1 - (1-a) \left(1 - \frac{i\Delta f}{f_0} \right) + ime^{i\omega t} \left(1 - (1-a) \left[h(f) - h^2(f) \frac{i\Delta f}{f_0} \right] \right) \right. \\ & \left. + ime^{-i\omega t} \left(1 - (1-a) \left[h(-f) - h^2(-f) \frac{i\Delta f}{f_0} \right] \right) \right]. \quad (5.35) \end{aligned}$$

The transfer function $N_F(f)$ from frequency modulation to relative power modulation in reflection of the resonator can be calculated:

$$N_F(f) = \frac{2\Delta f}{a^2 \cdot f_0^2} h(f), \quad [N_F(f)] = \frac{1}{\text{Hz}}. \quad (5.36)$$

The coupling between residual frequency noise and power noise depends on the frequency offset Δf and the impedance matching a . For example, an ACC with a bandwidth of $f_0 = 10$ kHz, an impedance matching of $a=0.1$, and a frequency offset of $\Delta f = 10$ Hz with a residual frequency noise level of $10 \text{ mHz Hz}^{-1/2}$ would cause a technical relative power noise in reflection of the ACC of $2 \times 10^{-8} \text{ Hz}^{-1/2}$ for frequencies $f < f_0$.

In the experiment the noise contribution can be reduced on the one hand by lowering the coupling factor N_F via the frequency offset Δf , and on the other hand by reducing the residual frequency noise with a high-bandwidth stabilization.

If the optical ac coupled detector is part of a power stabilization following scheme D or E (see Sec. 5.2), the effect of the control loop has to be taken into account as well, to estimate the power noise measured by the independent out-of-loop detector. A similar calculation as used for N_F yields the transfer functions $N_{F,\text{ool,d}}$ and $N_{F,\text{ool,e}}$ from frequency fluctuations to relative power fluctuations of the out-of-loop beams $A_{\text{ool,d}}$ and $A_{\text{ool,e}}$:

$$N_{F,\text{ool,d}}(f) = \frac{N_F(f)}{G(f)}, \quad N_{F,\text{ool,e}}(f) = \left(\frac{1}{a^2 \cdot G(f)} - 1 \right) \cdot \frac{2\Delta f}{f_0^2} h^2(f). \quad (5.37)$$

At first, the power stabilization experiment performed was limited by residual frequency noise (for an impression, see Fig. 5.23, in Sec. 5.5). Therefore the bandwidth of the frequency stabilization loop was increased to about 1 MHz and the frequency offset Δf was electronically compensated prior to each measurement. As a result, an in-loop measurement indicates that the residual frequency noise between the laser frequency and the resonance frequency of the ACC was between $\approx 0.3 \text{ mHz Hz}^{-1/2}$ and $\approx 10 \text{ mHz Hz}^{-1/2}$ for Fourier frequencies between 300 Hz and 100 kHz. A frequency offset of below 20 Hz can be deduced from the final power stability achieved.

5.4.2 Mode Fluctuations

Another coupling is caused by mode fluctuations. In this regard, modes can be defined by the polarization state, the different laser frequencies (carrier, sideband frequency) or the spatial intensity distribution of the beam. Even with a constant total power of the incoming beam, a power exchange between resonant and non-resonant modes causes power fluctuations in reflection of the resonator. Such mode fluctuations are produced by, e.g., beam pointing fluctuations, polarization fluctuations, or amplitude fluctuations of modulation sidebands. The following model is used to describe the noise coupling of mode fluctuations.

Consider the following complex field amplitude U_{in} that is coupled to the ACC. The amplitude of resonant modes can be described by U_0 and of non-resonant modes by U_1 such that:

$$U_{\text{in}} = U_0 \cdot \left(1 - \frac{|U_1|^2}{|U_0|^2} m e^{i\omega t}\right) + U_1 \cdot (1 + m e^{i\omega t}). \quad (5.38)$$

Power is exchanged between the two modes with a modulation index m at an angular frequency ω , whereas for small m the total power of the beam $\propto |U_{\text{in}}|^2$ stays almost constant assuming U_0 and U_1 are orthogonal. The relative power modulation of the non-resonant modes is $2me^{i\omega t}$ in first order. The input field U_{in} excites the following resonator-internal field:

$$U_{\text{circ}} \propto U_0 \left(1 - h(f) \cdot \frac{|U_1|^2}{|U_0|^2} m e^{i\omega t}\right). \quad (5.39)$$

For a resonator with high finesse the field in reflection is

$$U_{\text{refl}} = aU_0 + U_1 + m e^{i\omega t} \left[U_1 - [1 - (1 - a)h(f)] \frac{|U_1|^2}{|U_0|^2} U_0 \right]. \quad (5.40)$$

Thus the transfer function from relative power fluctuations of the non-resonant modes to relative power fluctuations in reflection of the resonator is, for $a \ll 1$, in first order given by

$$N_M(f) \approx \frac{|U_1|^2}{a^2|U_0|^2 + |U_1|^2}, \quad [N_M(f)] = 1. \quad (5.41)$$

This transfer function is independent of the modulation frequency f and depends on the impedance matching a and the power ratio between resonant and non-resonant modes.

This transfer function was verified in an experiment: The EOAM was used to generate strong amplitude modulation sidebands at 5 MHz, far above the ACC bandwidth, and the transfer function from a further amplitude modulation of these sidebands to the power in reflection on detector LPD was measured.

In case the optical ac coupling is used in a power stabilization following scheme D or E (see Sec. 5.2), the transfer function from relative power fluctuations of the non-resonant modes to relative power fluctuations of the out-of-loop beams $A_{\text{ool,d}}$ and $A_{\text{ool,e}}$ can be derived in a similar way:

$$N_{M,\text{ool,d}}(f) = \frac{N_M(f)}{G(f)}, \quad N_{M,\text{ool,e}}(f) = \left[\frac{N_M(f)}{G(f)} - \frac{|U_1|^2}{|U_0|^2} \right] \cdot h(f). \quad (5.42)$$

In general this kind of noise coupling was reduced in the experiment by transmitting the beam upstream of the ACC through a mode-cleaner. The mode-cleaner reduced the non-resonant modes U_1 in the input beam for the ACC. Because of a very

good mode matching between mode-cleaner and ACC, the power in non-resonant modes was very small. Hence the experiments performed were not limited by power exchange fluctuations between injected resonant and non-resonant modes.

5.4.3 Resonator-internal Scattering

Resonator-internal scattering can excite higher-order transverse modes [Kla05] or the countercirculating fundamental mode in a ring resonator. This is an additional loss mechanism for the fundamental mode and thereby the impedance matching and the power in reflection of the resonator are changed. A fluctuation of the scattering strength then causes power fluctuations in the optical ac coupling scheme.

Several different experiments were performed in this thesis and showed that the scattering strength is time dependent and introduces noise in addition to the static finesse reduction studied in [Kla05]. A model was developed and verified to explain the effects observed. Afterwards the noise couplings in the experiment could be reduced step by step, leading to the final stability in the power stabilization experiment.

Model

In order to explain the effects caused by resonator-internal scattering, a model with multiple modes is necessary and a numerical time-domain model was chosen. Consider an ACC resonator with d eigenmodes. The field amplitude coupled into the resonator at time t is described by the vector $\vec{u}_0(t)$, where the d complex components of the vector represent the complex field amplitudes of the modes. The vector $\vec{u}_n(t)$ is the remaining part of the injected amplitude $\vec{u}_0(t - n \cdot \Delta t)$ after n round-trips in the resonator, where Δt is the round-trip time ($\Delta t = L/c$ with L the round-trip length of the resonator). The total circulating amplitude inside the resonator is thus given by:

$$\vec{U}_{\text{circ}}(t) = \sum_{n=0}^{\infty} \vec{u}_n(t). \quad (5.43)$$

During one round-trip in the resonator the phase of the fields $\vec{u}_0(t)$ is shifted due to the optical path length and the round-trip Gouy phase of the resonator, and furthermore the amplitude is reduced due to transmission and absorption losses at the mirrors and potential resonator-internal apertures. One round-trip in the resonator is described by the propagation matrix $\mathcal{P}(t)$:

$$\mathcal{P}(t) = \begin{pmatrix} r_1(t) \cdot e^{i\phi_1(t)} & & \\ & \ddots & \\ & & r_d(t) \cdot e^{i\phi_d(t)} \end{pmatrix}, \quad (5.44)$$

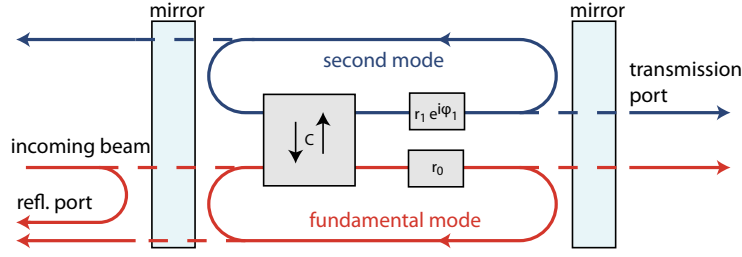


Figure 5.11: Resonator model ($d=2$) used to simulate the complex field amplitudes inside and outside the resonator. To simplify matters, only two possible modes and a coupling between them are considered.

where the $r_k(t)$ describe the reduction of the amplitudes and $\phi_k(t)$ are the phase shifts per round-trip. Scattering causes a coupling between the modes, described by the matrix $\mathcal{S}(t)$:

$$\mathcal{S}(t) = \begin{pmatrix} \tau_{11}(t) & \cdots & \rho_{d1}(t) \\ \vdots & \ddots & \\ \rho_{1d}(t) & & \tau_{dd}(t) \end{pmatrix}, \quad (5.45)$$

where ρ_{lm} describes the coupling between mode l and m , and τ_{kk} is the amplitude fraction not scattered and remaining in mode k . Because of energy conservation, the matrix is unitary ($\mathcal{S}^\dagger \mathcal{S} = I$), and $|\mathcal{S}^T| = |\mathcal{S}|$ due to reciprocal scattering [Sie86, Chap. 11.1].

Using these two matrices, one round-trip in the resonator can be described and the amplitudes $\vec{u}_n(t)$ can be computed recursively:

$$\begin{aligned} \vec{u}_n(t) &= \mathcal{S}(t - \Delta t) \mathcal{P}(t - \Delta t) \vec{u}_{n-1}(t - \Delta t) \\ &= \prod_{k=1}^n [\mathcal{S}(t - k\Delta t) \mathcal{P}(t - k\Delta t)] \cdot \vec{u}_0(t - n\Delta t). \end{aligned} \quad (5.46)$$

Now the resonator-internal field \vec{U}_{circ} can be numerically calculated in the time-domain and with it the field in reflection \vec{U}_{refl} and transmission \vec{U}_{trans} of the resonator.

The effects observed in the experiments were adequately explained with a simple two-mode model $d=2$ (Fig. 5.11). One mode is the fundamental mode of the resonator and the second mode is either a higher-order transverse mode or the counter-circulating fundamental mode in the ring resonator used as ACC. The matrices are simplified [Pas06]

$$\mathcal{P}(t) = \begin{pmatrix} r_0(t)e^{i\phi_0(t)} & 0 \\ 0 & r_1(t)e^{i\phi_1(t)} \end{pmatrix}, \quad (5.47)$$

$$\mathcal{S}(t) = \begin{pmatrix} \sqrt{1-C(t)^2} & iC(t) \\ iC(t) & \sqrt{1-C(t)^2} \end{pmatrix}, \quad (5.48)$$

where r_0 and ϕ_0 describe the propagation of the fundamental mode and r_1 and ϕ_1 the propagation of the second mode. Due to the boundary conditions for \mathcal{S} , this matrix depends in the case $d=2$ on only one parameter C . A power fraction C^2 is exchanged per round-trip between the two modes.

The effects of resonant scattering to higher-order spatial modes and to the countercirculating fundamental mode can be simulated. The model parameters for the two cases were determined as follows: In case of higher-order spatial modes, r_0 and r_1 can be determined from the round-trip losses inside the resonator, i.e. from the mirror transmissions and absorptions. A resonator-internal aperture causing mainly higher losses for the higher-order spatial mode can be simulated by reducing r_1 . At the normal operating point of the optical ac coupling, the fundamental mode is resonant, i.e. $\phi_0(t)=0$. The phase ϕ_1 of the higher-order mode then depends only on the round-trip Gouy phase ζ and the TEM mode order l, m . The Gouy phase in turn depends on the radius of curvature R and the round-trip length L of the resonator, assuming the resonator geometry of the ACC already described:

$$\phi_1(\zeta) = \zeta(R, L) \cdot (l + m) + \pi \cdot l, \quad \zeta(R, L) = 2 \cdot \arctan \left(1/\sqrt{2R/L - 1} \right). \quad (5.49)$$

Small absorptions of the high-power fundamental mode at the mirror coatings cause a thermal mirror deformation. These deformations can be interpreted in first order as change in radius of curvature [Ueh97]. Thus R depends on the average power P_{avg} in the fundamental mode, due to the thermal lowpass. This dependence was linearized in the model:

$$R(P_{\text{avg}}) = R_0 + R_P \cdot P_{\text{avg}}. \quad (5.50)$$

The remaining undefined parameters R_0 , R_P , and C were determined by fitting the model to the measurements described later on in this section. Afterwards this model was used to calculate the reflected power as function of the input power for different, varied resonator parameters (impedance matching, finesse, aperture size, scattering strength) and the influence of fluctuating parameters ϕ_1 and C on the reflected power noise, as described in more detail later on.

In the second case, with countercirculating fundamental mode, $r_0=r_1$ and both parameters are determined from the transmission and absorption of the mirrors. At the normal operating point the fundamental mode is resonant, i.e. $\phi_0=0$, and since the countercirculating mode has the same resonance frequency, $\phi_1=0$ as well. The coupling factor C was determined from measurements in the experiment, as described later on in this section. Using this model, the countercirculating power as function of C and the transfer function from fluctuations of C to fluctuations of various transmitted and reflected beams were calculated, as described later on in this subsection.

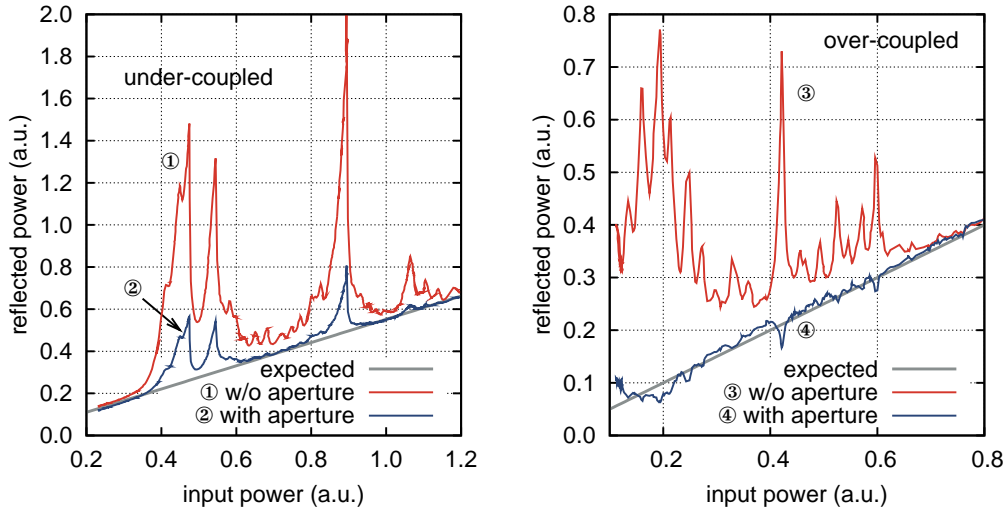


Figure 5.12: Excitation of higher-order transverse modes by resonator-internal scattering for an under-coupled (left) and an over-coupled (right) ACC. The power in reflection was measured with and without aperture as function of the input power. The power expected in reflection without scattering is shown for reference.

Higher-order Spatial Modes

In the power stabilization experiment the excitation of higher-order transverse modes was first observed with an ACC without internal aperture. The power on detector LPD was measured as a function of the input power of the ACC while the resonator was locked (Fig. 5.12). The power on LPD should increase linearly with the input power. However, dependent on the circulating power, the curvature of the resonator mirrors was slightly changed due to absorption of the Gaussian beam, as already mentioned. Thus the round-trip Gouy phase was changed and the resonance frequencies of the higher-order transverse modes were shifted in relation to the fundamental mode. Therefore many different higher-order transverse modes became resonant, indicated by a sudden power increase on detector LPD when the input power was raised. The field of the higher-order mode leaking out of the resonator into the reflection port cannot destructively interfere with the fundamental mode and hence the power on LPD is increased.

In addition to this, the impedance matching changed due to a resonant higher-order mode. The coupling between the resonant higher-order mode and the fundamental mode is an additional power loss for the fundamental mode. The measurement was once performed with an under-coupled (Fig. 5.12, left) and once with an over-coupled ACC (Fig. 5.12, right). In order to measure approximately the fundamental power in reflection in conjunction with the total reflected power on

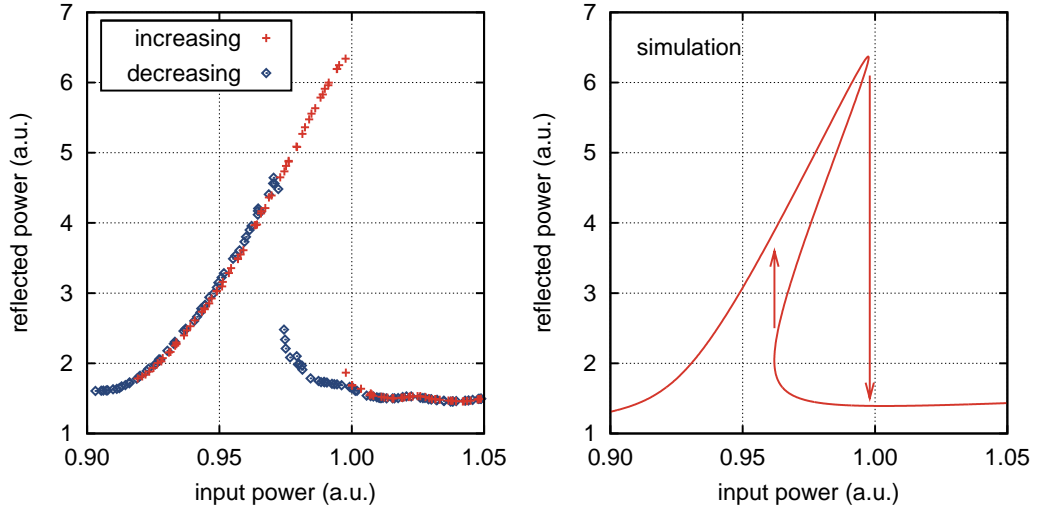


Figure 5.13: Bistability at the resonance of a strong higher-order transverse mode excited by resonator-internal scattered light, measured at increasing and decreasing input power (left) and simulated (right).

detector LPD, the photodetector TPD_1 placed behind a small aperture ($\approx 0.75w_0$) was used. The measurement clearly shows that the additional losses for the fundamental mode due to the higher-order spatial modes worsen the impedance matching in the under-coupled case and the power of the fundamental mode in reflection is increased (Fig. 5.12, ②). In the over-coupled case, the additional losses improve the impedance matching and the power of the fundamental mode decreases in reflection (Fig. 5.12, ④).

With a CCD (charge-coupled device) camera, the spatial power distribution of the beam in reflection of the ACC was analyzed. Some of the higher-order modes were identified at specific input power levels by this measurement (e.g. $\text{TEM}_{1,9}$, $\text{TEM}_{7,3}$, $\text{TEM}_{9,1}$, or $\text{TEM}_{20,0}$), which had, as calculated, resonance frequencies close to the fundamental mode.

The coupling between higher-order transverse modes and the fundamental mode as well as the power increase on detector LPD was calculated using the two-mode model. The different effects for under- and over-coupled resonators on the reflected power of the fundamental mode was verified with the model. The power in higher-order transverse modes depended quadratically on the finesse of the ACC under constant power scattering in the model. This means that this effect becomes increasingly significant for high finesse resonators.

A detailed analysis of the reflected power measurement (Fig. 5.12) revealed that the peaks were asymmetric and even bistable for some strong higher-order modes (Fig. 5.13, left). This asymmetry is caused by two effects influencing the resonator-internal fundamental power. The resonance of the higher-order mode depends on

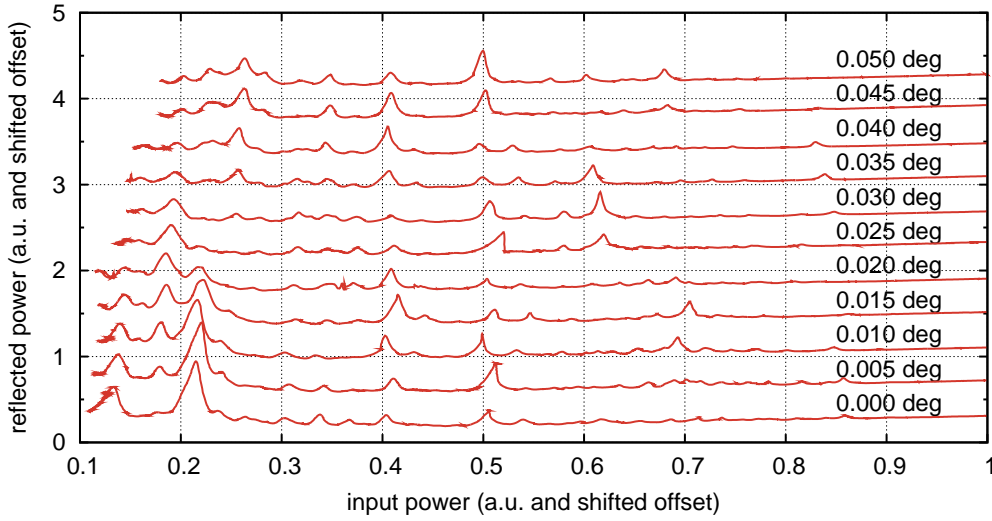


Figure 5.14: Excitation of higher-order transverse modes by resonator-internal scattering at different tilt angles of the curved mirror of the ACC.

the Gouy phase, which in turn depends on the average fundamental mode power. By increasing the input power, the fundamental mode power is in general increased as well, but as soon as a higher-order mode gets resonant, power from the fundamental mode is transferred to the higher-order mode reducing the fundamental power. This effect was qualitatively verified with the model (Fig. 5.13, right).

A transfer function from a modulation of the input power to the power in reflection of the ACC was measured with partly resonant higher-order mode (in Fig. 5.13 at an input power of about 0.95). The expected thermal lowpass was verified and a corner-frequency of about 100 Hz was measured.

The scattering and the mode structure in Fig. 5.12 changed significantly as soon as the curved mirror of the resonator was tilted in steps of only 0.005° – the smallest controlled steps that could be performed in the experiment (Fig. 5.14). Such a tilt would cause the fundamental mode to move only $\approx 20\ \mu\text{m}$ on the curved mirror surface. Thus the scattering strength C^2 seems to depend very sensitively on the beam position on the resonator mirrors.

The round trip Gouy phase of the ACC was designed in such way that only the resonance frequencies of transverse modes with high mode order were close to the resonance frequencies of the fundamental mode. After the installation of a resonator-internal aperture, the losses for these higher-order modes have been increased without introducing significant losses for the fundamental mode. Thereby the excitation of higher-order transverse modes by scattered light was reduced (Fig. 5.15). Simulations, in which the factor r_1 (Eq. 5.47) was reduced to account for the aperture, verified these results.

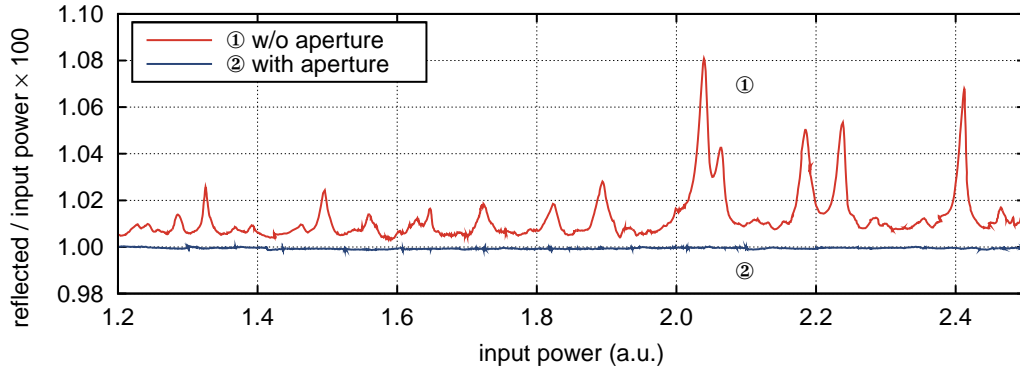


Figure 5.15: Suppression of higher-order transverse modes by a resonator-internal aperture. The power in reflection was measured with and without aperture as function of the input power.

The higher-order modes excited by resonator-internal scattering disturb the optical ac coupling technique, since they influence important parameters, such as the impedance matching, and they cause a higher parasitic power in reflection of the resonator reducing the maximal gain g (see Sec. 5.1). However, the biggest problem, revealed in further experiments, is that the coupling C seems to fluctuate, as described in the following.

Scattering Strength Fluctuations

Non-stationary scattering between the fundamental mode and higher-order transverse modes caused power fluctuations at the in-loop detector LPD in the power stabilization experiment. A typical power stability measured out-of-loop that was limited by scattering is shown in Fig. 5.16, ①. For frequencies below about 4 kHz the scattering caused a relative power noise of about $10^{-6} \text{ Hz}^{-1/2}$ that rolls off towards higher frequencies due to the optical ac coupling transfer function.

In one experiment the free-running power noise on LPD was measured as function of the input power: The input power was slowly varied with the EOAM, while the time signal of the LPD detector was recorded with an A/D converter card in a computer. Afterwards the signal recorded was split into small segments. For each segment, the average power and the relative power noise at 3.5 kHz of detector LPD was determined. The power noise increased significantly as soon as a higher-order transverse mode became resonant (Fig. 5.17, left) and the power noise was higher when more power was circulating in the higher-order mode. This pointed to the fact that the scattering strength between fundamental mode and higher-order mode was fluctuating. A hypothesis, namely, that the Gouy phase was fluctuating, was ruled out with this measurement since in such a case the power noise had to be maximal at input powers corresponding to the steep slopes (Fig. 5.17, ①, at input power of about 0.95) which was not the case.

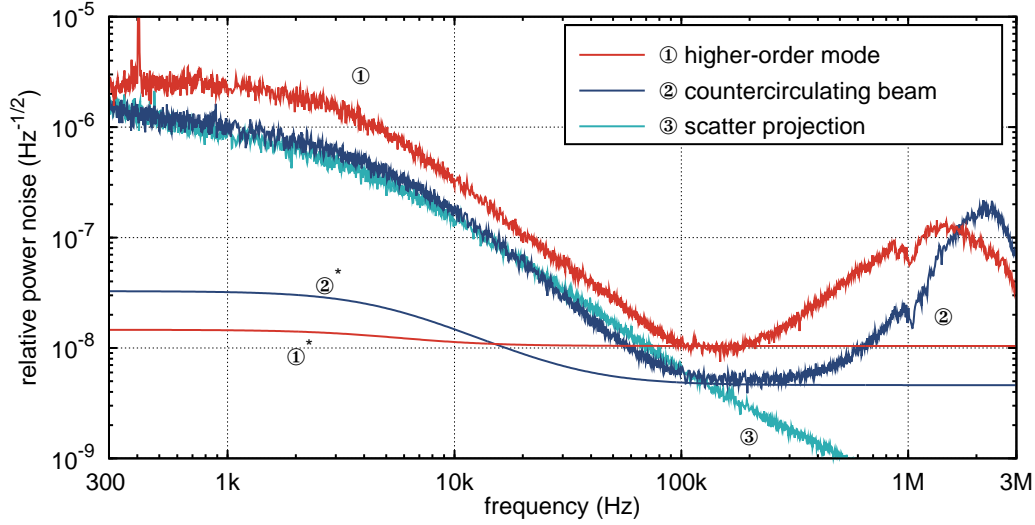


Figure 5.16: Typical out-of-loop power noise measurements performed with the HPD detector. Scattering to higher-order modes ① or into the countercirculating fundamental mode ② limited the power stability. The expected limits without any scattering are shown as smooth solid lines (①*, ②*). For the case of scattering to the countercirculating fundamental mode, a projection of the power noise due to scattering is shown ③.

The model was used to verify the power noise dependence on the input power. Two simulations were performed, once assuming that the scattering strength C was fluctuating and once that the Gouy phase or ϕ_1 was fluctuating (Fig. 5.17, right). The simulations showed a significant difference between the power noise in reflection of the ACC, depending on which parameter is actually fluctuating (Fig. 5.17, ④ and ⑤). The measurement agrees qualitatively very well with the simulation assuming a fluctuating C (Fig. 5.17, ② and ④). However, the origin of these fluctuations is unknown.

Independent of any optical ac coupling or power stabilization experiments, scattering to resonant higher-order modes can degrade the passive filtering effect of an optical resonator (see Sec. 3.1.2). In the experiment a free-running relative power noise of the laser of about $2 \times 10^{-7} \text{ Hz}^{-1/2}$ was measured, which increased to about $1 \times 10^{-6} \text{ Hz}^{-1/2}$ up to frequencies of several kilohertz in the transmitted beam of the ACC due to scattering to a higher-order transverse mode (Fig. 5.18). No power stabilization or optical ac coupling was used in this measurement. Thus fluctuating resonator-internal scattering could be of relevance to many experiments using optical resonators.

As already mentioned, a resonator-internal aperture effectively prevented a resonant coupling between fundamental mode and higher-order spatial mode. Thus no resonant higher-order mode is available to which power could be transferred in a

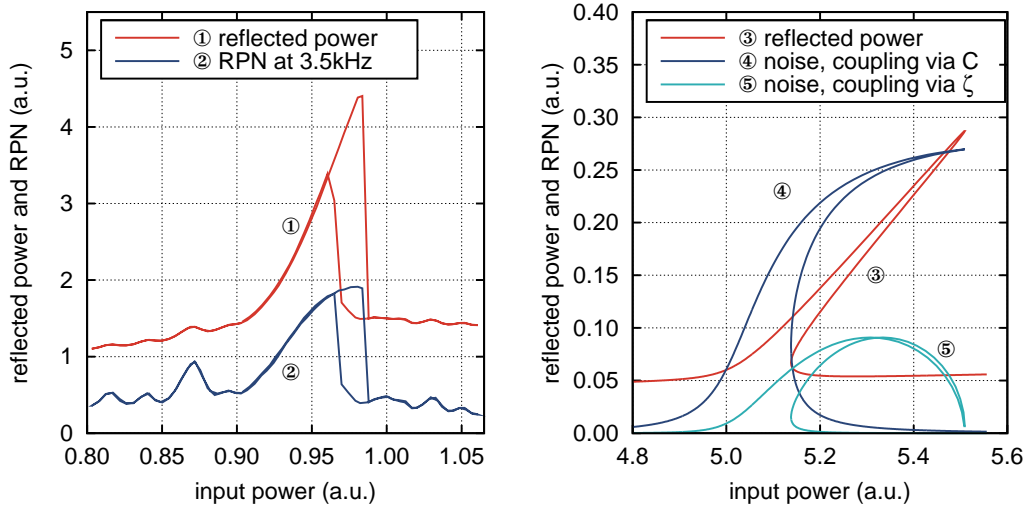


Figure 5.17: Power noise at the detector LPD as function of the input power, measured (left) and simulated (right). The average power reflected and the relative power noise at 3.5 kHz was measured, once for increasing and once for decreasing input power. The simulation shows the expected power noise assuming a fluctuating scatter strength C or a fluctuating Gouy phase ζ .

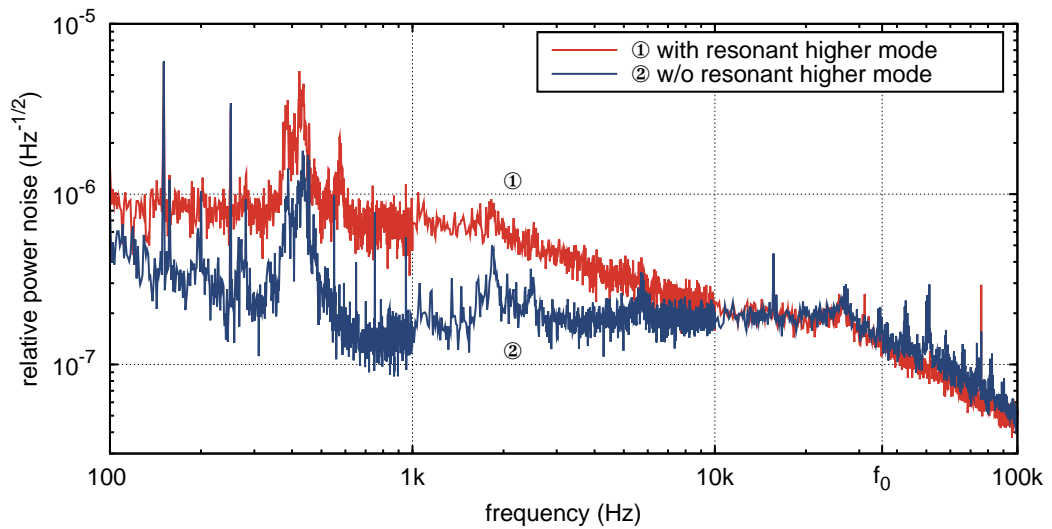


Figure 5.18: Free-running power noise in transmission of the ACC with and without resonant higher-order transverse mode excited by resonator-internal scattering.

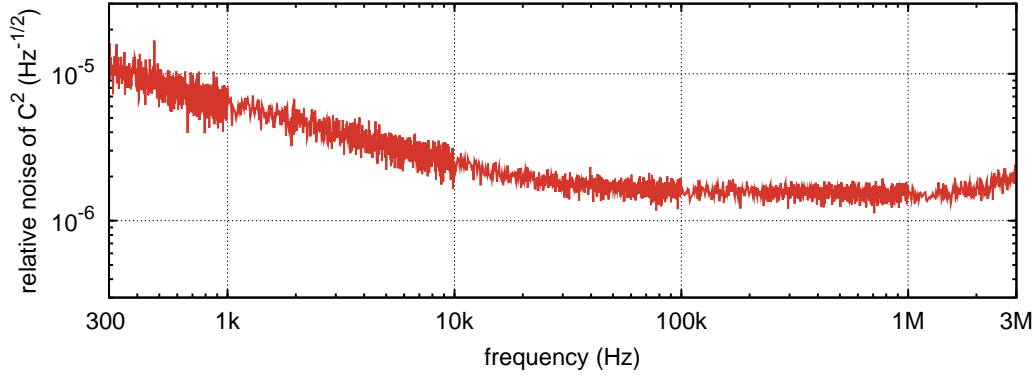


Figure 5.19: Relative scattering strength noise projected from a power noise measurement at detector TPD_3 . The average scattering strength was between $C^2 = 10^{-11}$ to 10^{-10} .

fluctuating way. This noise coupling was completely suppressed in the experiments by using the aperture. However, the scattering still excited the countercirculating fundamental mode in the ring resonator, as described in the following.

Countercirculating Fundamental Mode

The aperture could not avoid an excitation of the countercirculating fundamental mode by scattered light. This was observed with a similar ACC that had a resonator-internal aperture but showed a strong scattering into the countercirculating fundamental mode (100 to 400 μW hitting photodetector TPD_3 at 680 mW input power). The cause for the increased scattering of this specific ACC is unknown but might be connected to an outgassing of the epoxy resin used or the o-rings for the vessel. The scattering occurred presumably at the curved mirror of the resonator since the incidence angle was 3° , much smaller than for the other two mirrors with 44° and the bidirectional reflectance distribution function (BRDF) normally decreases with increasing scattering angle [Kla07]. To fit the power levels of the countercirculating mode and the input power to the model, a coupling factor of $C^2 = 10^{-11}$ to 10^{-10} has to be assumed.

The scattering fluctuations caused power fluctuations on the detector LPD in the same way as described before in the case of higher-order spatial modes (Fig. 5.16, ②). The power fluctuations of the countercirculating mode have been measured with photodetector TPD_3 . The relative power noise was about $1 \times 10^{-5} \text{ Hz}^{-1/2}$ for frequencies below the ACC bandwidth. The two-mode model was used to numerically calculate the transfer function from power fluctuations on detector TPD_3 to power fluctuations on detector HPD with a fluctuating coupling factor C . The power noise on the out-of-loop detector caused by scattering was estimated by a projection of the measured noise on TPD_3 , using this transfer function (Fig. 5.16, ③). The absolute level of the transfer function was adjusted to match the measurement

since the detectors TPD₃ and LPD were not calibrated for absolute power fluctuations. Furthermore, the transfer function from power noise on detector TPD₃ to the detector HPD was measured and agreed with the simulation results. In addition, the power noise at TPD₃ was projected to the relative noise of C^2 using the simulated transfer functions (Fig. 5.19).

These results represent further evidence for the fluctuating scattering effect. Still the cause of the coupling factor fluctuations could not be determined. The linear spectral density of C^2 slowly decreases towards higher frequencies and levels off at a relative noise of about $2 \times 10^{-6} \text{ Hz}^{-1/2}$ (Fig. 5.19). No obvious mechanical resonances are present in the spectrum and thus a mechanical excitation of the fluctuations seems unlikely. Here more detailed investigations are necessary.

Only by building a new ACC using glues and vessel o-rings having low outgassing, was the scattering to the countercirculating mode reduced and the noise coupling was suppressed. This ACC showed almost no excitation of the countercirculating fundamental mode ($<15 \mu\text{W}$ hitting photodetector TPD₃ at 680 mW input power, $C^2 < 2 \times 10^{-12}$).

Summary and Discussion

In first experiments, resonator-internal scattering to higher-order spatial modes and the countercirculating fundamental mode limited the sensitivity of the optical ac coupled in-loop detector in the power stabilization experiment. Only scattering to *resonant* modes caused an effective coupling to the fundamental mode used for the optical ac coupling. Fluctuations of the coupling factor then caused power fluctuations of the resonator-internal fundamental mode field.

The influence of scattering to higher-order modes can be effectively suppressed by resonator-internal apertures, which also suppresses noise caused by a fluctuating coupling factor. However, by this means the resonant coupling to the countercirculating mode could not be prevented and only a resonator with less scattering improved the out-of-loop power stability in the experiment. In the future, scattering to the countercirculating fundamental mode can probably be reduced with a resonator geometry with larger incidence angles of the mirrors or can be avoided completely by using a linear resonator. According to the model, the effects of the resonator-internal scattering can be reduced by lowering the finesse of the resonator. The noise source was traced back to a fluctuating scattering strength C , using several experiments and the model developed, whereas the fluctuating nature of the scattering remains unexplained.

Furthermore, experiments showed that scattering can degrade the passive filtering effect of an optical resonator for power noise. Resonant scattering caused power fluctuations of the fundamental mode, such that a relative power noise of about $1 \times 10^{-6} \text{ Hz}^{-1/2}$ was observed in the transmitted beam. This effect could be of relevance to many precision experiments using optical resonators.

The effects connected to the resonator-internal scattering were very well described by a numerical time-domain model, which yielded important results about the

coupling mechanism of the noise source. The model was verified in the experiments and can be used in future experiments to better estimate the coupling of scattering in optical ac coupling schemes.

5.5 Results

Two main experiments with optical ac coupled photodetectors were performed and demonstrated the high sensitivity of this detection technique for power fluctuations in two frequency bands. Furthermore, the compatibility of this detection technique with an active power stabilization was shown. In the following the results of the two experiments are described and discussed.

Power Sensing Experiment

This experiment demonstrated the high sensitivity of an optical ac coupled photodetector at frequencies of several megahertz. First of all, the transfer function $G(f)$ was measured (Fig. 5.20) and was compared to the model (see Sec. 5.1, Eq. 5.4). The transfer function agreed very well with the model using the parameters $f_0 = 34.4 \pm 0.3$ kHz and $|g| = 15.3 \pm 0.3$. As predicted, the transfer function for the under-coupled and over-coupled case differed only in their phases. A carrier reduction to 0.39% of the original power was measured that would yield a $|g| = 15.9$. The small discrepancy between this value and the measured one can be explained by a fraction of 0.035% power in parasitic modes. This power was estimated to be $\geq 0.02\%$, using the modescan technique (see Sec. 2.2.1) and detector TPD₂.

Afterwards, the optical ac coupled power noise of the laser was measured with detector LPD. To verify the measurement, the RPN was measured in a traditional setup with detector HPD once again. The measurement of the RPN (Fig. 5.21, ③) agreed within the measurement and calibration accuracy (≈ 1 dB) up to ≈ 4 MHz with the traditional measurement (Fig. 5.21, ②). At higher frequencies, the traditional measurement was limited by quantum noise (2.5×10^{-9} Hz^{-1/2}, 50 mA photocurrent).

The frequency of the laser relaxation oscillation (989 kHz) and the quality factor ($q=16$) of the resonance were determined from measurement data below 2 MHz in order to predict the RPN for frequencies ≥ 4 MHz (Fig. 5.21, ④). The measurement using the optical ac coupling agreed with the predicted RPN. From about 10 MHz this measurement was limited by quantum noise. Even though the detector LPD was operated at a photocurrent of only 3 mA a quantum noise limited sensitivity of 7×10^{-10} Hz^{-1/2} was achieved, for which in a traditional setup one would have to detect a photocurrent of 702 mA.

Then the power in front of the mode-cleaner was reduced to about 0.4% and the laser frequency was set off-resonant to the ACC. In this case, the ACC acted like a high-reflectivity mirror and the transfer function was measured as $G(f) \equiv 1$, as expected. At a photocurrent of 3 mA the RPN was then measured with detector LPD. The comparison of the two measurements with detector LPD – once with

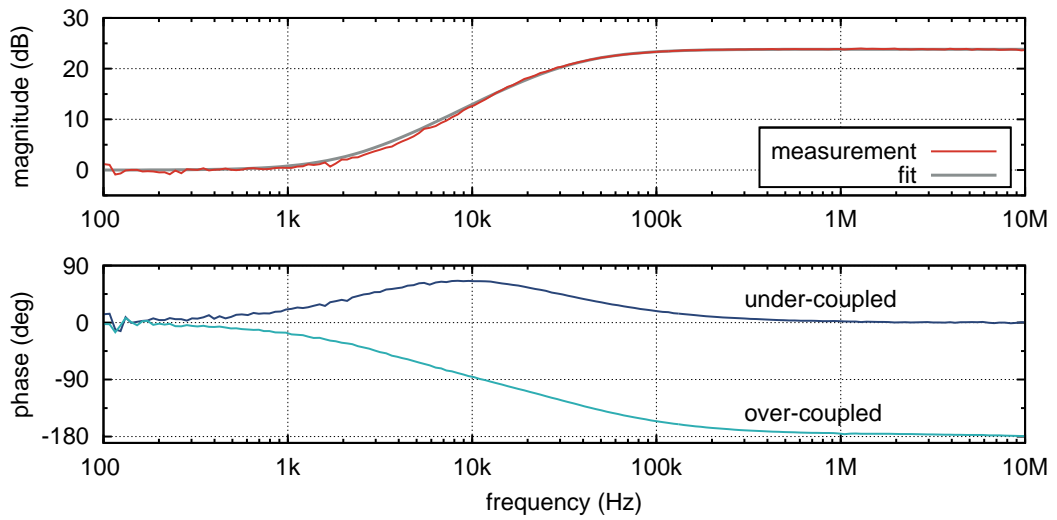


Figure 5.20: Transfer function $G(f)$ of relative power fluctuations from the ACC input beam to the reflected beam, measurement and fitted model. The lower plot shows the phase dependence of the transfer function on the impedance matching of the ACC.

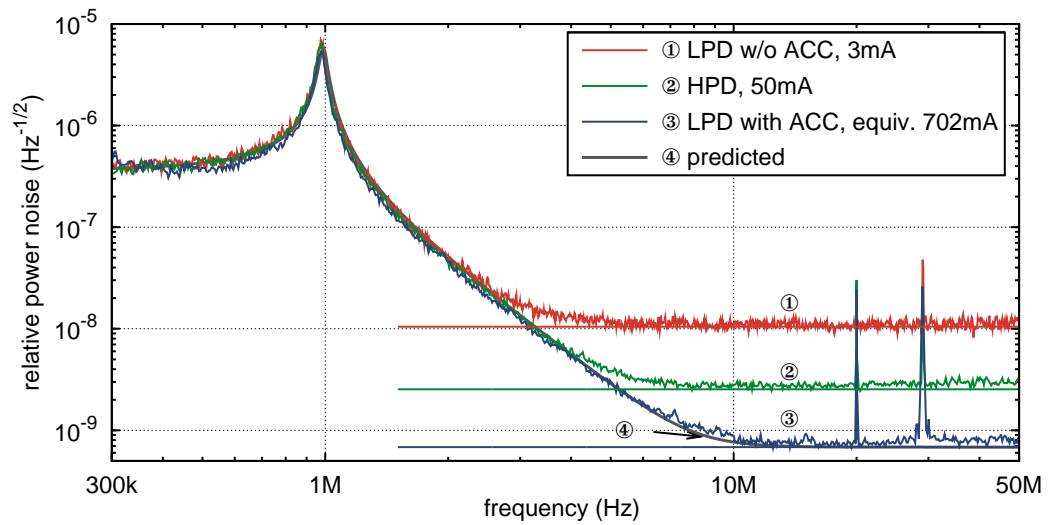


Figure 5.21: Measured power noise of the NPRO. The laser relaxation oscillation at 1 MHz and the steep roll-off towards higher frequencies was measured. The quantum noise limits for the different measurements are shown as horizontal lines. The signals at 20 MHz were injected and those around 29 MHz were due to the modulation for the PDH locking of the mode-cleaner.

locked (Fig. 5.21, ③) and once with unlocked ACC (Fig. 5.21, ④) – clearly showed the gain in sensitivity of this method by $G(f)$.

Furthermore, a power modulation signal was injected with the EOAM at 20 MHz in all three measurements. This calibration signal had the same amplitude in all three measurements (see Fig. 5.21) and thus verified the calibration. The signal at 29 MHz is caused by the modulation for the PDH locking of the mode-cleaner and its amplitude varied between the measurements since it sensitively depends on spurious locking offsets.

Power Stabilization Experiment

This experiment demonstrated on the one hand the high sensitivity of an optical ac coupled detector at lower frequencies near the ACC bandwidth and on the other hand the feasibility of a power stabilization utilizing this novel detection technique. The optical ac coupled detector was used as in-loop detector in an active power stabilization of an NPRO for frequencies between 1 kHz and 1 MHz

As already mentioned, a quasi-monolithic ACC was used. Therefore the transfer function $G(f)$ was measured again. A fit of the model (see Eq. 5.4) to the data yielded $f_0 = 35.7$ kHz and $g=11.2$.

Afterwards the out-of-loop relative power noise was measured with detector HPD in three different conditions (Fig. 5.22): First the free-running power noise of the laser (with Noise Eater activated) was measured. The relative power noise was about $2 \times 10^{-7} \text{ Hz}^{-1/2}$ (Fig. 5.22, ①) which is a typical value for these laser models (see Sec. 2.3.1).

Then the power stabilization control loop was closed (Fig. 5.22, ③). The out-of-loop power noise dropped in the whole measurement frequency band by up to 33 dB. The best power stability was $3.7 \times 10^{-9} \text{ Hz}^{-1/2}$ at frequencies around 200 kHz. The expected limit, given by scheme D (see Sec. 5.2), was composed of the quantum noise of the in-loop detector (LPD, 0.3 mA photocurrent, $3.3 \times 10^{-8} \text{ Hz}^{-1/2}/G(f)$, see Sec. 5.1) and the quantum noise of the out-of-loop detector (HPD, 60 mA photocurrent, $2.3 \times 10^{-9} \text{ Hz}^{-1/2}$). The power stability achieved was very close to this limit. For frequencies between 3 kHz and 20 kHz, the power noise measured was about 3 dB above the expected limit. The source of this excess noise, which is at a level similar to the quantum noise of the in-loop detector, is unknown. For frequencies between 300 Hz and 1 kHz, the power noise was dominated by mechanical resonances of the setup and for frequencies above 500 kHz, the stabilization was loop gain limited.

Finally, the laser frequency was not stabilized to the ACC such that the ACC acted as a normal high-reflectivity mirror. This setup was now equivalent to a traditional power stabilization setup. The power stabilization controller was slightly modified to compensate for the missing amplification g at the unity-gain frequency, and the attenuation in front of the detector LPD was increased. With unchanged power levels on the in- and out-of-loop photodetectors, the power stabilization loop was closed. As expected, the power noise at the out-of-loop detector (Fig. 5.22, ②)

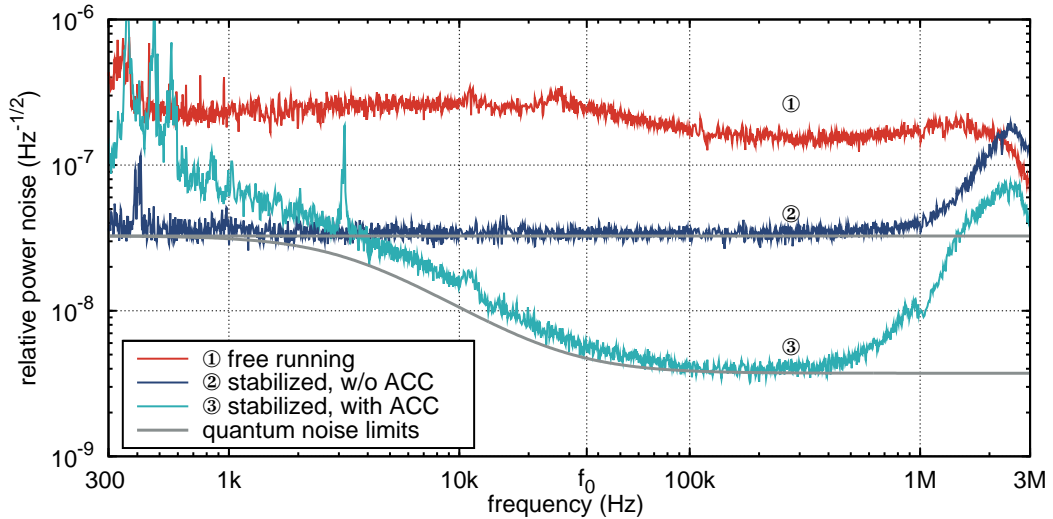


Figure 5.22: Out-of-loop measured power noise using different power stabilization schemes. The results are close to their quantum noise limits. With optical ac coupling the power stability ③ achieved is significantly better than with the equivalent traditional stabilization scheme ②.

was limited at a level of the quantum noise of the in-loop detector (LPD, 0.3 mA photocurrent, $3.3 \times 10^{-8} \text{ Hz}^{-1/2}$) up to frequencies of about 1 MHz (see scheme B in Sec. 5.2).

A comparison of the power stabilization with and without optical ac coupling (Fig. 5.22, ② and ③) clearly shows the experimental proof of the sensitivity improvement of the optical ac coupling technique in the frequency band around and above the ACC corner frequency. For frequencies above 4 kHz the out-of-loop power stability was improved by up to a factor of 9 by using the optical ac coupling scheme. As part of the out-of-loop noise can be attributed to the out-of-loop detector, this stability is consistent with an improved quantum noise limited performance of the stabilization loop by a factor of 11.2.

As already mentioned, several technical noise sources limited the sensitivity of the in-loop detector and different noise couplings were reduced step by step (see Sec. 5.4) to achieve the power stability presented. Fig. 5.23 shows the development of the out-of-loop performance over several months during which the effects of residual frequency noise and the resonator internal scattering were found and eliminated. These measurements give a good impression of the significance of these effects in the different frequency ranges.

Discussion

In the power sensing experiment, a sensitivity of $7 \times 10^{-10} \text{ Hz}^{-1/2}$ was achieved, which is to my knowledge the most sensitive power noise measurement so far and in particular the first measurement below $10^{-9} \text{ Hz}^{-1/2}$. The coupling of technical

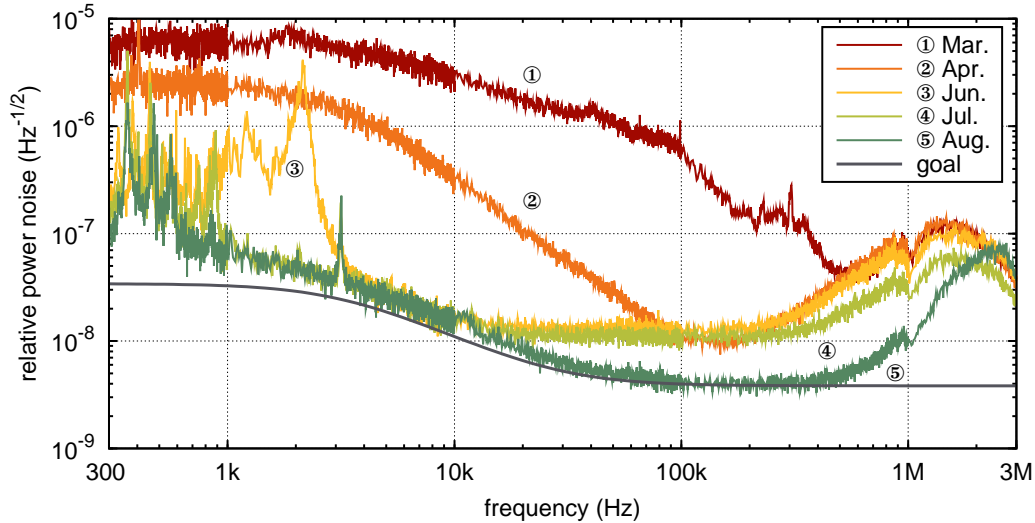


Figure 5.23: Five months’ history of the out-of-loop measured power noise. Measurements were limited by residual frequency noise ①, resonator-internal scattering ① and ②, mechanical resonances of the ACC with mirror mount ③, and out-of-loop detector quantum noise ④.

noise sources was negligible at these frequencies and did not limit the experiment. The maximum gain $|g|$ seemed to be limited only by the controllability of the impedance matching and the power in parasitic modes. Thus in the future, the power in parasitic modes could be reduced with another mode-cleaner in front of the detector LPD, or in principle also with a confocal resonator as ACC that would have fewer non-resonant modes.

With the optical ac coupling it is possible to construct high-speed photodetectors using small photodiodes that are limited by equivalent photocurrents that are more than 100 times larger than in traditional setups. High-speed high-sensitivity photodetectors are, e.g., necessary to detect radio frequency sidebands in optical communication links or for stabilizing optical resonators [Bla01, Dre83] or interferometers. Thus the optical ac coupling could replace complex arrays of photodiodes [Ueh94, Jen02]. Furthermore, only a fraction of the traditionally needed laser power is detected whereby more power remains for subsequent experiments.

An active power stabilization experiment with optical ac coupled in-loop detector was demonstrated for the first time, achieving a quantum noise limited power stability at frequencies above about 20 kHz. Several noise sources (see Sec. 5.4) limited the achieved power stability in first experiments. In particular, resonator-internal scattering was a critical noise source at these frequencies. This effect might be of future relevance to high precision experiments utilizing optical resonators.

Experiments with stringent power-stability requirements can use this technique to improve the power stability by about one order of magnitude⁸. In the future one ap-

⁸Considering current technical limitations.

plication could be the power stabilization for next generation GWDs. These detectors require very high power stabilities at rather low frequencies (see Sec. 3.2). The full stability gain of the optical ac coupling power stabilization scheme is reached only for frequencies above the resonator bandwidth. Though, due to the kilometer long baseline of such detectors, resonators with very low bandwidth will exist such as the power recycling cavity. However, before the optical ac coupling technique can be implemented using the power recycling cavity, several technical problems have to be solved: For example, the impedance matching of the power recycling cavity needs to be adjusted, maybe by using an etalon [Hil09a] as power recycling mirror, or the parasitic power caused by phase modulation control sidebands reflected at the power recycling cavity have to be reduced, maybe by using another mode-cleaner.

5.6 Summary

The optical ac coupling technique significantly improves the quantum limited sensitivity of a photodetector for power fluctuations in front of a resonator, without increasing the laser power on the detector.

The transfer function of the optical ac coupling, the influence of parasitic modes, and the quantum limit of this novel detection technique were described (Sec. 5.1). The average power on the photodetector in reflection of the resonator is much smaller than the power needed for a traditional detection of equal sensitivity. Hence on the one hand high-sensitivity, high-speed detectors with small photodiodes can be built and on the other hand more power for potential downstream experiments is left, which is an advantage especially for active power stabilizations.

The quantum limit of a power stabilization utilizing the optical ac coupling was derived and compared with the limit of other power stabilization schemes (Sec. 5.2). This comparison showed that the scheme with optical ac coupling reaches the best performance for frequencies above the resonator bandwidth, considering the theoretical quantum limit (Sec. 5.2.1) as well as the power stability achieved with certain technical constraints (Sec. 5.2.2). Compared to a traditional power stabilization scheme, commonly used, an up to 6 dB better quantum limit for the residual relative power noise can be achieved and a limit very close to the fundamental quantum limit of the original beam can be reached. Associated with this better limit is the higher available out-of-loop beam power of nearly 100%, compared to 50% in the traditional scheme.

Besides these theoretical aspects, the technique was demonstrated experimentally. The, to my knowledge, best sensitivity for power fluctuations, $7 \times 10^{-10} \text{ Hz}^{-1/2}$, was demonstrated at radio frequencies (Sec. 5.5). The sensitivity of the optical ac coupled detector was in this experiment a factor of 15 higher than the sensitivity of the photodetector alone.

The technique was demonstrated not only at frequencies of several megahertz, but also at frequencies near the resonator bandwidth. For this experiment an optical ac

coupled photodetector was used as in-loop detector in an active power stabilization of an NPRO at frequencies from about 1 kHz to 1 MHz. The feasibility of a power stabilization involving the optical ac coupling technique was demonstrated for the first time. The achieved power stability agreed very well with the expected quantum limit and was up to a factor of 9 better at frequencies around 200 kHz than an equivalent traditional stabilization (Sec. 5.5).

At these low frequencies, the power stability was at first limited by several technical noise sources, such as residual frequency noise or resonator-internal scattering. Models describing these noise couplings were developed and were verified in the experiments (Sec. 5.4). Afterwards it was possible to reduce the couplings and noise sources step by step. The models can be used to better estimate technical noise contributions in future experiments. One noise source, fluctuating resonator-internal scattering, which was identified, can limit not only the performance of optical ac coupling schemes, but also many other experiments using optical resonators.

All in all the optical ac coupling technique was investigated theoretically and experimentally. For the power stabilization in future GWDs, the optical ac coupling technique is particularly suitable since on the one hand an extremely high power stability is required and on the other hand a suitable resonator, the power recycling cavity, is available anyway.

Conclusion

Stable lasers and sensitive sensors are the key components in many precision experiments. Many aspects of this thesis are associated on the one hand with the on-going laser stabilization for Advanced LIGO and on the other hand with the optical ac coupling technique.

The diagnostic breadboard, developed in this thesis, and the characterization of the functional prototype of the Advanced LIGO laser yielded essential results (Chapter 2) for developing an appropriate laser stabilization and for improving the laser performance in following prototypes. Furthermore, the DBB is a crucial component in the anticipated, automated monitoring of the complex Advanced LIGO laser system. Important parts of the laser stabilization were developed, such as the pre-mode-cleaner (Chapter 3) or the high-sensitivity photodiode array, which for the first time achieved a power noise sensitivity required for the Advanced LIGO power stabilization (Chapter 4). In conclusion, these instruments, components, and concepts are a solid foundation for the on-going characterization and stabilization of the Advanced LIGO laser and are therefore indispensable parts of the Advanced LIGO detector. This GWD will presumably reach its design sensitivity in a few years and will start the era of gravitational wave astronomy.

With the optical ac coupling, a high-sensitivity technique for detecting laser power fluctuations was developed and was demonstrated in several experiments achieving an unprecedented sensitivity for power fluctuations (Chapter 5). Besides technical advantages, this technique employed in a power stabilization allows one to beat the quantum-limit of traditional power stabilizations by up to 6 dB. This technique is important for many experiments with high power-stability requirements, such as next generation GWDs, and opens a whole new range of achievable power stabilities, which seemed to be inaccessible due to technical limits before.

Bibliography

- [Abb01] R. S. Abbott and P. J. King. Diode-pumped Nd:YAG laser intensity noise suppression using a current shunt. *Rev. Sci. Instrum.*, 72(2):1346–1349, 2001. [web link](#).
- [Abb08a] R. Abbott, R. Adhikari, S. Ballmer, L. Barsotti, M. Evans, P. Fritschel, V. Frolov, G. Mueller, B. Slagmolen, and S. Waldman. AdvLIGO Interferometer Sensing and Control Conceptual Design. Technical Report T070247-01-I, LIGO Scientific Collaboration, 2008. [web link](#).
- [Abb08b] R. Abbott, R. Adhikari, M. Flanagan, P. Fritschel, E. Gustafson, G. Mueller, D. Nolting, D. Reitze, and R. Savage. PSL Preliminary Design Review (PDR) report. Internal Working Note L080112-00-D, LIGO Scientific Collaboration, 2008. [web link](#).
- [Abr92] A. Abramovici, W. E. Althouse, R. W. P. Drever, Y. Gürsel, S. Kawamura, F. J. Raab, D. Shoemaker, L. Sievers, R. E. Spero, K. S. Thorne, et al. LIGO: The Laser Interferometer Gravitational-Wave Observatory. *Science*, 256(5055):325–333, 1992. [web link](#).
- [Ace02] F. Acernese, P. Amico, N. Arnaud, C. Arnault, D. Babusci, G. Ballardin, F. Barone, M. Barsuglia, F. Bellachia, J. L. Beney, et al. The present status of the VIRGO Central Interferometer. *Class. Quantum Grav.*, 19(7):1421–1428, 2002. [web link](#).
- [Adv07] Advanced LIGO Team. Advanced LIGO Reference Design. Technical Report M060056-10-M, LIGO Scientific Collaboration, 2007. [web link](#).
- [Ami02] R. Amin, G. Müller, M. Rahkmanov, D. Reitze, D. Tanner, and S. Wise. Input Optics Subsystem Conceptual Design Document. Technical Report T020027-00-D, LIGO Scientific Collaboration, 2002. [web link](#).
- [And84] D. Z. Anderson. Alignment of resonant optical cavities. *Appl. Opt.*, 23(17):2944–2949, 1984. [web link](#).

Bibliography

- [And01] M. Ando, K. Arai, R. Takahashi, G. Heinzl, S. Kawamura, D. Tatsumi, N. Kanda, H. Tagoshi, A. Araya, H. Asada, et al. Stable Operation of a 300-m Laser Interferometer with Sufficient Sensitivity to Detect Gravitational-Wave Events within Our Galaxy. *Phys. Rev. Lett.*, 86(18):3950–3954, 2001. [web link](#).
- [Ara97] A. Araya, N. Mio, K. Tsubono, K. Suehiro, S. Telada, M. Ohashi, and M. Fujimoto. Optical mode cleaner with suspended mirrors. *Appl. Opt.*, 36(7):1446–1453, 1997. [web link](#).
- [Ara07a] M. A. Arain, A. Lucianetti, R. Martin, G. Mueller, V. Quetschke, D. Reitze, D. B. Tanner, L. Williams, and W. Wu. Input Optics Subsystem Preliminary Design Document. Technical Report T060269-02-D, LIGO Scientific Collaboration, 2007. [web link](#).
- [Ara07b] M. A. Arain, V. Quetschke, J. Gleason, L. F. Williams, M. Rakhmanov, J. Lee, R. J. Cruz, G. Mueller, D. B. Tanner, and D. H. Reitze. Adaptive beam shaping by controlled thermal lensing in optical elements. *Appl. Opt.*, 46(12):2153–2165, 2007. [web link](#).
- [Ari92] A. Arie, S. Schiller, E. Gustafson, and R. Byer. Absolute frequency stabilization of diode-laser-pumped Nd:YAG lasers to hyperfine transitions in molecular iodine. *Opt. Lett.*, 17(17):1204–1206, 1992. [web link](#).
- [Ari93] A. Arie and R. Byer. Frequency stabilization of the 1064-nm Nd:YAG lasers to Doppler-broadened lines of iodine. *Appl. Opt.*, 32(36), 1993. [web link](#).
- [Avi04] S. Avino, E. Calloni, F. Barone, R. DeRosa, L. DiFiore, L. Milano, and S. Restaino. First results on an adaptive optics pre-mode cleaning system based on interferometric phase-front detection. *Class. Quantum Grav.*, 21:S947–S950, 2004. [web link](#).
- [Avi06] S. Avino, E. Calloni, A. Tierno, B. Agrawal, R. De Rosa, L. Di Fiore, L. Milano, and S. Restaino. Low-noise adaptive optics for gravitational wave interferometers. *Class. Quantum Grav.*, 23:5919–5926, 2006. [web link](#).
- [Bac04] H. A. Bachor and T. C. Ralph. *A Guide to Experiments in Quantum Optics*. WILEY-VCH, 2004. [web link](#).
- [Bak02] J. Baker, F. Barone, E. Calloni, R. De Rosa, L. Di Fiore, A. Eleuteri, L. Milano, S. Restaino, and K. Quipiani. An adaptive optics approach to the reduction of misalignments and beam jitters in gravitational wave interferometers. *Class. Quantum Grav.*, 19(7):1813–1818, 2002. [web link](#).
- [Bar73] R. Barger, M. Sorem, and J. Hall. Frequency stabilization of a cw dye laser. *Appl. Phys. Lett.*, 22:573, 1973. [web link](#).

- [Bar05] B. W. Barr, K. A. Strain, and C. J. Killow. Laser amplitude stabilization for advanced interferometric gravitational wave detectors. *Class. Quantum Grav.*, 22:4279–4283, 2005. [web link](#).
- [Bar06] P. Barriga, C. Zhao, L. Ju, and D. G. Blair. Self-Compensation of Astigmatism in Mode-Cleaners for Advanced Interferometers. *J. Phys. Conf. Ser.*, 32:457–463, 2006. [web link](#).
- [Bil81] H. Billing, W. Winkler, R. Schilling, A. Rüdiger, K. Maischberger, and L. Schnupp. The Munich Gravitational Wave Detector Using Laser Interferometry. *Quantum Optics, Experimental Gravity, and Measurement Theory*, 94, 1981.
- [Bla01] E. D. Black. An introduction to Pound-Drever-Hall laser frequency stabilization. *Am. J. Phys.*, 69(1):79–87, 2001. [web link](#).
- [Bon96] F. Bondu, P. Fritschel, C. N. Man, and A. Brillet. Ultrahigh-spectral-purity laser for the VIRGO experiment. *Opt. Lett.*, 21:582–584, 1996. [web link](#).
- [Bor08a] R. Bork. AdvLIGO CDS Realtime Code Generator (RCG) Application Developer’s Guide. Technical Report LIGO-T080135-00-C, LIGO Scientific Collaboration, 2008.
- [Bor08b] R. Bork and CDS Staff. AdvLIGO Control and Data Acquisition System Preliminary Design. Technical Report LIGO-T080182-00-C, LIGO Scientific Collaboration, 2008.
- [Buc98] B. C. Buchler, E. H. Huntington, C. C. Harb, and T. C. Ralph. Feedback control of laser intensity noise. *Phys. Rev. A*, 57:1286–1294, 1998. [web link](#).
- [Bul08] A. Bullington, B. Lantz, M. Fejer, and R. Byer. Modal frequency degeneracy in thermally loaded optical resonators. *Appl. Opt.*, 47(15):2840–2851, 2008. [web link](#).
- [Cal97] E. Calloni, F. Barone, L. Di Fiore, A. Grado, P. La Penna, and L. Milano. Effects of misalignment and beam jitter in Fabry-Perot laser stabilization. *Opt. Commun.*, 142:50–54, 1997. [web link](#).
- [Cal03] E. Calloni, J. T. Baker, F. Barone, R. DeRosa, L. D. Fiore, L. Milano, and S. R. Restaino. Adaptive optics approach for prefiltering of geometrical fluctuations of the input laser beam of an interferometric gravitational waves detector. *Rev. Sci. Instrum.*, 74(4):2570–2574, 2003. [web link](#).
- [Che90] C. Chen and M. Win. Frequency noise measurement of diode-pumped Nd:YAG ring lasers. *IEEE Photonic. Tech. L.*, 2(11):772–774, 1990. [web link](#).

Bibliography

- [Clu00] D. A. Cluble, K. D. Skeldon, B. W. Barr, G. P. Newton, K. A. Strain, and J. Hough. Ultrahigh level of frequency stabilisation of an injection locked Nd:YAG laser with relevance to gravitational wave detection. *Opt. Commun.*, 186:177–184, 2000. [web link](#).
- [Con03] L. Conti, M. D. Rosa, and F. Marin. High-spectral-purity laser system for the AURIGA detector optical readout. *J. Opt. Soc. Am. B*, 20:462–468, 2003. [web link](#).
- [Cra02] G. A. Cranch. Frequency noise reduction in erbium-doped fiber distributed-feedback lasers by electronic feedback. *Opt. Lett.*, 27(13):1114–1116, 2002. [web link](#).
- [Csö03] M. Csörnyei, T. Bercei, and P. R. Herczfeld. Noise Suppression of Nd:YVO₄ Solid-State Lasers for Telecommunication Applications. *J. Lightwave Technol.*, 21(12):2983, 2003. [web link](#).
- [Csö05] M. Csörnyei, T. Bercei, and T. Marozsák. All-optical intensity noise suppression for solid-state and semiconductor lasers. *Journal of Telecommunications and Information Technology*, 2:65–70, 2005. [web link](#).
- [Cut02] C. Cutler and K. Thorne. An overview of gravitational-wave sources. In *Proceedings of the 16th International Conference on General Relativity & Gravitation*, page 72. World Scientific, 2002. [web link](#).
- [Daw08] S. T. Dawkins and A. N. Luiten. Single actuator alignment control for improved frequency stability of a cavity-based optical frequency reference. *Appl. Opt.*, 47(9):1239–1246, 2008. [web link](#).
- [Day91] T. Day. *Frequency-Stabilized Solid State Lasers for Coherent Optical Communications*. Ph.D. thesis, Stanford University, 1991. [web link](#).
- [Day92] T. Day, E. K. Gustafson, and R. L. Byer. Sub-Hertz Relative Frequency Stabilization of Two-Diode Laser-Pumped Nd:YAG Lasers Locked to a Fabry-Perot Interferometer. *IEEE J. Quantum Electron.*, 28, 1992. [web link](#).
- [Del06] V. Delaubert, N. Treps, M. Lassen, C. C. Harb, C. Fabre, P. K. Lam, and H.-A. Bachor. TEM₁₀ homodyne detection as an optimal small-displacement and tilt-measurement scheme. *Phys. Rev. A*, 74(5):053823, 2006. [web link](#).
- [Dre83] R. W. P. Drever, J. L. Hall, F. V. Kowalski, J. Hough, G. M. Ford, A. J. Munley, and H. Ward. Laser Phase and Frequency Stabilization Using an Optical Resonator. *Appl. Phys. B*, 31(2):97–105, 1983. [web link](#).
- [Dub04] M. Dubois, K. C. Burr, and T. E. Drake. Laser Phase Noise Reduction for Industrial Interferometric Applications. *Appl. Opt.*, 43(22):4399–4407, 2004. [web link](#).

- [EPI] Experimental Physics and Industrial Control System. <http://www.aps.anl.gov/epics/>.
- [Fla05] R. Flaminio, A. Freise, A. Gennai, P. Hello, P. L. Penna, G. Losurdo, H. Lueck, N. Man, A. Masserot, B. Mours, et al. Advanced Virgo White Paper. Technical Report VIR-NOT-DIR-1390-304, VIRGO collaboration, 2005. [web link](#).
- [Fre93] J. Freeman and J. Conradi. Gain modulation response of erbium-doped fiber amplifiers. *IEEE Photonic. Tech. L.*, 5(2):224–226, 1993. [web link](#).
- [Fre95] I. Freitag, A. Tünnermann, and H. Welling. Power scaling of diode-pumped monolithic Nd:YAG lasers to output powers of several watts. *Opt. Commun.*, 115:511–515, 1995. [web link](#).
- [Fre04] M. Frede, R. Wilhelm, M. Brendel, C. Fallnich, F. Seifert, B. Willke, and K. Danzmann. High power fundamental mode Nd:YAG laser with efficient birefringence compensation. *Opt. Express*, 12:3581–3589, 2004. [web link](#).
- [Fre05] M. Frede, R. Wilhelm, D. Kracht, and C. Fallnich. Nd:YAG ring laser with 213 W linearly polarized fundamental mode output power. *Opt. Express*, 13:7516–7519, 2005. [web link](#).
- [Fre07a] M. Frede. *Einfrequentes Laserlicht höchster Brillianz*. PhD thesis (in German), Universität Hannover, 2007. [web link](#).
- [Fre07b] M. Frede, B. Schulz, R. Wilhelm, P. Kwee, F. Seifert, B. Willke, and D. Kracht. Fundamental mode, single-frequency laser amplifier for gravitational wave detectors. *Opt. Express*, 15:459–465, 2007. [web link](#).
- [Fri89] P. Fritschel, A. Jeffries, and T. J. Kane. Frequency fluctuations of a diode-pumped Nd:YAG ring laser. *Opt. Lett.*, 14:993–995, 1989. [web link](#).
- [Fri93] P. Fritschel. Notes on the laser frequency stabilization. Technical Report VIR-NOT-LAL-1380-51, VIRGO collaboration, 1993. [web link](#).
- [Fri98] P. Fritschel, N. Mavalvala, D. Shoemaker, D. Sigg, M. Zucker, and G. González. Alignment of an interferometric gravitational wave detector. *Appl. Opt.*, 37:6734–6747, 1998. [web link](#).
- [Fri01] P. Fritschel et al. Advanced LIGO Systems Design. Technical Report T010075-00-D, LIGO Scientific Collaboration, 2001. [web link](#).
- [Fri03] P. Fritschel. Second generation instruments for the Laser Interferometer Gravitational Wave Observatory (LIGO). *Proc. SPIE*, 4856(22):282–291, 2003. [web link](#).

Bibliography

- [Fri08] P. Fritschel et al. Advanced LIGO Systems Design. Technical Report T010075-01-I, LIGO Scientific Collaboration, 2008. [web link](#).
- [Goß03] S. Goßler, M. M. Casey, A. Freise, A. Grant, H. Grote, G. Heinzl, M. Heurs, M. E. Husman, K. Kötter, V. Leonhardt, et al. Mode-cleaning and injection optics of the gravitational-wave detector GEO600. *Rev. Sci. Instrum.*, 74(8):3787–3795, 2003. [web link](#).
- [Gra88] S. Grafström, U. Harbarth, J. Kowalski, R. Neumann, and S. Noehte. Fast Laser Beam Position Control with Submicroradian Precision. *Opt. Commun.*, 65:121–126, 1988. [web link](#).
- [Gra01] J. Gray, P. Thomas, and X. D. Zhu. Laser pointing stability measured by an oblique-incidence optical transmittance difference technique. *Rev. Sci. Instrum.*, 72:3714–3717, 2001. [web link](#).
- [Gra07] M. Gray, J. Chow, K. McKenzie, and D. McClelland. Using a Passive Fiber Ring Cavity to Generate Shot-Noise-Limited Laser Light for Low-Power Quantum Optics Applications. *IEEE Photonic. Tech. L.*, 19(14):1063–1065, 2007. [web link](#).
- [Gre98] C. Greiner, B. Boggs, T. Wang, and T. W. Mossberg. Laser frequency stabilization by means of optical self-heterodyne beat-frequency control. *Opt. Lett.*, 23(16):1280–1282, 1998. [web link](#).
- [Gro02] H. Grote, G. Heinzl, A. Freise, S. Gossler, B. Willke, H. Lueck, H. Ward, M. Casey, K. A. Strain, D. Robertson, et al. The automatic alignment system of GEO600. *Class. Quantum Grav.*, 19:1849–1855, 2002. [web link](#).
- [Gro04] H. Grote, G. Heinzl, A. Freise, S. Gossler, B. Willke, H. Lueck, H. Ward, M. M. Casey, K. A. Strain, D. Robertson, et al. Automatic beam alignment for the mode-cleaner cavities of GEO600. *Appl. Opt.*, 43:1938–1945, 2004. [web link](#).
- [Hal05] J. Hald and V. Ruseva. Efficient suppression of diode-laser phase noise by optical filtering. *J. Opt. Soc. Am. B*, 22(11):2338–2344, 2005. [web link](#).
- [Han80] T. Hansch and B. Couillaud. Laser frequency stabilization by polarization spectroscopy of a reflecting reference cavity. *Opt. Commun.*, 35(3):441–444, 1980. [web link](#).
- [Har94] C. Harb, M. Gray, H. Bachor, R. Schilling, P. Rottengatter, I. Freitag, and H. Welling. Suppression of the Intensity Noise in a Diode-Pumped Neodymium:YAG Nonplanar Ring Laser. *IEEE J. Quantum Electron.*, 30(12):2907–2913, 1994. [web link](#).

- [Hei99] G. Heinzl, A. Rüdiger, R. Schilling, K. Strain, W. Winkler, J. Mizuno, and K. Danzmann. Automatic beam alignment in the Garching 30-m prototype of a laser-interferometric gravitational wave detector. *Opt. Commun.*, 160(4-6):321 – 334, 1999. [web link](#).
- [Hei00] G. Heinzl. LISO – Program for Linear Simulation and Optimization of analog electronic circuits, 2000. ghh@mpq.mpg.de.
- [Her02] S. Herden. *Vergleichende Untersuchung von Hochleistungs-YAG-Lasern*. Diploma thesis (in German), Universität Hannover, 2002.
- [Hil06] M. Hildebrandt, M. Frede, P. Kwee, B. Willke, and D. Kracht. Single-frequency master-oscillator photonic crystal fiber amplifier with 148 W output power. *Opt. Express*, 14(23):11071–11076, 2006. [web link](#).
- [Hil09a] S. Hild, A. Freise, M. Mantovani, S. Chelkowski, J. Degallaix, and R. Schilling. Using the etalon effect for in situ balancing of the Advanced Virgo arm cavities. *Class. Quantum Grav.*, 26(2):025005 (12pp), 2009. [web link](#).
- [Hil09b] S. Hild, H. Grote, J. Degallaix, S. Chelkowski, K. Danzmann, A. Freise, M. Hewitson, J. Hough, H. Lück, M. Prijatelj, et al. DC-readout of a signal-recycled gravitational wave detector. *Class. Quantum Grav.*, 26(5):055012, 2009. [web link](#).
- [Hil09c] M. Hildebrandt. *Brillouin scattering in high-power narrow-linewidth fiber amplifiers*. Ph.D. thesis, Universität Hannover, 2009. [web link](#).
- [Hsu04] M. T. L. Hsu, V. Delaubert, P. K. Lam, and W. P. Bowen. Optimal optical measurement of small displacements. *J. Opt. B*, 6:495–501, 2004. [web link](#).
- [Hun07] E. H. Huntington, C. C. Harb, M. Heurs, and T. C. Ralph. Quantum noise limits to simultaneous quadrature amplitude and phase stabilization of solid-state lasers. *Phys. Rev. A*, 75(1):013802, 2007. [web link](#).
- [Iva07] E. Ivanov and L. Hollberg. Wide-band suppression of laser intensity noise. In *IEEE International Frequency Control Symposium, 2007 Joint with the 21st European Frequency and Time Forum*, pages 1082–1087. 2007. [web link](#).
- [Jen02] O. Jennrich, G. Newton, K. D. Skeldon, and J. Hough. A high power photodetection system for use with laser interferometric gravitational wave detectors. *Opt. Commun.*, 205:405–413, 2002. [web link](#).
- [Kan85] T. J. Kane and R. L. Byer. Monolithic, unidirectional single-mode Nd:YAG ring laser. *Opt. Lett.*, 10:65–67, 1985. [web link](#).

Bibliography

- [Kan90] T. Kane. Intensity noise in diode-pumped single-frequency Nd:YAG lasers and its control by electronic feedback. *IEEE Photonic. Tech. L.*, 2(4):244–245, 1990. [web link](#).
- [Kaw97] S. Kawamura, A. Abramovici, and M. E. Zucker. Improved multistage wide band laser frequency stabilization. *Rev. Sci. Instrum.*, 68(1):223–229, 1997. [web link](#).
- [Kéf09] F. Kéfélian, H. Jiang, P. Lemonde, and G. Santarelli. Ultralow-frequency-noise stabilization of a laser by locking to an optical fiber-delay line. *Opt. Lett.*, 34(7):914–916, 2009. [web link](#).
- [Kim07] D. Kim, H. Rhee, J. Song, and Y. Lee. Laser output power stabilization for direct laser writing system by using an acousto-optic modulator. *Rev. Sci. Instrum.*, 78:103110, 2007. [web link](#).
- [Kin08] P. King, R. Savage, P. Wessels, and B. Willke. PSL Preliminary Design. Internal Technical Report T080195-01-D, LIGO Scientific Collaboration, 2008. [web link](#).
- [Kla05] T. Klaassen, J. de Jong, M. van Exter, and J. Woerdman. Transverse mode coupling in an optical resonator. *Opt. Lett.*, 30(15):1959–1961, 2005. [web link](#).
- [Kla07] T. Klaassen, M. P. van Exter, and J. P. Woerdman. Characterization of scattering in an optical Fabry-Perot resonator. *Appl. Opt.*, 46:5210–5215, 2007. [web link](#).
- [Kob07] S. Kobtsev, S. Kandrushin, and A. Potekhin. Long-term frequency stabilization of a continuous-wave tunable laser with the help of a precision wavelengthmeter. *Appl. Opt.*, 46(23):5840–5843, 2007. [web link](#).
- [Kur03] K. Kuroda, M. Ohashi, S. Miyoki, T. Uchiyama, H. Ishitsuka, K. Yamamoto, K. Kasahara, M.-K. Fujimoto, S. Kawamura, R. Takahashi, et al. Current status of large-scale cryogenic gravitational wave telescope. *Class. Quantum Grav.*, 20(17):S871–S884, 2003. [web link](#).
- [Kwe05] P. Kwee. *Charakterisierung von Lasersystemen für Gravitationswellendetektoren*. Diploma thesis (in German), Universität Hannover, 2005. [web link](#).
- [Kwe07] P. Kwee, F. Seifert, B. Willke, and K. Danzmann. Laser beam quality and pointing measurement with an optical resonator. *Rev. Sci. Instrum.*, 78:1–10, 2007. [web link](#).
- [Kwe08a] P. Kwee and B. Willke. Automatic laser beam characterization of monolithic Nd:YAG nonplanar ring lasers. *Appl. Opt.*, 47(32):6022–6032, 2008. [web link](#).

- [Kwe08b] P. Kwee, B. Willke, and K. Danzmann. Optical ac coupling to overcome limitations in the detection of optical power fluctuations. *Opt. Lett.*, 33(13):1509–1511, 2008. [web link](#).
- [Kwe09a] P. Kwee, B. Willke, and K. Danzmann. Laser power stabilization using optical ac coupling and its quantum and technical limits. *Appl. Opt.*, 48(28):5423–5431, 2009. [web link](#).
- [Kwe09b] P. Kwee, B. Willke, and K. Danzmann. Shot-noise-limited laser power stabilization with a high-power photodiode array. *Opt. Lett.*, 34(19):2912–2914, 2009. [web link](#).
- [Lab07] J. Labaziewicz, P. Richerme, K. Brown, I. Chuang, and K. Hayasaka. Compact, filtered diode laser system for precision spectroscopy. *Opt. Lett.*, 32(5):572–574, 2007. [web link](#).
- [Lay79] H. Layer. Acousto-optic modulator intensity servo. *Appl. Opt.*, 18, 1979. [web link](#).
- [Lev96] M. Levesque, A. Mailloux, M. Morin, P. Galarneau, Y. Champagne, O. Plomteux, and M. Tiedtke. Laser pointing stability measurements. *SPIE*, 2870:216–224, 1996. [web link](#).
- [LIG09a] LIGO Scientific Collaboration. Advanced LIGO anticipated sensitivity curves. Internal Technical Report T0900288-02, LIGO Scientific Collaboration, 2009. [web link](#).
- [LIG09b] LIGO Scientific Collaboration. GWINC – Gravitational Wave Interferometer Noise Calculator, 2009. <http://lhocds.ligo-wa.caltech.edu:8000/advligo/GWINC/>.
- [Liu09] T. Liu, Y. N. Zhao, V. Elman, A. Stejskal, and L. J. Wang. Characterization of the absolute frequency stability of an individual reference cavity. *Opt. Lett.*, 34(2):190–192, 2009. [web link](#).
- [Lud07] A. D. Ludlow, X. Huang, M. Notcutt, T. Zanon-Willette, S. M. Foreman, M. M. Boyd, S. Blatt, and J. Ye. Compact, thermal-noise-limited optical cavity for diode laser stabilization at 1×10^{-15} . *Opt. Lett.*, 32(6):641–643, 2007. [web link](#).
- [Mae96] R. Maestle, W. Plass, J. Chen, C. Hembd-Soellner, A. Giesen, H. Tiziani, and H. Hugel. Investigation of beam pointing stability, far field divergence angle and power density distribution of a high power CO₂-laser. *SPIE*, 2870:319–325, 1996. [web link](#).
- [Mee88] B. J. Meers. Recycling in laser-interferometric gravitational-wave detectors. *Phys. Rev. D*, 38(8):2317–2326, 1988. [web link](#).

Bibliography

- [Mei06] H. Mei, S. Chen, and W. Ni. Suspension of the fiber mode-cleaner launcher and measurement of the high extinction-ratio (10^{-9}) ellipsometer for the Q&A experiment. *J. Phys. Conf. Ser.*, 32:236–243, 2006. [web link](#).
- [Mil87] G. J. Milburn, M. D. Levenson, R. M. Shelby, S. H. Perlmutter, R. G. DeVoe, D. F. Walls, A. R. Center, and S. Jose. Optical-fiber media for squeezed-state generation. *J. Opt. Soc. Am. B*, 4:1476–1489, 1987. [web link](#).
- [Mio07] N. Mio, T. Ozeki, K. Machida, and S. Moriwaki. Laser Intensity Stabilization System Using Laser-Diode-Pumped Nd:YAG Rod-Laser Amplifier. *Jpn. J. Appl. Phys.*, 46(8A):5338–5341, 2007. [web link](#).
- [Mis73] C. Misner, K. S. Thorne, and J. A. Wheeler. *Gravitation*. W. H. Freeman, 1973.
- [Mor94a] E. Morrison, B. J. Meers, D. I. Robertson, and H. Ward. Automatic alignment of optical interferometers. *Appl. Opt.*, 33:5041–5049, 1994. [web link](#).
- [Mor94b] E. Morrison, B. J. Meers, D. I. Robertson, and H. Ward. Experimental demonstration of an automatic alignment system for optical interferometers. *Appl. Opt.*, 33:5037–5040, 1994. [web link](#).
- [Mue00] G. Mueller, Q. Shu, R. Adhikari, D. B. Tanner, D. Reitze, D. Sigg, N. Mavalvala, and J. Camp. Determination and optimization of mode matching into optical cavities by heterodyne detection. *Opt. Lett.*, 25:266–268, 2000. [web link](#).
- [Mue09] G. Mueller. Pointing requirements for Advanced LIGO. Internal Technical Report T0900142, LIGO Scientific Collaboration, 2009. [web link](#).
- [Mül02] G. Müller, R. Amin, M. Rakhmanov, D. Reitze, D. Tanner, and S. Wise. Input Optics Subsystem Design Requirements Document. Internal Technical Report T020020-02-D, LIGO Scientific Collaboration, 2002. [web link](#).
- [Mül05] H. Müller, S. Chiow, Q. Long, C. Vo, and S. Chu. Active sub-Rayleigh alignment of parallel or antiparallel laser beams. *Opt. Lett.*, 30(24):3323–3325, 2005. [web link](#).
- [Mül08] G. Müller. Personal communication, 2008. mueller@phys.ufl.edu.
- [Mus97] M. Musha, S. Telada, K. Nakagawa, M. Ohashi, and K. Ueda. Measurement of frequency noise spectra of frequency-stabilized LD-pumped Nd:YAG laser by using a cavity with separately suspended mirrors. *Opt. Commun.*, 140(4-6):323–330, 1997. [web link](#).

- [Mus01] M. Musha, T. Kanaya, K. Nakagawa, and K. Ueda. Intensity and frequency noise characteristics of two coherently-added injection-locked Nd:YAG lasers. *Appl. Phys. B*, 73(3):209–214, 2001. [web link](#).
- [Nag98] S. Nagano, M. Musha, L. Ying, N. Mio, and K. Ueda. Investigation of an Injection-Locked Nd:YAG Laser for the Gravitational Wave Detection. *Laser Phys.*, 8(3):686–691, 1998. [web link](#).
- [Nag02] S. Nagano, M. A. Barton, H. Ishizuka, K. Kuroda, S. Matsumura, O. Miyakawa, S. Miyoki, D. Tatsumi, T. Tomaru, T. Uchiyama, et al. Development of a light source with an injection-locked Nd:YAG laser and a ring-mode cleaner for the TAMA 300 gravitational-wave detector. *Rev. Sci. Instrum.*, 73(5):2136–2142, 2002. [web link](#).
- [Nag03] S. Nagano, S. Kawamura, M. Ando, R. Takahashi, K. Arai, M. Musha, S. Telada, M. Fujimoto, M. Fukushima, Y. Kozai, et al. Development of a multistage laser frequency stabilization for an interferometric gravitational-wave detector. *Rev. Sci. Instrum.*, 74:4176, 2003. [web link](#).
- [Nak94] K. Nakagawa, A. Shelkownikov, T. Katsuda, and M. Ohtsu. Absolute frequency stability of a diode-laser-pumped Nd:YAG laser stabilized to a high-finesse optical cavity. *Appl. Opt.*, 33(27):6383–6386, 1994. [web link](#).
- [Naz06] T. Nazarova, F. Riehle, and U. Sterr. Vibration-insensitive reference cavity for an ultra-narrow-linewidth laser. *Appl. Phys. B*, 83(4):531–536, 2006. [web link](#).
- [NKT09] NKT Photonics. Koheras BoostiK System, 2009. http://www.nktphotonics.com/files/files/datasheet_koheras_boostik-system.pdf.
- [Noc04] F. Nocera. LIGO laser intensity noise suppression. *Class. Quantum Grav.*, 21:S481–S485, 2004. [web link](#).
- [Nov02] S. Novak and A. Moesle. Analytic model for gain modulation in EDFAs. *J. Lightwave Technol.*, 20(6):975, 2002. [web link](#).
- [Num04] K. Numata, A. Kemery, and J. Camp. Thermal-Noise Limit in the Frequency Stabilization of Lasers with Rigid Cavities. *Phys. Rev. Lett.*, 93:1–4, 2004. [web link](#).
- [Oha08] M. Ohashi. Status of LCGT and CLIO. *J. Phys. Conf. Ser.*, 120(3):032008 (3pp), 2008. [web link](#).
- [Ott00] D. Ottaway, P. Veitch, C. Hollitt, D. Mudge, M. Hamilton, and J. Munch. Frequency and intensity noise of an injection-locked Nd:YAG ring laser. *Appl. Phys. B*, 71(2):163–168, 2000. [web link](#).

Bibliography

- [Pas06] R. Paschotta. Beam quality deterioration of lasers caused by intracavity beam distortions. *Opt. Express*, 14(13):6069–6074, 2006. [web link](#).
- [Pöl09] J. H. Pöld. *Stabilization of the Advanced LIGO 200 W Laser*. Diploma thesis, Leibniz Universität Hannover, 2009.
- [Que03] V. Quetschke. *Korrelationen von Rauschquellen bei Nd:YAG Lasersystemen*. PhD thesis (in German), University Hannover, 2003. [web link](#).
- [Que06] V. Quetschke, J. Gleason, M. Rakhmanov, J. Lee, L. Zhang, K. Y. Franzen, C. Leidel, G. Mueller, R. Amin, D. B. Tanner, et al. Adaptive control of laser modal properties. *Opt. Lett.*, 31:217–219, 2006. [web link](#).
- [Rob86] N. Robertson, S. Hoggan, J. Mangan, and J. Hough. Intensity stabilisation of an argon laser using an electro-optic modulator—Performance and limitations. *Appl. Phys. B*, 39(3):149–153, 1986. [web link](#).
- [Rol04] J. Rollins, D. Ottaway, M. Zucker, R. Weiss, and R. Abbott. Solid-state laser intensity stabilization at the 10^{-8} level. *Opt. Lett.*, 29(16):1876–1878, 2004. [web link](#).
- [Rom05] A. Romann, D. S. Rabeling, G. Vine, J. H. Chow, M. B. Gray, and D. E. McClelland. Automatic alignment of a rigid spacer cavity. *Gen. Relativ. Gravit.*, 37:1591–1599, 2005. [web link](#).
- [Row94] S. Rowan, A. M. Campbell, K. Skeldon, and J. Hough. Broadband Intensity Stabilization of a Diode-pumped Monolithic Miniature Nd:YAG Ring Laser. *J. Mod. Optic.*, 41:1263–1269, 1994. [web link](#).
- [Rüd81] A. Rüdiger, R. Schilling, L. Schnupp, W. Winkler, H. Billing, and K. Maischberger. A mode selector to suppress fluctuations in laser beam geometry. *Opt. Acta*, 28(5):641–658, 1981. [web link](#).
- [Ruo97] G. Ruoso, R. Storz, S. Seel, S. Schiller, and J. Mlynek. Nd:YAG laser frequency stabilization to a supercavity at the 0.1 Hz level. *Opt. Commun.*, 133(1-6):259 – 262, 1997. [web link](#).
- [Sal88] C. Salomon, D. Hils, and J. L. Hall. Laser stabilization at the millihertz level. *J. Opt. Soc. Am. B*, 5(8):1576–1587, 1988. [web link](#).
- [Sam90] N. M. Sampas and D. Z. Anderson. Stabilization of laser beam alignment to an optical resonator by heterodyne detection of off-axis modes. *Appl. Opt.*, 29:394–403, 1990. [web link](#).
- [Sam93] N. Sampas, E. Gustafson, and R. Byer. Long-term stability of two diode-laser-pumped nonplanar ring lasers independently stabilized to two Fabry-Perot interferometers. *Opt. Lett.*, 18(12):947–949, 1993. [web link](#).

- [Sar05] S. Saraf, K. Urbanek, R. L. Byer, and P. J. King. Quantum noise measurements in a continuous-wave laser-diode-pumped Nd:YAG saturated amplifier. *Opt. Lett.*, 30(10):1195–1197, 2005. [web link](#).
- [Sau94] P. R. Saulson. *Fundamentals of Interferometric Gravitational Wave Detectors*. World Scientific, 1994.
- [Sch95] S. Schiller, S. Seel, R. Storz, and J. Mlynek. Experimental studies of cryogenic optical resonators. *SPIE*, 2378:138, 1995. [web link](#).
- [Sch99] B. Schutz. Gravitational wave astronomy. *Class. Quantum Grav.*, 16:131–156, 1999. [web link](#).
- [Sch05] R. Schilling. OptoCad – A Fortran 95 module for tracing Gaussian beams through an optical set-up, 2005. <http://www.rzg.mpg.de/~ros/OptoCad/>.
- [See97] S. Seel, R. Storz, G. Ruoso, J. Mlynek, and S. Schiller. Cryogenic Optical Resonators: A New Tool for Laser Frequency Stabilization at the 1 Hz Level. *Phys. Rev. Lett.*, 78(25):4741–4744, 1997. [web link](#).
- [Sei06] F. Seifert, P. Kwee, M. Heurs, B. Willke, and K. Danzmann. Laser power stabilization for second-generation gravitational wave detectors. *Opt. Lett.*, 31(13):2000–2002, 2006. [web link](#).
- [Sei09] F. Seifert. *Power Stabilization of High Power Lasers for Second Generation Gravitational Wave Detectors*. Ph.D. thesis, Universität Hannover, 2009.
- [Sha99] D. A. Shaddock, M. B. Gray, and D. E. McClelland. Frequency locking a laser to an optical cavity by use of spatial mode interference. *Opt. Lett.*, 24(21):1499–1501, 1999. [web link](#).
- [Sho88] D. Shoemaker, R. Schilling, L. Schnupp, W. Winkler, K. Maischberger, and A. Rüdiger. Noise behavior of the Garching 30-meter prototype gravitational-wave detector. *Phys. Rev. D*, 38(2):423–432, 1988. [web link](#).
- [Sho89] D. Shoemaker, A. Brillet, C. N. Man, O. Crégut, and G. Kerr. Frequency-stabilized laser-diode-pumped Nd:YAG laser. *Opt. Lett.*, 14(12):609–611, 1989. [web link](#).
- [Sie86] A. E. Siegman. *Lasers*. Mill Valley, CA, Univ. Science Books, 1986.
- [Sie90] A. E. Siegman. New developments in laser resonators. *SPIE*, 1224:2–14, 1990. [web link](#).
- [Sla02] B. J. J. Slagmolen, D. A. Shaddock, M. B. Gray, and D. E. McClelland. Frequency Stability of Spatial Mode Interference (Tilt) Locking. *IEEE J. Quantum Electron.*, 38:1521–1528, 2002. [web link](#).

Bibliography

- [Sla05] B. Slagmolen, M. Barton, C. Mow-Lowry, G. Vine, D. Rabeling, J. Chow, A. Romann, C. Zhao, M. Gray, and D. McClelland. Alignment locking to suspended Fabry-Perot cavity. *Gen. Relativ. Gravit.*, 37(9):1601–1608, 2005. [web link](#).
- [Som06] K. Somiya, Y. Chen, and N. Mio. Frequency noise and intensity noise of next-generation gravitational-wave detectors with RF/DC readout schemes. *Phys. Rev. D*, 73:1–17, 2006. [web link](#).
- [Sto98] R. Storz, C. Braxmaier, K. Jäck, O. Pradl, and S. Schiller. Ultrahigh long-term dimensional stability of a sapphire cryogenic optical resonator. *Opt. Lett.*, 23(13):1031–1033, 1998. [web link](#).
- [Tac96] S. Taccheo, P. Laporta, O. Svelto, and G. De Geronimo. Intensity noise reduction in a single-frequency ytterbium-codoped erbium laser. *Opt. Lett.*, 21(21):1747–1749, 1996. [web link](#).
- [Tak08] K. Takahashi, M. Ando, and K. Tsubono. Stabilization of laser intensity and frequency using optical fiber. *J. Phys. Conf. Ser.*, 122:012016, 2008. [web link](#).
- [Tau95] M. S. Taubman, H. Wiseman, D. E. McClelland, and H. A. Bachor. Intensity feedback effects on quantum-limited noise. *J. Opt. Soc. Am. B*, 12(10):1792–1800, 1995. [web link](#).
- [Tsu92] K. Tsubono and S. Moriwaki. Shot-Noise Limited Low-Frequency Intensity Noise of a Nd:YAG Laser. *Jpn. J. Appl. Phys.*, 31(Part 1, No. 4):1241–1242, 1992. [web link](#).
- [Ueh93] N. Uehara and K. Ueda. 193-mHz beat linewidth of frequency-stabilized laser-diode-pumped Nd:YAG ring lasers. *Opt. Lett.*, 18(7):505–507, 1993. [web link](#).
- [Ueh94] N. Uehara and K. Ueda. Ultrahigh-frequency stabilization of a diode-pumped Nd:YAG laser with a high-power-acceptance photodetector. *Opt. Lett.*, 19:728–730, 1994. [web link](#).
- [Ueh97] N. Uehara, E. K. Gustafson, M. M. Fejer, and R. L. Byer. Modeling of efficient mode-matching and thermal-lensing effect on a laser-beam coupling into a mode-cleaner cavity. *Proc. SPIE*, 2989:57–68, 1997. [web link](#).
- [VIR07] VIRGO collaboration. Advanced Virgo Conceptual Design. Technical Report VIR-042A-07, VIRGO collaboration, 2007. [web link](#).
- [Web04] S. A. Webster, M. Oxborrow, and P. Gill. Subhertz-linewidth Nd:YAG laser. *Opt. Lett.*, 29(13):1497–1499, 2004. [web link](#).
- [Whi65] A. D. White. Frequency Stabilization of Gas Lasers. *IEEE J. Quantum Electron.*, QE-1:349–357, 1965. [web link](#).

- [Wil98] B. Willke, N. Uehara, E. K. Gustafson, R. L. Byer, P. J. King, S. U. Seel, and R. L. Savage. Spatial and temporal filtering of a 10-W Nd:YAG laser with a Fabry-Perot ring-cavity premode cleaner. *Opt. Lett.*, 23:1704–1706, 1998. [web link](#).
- [Wil00] B. Willke, S. Brozek, K. Danzmann, V. Quetschke, and S. Gossler. Frequency stabilization of a monolithic Nd:YAG ring laser by controlling the power of the laser-diode pump source. *Opt. Lett.*, 25:1019–1021, 2000. [web link](#).
- [Wil02] B. Willke, P. Aufmuth, C. Aulbert, S. Babak, R. Balasubramanian, B. W. Barr, S. Berukoff, S. Bose, G. Cagnoli, M. M. Casey, et al. The GEO 600 gravitational wave detector. *Class. Quantum Grav.*, 19(7):1377–1387, 2002. [web link](#).
- [Wil08] B. Willke, K. Danzmann, M. Frede, P. King, D. Kracht, P. Kwee, O. Puncken, R. L. Savage, B. Schulz, F. Seifert, et al. Stabilized lasers for advanced gravitational wave detectors. *Class. Quantum Grav.*, 25(11):114040 (9pp), 2008. [web link](#).
- [Wil09] B. Willke, P. King, R. Savage, and P. Fritschel. Pre-Stabilized Laser Design Requirements. Internal Technical Report T050036-v2, LIGO Scientific Collaboration, 2009. [web link](#).
- [Win09] L. Winkelmann. Personal communication, l.winkelmann@lzh.de, 2009.
- [Yos82] T. Yoshino, S. Umegaki, H. Inoue, and K. Kurosawa. Light Intensity Stabilization Using Highly-Efficient Faraday Rotator. *Jpn. J. Appl. Phys.*, 21(4):612–616, 1982. [web link](#).
- [Zaw02] I. Zawischa, M. Brendel, K. Danzmann, C. Fallnich, M. Heurs, S. Nagano, V. Quetschke, H. Welling, and B. Willke. The GEO600 laser system. *Class. Quantum Grav.*, 19:1775–1781, 2002. [web link](#).
- [Zaw03] I. Zawischa. *Injektionsgekoppelte diodengepumpte Nd:YAG- und Nd:YVO₄-Laser für terrestrische interferometrische Gravitationswellendetektoren*. PhD thesis (in German), Universität Hannover, 2003. [web link](#).
- [Zha03] J. Zhang, H. Ma, C. Xie, and K. Peng. Suppression of Intensity Noise of a Laser-Diode-Pumped Single-Frequency Nd:YVO₄ Laser by Optoelectronic Control. *Appl. Opt.*, 42(6):1068–1074, 2003. [web link](#).

Index

- 1550 nm, 7, 36
- Aberration, 33, 49, 50, 60
- ACC, 98, 99, 102, 103, 105, 107, 109, 110, 113, 118, 119
- Acoustic shielding, 11, 47, 57, 62, 75, 99
- Advanced LIGO, 51
 - PMC, 60
 - requirements, 54, 56–58, 60
 - sensitivity, 53
 - stabilization, 50, 70, 78
- Advanced LIGO laser, 31, 51
 - aberrations, 33
 - beam quality, 32, 60, 61
 - characterization, 31
 - corona, 33
 - frequency noise, 32, 57
 - functional prototype, 31
 - pointing fluctuations, 32, 59
 - power noise, 33, 55
 - power stabilization, *see* Power stab.
- Air particles, 29, 31, 44, 75, 79
- Alignment, 13, 22
 - control loop, 18
 - photodiode array, *see* Photodiode array
- Amplitude modulation sidebands, 109
- Amplitude quadrature operator, 65
- Anti-aliasing filter, 22, 24, 74, 76
- Anti-imaging filter, 24
- AOM, 10, 34, 44, 47, 54, 58
- Aperture, 114
 - resonator-internal, 100, 112, 113, 115, 117, 119
- Astigmatism, 6, 14, 33, 50
- Bandwidth, 41
 - diagnostic breadboard, 7
 - dither-lock, 16
 - frequency stabilization, 11, 100
 - photodetector, 9, 73, 99–101
 - pointing stabilization, 13
 - power stabilization, 76, 101, 105
- Battery power supply, 77
- Beam attenuator, 89, 96
- Beam parameter, 4
 - cross coupling, 44
- Beam quality, 5, 14
 - aberrations, *see* Aberration
 - fundamental power, 5, 15, 32, 49, 60, 61
 - measurement method, 14
 - mode-cleaner, 50
 - modescan, *see* Modescan
 - photonic crystal fiber laser, 35
 - stabilization, 49, 60
- Beam quality actuator
 - deformable mirror, 50
- Beat frequency, 46
- Bistability, 114
- Brewster angle, 72
- Brillouin scattering, 34
- Cabling, 77
- Calibration, 12–14, 23, 24, 73, 101, 123
 - accuracy, 78, 121
- Canonical quantization, 66, 67, 89
- Carrier amplitude, 65
- Carrier reduction, 85, 95, 121
- Characterization, 25
 - beam quality, 32, 35

Index

- frequency noise, 36
 - long-term, 28
 - pointing fluctuations, 30
 - power noise, 28, 33
- Coherent beam, 64–66
- Computer interface, 22
 - Advanced LIGO CDS, 23
 - laboratory, 22
- Control loop, 43
 - beam quality, 50
 - computer interface, 22
 - digital, 24
 - frequency stabilization, 11, 57, 100, 107, 108
 - multi-stage, 47
 - noise coupling, 56, 60
 - phase loss, *see* Phase loss
 - pointing stabilization, 13, 18, 48, 58
 - power stabilization, 54, 66, 76, 89, 101, 105, 106, 108, 109
 - sensor noise, 40
- Cooling, 32, 70, 72
- Corona, 33
- Countercirculating mode, 111, 119
 - scattering, *see* Resonator-int. scat.
- Coupling mechanism, 39, 53, 54, 57, 58, 75, 78, 106
- Cross coupling
 - beam parameters, 44
- Cryogenic, 36, 46
- Current source, 73

- DAQ, 20, 22, 24, 74, 76, 116
- DC-readout, 51, 54
- Deformable mirror, 49, 50
- Demodulation, 11, 12, 16
- Diagnostic breadboard, 7, 51
 - automation, 21
 - fabrication, 7
 - monitoring, 28
 - optical design, 7, 12, 18
 - remote control, 21
 - sensitivity, *see* Sensitivity
 - wavelength, 7
- Dither-lock, 11, 16, 46
- DWS, 12, 16, 18, 48, 59
- Dynamic range
 - actuator, 34, 41, 55
 - photodetector, 20

- Ellipticity, 6, 14, 33
- EOAM, 44, 75, 98, 106, 109, 116
- EOM, 44, 47, 51, 57, 75, 98, 104
- EPICS, 22, 24
- Etalon
 - power recycling mirror, 126
- Expectation value, 64, 65
- Experimental setup, 8, 71, 76, 99

- Faraday effect, 44
- Feedback control loop, *see* Control loop
- Fiber
 - amplifier, 34, 36
 - bundle, 32
 - laser, 36
 - spatial filtering, 48, 50
- Finesse, 11, 43, 49, 54, 59, 61, 75, 98, 100, 114, 120
- Flowbox, 30
- Fock states, 65
- Frame builder, 24
- Free-running noise, 39, 54
 - power, 77, 92, 95, 116, 118, 123
- Frequency actuator
 - AOM, 47
 - EOM, 47
 - PZT, 47
 - resonator length, 47
 - temperature, 47
- Frequency discriminator, 46
- Frequency noise, 5
 - Advanced LIGO laser, 32
 - erbium fiber laser, 36
 - measurement method, 10
 - quantum noise, 45
- Frequency offset, 107
- Frequency reference, 10, 46, 58
 - acoustic shielding, 11, 57
 - reference cavity, *see* Reference cavity
- Frequency stabilization, 45
 - actuators, 57, 76, 98
 - Advanced LIGO, 57
 - requirement, 57
 - review, 45
- Fringe locking, 46
- Frontend
 - computer, 23
 - laser, 31
- FSR, 11, 14, 43, 54, 61
- Functional prototype, *see* Adv. LIGO laser

- Fundamental mode, 5, 15, 32, 35, 60
- Fundamental power, *see* Beam quality
- Galvanometer scanner, 49
- Germanium, 13
- Glass filter
 - absorbing, 72
- Gouy phase, 15, 18, 49, 59, 61, 110, 112, 113, 115
 - fluctuations, 116
- Gravitational wave, 50
 - channel, 50, 53, 54, 57, 58, 60
 - detection band, 6
- Gravitational wave detector, 50
- Ground loop, 72, 76
- Hänsch-Couillaud, 46, 100, 103, 105
- Heater, 58, 61
- HEPA, 75, 79
- Hermite-Gaussian modes, 4, 6, 14
- High power detector, *see* Photodiode array
- High power oscillator, *see* Adv. LIGO laser
- Higher-order mode, 6, 14, 15, 17, 48, 86, 111, 113, 114
 - bistable, *see* Bistability
 - losses, 34, 112
 - scattering, *see* Resonator-int. scat.
 - suppressed, 49, 115
- Hyperfine transition
 - iodine, 46
- IMC, 33, 51, 53, 54, 56, 58–60, 77
- Impedance
 - electrical, 17
 - optical, *see* Impedance matching
- Impedance matching, 84, 85, 89, 100, 102, 104, 108, 113, 125
 - over-coupled, 85, 113, 121
 - under-coupled, 85, 100, 113, 121
- In-loop, 64, 66, 68, 72, 74–76, 89, 102
- InGaAs, 9, 21, 72, 99–101, 105
- Injection locking, 31, 51
- Interferometer
 - Fizeau, 46
 - Mach-Zehnder, 43, 46
 - Michelson, *see* Michelson interfer.
- Interlock, 10, 24, 100
- IO, 51, 58
- Iodine, 46
- Laser
 - Advanced LIGO, *see* Adv. LIGO laser
 - amplifier, 26, 34, 36
 - characterization, *see* Characterization
 - Enhanced LIGO, 26
 - erbium fiber laser, 36
 - master, 28, 31, 34
 - monitoring, 21
 - NPRO, *see* NPRO
 - photonic crystal fiber, 34
 - saturated amplifier, 43
 - stabilization, *see* Stabilization
- Lateral beam jitter, *see* Pointing fluct.
- Linear spectral density, 42, 45, 47, 69
 - definition, 66
- LISO, 17, 73
- Lock acquisition, 23, 24, 58
- Loop gain, 66, 89
 - bandwidth, *see* Bandwidth
 - high gain limit, 91
 - limited, 123
- Low frequency noise, 63
- Lowering operator, 65
- Master laser, *see* Laser
- Measurement band
 - diagnostic breadboard, 7
 - gravitational wave, 6
- Mechanical resonance, 79, 99, 123, 125
- Michelson interferometer, 46, 50
- Mirror transmission
 - angle dependence, 103
- MISER, *see* NPRO
- Modal analysis, *see* Modescan
- Modal weights, 4
- Mode fluctuations
 - optical ac coupling, 108
- Mode matching, 6, 13, 14, 22, 85, 98, 110
- Mode-cleaner, 33, 49, 60, 78, 125, *see also* Resonator
 - cascaded, 49
 - input mode-cleaner, *see* IMC
 - output mode-cleaner, 51
 - pre-mode-cleaner, *see* PMC
 - scattering, 117
 - spatial filtering, 12, 14, 15, 33, 45, 48, 75, 98, 104, 109
 - suspended, 53
 - temporal filtering, 16, 43, 46, 54, 56, 64, 85, 89, 91, 94, 102, 106, 117

Index

- Modescan, 13, 14, 20, 32, 35, 121
 - corona, 33
- Monte Carlo simulation, 60
- Nd:YAG, 26, 32
- Nd:YVO₄, 31
- Noise
 - quantum, *see* Quantum noise
 - resistor, *see* Resistor current noise
 - technical, 42, 45, 47, 64, 70
 - thermal, *see* Thermal noise
- Noise Eater, 26, 28, 98, 123
- Non-classical light, 64
- Non-resonant modes, 17, 86, 109
 - phase reference, 103
- NPRO, 26, 31, 34, 51, 56, 57, 75, 97, 98
 - characterization, 26
 - long-term, 28
 - Noise Eater, *see* Noise Eater
 - pointing fluctuations, 30
 - power noise, 28, 122
- Optical ac coupled detector, *see* Photodet.
- Optical ac coupling, 42, 83, 84
 - gain, 86
 - gravitational wave detector, 126
 - history, 124, 125
 - noise coupling, 106
 - power sensing experiment, 97, 101, 121
 - power stabilization experiment, 97, 101, 107, 113, 120, 123
 - quantum noise, 87
 - sensitivity, *see* Sensitivity
 - transfer function, 85, 86, 101, 116, 121, 122
- Optical resonator, *see* Resonator
- OptoCAD, 70
- Orthogonalization
 - alignment control loop, 18
- Out-of-loop, 64, 68, 72, 74–76, 88, 102
 - available power, 96
- Outgassing, 72, 119, 120
- Over-coupled, *see* Impedance matching
- Parasitic modes, 86, 95, 100, 103, 104, 116, 121, 125
- Paraxial approximation, 4
- PDH, 11, 32, 46, 51, 57, 75, 98, 104
- Phase loss, 106
- Phase modulation, 107
 - generation, 11, 16, 51, 53, 98
 - sidebands, 55, 75
- Phase noise, 45, 107
- Phase reference, 103
- Photodetector, 44, 54–56
 - array, *see* Photodi. array
 - electronic offset, 20
 - germanium, *see* Germanium
 - high dynamic range, 20
 - high-speed, 125
 - InGaAs, *see* InGaAs
 - low frequency noise, 63
 - optical ac coupled, 85
 - quadrant, 11, 12, 18
 - quantum efficiency, *see* Quantum eff.
 - silicon, *see* Silicon
- Photodiode array, 63, 70, 75
 - alignment, 72, 78
 - design, 70, 73
 - electronic noise, 74
 - pointing fluctuations, 72, 78
 - power stabilization, 75
 - responsivity, 74
- Photon number operator, 64, 89
 - expectation value, 65
 - linearized, 65
 - variance, 65, 89
- Piezoelectric element, *see* PZT
- PMC, 51, 56, 58, 60
 - Advanced LIGO, 60
- Pointing, 6
 - reference, 12, 48
 - reference system, 59
 - tilt and translation, 12, 18, 48
- Pointing actuator
 - deformable mirror, 49
 - EOM, 49
 - galvanometer scanner, 49
 - PZT, 49
- Pointing fluctuations, 6, 18, 108
 - acoustic coupling, 31
 - Advanced LIGO laser, 58
 - characterization, 30
 - coupling, 33, 44, 47, 58
 - environment parameters, 30
 - flowbox, 30
 - measurement method, 12
 - NPRO, 30

- photodiode, *see* Photodiode array
- quantum noise, 47
- Pointing modulation, 76
- Pointing projection, 19
- Pointing stabilization, 47, 60, 75, 98
 - Advanced LIGO, 58
 - requirement, 58
 - review, 47
- Pound-Drever-Hall, *see* PDH
- Power actuator
 - AOM, 44
 - dynamic range, 34, 55
 - EOAM, 44
 - Faraday effect, 44
 - laser pump power, 44
- Power fluctuations, 5
 - Advanced LIGO laser, 33, 55
 - gravitational wave band, 54
 - measurement method, 9
 - Noise Eater, *see* Noise Eater
 - NPRO, 28, 77, 121–123
 - quantum noise, 42, 64
 - radio frequencies, 56
 - relative, 5
 - sidebands, 84
- Power line coupling, 73, 78
- Power recycling, 51
- Power recycling cavity, 54, 126
- Power spectrum
 - definition, 65
- Power stabilization, 42, 60, 75
 - Advanced LIGO, 54, 70, 78
 - beam size, 79
 - case study, 95
 - control loop, *see* Control loop
 - feasibility, 123
 - gravitational wave detector, 126
 - history, 45
 - model, 66, 88
 - optical ac coupling, 89, 93, 94, 97
 - optimal, 91, 93–95
 - passive, 89–91
 - pointing fluctuations, 80
 - quantum limit, 66, 68, 69, 77, 87, 90–94
 - requirement, 54, 56
 - resonator filtering, *see* Mode-cleaner
 - result, 78, 124
 - schemes, 88, 92
 - technical limit, 95
 - traditional, 63, 64, 89, 91
- Pre-stabilized laser, *see* PSL
- Precursor experiment, 70
- Program, 23, 60
 - realtime, 24
- Propagation matrix, 110
- PSL, 51, 52, 60
- PZT
 - hysteresis, 14
 - interlock, 24
 - modulation, 16
 - nonlinearity, 14
 - NPRO, 57, 76, 98
 - resonator, 11, 14, 61, 98
 - tilt, 18, 49, 76
- Quantum efficiency, 67, 69, 74
- Quantum noise, 10, 29, 42, 44, 47, 56, 60, 64, 69, 74, 75, 87, 88, 121, 123
 - frequency, 45
 - gravitational wave detector, 51, 53
 - photocurrent, 69
 - pointing, 47
 - power noise, 42
 - power stabilization, *see* Power stab.
- Radiation pressure, 54
- Raising operator, 65
- Ray tracing, 103
- Rayleigh length, 20
- Realtime program, 24
- Reference cavity, 12, 53, 57, 58
- Relaxation oscillation, 26, 29, 43, 95, 97, 98, 122
 - model, 101, 121
- Residual frequency noise, 54, 107, 125
 - coupling transfer function, 108
- Residual pointing noise, 54, 108
- Resistor current noise, 44, 73
- Resonance circuit, 16, 17
- Resonant scattering, *see* Resonator-internal scattering
- Resonant sideband extraction, 51
- Resonator, *see also* Mode-cleaner
 - bow-tie, 61
 - confocal, 125
 - diagnostic breadboard, 10
 - field equations, 89
 - filter effect, *see* Mode-cleaner

Index

- frequency discriminator, 46
- frequency reference, *see* Freq. ref.
- high-finesse, 85, 89, 103
- model, 111
- noise coupling, 106
- rigid-spacer, 46, 49
- scattering, 117
- suspended, 46, 49
- transfer function, 43
- Resonator locking methods, 46
- Resonator-internal scattering, 40, 110, 112, 125
 - countercirculating mode, 119
 - fluctuations, 116
 - higher-order modes, 113
 - limited measurement, 116, 117
 - linear resonator, 120
 - model, 110, 111
 - projection, 117, 119
 - suppressed, 115, 120
 - two-mode model, *see* Two-mode m.
- RIN, *see* Power fluctuations
- RPN, *see* Power fluctuations
- Scattering
 - back scattering, 70, 72
 - BRDF, 119
 - resonator-internal, *see* Resonator-internal scattering
- Scattering matrix, 111
- Scattering strength, 112, 115
 - fluctuations, 117
 - noise spectrum, 120
- Sensitivity
 - Advanced LIGO, 53
 - diagnostic breadboard, 10, 12, 14, 15
 - optical ac coupling, 83, 85–87, 97, 121–124
 - photodiode array, 75, 78
- Shack-Hartmann sensor, 48, 50
- Shot noise, *see* Quantum noise
- Shutter, 10, 100
- Signal conditioning, 9, 20, 24, 73, 84
- Signal recycling, 51
- Silicon
 - photodiode, 13
 - test mass, 7, 36
- Stabilization, 39, 40
 - active, 40, 43
 - cascaded, 41, 54, 58, 59
 - hierarchical, 54, 57
 - multi-stage, 47
 - passive, 40
- Tank, 11, 45, 47, 57, 58, 62, 70, 73, 75, 77, 79, 99
- TEM, *see* Fundamental mode, *see* Hermite-Gaussian modes, *see* Higher-order mode
- Temperature control, 58, 61, 76, 98
- Thermal aberration, 50, 60
- Thermal drift, 78
- Thermal effects, 70
- Thermal lens, 50
- Thermal lowpass, 112, 115
- Thermal mirror deformation, 112, 113
- Thermal noise, 47, 53
- Thermo-sensitive paper, 72
- Tidal force, 58
- Tilt, 13, 18, 49, 100, 102, 103
 - scattering, 115
- Tilt locking, 46, 104
- Time delay, 24
 - phase loss, *see* Phase loss
- Transmission lock, *see* Dither-lock
- Two-mode model, 111, 114
- Under-coupled, *see* Impedance matching
- Vacuum, 47, 52, 55, 57, 77, 79
- Vacuum compatible, 70, 72
- Vacuum fluctuations, 66–68, 89, 91, 94
- Vacuum state, 65
- Variance, 65
 - spectral, 65
- Zener diode, 21

About the Author

Patrick Kwee, born on 10th June 1979 in Hannover, Germany, received the Abitur from Schillerschule Hannover in 1998 and afterwards fulfilled alternative civilian service. He studied physics at the University of Hannover, spending one year abroad at the NUI Maynooth, Ireland, and received the diploma degree in physics in 2005 for work on laser system characterization. Since then, he is a research associate at Max-Planck-Institut für Gravitationsphysik (Albert-Einstein-Institut) and Leibniz Universität Hannover. He got a scholarship from the International Max Planck Research School on Gravitational Wave Astronomy and is currently employed by the Cluster of Excellence QUEST (Centre for Quantum Engineering and Space-Time Research).